TECHNISCHE UNIVERSITÄT MÜNCHEN
Fakultät für Chemie

Solver development and application of dense fluid-solid flows using CFD

Daniel Jakob Hirche

Vollständiger Abdruck der von der Fakultät für Chemie der Technischen Universität München zur Erlangung des akademischen Grades eines

Doktors der Ingenieurwissenschaften (Dr.-Ing.)

genehmigten Dissertation.

Vorsitzender: Hon.-Prof. Dr. Richard W. Fischer

Prüfer der Dissertation: 1. Prof. Dr.-Ing. Kai-Olaf Martin Hinrichsen
2. Prof. Dr.-Ing. Hartmut Spliethoff

Die Dissertation wurde am 21.02.2022 bei der Technischen Universität München eingereicht und durch die Fakultät für Chemie am 04.08.2022 angenommen.

Danksagung

Während meiner Promotion haben mich zahlreiche Personen begleitet, beraten und unterstützt. Im Folgenden möchte ich mich bei allen Beteiligten bedanken.

Als erstes gilt ein großer Dank meinem Doktorvater, Herrn Prof. Dr.-Ing. Kai-Olaf Hinrichsen. Danke für das erbrachte Vertrauen, mir die Chance zu geben, in Ihrer Arbeitsgruppe zu promovieren und meine eigenen Ideen umzusetzen. Durch Sie konnte ich meine Forschungsergebnisse auf zahlreichen nationalen und internationalen Konferenzen vorstellen. Sie hatten trotz Ihres vollen Terminkalenders immer ein offenes Ohr, falls es Probleme, Schwierigkeiten oder Unstimmigkeiten gab. Vielen Dank für die Betreuung der letzten Jahre!

Weiterhin spreche ich einen Dank an alle meine ehemaligen Kollegen am Lehrstuhl aus. Durch die zahlreichen Kaffee-Runden (auch für mich als Tee-Trinker), gemeinschaftliche Mittagessen, Feierabendbiers und Aktivitäten außerhalb des Lehrstuhls, konnte ich auch mal vom Alltagsstress abschalten. Neben den fachlichen Aspekten konnte man auch über private Angelegenheiten sprechen und alle hatten ein offenes Ohr dafür. Danke an Chris, Flo, Jennie, Johanna, Julia, Matthias, Moritz, My, Nini, Philipp, Sebastian, Stefan, Tabea und Thomas.

Ohne die Zusammenarbeit mit Heidi wäre meine Promotion nicht möglich gewesen. Danke für all die Hilfe, die du mir gerade im bürokratischen Dschungel "Universität" gegeben hast. Du warst immer da, hast uns geholfen und für uns gekämpft, wo es nur möglich war.

Ein weiterer Dank geht an Dr. Thomas Michel. Du hast uns sehr oft den Rücken freigehalten. Ich erinnere mich gerne an die schönen Diskussionen mit dir in der Kaffeeküche zurück.

Durch die zahlreiche Unterstützung der TC2 könnten wir den grandiosen Sieg als Underdog während des Fussballturniers der Fakultät Chemie einheimsen (aber leider nicht mehr verteidigen). Danke an alle Beteiligten der Fussballtruppe!

Während der Promotion haben mich zahlreiche Studenten begleitet, die bei mir eine Abschlussarbeite schreiben "durften". Ich hoffe, ihr alle habt während der Zeit am Lehrstuhl Spaß gehabt und ich konnte euch die Thematik von CFD näherbringen. Viele Dank an Alamelu, Barbara, Dan-Ioan, Dilbeste, Fabi, Katharina, Lucas, Michi, Ng Wei, Nini, Rebecca und Sei-Toh.

Und zu guter Letzt will ich mich bei meiner Familie und Freundin bedanken. Danke an meine Mutter und Vater, dass ihr mir über all die Jahre das Studium finanziert und mir bei Problemen immer zur Seite gestanden habt. Meinem Bruder bin ich zu großem Dank verpflichtet, da er mich gerade zu Anfang des Studiums sehr unterstützt hat. Danke auch an meine Freundin, die mich während der Promotion und den manchmal daraus resultieren Gefühlsschwankungen ertragen hat und zu mir gestanden ist. Ebenfalls ein Dankeschön an die vierbeinige Fellnase zu Hause. Egal wie gestresst ich war, sie hat sich immer überschwenglich gefreut, mich zu sehen.

Abstract

The need for simulations in the field of fluidization technology became more urgent, as experimental set-ups are expensive and time-consuming. Multiple parameter studies can be set-up with simulations and due to the increasing computational power over the last years, the simulation speed increased immensely. The numerical simulation of multiphase flows regarding fluid-solid flows can be performed with different modeling approaches.

In this thesis, the most common models, i.e., the Two-Fluid Model, CFD-DEM, the Coarse-Grain method and Multiphase Particle-In-Cell, were used, evaluated and compared to newly developed solvers. Those developed solvers had the purpose to increase the accuracy of the results or speed up the numerical simulations. One of the newly developed solvers aims to bridge the gap between the Two-Fluid Model and CFD-DEM. Opposed to a solver based on the Multiphase Particle-In-Cell method, using this solver, the particles are treated in a Eulerian and a Lagrangian way, a hybrid approach. The number of particles treated in their respective manner is set by a user-defined ratio. With this ratio, the simulation set-up gains an additional degree of freedom; more particles treated in a Lagrangian way result in more accurate simulation results, while a higher ratio for a Eulerian treatment of the particles decreases the simulation time drastically. The solver was validated with experimental data from literature and compared to solvers using conventional methods, such as the Two-Fluid Model, CFD-DEM and the Multiphase Particle-In-Cell method. Depending on the particle properties and size of the reactor, the newly developed hybrid solver shows advantages in flexibility and therefore the accuracy and simulation speed can be adjusted based on the number of particles treated as Lagrangian or Eulerian particles. Further adjustments for the solver can be made, e.g., a more sophisticated algorithm for determining the positions of transforming Eulerian to Lagrangian particles. This could improve the accuracy of the simulation results.

Further modifications for CFD-DEM solvers have been proposed in this thesis to increase the accuracy of CFD-DEM simulations. Conventional CFD-DEM solvers use a single grid for calculations of both the fluid phase and the particles. A dual-grid approach was proposed in literature where another numerical grid is introduced and the calculation of the fluid phase and Lagrangian particles are decoupled in regards to the numerical grid.

Problems could arise with the dual-grid approach when the Lagrangian grid is too coarse. Here, a solver was developed, adding a third grid. On this third grid, important parameters for the fluid-particle coupling, as well as properties used for results, e.g., particle velocities, are calculated and mapped onto the fluid or the solid grid. Overall improvements were visible in terms of accuracy when using the three-grid solver compared to a single-grid and dual-grid solver. The additional time for the parameter-interpolation due to the third grid is, however, negligible.

A CFD-DEM simulation was performed to improve the efficiency of fouling mitigation in an anaerobic fluidized bed membrane bioreactor. First, the solver was validated with experimental data from literature and in a second step the geometry of the reactor was modified to increase particle momentum and hence fouling mitigation. Different particle diameters were investigated, as well as different extents of geometry changes. Depending on the geometry and particle diameters, a uniform distribution of particle momentum and therefore fouling mitigation over the whole membrane area is not guaranteed. With geometry changes of the reactor and the right choice of particle diameter an optimum uniform fouling mitigation with a low energy input used for fluidizing the particles can be achieved.

Kurzzusammenfassung

Der Einsatz von Simulationen im Bereich der Fluidisierungstechnologie wird immer präsenter, da experimentelle Aufbauten oft teuer und zeitaufwändig sind. Mehrere Parameterstudien können durch Simulationen aufgesetzt werden und durch die steigende Rechenkapazität der letzten Jahre ist die Rechengeschwindigkeit ebenfalls stark gestiegen. Die numerische Simulation von Mehrphasenströmung unter der Berücksichtigung von Fluid- und Feststoffströmungen kann unter Zuhilfenahme von verschiedenen Modellierungsansätzen realisiert werden.

In dieser Arbeit wurden die gängigsten Modelle, wie das Two-Fluid Model, CFD-DEM, die Coarse-Grain Methode und Multiphase Particle-In-Cell, verwendet, evaluiert und mit neu entwickelten Solvern verglichen. Diese entwickelten Solver hatten das Ziel die Genauigkeit der Ergebnisse, sowie die Geschwindigkeit der numerischen Simulation zu steigern. Einer der neu entwickelten Solver hat das Ziel die Lücke zwischen dem Two-Fluid Model und CFD-DEM zu füllen. Anders als die Multiphase Particle-In-Cell Methode werden mit diesem Solver die Feststoffpartikel in einem hybriden Ansatz als Euler und Lagrange-Partikel berücksichtigt. Mithilfe eines vom Benutzer bestimmten Verhältnisses kann die Anzahl der Euler oder Lagrange-Partikel festgelegt werden. Mit diesem Verhältnis bekommt die Simulationen einen zusätzlichen Freiheitsgrad; mehr Lagrange-Partikel resultieren in genaueren Ergebnissen, wohingegen mehr Euler-Partikel die Simulationszeit drastisch verkürzen. Der Solver wurde durch experimentelle Daten aus der Literatur validiert und mit anderen Solvern verglichen, die herkömmliche Ansätze verwenden, wie das Two-Fluid Model, CFD-DEM und die Multiphase Particle-In-Cell Methode. Abhängig von den Partikeleigenschaften und der Reaktordimension zeigte der neu entwickelte Solver Vorteile im Bereich der Flexibilität und dadurch konnte die Genauigkeit der Ergebnisse und die Simulationsgeschwindigkeit durch die Anzahl an Euler- und Lagrange-Partikel eingestellt werden. Um die Genauigkeit der Simulationsergebnisse weiter zu verbessern kann ein komplexerer Algorithmus zur Positionsbestimmung bei der Transformation von Euler- zu Lagrange-Partikeln implementiert werden.

Weitere Modifikationen für CFD-DEM Solver wurden in dieser Arbeit erarbeitet, um die Genauigkeit von CFD-DEM Simulationen zu erhöhen. Konventionelle CFD-DEM Solver

verwenden ein einzelnes numerisches Rechengitter, um sowohl die Fluid als auch die Feststoffphase zu berechnen. In der Literatur wurde ein *dual-grid* Ansatz vorgeschlagen, bei dem ein zusätzliches numerisches Rechengitter eingeführt wird, wodurch die Berechnung der fluiden und festen Phase auf verschiedenen Rechengittern durchgeführt und damit entkoppelt wird. Durch Wahl eines zu groben Lagrange-Rechengitters können jedoch Probleme entstehen. In dieser Arbeit wurde ein Solver entwickelt, bei dem ein drittes numerisches Rechengitter eingeführt wird. Mithilfe dieses dritten Rechengitters werden wichtige Parameter für die Kopplung von Fluid und Feststoff, sowie wichtige Vergleichsparameter, z.B. Partikelgeschwindigkeiten, berechnet und auf die anderen beiden Fluid- und Feststoffgitter übertragen. Allgemein wurden Verbesserungen der Genauigkeit der Simulationsergebnisse durch den Einsatz des *three-grid* Solvers im Vergleich zu Solvern mit einem *single-* und *dual-grid* beobachtet. Die zusätzliche Simulationszeit bedingt durch das dritte numerische Rechengitter und die dadurch entstehenden Interpolationen fällt gering aus und kann vernachlässigt werden.

Simulationen auf Basis von CFD-DEM wurden durchgeführt, um die Effizienz der Ablagerung von Fouling in anaeroben Wirbelschicht-Biomembranreaktoren zu verbessern. In einem ersten Schritt wurde der Solver mithilfe von experimentellen Daten aus der Literatur validiert und anschließend wurde die Geometrie des Reaktors modifiziert, um den Partikelimpuls zu erhöhen und damit auch die Foulingablagerung zu minimieren. Es wurden verschiedene Partikelgrößen und Geometrien untersucht. Abhängig von der Reaktorgeometrie und der Partikelgröße kann eine gleichmäßige Verteilung des Partikelimpulses auf die Membran nicht garantiert werden. Durch eine Änderung der Geometrie und der Wahl einer passenden Partikelgröße kann ein Optimum aus gleichmäßiger Foulingverhinderung mit gleichzeitigem geringen Energieeintrag, der notwendig für die Fluidisierung der Partikel ist, erreicht werden.

Nomenclature

Latin Symbols

A	area	m^2
$\mathbf{a}$	acceleration	$\mathrm{m/s}^2$
a	modeling parameter	-
b	parameter for spring theory	-
C	coefficient	-
Co	Courant number	-
$\overline{\overline{D}}$	strain rate tensor	$1/\mathrm{s}$
d	diameter	m
e	coefficient of restitution	-
E	Young's modulus	$\mathrm{kg/(m\,s^2)}$
$\mathbf{F}$	force	$\mathrm{kg\,m/s}^2$
F	dimensionless drag force	-
F_f	face flux	$\mathrm{kg/s}$
Fr	empirical constant	-
f	factor	-
f	Liouville equation	-
f_x	interpolation factor	-
Ga	Galileo number	-
$\mathbf{g}$	gravitational acceleration	$\mathrm{m/s}^2$
g_0	radial distribution function	-
H	height	m
h	height	m
h	representative grid size	m
I	moment of inertia	$\mathrm{kg\,m}^2$
$\overline{\overline{I}}$	unit tensor	-
$\mathbf{I}$	cell-averaged particle momentum	$\mathrm{kg\,m/s}$
J_s	dissipation of energy	$\mathrm{kg/(m\,s}^3)$
k	spring stiffness	$\mathrm{kg/s}^2$
l	impediment length	m

l	length	m
m	mass	kg
$\mathbf{M}$	momentum per unit volume	$\mathrm{kg}/(\mathrm{m}^2\,\mathrm{s}^2)$
M_{red}	reduced mass	kg
N	total number	-
$\mathbf{n}$	unit vector in normal direction	-
n	number	-
P	Power	W
P	empirical constant	-
p	pressure	$\mathrm{kg}/(\mathrm{m}\,\mathrm{s}^2)$
P_{s}	modeling parameter	-
q	function for GCI calculation	-
R_{L}	ratio of L-Particles to all particles	-
$\mathcal{R}$	sum of discretized terms	-
Re	Reynolds number	-
r	radius	m
r	refinement factor	-
S	surface area	m^2
$\overline{\overline{T}}$	stress tensor	$\mathrm{kg}/(\mathrm{m}\,\mathrm{s}^2)$
$\mathbf{T}$	torque	$\mathrm{kg}\,\mathrm{m}^2/\mathrm{s}^2$
$\mathbf{t}$	unit vector in tangential direction	-
T	diffusion time	s
t	time	s
U_{r}	ratio of terminal velocities	-
$\mathbf{u}$	velocity	m/s
$\mathbf{u}_0$	superficial velocity	m/s
V	volume	m^3
w	blending function for HKL-drag correlation	-
x	axis coordindate	m
y	axis coordindate	m
z	axis coordindate	m

Greek Symbols

α	volume fraction	-
α_{n}	empirical constant	-
β	momentum exchange coefficient	$\mathrm{kg}/(\mathrm{m}^3\,\mathrm{s})$
Γ	arbitrary diffusivity	a.u.
γ	blending factor	-
γ_{s}	energy dissipation due to collisions	$\mathrm{kg}/(\mathrm{m}\,\mathrm{s}^3)$

Δ	difference	-
δ	difference of solutions	-
ϵ^{d}	discretization error	-
ε	volume fraction fluid phase	-
ζ	bulk viscosity	$\mathrm{kg}/(\mathrm{m\,s})$
η	shear viscosity	$\mathrm{kg}/(\mathrm{m\,s})$
η	damping coefficient	-
θ_{s}	granular temperature	$\mathrm{m}^2/\mathrm{s}^2$
κ_{s}	granular thermal conductivity	$\mathrm{kg}/(\mathrm{m\,s})$
μ_{f}	Coulomb friction coefficient	-
μ_{fr}	friction coefficient	-
ν	Poisson ratio	-
ν	kinematic viscosity	m^2/s
ρ	density	kg/m^3
$\overline{\overline{\tau}}$	viscous stress tensor	$\mathrm{kg}/(\mathrm{m\,s}^2)$
τ	pseudo-time	s
τ_{e}	turnover time of large eddies	s
τ_{K}	Kolmogorov time scale	s
τ_{p}	particle response time	s
Φ	extensive property	a.u.
ϕ	intensive property	a.u.
ϕ	angle of internal friction	$^\circ$
ψ	sphericity	-
ω	angular velocity	$1/\mathrm{s}$

Sub- and Superscript

b	buoyancy
BD	Blended Differencing
bf	bubbling fluidization
bg	background
bub	bubble
c	contact
c	coarse
CD	Central Differencing
CG	coarse grain
col	collisional
d	drag
E	Eulerian
EE	Eulerian-Eulerian

EEL	Eulerian-Eulerian-Lagrangian
EL	Eulerian-Lagrangian
eff	effective
ext	extrapolated
f	fine
f	fluid phase
f	face
g	gravity
g	gas phase
kin	kinetic
L	Lagrangian
max	maximum
mf	minimum fluidization
N	neighbor cell
n	empirical constant
n	normal
nc	non-contact
norm	normalized
ol	overlap
orig	original
P	owner cell
p_ϵ	exponent
p	particle
rel	relative
s	solid phase
sv	surface specific
t	tangential
UD	Upwind Differencing
vm	virtual mass
w	wall

Abbreviations

AeMBR	Aerobic Membrane Bioreactor
AnMBR	Anaerobic Membrane Bioreactor
AnFMBR	Anaerobic Fluidized Membrane Bioreactor
CFD	Computational Fluid Dynamics
CG	Coarse Grain
CPU	Central Processing Unit
CV	Control Volume

D	Dual-grid
DPVM	Divided Particle Volume Method
DEM	Discrete Element Method
DFT	Density Functional Theory
DNS	Direct Numerical Simulation
FCC	Fluid Catalytic Cracking
FDM	Finite Difference Method
FEM	Finite Element Method
FVM	Finite Volume Method
GAC	Granular Activated Carbon
GCI	Grid Convergence Index
GPU	Graphical Processing Unit
H&G	Huilin and Gidaspow
HKL	Hill-Koch-Ladd
IBM	Immersed Boundary Method
LBM	Lattice-Boltzmann Method
LPT	Lagrangian Particle Tracking
MBR	Membrane Bioreactor
MP-PIC	Multiphase Particle-In-Cell
PAC	Powdered Activated Carbon
PCM	Particle Centroid Method
PEPT	Positron Emission Particle Tracking
PET	Polyethylene Terephtalate
S	Single-grid
S&O	Syamlal and O'Brien
T	Three-level Grid
TFM	Two-Fluid Model
TMP	Transmembrane Pressure
W&Y	Wen and Yu

Contents

1 Introduction

1.1 Motivation

The state of fluidization of particles occurs if the resulting drag force of a fluid flow through a bed of resting particles equals the weight of said particles. Then, the solid phase is suspended in the fluid phase and the particle bed behaves like a fluid, hence the term *fluidization*. Fluidization can occur between a wide range of fluid and solid phase combinations, as well as different particle sizes. The average particle size in a fluidized bed lies between 30 µm and 2 cm [1]. Fluidized beds are used in industrial-scale units for both catalytic and non-catalytic processes. The first commercial fluidized bed reactor dates back to the early 1920s when the first operating fluidized bed was utilized for the process of coal gasification by Winkler known as the High-Temperature-Winkler process [2]. The most prominent application of a fluidized bed reactor might be the process of Fluid Catalytic Cracking (FCC) to produce gasoline and other petroleum products from crude oil. The first FCC units were built in 1942 at the Baton Rouge Refinery in Louisiana, US by a company which is now known as ExxonMobil [3]. Here, a fluidized bed of particles is used to carry over energy in form of heat between the different reactors. Heavier hydrocarbons are cracked down to lower hydrocarbons in the riser reactor. The employment of the first fluidized bed reactor for an FCC unit was the beginning of other companies using the fluidization technology incorporating to industrial-scale chemical processes. In the later years more and more commercial units with fluidized bed reactors were applied, such as reactors used for naphthalene oxidation to synthesize phthalic anhydride or polyethylene production plants by Dow Chemical [1, 4, 5]. Also non-catalytic fluidized bed reactors were used for roasting of sulfide ores by BASF, calcination of lime, dolomite and clay or for power generation [1]. The Synthol process introduced by Sasol in 1955 employed a fluidized bed reactor combining the Lurgi and the Fischer-Tropsch process. The Lurgi process was used for synthesis gas production with the reaction of steam and coke, while the Fischer-Tropsch process converted the synthesis gas to light oils and gasoline [4]. At first a dense bubbling fluidized bed reactor was used for this process. A scale-up was performed from a pilot-scale plant to an industrial-scale unit with a diameter of 7 m. While the yield of the pilot-plant was satisfactory, it

dropped by 50 % in the industrial-scale used unit. Hence, the dense bubbling fluidized bed was replaced by a circulating fluidized bed to increase heat-exchange and gas-solid mass transfer rates, resulting to higher yields in the commercial unit. This example was one of the turning points in the research of fluidized beds and reactors. Before this, most of the research was done by experiments with rudimentary data capturing techniques, e.g., simple visual images taken with a camera of a bubbling fluidized bed or pressure drop measurements [4]. Since the 1950s more attention was paid to more sophisticated experimental data capturing gadgets, e.g., using X-ray [6] or optical sensors [7]. Also this was the start of the theoretical research of fluidized beds. Toomey and Johnstone [8] and Mickley and Fairbanks [9] were the first proposing a two-phase theory to model bubbling fluidized beds. More and more novel techniques for experimental data acquisition became available, like Positron Emission Particle Tracking (PEPT) [10] to track individual particles based on their positions to conclude on their axial and horizontal velocities on a moving fluidized bed. Also the modeling approaches have been enhanced to account for emulsion phases and chemical reactions for a better understanding of the hydrodynamics in the fluidized bed (cf. Foscolo and Gibilaro [11]). Furthermore, mapping regimes and classification of fluidization types based on particle and fluid properties, as well as superficial velocities were proposed [12, 13]. The 1990s marked the beginning of Computational Fluid Dynamics (CFD) to use numerical simulations in order to depict the hydrodynamics of multiphase flows. CFD provides a far better insight into the dynamics of a fluidized bed than the modeling approaches proposed so far. The use of a numerical simulation, e.g., CFD, is extremely computational expensive and was only possible at this time due to the increasing computing power; computational processors were increasing in performance and the production costs sank rapidly. Discrete Element Method (DEM) based approaches coupled with CFD were first proposed by Tsuji et al. [14] to solve multiphase flows consisting of a fluid and particles. The particles were tracked individually with a Lagrangian Particle Tracking (LPT) algorithm. More approaches, like the Two-Fluid Model (TFM), to solve fluid-solid multiphase flows for industrial-scale geometries were introduced [15]. In recent years, novel experimental techniques were presented, using magnetic resonance imaging [16] for exact measurements to capture, for example bubble expansions or bubble rise velocities precisely in three-dimensional fluidized beds. The work in the numerical simulation of multiphase flow switches to the use of Graphical Processing Units (GPU) instead of Central Processing Units (CPU) to increase the simulation speed for a more detailed simulation of particles including chemical reactions [17, 18].

There exists a vast variety of different software-packages for CFD simulations. The most used commercial software-packages in the field of academic research and industrial application include the ANSYS® framework of CFX® and Fluent®, as well as COMSOL® Multiphysics. Popular open-source software for the simulation of multiphase flows are for

example MFIX® or the C++ based software OpenFOAM®. Nowadays, the technology of fluidization of particles is used in many different areas of industrial-scale operations, e.g., physical, chemical, petrochemical, electrochemical and biochemical operations [19, 20]. Although the study of fluidization processes has been going on for over 100 years, many uncertainties still have to be unraveled. Due to the increasing computational power over the last decades, more and more simulations instead of experiments are used to investigate fluid-solid interactions.

1.2 Outline

This work is focused on the numeric simulation of multiphase flows by means of CFD. The multiphase flows consist of either a gas-solid or a liquid-solid flow. The main application for these types of flows in the simulations are fluidized bed reactors. Different models for the numeric simulation of multiphase flows are used in the following, including Eulerian-Eulerian and Eulerian-Lagrangian approaches with some of their respective sub-models, i.e., a Coarse Grain (CG) model and the Multiphase Particle-In-Cell (MP-PIC) method. All simulations were carried out using the open-source C++ based software package OpenFOAM® version 4.1 due to its highly modifiable source code and vast CFD community. Solvers were created and modified to accelerate simulations, make them more robust and to increase accuracy. Also, simulations were performed to study a novel-reactor approach using CFD-DEM.

Chapter 2 presents the theoretical work in the study of fluidized bed reactors and the numerical simulation of multiphase flows. Particular focus is set on the discretization of the generic transport equation, the simulation of fluid-solid flows using different CFD approaches, as well as the determination of the drag coefficient to couple the fluid and solid phases.

Chapter 3 compares the most widely used CFD model for simulating gas-solid flows in a fluidized bed: TFM, CFD-DEM and MP-PIC. Additionally, a new solver was developed, combining TFM and CFD-DEM to increase simulation speed and accuracy when necessary and applicable. The newly developed solver is investigated based on accuracy, robustness and simulation speed and is compared to TFM, CFD-DEM and MP-PIC. Different types of fluidized bed reactors from literature are used for validating and comparing the different approaches. This chapter was published in a similar way in:
D. Hirche, F. Birkholz, O. Hinrichsen, "A hybrid Eulerian-Eulerian-Lagrangian model

for gas-solid simulations", *Chemical Engineering Journal* **2019**, *377*, 119743, DOI 10.1016/j.cej.2018.08.129.

Chapter 4 presents an extended version of a dual-grid approach for CFD-DEM simulations. Here, an additional third grid is introduced to increase the accuracy for the Eulerian and Lagrangian coupling and to extend the somewhat limited applicability of CFD-DEM simulation due to the cell-size to particle size requirement to a wider range, while also increasing the fluid flow resolution. The newly developed three-grid approach is validated with different fluidized and spouting bed set-ups, both 2D and 3D, and compared to a conventional single-grid and dual-grid approach. Furthermore, the CG method is applied to increase the simulation speed. This chapter was published in a similar way in:
D. Hirche, O. Hinrichsen, "Implementation and evaluation of a three-level grid method for CFD-DEM simulations of dense gas-solid flows", *Chemical Engineering Journal Advances* **2020**, *4*, 100048, DOI 10.1016/j.ceja.2020.100048.

Chapter 5 applies CFD to model a fluidized bed in an anaerobic membrane bioreactor for wastewater treatment. After an initial validation of the used CFD-DEM solver with experimental data from literature, changes of the reactor geometry are made to enhance fouling mitigation of the membrane and therefore increase energy efficacy of the overall process. This project was done in collaboration with the research group of Professor Jia Wei Chew from the School of Chemical and Biomedical Engineering, Nanyang Technological University in Singapore. Funding was received from the Federal Ministry of Education and Research of Germany (project number 01DP16014) and the Joint Singapore-Germany Research Project Fund (SGP-PROG3-019). This chapter was published in a similar way in:
D. Hirche, J.W. Chew, O. Hinrichsen, "CFD-DEM study of geometry changes in an AnFMBR towards particle momentum", *Chemical Engineering Journal* **2020**, *379*, 122336, DOI 10.1016/j.cej.2019.122336.

2 Theoretical Background on Multiphase Flows

Multiphase flows consisting of a fluid and solid phase can be comprised of a gas or liquid as a continuum. Before discussing the numerical approaches for solving gas-solid or liquid-solid flows in Computational Fluid Dynamics, the state of fluidization will be defined.

2.1 Fluidized Bed Reactors

Fluidization describes the process of a fluid flowing through a bed of resting particles with a certain velocity so that the particles begin to move. A fluid flow through a bed of resting particles where the velocity is not great enough to fluidize the particles is called a fixed bed reactor or a flow through a packed bed. When the fluid velocity reaches a certain threshold, the minimum fluidization velocity $\mathbf{u}_{\mathrm{mf}}$, the particles are fluidized by the fluid flow. The term *fluidization* is used as the fluidized particle bed behaves like a fluid. This can be best illustrated when an object with a low density is brought into a fluidized bed. Depending on the intensity of the fluidization, the bed density changes, i.e., higher gas velocity equals higher bed gas fraction and therefore lower bed density. So the object can either float on top of the fluidized particles, sink into the bed or remain in the initial position. The sunk object can also surface to the top once the fluidization is stopped as the density of the bed increases. Furthermore, the surface of a fluidized bed when the reactor is tilted moves according to the tilt angle. A horizontal surface is the result analog to a liquid tilted in a container [5]. Depending on the fluid properties, fluid flow velocity and particle properties, certain fluidization states can occur. The particle size has a higher impact on the fluidization behavior than the density or shape of the particles [1]. Figure 2.1 gives an overview of different states a fluidized bed can have.

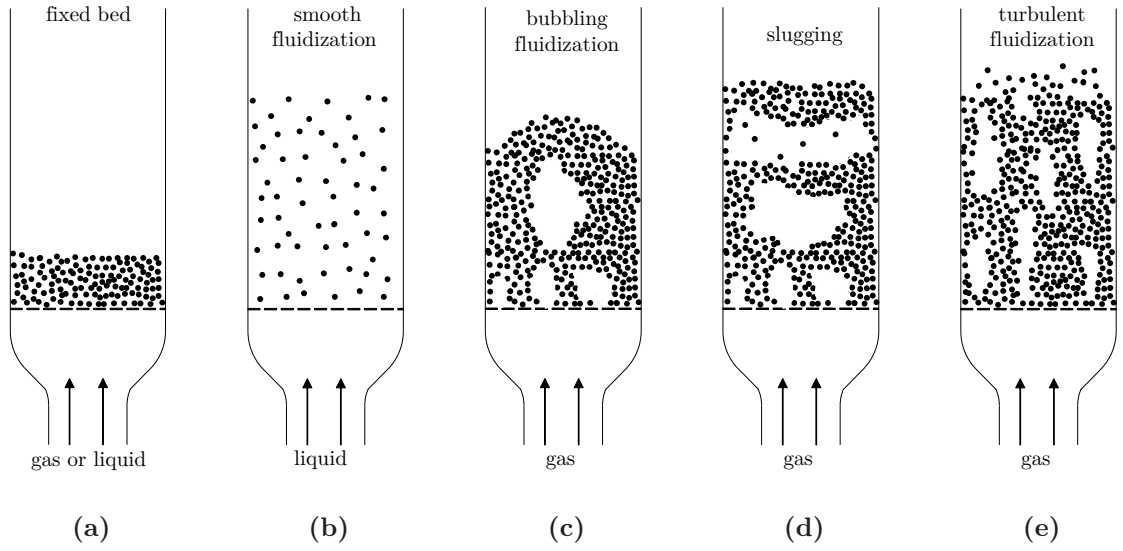

Figure 2.1: Different states of a flow through a particle bed with increasing fluid velocities for an upward flow (modified from [5]).

Figure 2.1a describes not a state of a fluidized bed, but a fixed bed. Here, the minimum fluidization velocity is not reached yet by the fluid flow and thus, the particles are still resting in a particle bed. Once the fluid flow reaches the minimum fluidization velocity $\mathbf{u}_{\mathrm{mf}}$, a fluidized state occurs as the particles are suspended in the fluid. At this point the particles are still resting and therefore this state can not be visually distinguished from the fixed bed state. A slight increase in the fluid flow results into an expansion of the particle bed (cf. Figure 2.1b and 2.1c). Here, the fluid and particle properties play an important role on the different occurring fluidized states of the bed. For liquid-fluidizations, i.e., the fluid is comprised of a liquid, the fluidized bed transitions to a smooth expansion of the bed while with a gas, bubbles begin to form while the bed expands. For certain types of particles, also a smooth fluidization can occur while using a gaseous flow as a continuous phase. Bubbles begin to form if a certain fluid flow velocity is exceeded, called the minimum bubbling velocity $\mathbf{u}_{\mathrm{bf}}$. A further increase in fluid flow velocity results in an increase in bubble size and bubble rise velocity. In the state of slugging fluidization (cf. Figure 2.1d) the bubble size can occupy the whole cross-sectional area of the reactor. The turbulent fluidization in Figure 2.1e is characterized by turbulent motions of particle clusters and bubbles disappear as clear boundaries can not be observed. Furthermore, entrainment occurs, i.e., carryover of particles out of the reactor.

Particles of different sizes and densities fluidized by air result in different fluidization behaviors. Geldart [12] summarized experimental findings and correlations to classify fluidized particles based on their fluidization behavior. The so-called Geldart diagram (cf. Figure 2.2) is used for the determination of which kind of fluidization will occur based on the particle-air system.

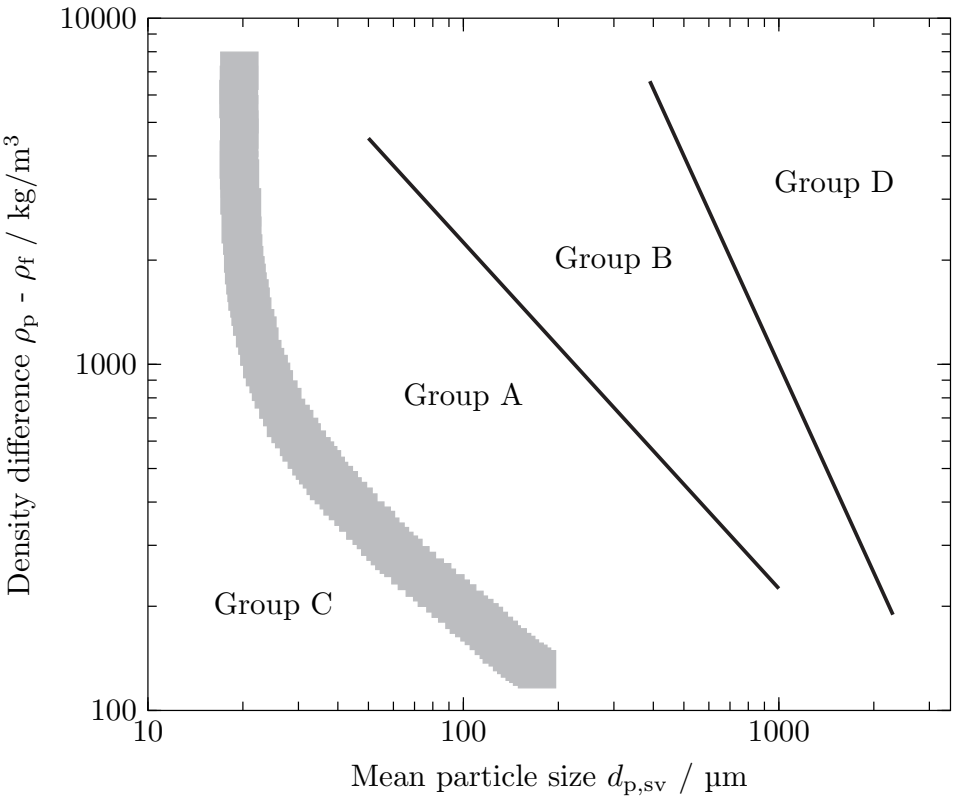

Figure 2.2: Powder classification in different groups based on particle properties (specific surface diameter $d_{p,sv}$ and density difference of solid and gas phase $\rho_p - \rho_f$) and fluidization behaviors by air (modified from [12]).

The particles are classified in four groups:

Group A: Fluidized beds consisting of particles with a rather small diameter and/or low density are prone to exhibit an expansion before bubbling occurs when fluidized with air. Typical particles belonging to the group A Geldart classification include cracking catalysts.

Group B: Small to medium sized particles with a density of $400\,\mathrm{kg/m^3} < \rho_p < 1400\,\mathrm{kg/m^3}$ are described by group B. Here, above the point of minimum fluidization bubble formation starts. Sand is a typical material that can be classified as group B according to this classification.

Group C: Group C particles according to the Geldart classification are cohesive particles and have small sizes. They are difficult to fluidize unless additional agents are added or

external forces, e.g., in form of a stirrer, are applied. Milk powder can be classified as a group C particle due to its cohesive property.

Group D: Particulates with large diameters and/or high densities are classified by group D particles. Bubbling formation occurs and due to the relatively high mass of the particles and great interstitial velocities during the fluidization, attrition of the particles might be a problem. Most of the fluidized beds based on this group of particles can be categorized as spouted fluidized beds. Coffee beans during the process of coffee roasting is a typical group D particle according to the Geldart classification.

The boundary between Geldart group A and B particles can be found by using the following correlated quantity equation:

$$\frac{d_\mathrm{p}}{\mu\mathrm{m}} \cdot \frac{(\rho_\mathrm{s} - \rho_\mathrm{f})}{\mathrm{kg/m^3}} = 2.25 \cdot 10^5. \tag{2.1}$$

Furthermore, to distinguish group B and D particles, the following equation can be used:

$$\frac{d_\mathrm{p}^2}{\mu\mathrm{m}^2} \cdot \frac{(\rho_\mathrm{s} - \rho_\mathrm{f})}{\mathrm{kg/m^3}} = 10^9. \tag{2.2}$$

The boundary between group C and A particles (cf. Figure 2.2) is based on experimental observation. Besides the Geldart classification, which has become the standard classification for fluidized particles, other researchers proposed their own classifications based on different approaches. The most prominent ones include the classifications according to the work of Molerus [21] or of Grace [13]. Grace [13] also proposed a regime map for the operation of different types of fluidized bed reactors. Figure 2.1 depicts a cylindrical or cuboid reactor shape. In industry several other reactor types are used to satisfy the specific need. The most prominent reactor types used in the fluidization technology also include a spouted bed, where a high superficial velocity in a small spacial area is used, usually in the center bottom of the reactor. A fountain with a high fluid fraction is the result of this reactor. The area around the spouting inlet can either be fluidized or no fluid can flow through it. Spouted fluidized beds are commonly used in the coal processing industry or for granulation of particles [22, 23]. For processes where the particles are needed to be treated in a separate process or even replaced, the circulating fluidized bed reactor is the common choice. Here, the superficial velocity is exceeding the terminal velocity and entrainment of the particles occur. The particles exit the reactor through a defined pipe and are collected, usually through a cyclone to remove fine powders due to abrasion. In the next reactor, the particles can be regenerated, treated or even additional particles can be added before the particles are entering the main reactor again. The process of

Fluid Catalytic Cracking (FCC) uses those kinds of reactors in a commercial scale. A description of other used reactor types can be found elsewhere [24].

An important parameter for the characterization of a fluidized bed is the minimum fluidization velocity $\mathbf{u}_{\mathrm{mf}}$. This velocity marks the boundary between a fixed bed and a fluidized bed. Figure 2.3 shows a typical graph for determining the minimum fluidization behavior. Here, the resulting pressure drop Δp is recorded for different superficial velocities $\mathbf{u}_0$.

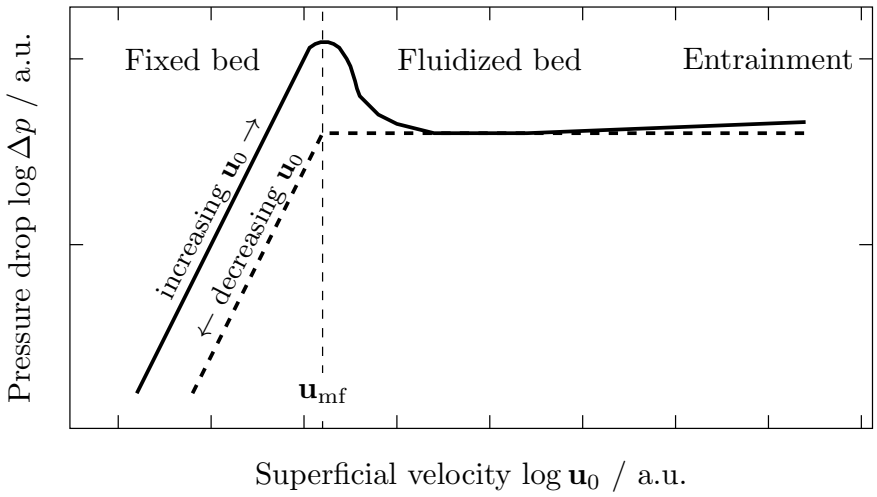

Figure 2.3: Pressure drop-velocity diagram for an arbitrary fluidized bed consisting of monodisperse particles with indication of fixed bed, fluidized bed and resulting minimum fluidization velocity $\mathbf{u}_{\mathrm{mf}}$.

According to the Ergun equation (cf. chapter 2.3.3) the pressure drop increases linear to the superficial velocity, when the flow through the packed bed is laminar. Once the pressure drop is equal to the pressure due to the weight of the particle bed, the particles in the fixed bed begin to move. At this point the transition between a fixed and a fluidized bed occurs. The velocity needed is called the minimum fluidization velocity. After the fluidization of particles, a further increase in superficial velocity does not effect the pressure drop, as it stays constant in the fluidization state. At high superficial velocities, the pressure drop increases again due to the higher contribution of the fluid flow towards it, the acceleration of particles and increasing particle-wall collisions. In most cases, entrainment occurs which is not beneficial for a fluidized bed, unless a pneumatic transport of solid good is needed. For an ideal particle bed with no cohesion or friction effects, the pressure drop versus superficial velocity curve is identical for increasing and decreasing velocities. But due to inter-particle forces the transition between the fixed and fluidized bed requires a higher energy, i.e., pressure drop according to the maximum in Figure 2.3. A decrease of the superficial velocity from a fluidized state does not follow the maximum pressure drop, as the cohesion and friction forces are not present for the decrease in velocity.

Compared to other fluid-solid contact reactors, the fluidized bed has its advantages in the fast mixing process of the particles and the fluid. Mass and heat transfer are very high, resulting into an almost isothermal condition throughout the fluidized particle bed. Furthermore, temperature changes due to exo- or endothermic reactions, are easily handled intrinsically by the fluidized bed because of the high mixing characteristics between the solid and fluid phase. This also gives a great margin of safety for highly exothermic reactions or temperature runaways [5]. A common practice for heat removal for fluidized bed reactors is the implementation of heat exchangers in the form of immersed pipes. As the heat transfer between the particles and the surrounding fluid, as well as immersed objects, is very high, the heat exchange surface of the immersed objects can be smaller than for immersed heat exchangers used in fixed bed reactors.

However, for certain cases the use of a fluidized bed reactor is not beneficial. Considering the fast mixing process of a fluidized bed and the random motion of particles, the residence time of particles in the reactor, especially for circulating fluidized beds, is not uniform. This can lead to unwanted yields and poor conversion for chemical reactions. Furthermore, a higher energy is needed to fluidize the particles compared to an operation in a fixed bed. This means, that the fluid flow must exceed the minimum fluidization or even the minimum bubbling velocity depending on the desired operation state of the fluidized bed. Due to this relatively high fluid flows, the velocity of the particles is also high. This results in abrasion of the particles or damages on the reactor walls or immersed objects like heat exchangers. Circulating and spouted beds with particles of group D according to the Geldart classification are especially prone to abrasion due to their size, weight and momentum in the fluidized state.

Most of the common used fluidized beds consist of a solid and gaseous phase. Besides the gas-solid fluidized bed, liquid-solid fluidized beds are also used, especially due to the smaller minimum fluidization velocity required to fluidize the particles. A type of liquid-solid fluidization reactor that has caught recent attention, is used to decrease the required energy in water pollution removal in Membrane Bioreactors (MBR). MBRs are mostly used for municipal [25] and industrial wastewater treatment [26, 27]. The water pollutants include pharmaceuticals, pesticides, solvents, petrochemicals, lubricants among others [28]. Its potential to remove organic and inorganic compounds from a feed combining a biological treatment and a filtration process through a membrane was proven useful in a wide field of areas [29, 30]. The membrane configuration can be external, i.e., membrane is located outside of the bioreactor or immersed in the reactor. Different membrane modules can be used for the micro- or ultrafiltration for the wastewater filtration process. These include tubular, flat sheet and hollow fiber membranes [31]. The MBR processes can be differentiated into aerobic and anaerobic ones. Using an aerobic process in an aerobic membrane bioreactor (AeMBR) sludge is activated by aeration. This

process is very energy demanding and the aeration process accounts for over 50 % of the total energy input but has its advantages in terms of handling process flows [32]. Due to the high amount of energy consumption the anaerobic membrane bioreactor (AnMBR) was introduced for better energy recovery. Biogas, mostly consisting of methane, is produced by anaerobic conversion of organic compounds in wastewater and hence, this process has the potential to perform at an energy neutral or even surplus level [33, 34]. Deposition and precipitation of fouling material onto the membrane layers must be either inhibited or purged off. An increase of the fouling cake layer results into an increase of the transmembrane pressure (TMP) and therefore into a higher energy input or no filtration of wastewater [35]. The aeration in an AeMBR acts as a gas purging routine to mitigate or scour off existing fouling particulates due to the shear force at the membrane layer [36]. This step is crucial for an economic and energy saving process of wastewater treatment in an MBR. Other techniques to control membrane fouling can be categorized in physical, chemical and biological schemes [37]. Aeration with an inert gas, e.g., nitrogen-rich gas, is also used for fouling control in AnMBR's, both in a continuous or intermittent way. A recently newly developed approach is the use of a fluidized bed in an anaerobic fluidized membrane bioreactor (AnFMBR), where particles, e.g., granular activated carbon (GAC) [38–40], glass beads [41] or zeolites [42], while GAC is the preferred choice [43], are introduced in the MBR. Figure 2.4 shows a schematic overview of an AnFMBR with an immersed membrane in a rectangular reactor.

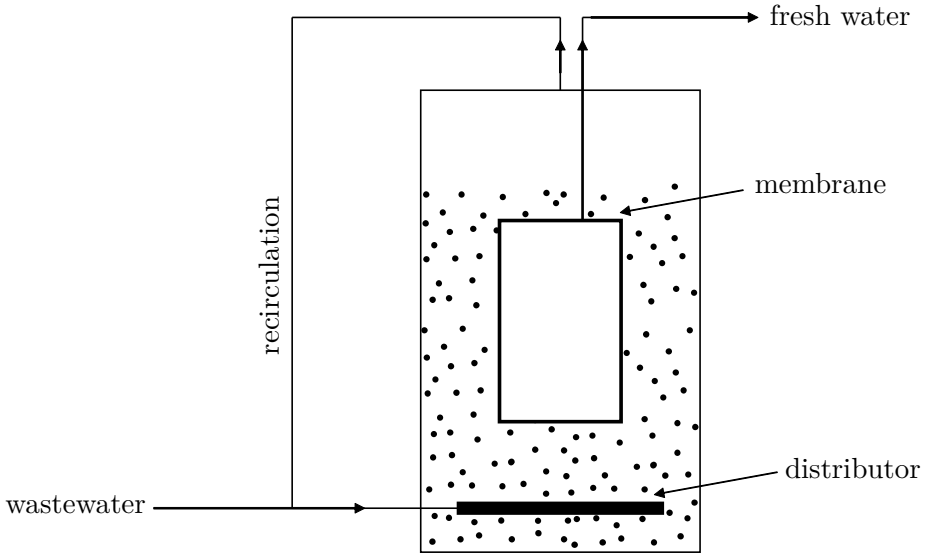

Figure 2.4: Schematic overview of a a lab-scale anaerobic membrane bioreactor used for wastewater treatment with fluidized particles.

An increased wastewater feed stream is introduced to exceed the minimum fluidization velocity of the particles and a fluidized bed is achieved. Due to the small differences in density between disperse and continuous phase, as well as the diameter of the particles being greater than 1 mm to avoid clogging of the membrane itself, a homogenous fluidized

bed is formed with almost no bubbles visible. The increased velocity of the fluidized particles results in a particle momentum which is able to scour off existing fouling on the membrane. Most of the energy input, however, is used for the fluidization of the particles as it scales with inlet velocity and pressure drop. Several approaches were made to increase efficiency of the AnFMBR both experimentally [44, 45] and using numerical simulations [46–48].

2.2 Numerical Simulation of Fluid Flows

In this chapter, the numerical formulas are presented for solving fluid flows according to the Finite Volume Method.

2.2.1 Physical Modeling of Fluid flows

A generic transport equation is needed from which several crucial balances can be derived. Therefore, an extensive property Φ is considered. The rate of change of this arbitrary extensive property is based on its time-dependent control volume of the mass $V_m(t)$ rather than on its control volume $V(t)$. This approach is a Lagrangian consideration of the property Φ. The movement of the fluid particles is tracked using the Lagrangian approach rather than the movement of a defined fixed region of fluid particles, which is called the Eulerian approach. For the later introduced Finite Volume Method (FVM), an intensive property, i.e., a property independent of the size of the control volume, is needed [49, 50].

The intensive property ϕ can be derived from the extensive property by integrating over the control mass[1]:

$$\Phi = \int_{V_m(t)} \rho\phi \, dV. \tag{2.3}$$

In order to further derive the generic transport equation, we need to apply the Leibniz' and the Gauss's Theorem [51, 52].

The Leibniz' theorem states a formula to differentiate a definite integral. The differentiated definite integral is composed of a term considering the change over time of the property ϕ and another term taking gains and losses across the bounds of the volume ∂V into account:

$$\frac{\mathrm{d}}{\mathrm{d}t} \int_{V(t)} \phi \, dV = \frac{\partial}{\partial t} \int_{V(t)} \frac{\partial \phi}{\partial t} \, dV + \int_{\partial V(t)} \phi \left(\mathbf{u}_S \cdot \mathbf{n}\right) \, dS, \tag{2.4}$$

where $\mathbf{n}$ is the unit vector orthogonal to the surface and pointing outward of the surface area S enclosed by the volume boundary $\partial V(t)$. $\mathbf{u}_S$ denotes the moving velocity of the

[1] The control mass is taken into account with the inclusion of the respective density ρ.

boundary ∂V. In the case of non-moving control volumes the moving velocity can be neglected and the equation reduces to

$$\frac{\mathrm{d}}{\mathrm{d}t}\int_{V(t)} \phi \, dV = \frac{\partial}{\partial t}\int_{V(t)} \phi \, dV. \tag{2.5}$$

The Gauss's theorem, sometimes called the divergence theorem, couples a relation between a surface and a volume integral. Applied to fluid mechanics, the Gauss theorem states that if the fluid motion with the velocity $\mathbf{u}$ into a control volume is higher than its outflow, a sink must be present (negative divergence). On the contrary, if the net flux of a control volume across the boundaries is positive, i.e., the fluid motion into the control volume across the boundaries is smaller compared to the flow outwards of the control volume, a source must be present (positive divergence):

$$\oint_S \mathbf{u} \cdot \mathbf{n} \; dS = \int_V \boldsymbol{\nabla} \cdot \mathbf{u} \; dV. \tag{2.6}$$

With the application of the Reynolds transport theorem[2] it is ensured, that the Lagrangian equivalent of an extensive value Φ in a mass volume V_m is transformed to a Eulerian equivalent intensive value ϕ in a control volume $V(t)$. The Reynolds transport theorem states that the total rate of change of the extensive property is contributed by two parts. Firstly, the change of the amount of property in a certain time in a certain control volume and secondly the increase or decrease of the property due to fluid motion across the boundaries, more commonly known as the convection flux through the boundary [50]:

$$\left(\frac{\mathrm{d}\Phi}{\mathrm{d}t}\right)_{V_m} = \frac{\mathrm{d}}{\mathrm{d}t}\int_{V(t)} \rho\phi \, dV + \oint_{\partial V(t)} \rho\phi \mathbf{u} \cdot \mathbf{n} \, dS. \tag{2.7}$$

Furthermore, the rate of change of the extensive property Φ is dependent on its volume and surface-based sources and sinks, S_V^ϕ and $\mathbf{S}_S^\phi$. Hence, Equation (2.7) can be stated as:

$$\frac{\mathrm{d}}{\mathrm{d}t}\int_{V(t)} \rho\phi \, dV + \oint_{\partial V(t)} \rho\phi \mathbf{u} \cdot \mathbf{n} \, dS = \int_{V(t)} S_V^\phi \, dV + \oint_{\partial V(t)} \mathbf{S}_S^\phi \cdot \mathbf{n} \, dS. \tag{2.8}$$

The surface based source contribution can be expressed based on a diffusion-like equation, i.e., a gradient approximation, with an arbitrary diffusivity corresponding to the intensive property Γ^ϕ:

$$\mathbf{S}_S^\phi = \Gamma^\phi \boldsymbol{\nabla}\phi \tag{2.9}$$

with $\boldsymbol{\nabla}\phi$ being the gradient of the intensive property ϕ.

[2] The Reynolds transport theorem is similiar to the Leibniz' theorem, as it is a three-dimensional generalization often applied in fluid mechanics.

Using the Leibniz' theorem to the first term of the l.h.s[3] and applying the Gauss's theorem to both surface integrals yields the integral form of the generic conservation equation for an arbitrary transported intensive property ϕ:

$$\frac{\partial}{\partial t}\int_{V(t)} \rho\phi \, dV + \int_{V(t)} \boldsymbol{\nabla} \cdot (\rho\phi\mathbf{u}) \, dV = \int_{V(t)} S_V^{\phi} \, dV + \int_{V(t)} \boldsymbol{\nabla} \cdot \left(\Gamma^{\phi}\boldsymbol{\nabla}\phi\right) \, dV. \quad (2.10)$$

The more common way of the generic transport equation in its differential form is depicted in Equation (2.11) and consists of a temporal, convective, diffusive and a (volumetric) source term, according to:

$$\underbrace{\frac{\partial(\rho\phi)}{\partial t}}_{\text{temporal}} + \underbrace{\boldsymbol{\nabla} \cdot (\rho\mathbf{u}\phi)}_{\text{convective}} - \underbrace{\boldsymbol{\nabla} \cdot \left(\Gamma^{\phi}\boldsymbol{\nabla}\phi\right)}_{\text{diffusive}} = \underbrace{S_V(\phi)}_{\text{source}}. \quad (2.11)$$

An arbitrary transported quantity is represented by the scalar ϕ with the prescribed velocity vector $\mathbf{u}$, the corresponding density of the fluid ρ and the diffusion coefficient Γ^{ϕ}. Additional sources or sinks affecting the transport of the quantity ϕ are expressed by the source term $S_V(\phi)$. Using the differentiated generic transport equation, several other equations can be derived which will be used in fluid mechanics. Here, we are only considering isothermal fluid flows (heat conductivity $\lambda \to \infty$) and hence can derive the continuity and momentum equation. The continuity equation called also the conservation of mass is derived from Equation (2.11) by substituting the transported quantity ϕ by unity, resulting to:

$$\frac{\partial\rho}{\partial t} + \boldsymbol{\nabla} \cdot (\rho\mathbf{u}) = 0. \quad (2.12)$$

Here, the diffusion term $\boldsymbol{\nabla} \cdot \left(\Gamma^{\phi}\boldsymbol{\nabla}\phi\right)$ yields zero for $\phi = 1$, as there is no diffusion effect regarding the transportation of mass. Furthermore, the condition for the source term $S_V\,(\phi = 1) = 0$ applies, if mass is not created nor transformed to energy. If the transported quantity in the generic transport equation is replaced by the velocity $\mathbf{u}$, the resulting equation is commonly known as the conservation of linear momentum or the momentum balance:

$$\frac{\partial(\rho\mathbf{u})}{\partial t} + \boldsymbol{\nabla} \cdot (\rho\mathbf{u}\mathbf{u}) - \boldsymbol{\nabla} \cdot \overline{\overline{T}} = \rho\mathbf{g}. \quad (2.13)$$

The convective transport is described by $\boldsymbol{\nabla} \cdot (\rho\mathbf{u}\mathbf{u})$ and the diffusive transport of the momentum can be described by introducing the stress tensor $\overline{\overline{T}}$, yielding the diffusion term in the momentum balance $\boldsymbol{\nabla} \cdot \overline{\overline{T}}$. The most common source terms affecting the momentum

[3] Here, $\mathbf{u}_S$ according to Equation (2.4) equals to zero is only valid, if the regarded control volumes do not change, i.e., a static mesh is considered. When a moving mesh is present, the surface integral on the r.h.s. of Equation (2.4) has to be included. Hence, the Gauss's theorem has to be applied to transform the surface integral to a volume integral.

for fluid flows are due to gravity $\rho\mathbf{g}$. Other source terms can include electromagnetic forces, surface tension forces and others if applicable [52]. For Newtonian fluids the term $\boldsymbol{\nabla} \cdot \overline{\overline{T}}$ can be split up in a pressure and a shear stress term depending on the viscous part of the stress tensor $\overline{\overline{\tau}}$ according to Enwald et al. [53]:

$$\boldsymbol{\nabla} \cdot \overline{\overline{T}} = \boldsymbol{\nabla} \cdot \left(-p\overline{\overline{I}} + \overline{\overline{\tau}}\right) = -\boldsymbol{\nabla} p + \boldsymbol{\nabla} \cdot \overline{\overline{\tau}}. \tag{2.14}$$

The Newtonian strain-stress relation shows the dependency of the viscous stress from the bulk viscosity and the shear viscosity, ζ and η, respectively:

$$\overline{\overline{\tau}} = \zeta \left(\boldsymbol{\nabla} \cdot \mathbf{u}\right) \overline{\overline{I}} + 2\eta \left[\overline{\overline{D}} - \frac{1}{3} \left(\boldsymbol{\nabla} \cdot \mathbf{u}\right) \overline{\overline{I}}\right]. \tag{2.15}$$

$\overline{\overline{I}}$ represents the unit tensor and the strain (deformation) rate tensor $\overline{\overline{D}}$:

$$\overline{\overline{D}} = \frac{1}{2} \left[\boldsymbol{\nabla}\mathbf{u} + \left(\boldsymbol{\nabla}\mathbf{u}\right)^{\mathrm{T}}\right]. \tag{2.16}$$

Stokes' assumption states that the bulk viscosity ζ can be neglected for most of the fluids, as it implies that the average normal viscous stress is zero (cf. Panton [54]) and the viscous part of the stress tensor reduces to:

$$\overline{\overline{\tau}} = \eta \left[\boldsymbol{\nabla}\mathbf{u} + \left(\boldsymbol{\nabla}\mathbf{u}\right)^{\mathrm{T}}\right] + \frac{2}{3}\eta \left(\boldsymbol{\nabla} \cdot \mathbf{u}\right) \overline{\overline{I}}. \tag{2.17}$$

In regards to incompressible fluids ($\rho = \text{const.}$) the continuity equation from Equation (2.12) can be further simplified to

$$\boldsymbol{\nabla} \cdot \mathbf{u} = 0 \tag{2.18}$$

and the momentum balance with the introduction of the viscous part of the stress tensor, the assumption of an incompressible flow with a constant viscosity ($\eta = \text{const.}$) yields

$$\frac{\partial \mathbf{u}}{\partial t} + \boldsymbol{\nabla} \cdot \mathbf{u}\mathbf{u} = -\frac{1}{\rho}\boldsymbol{\nabla} p + \mathbf{g} + \boldsymbol{\nabla} \cdot \nu\boldsymbol{\nabla}\mathbf{u} \tag{2.19}$$

with the kinematic viscosity ν. These two equations are crucial for determining an isothermal flow of an incompressible Newtonian fluid.

2.2.2 Finite Volume Method

In order to solve the aforementioned partial differential equations for the conservation of mass and momentum, they have to be discretized. This means, a continuum problem

must be approximated into a discrete set of quantities [55]. There exists several different discretization techniques, such as the Finite Element Method (FEM), Finite Difference Method (FDM) or the Finite Volume Method (FVM); the latter of which will be used in this thesis. Each of those discretization techniques uses the same procedure to solve the apparent problem:

- spatial discretization,
- temporal discretization and
- equation discretization.

In the following, those three steps are explained in reference to the FVM. The spatial discretization ensures, that the whole range of the system, volume and boundaries, is covered. This condition is fulfilled by the introduction of three-dimensional inter-connected cells. The cells are of a general polyhedral shape, e.g., the mostly used hexahedral cells or tetrahedral cells for more complex geometries, and must not overlap. Each cell represents a control volume (CV). Two adjacent arbitrary CV's, here cubic cells, are seen in Figure 2.5. Both cells are connected through a shared face f. The two centers of each cell, both owner and neighbor, are located with computational nodes, P and N, respectively. Using FVM a staggered or collocated approach can be applied. While in the staggered approach the properties ϕ are either stored in the cell center or the cell face, the collocated approach stores all properties ϕ in the cell center. Here, the collocated approach is used and therefore the properties are stored in the cell centers of both cells, ϕ_P and ϕ_N. The value of the property at the connecting cell face ϕ_f is calculated with an interpolation of the property values of the two adjacent cells, ϕ_P and ϕ_N. The position vector of a cell center $\mathbf{x}_P$ and a cell face center $\mathbf{x}_f$ are defined, such that the following equations are valid:

$$\int_{V_P} (\mathbf{x} - \mathbf{x}_P)\ dV \stackrel{!}{=} 0 \tag{2.20}$$

and

$$\int_{S_f} \left(\mathbf{x} - \mathbf{x}_f\right)\ dS \stackrel{!}{=} 0. \tag{2.21}$$

Above equations state the center of the cells and faces to be the geometrical centroid based on a volume or surface for an arbitrary shape.

$\mathbf{S}_f$ represents the outward pointing face area vector normal to the face f. The magnitude of the face area vector is equal to the area of the face. In the case of Figure 2.5 the numerical grid is orthogonal, as the connecting vector of the two centroids $\overrightarrow{PN}$ is parallel to the face

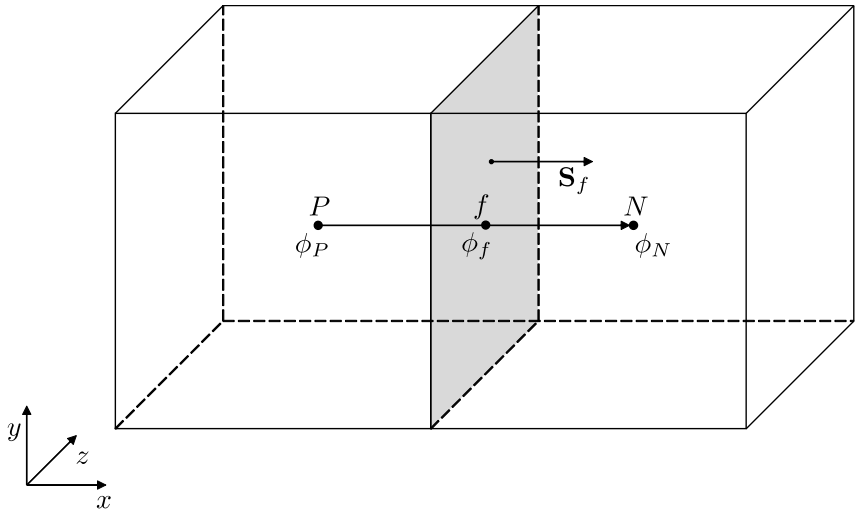

Figure 2.5: Two adjacent arbitrary (cubic) cells used in the collocated finite volume method.

area vector $\mathbf{S}_f$. Non-orthogonal numerical grids are referred to as *unstructured* and have the benefit of depicting more complex geometries but more sophisticated interpolation techniques are required [52, 56].

The temporal discretization includes the definition of a time-step. With a defined size of a time-step the continuous time is discretized into a finite number, i.e., $t = \sum \Delta t$. The time-step Δt might be defined as a constant value or as an adaptive time-step. However, the adaptive time-step has certain limitations regarding transient simulations.

All equations have some form of the general transport equation according to Equation (2.11). The following terms must be discretized for the:

- temporal derivative,
- convection term,
- diffusion term and
- source term.

In order to apply the FVM, Equation (2.11) must be first integrated over the control volume of the cell V_P to derive the integral form of the general transport equation:

$$\int_{V_P} \frac{\partial (\rho\phi)}{\partial t}\, dV + \int_{V_P} \boldsymbol{\nabla} \cdot (\rho \mathbf{u}\phi)\; dV - \int_{V_P} \boldsymbol{\nabla} \cdot \left(\Gamma^{\phi} \boldsymbol{\nabla}\phi\right)\; dV = \int_{V_P} S_V(\phi)\, dV. \quad (2.22)$$

Temporal derivative

The integration of the temporal derivative over the control volume V_P yields:

$$\int_{V_P} \frac{\partial (\rho\phi)}{\partial t}\, dV = \frac{\partial (\rho\phi)_P}{\partial t}\, V_P. \tag{2.23}$$

ρ_P and ϕ_P represent the density and the arbitrary property in the cell center P.

Convection term

The convection term is discretized by integrating over the control volume and applying the Gauss's Theorem to transform a volume integral into a surface integral. The surface integral can then be approximated with the summation of the convective flux of the property over all enclosed cell faces, according to:

$$\int_{V_P} \boldsymbol{\nabla} \cdot (\rho \mathbf{u} \phi)\ dV = \oint_S (\rho \mathbf{u} \phi)_f\ dS \approx \sum_f \mathbf{S}_f \cdot (\rho \mathbf{u} \phi)_f = \sum_f F_f \phi_f, \tag{2.24}$$

where F_f is the mass flux through the face f:

$$F_f = \mathbf{S}_f \cdot (\rho \mathbf{u})_f\,. \tag{2.25}$$

Differencing schemes are used to calculate the property ϕ_f on the cell face f. These cell face properties must be calculated when applying the collocated FVM as properties are only stored in the cell centers. To determine the face value of a property ϕ_f, the properties of the two adjacent cells are required, ϕ_P and ϕ_N. A flux dependent differencing scheme is the Upwind Differencing (UD) scheme. The face property ϕ_f is dependent on the direction of the flow:

$$\phi_f^{\mathrm{UD}} = \begin{cases} \phi_P & \text{for } F \geq 0 \\ \phi_N & \text{for } F < 0. \end{cases} \tag{2.26}$$

If no flux occurs or the flow direction points towards the neighbor cell, i.e., the fluid is flowing from the cell P to N and $F \geq 0$, the face value of the property is equal to the property stored in the cell center of the cell itself ϕ_N. If the direction of the flux points the other way, i.e., from the neighbor cell to the considered cell, the face value of the property is equal to the cell centered property of the neighbor cell, $\phi_f = \phi_N$. This differencing scheme is first order accurate and guarantees boundedness. The boundedness, however, is given at the cost of loss of accuracy due to numerical diffusion [52, 57]. Hence, the solution can be severely distorted in terms of accuracy.

A second-order accurate differencing scheme using a linear interpolation approach is the Central Differencing (CD) scheme. With the assumption of a linear trend of the property ϕ between the cell centers P and N, the face value can be determined with the interpolation factor f_x:

$$\phi_f^{\mathrm{CD}} = f_x \phi_P + (1 - f_x)\, \phi_N. \tag{2.27}$$

The interpolation factor f_x represents the ratio of the distances of cell-center $\rightarrow$ face and cell-center $\rightarrow$ cell-center, $\overline{fN}$ and $\overline{PN}$, respectively.

$$f_x = \frac{\overline{fN}}{\overline{PN}}. \tag{2.28}$$

It has been reported, that boundedness for the CD is not guaranteed for convection-dominated flows [58] resulting to an unphysical behavior.

A blended scheme combining the second order accuracy of CD and the boundedness of the UD is the Blended Differencing (BD) scheme [59]. The combination consists of a linear combination of the UD and CD (cf. Equations (2.26) and (2.27)):

$$\phi_f^{BD} = (1 - \gamma)\, \phi_f^{\mathrm{UD}} + \gamma \phi_f^{\mathrm{CD}}. \tag{2.29}$$

γ denotes the blending factor and is bounded between zero and unity, $0 \leq \gamma \leq 1$. While Peric [59] recommends a constant value for γ for all faces of the numerical grid, other reviews with more sophisticated approaches on the calculation of the blending factor, can be found in literature [57, 59–61].

Diffusion term

Analog to the convection term, the diffusion term is first integrated over the control volume V_P and then the Gauss's Theorem is applied. The resulting surface integral is then approximated by a summation of the corresponding property over the surrounding cell faces:

$$\int_{V_P} \boldsymbol{\nabla} \cdot \left(\Gamma^{\phi} \boldsymbol{\nabla} \phi \right) \, dV = \oint_S \left(\Gamma^{\phi} \boldsymbol{\nabla} \phi \right)_f \, dS \approx \sum_f \Gamma_f^{\phi} \boldsymbol{\nabla}_f \phi \cdot \mathbf{S}_f. \tag{2.30}$$

$\boldsymbol{\nabla}_f \phi$ denotes the face gradient and can be calculated for orthogonal meshes as:

$$\boldsymbol{\nabla}_f \phi \cdot \mathbf{S}_f = \left| \mathbf{S}_f \right| \frac{\phi_N - \phi_P}{\overline{PN}}. \tag{2.31}$$

For non-orthogonal meshes, the full gradient approximation is split up in an orthogonal contribution and a non-orthogonal correction term (cf. Ferziger and Perić [52]).

Source term

Due to numerical convergence issues, the source term is linearized in an explicit and implicit treatment part, according to

$$S_V(\phi) = S_I \phi_P + S_E, \tag{2.32}$$

where S_I and S_E represent the implicit and explicit part, respectively.

The integration of the source term over the control volume V_P results to:

$$\int_{V_P} S_V(\phi)\, dV = S_I \phi_P\, V_P + S_E\, V_P. \tag{2.33}$$

This treatment is second order accurate.

For steady-state simulations the temporal derivative yields zero, $\frac{\partial(\rho\phi)}{\partial t} = 0$. Considering transient conditions, the general transport equations must be first integrated over the control volume V_P and over time, yielding the time integration of the spatial discretized form:

$$\int_t^{t+\Delta t} \frac{\partial\left(\rho\phi\right)}{\partial t} V_P\, dt = \int_t^{t+\Delta t} \mathcal{R}\left(\phi\right)\, dt, \tag{2.34}$$

with $\mathcal{R}\left(\phi\right)$ representing the discretized terms of the convection, diffusion and source terms according to Equations (2.24), (2.30) and (2.33):

$$\mathcal{R}\left(\phi\right) = -\sum_f F_f \phi_f + \sum_f \Gamma_f^{\phi} \boldsymbol{\nabla}_f \phi \cdot \mathbf{S}_f + \left(S_I \phi_P + S_E\right) V_P. \tag{2.35}$$

Integrating Equation (2.34) from the limits t to $t + \Delta t$ yields[4]:

$$\rho_P \frac{\phi_P^{n+1} - \phi_P^n}{\Delta t} V_P = \mathcal{R}\left(\phi\right), \tag{2.36}$$

where the parameter n denotes the time-level, e.g., $\phi^n = \phi(t)$ and ϕ^{n+1} denotes the property ϕ at the time-level $t + \Delta t$.

There are several methods that can be applied to derive the interpolation type of equation for the temporal term. The explicit and implicit Euler methods will be explained in the following section.

[4] Note, that the density in the center of P does not have a corresponding time-level. This is only valid, if the density is constant over the defined time-period. Otherwise the term should be changed to $\frac{\rho_P^{n+1}\phi_P^{n+1} - \rho_P^n \phi_P^n}{\Delta t} V_P$.

Deriving the temporal term according to the explicit Euler method, values for the property ϕ in the convection, diffusion and source terms from the old time-step n are used:

$$\rho_P \frac{\phi_P^{n+1} - \phi_P^n}{\Delta t} V_P = \mathcal{R}\left(\phi^n\right), \tag{2.37}$$

According to the explicit Euler approach it is therefore possible to directly derive the value of the arbitrary property at the new time-step $n+1$, as the values for $\mathcal{R}\left(\phi^n\right)$ at the time-step n are known:

$$\phi_P^{n+1} = \phi_P^n + \frac{\Delta t}{\rho_P V_P} \mathcal{R}\left(\phi^n\right). \tag{2.38}$$

This method is first order accurate and a stability criterion exists for the explicit Euler method. Introducing the Courant-Friedrich-Lewis Number Co, the explicit Euler Method is unstable for $Co > 1$. The Courant-Friedrich-Lewis Number Co at the interconnecting face of two adjacent cells in accordance to Figure 2.5 is defined as:

$$Co = \frac{\mathbf{u}_f \Delta t}{\overline{PN}}. \tag{2.39}$$

Co is therefore dependent on the distance between two adjacent cells $\overline{PN}$, i.e., the cell sizes themselves, the chosen time-step Δt, and the occurring velocities on the interconnecting face of the two cells $\mathbf{u}_f$. While the velocities are not modifiable, as they are given based on the considered flow problem, the time-step can be reduced. The cell size can be increased to further lower the Co number and therefore prevent numerical instabilities and inaccuracies. An increase of the cell size may result in bad resolution of the numerical grid. Furthermore, a decrease of the time-step has a negative effect on the simulation time. A smaller time-step results in more equations to be solved until the final time-step is reached, hence, the simulation time increases and may become unfeasible to operate.

The spatial terms $\mathcal{R}\left(\phi\right)$ can also be discretized implicitly by using the implicit Euler method. Here, the new values of the arbitrary property are included in the calculation, resulting to:

$$\phi_P^{n+1} = \phi_P^n + \frac{\Delta t}{\rho_P V_P} \mathcal{R}\left(\phi^{n+1}\right). \tag{2.40}$$

According to Equation (2.40) the implicit Euler method is first-order accurate. In this case the Euler method also guarantees boundedness and is numerically stable. Further methods to discretize the temporal derivative include the backward method, which is second-order accurate as it uses three time levels n, $n+1$ and $n-1$, or the Crank-Nicolson scheme [62], which is second-order accurate and bounded.

2.3 Multiphase Flow Models

Multiscale approaches for the correct prediction of fluid-solid flows exist comprising of fluid-particle and particle-particle interaction in different levels of detail. Figure 2.6 shows a brief overview of the three main multiscale models used in engineering. The choice which model will produce accurate and relatively fast simulation results, depends on a number of factors. Popular and widely applied models for multiphase-flow consisting of at least one fluid and solid phase include the Direct Numerical Simulation (DNS), Eulerian-Lagrangian and Eulerian-Eulerian models.

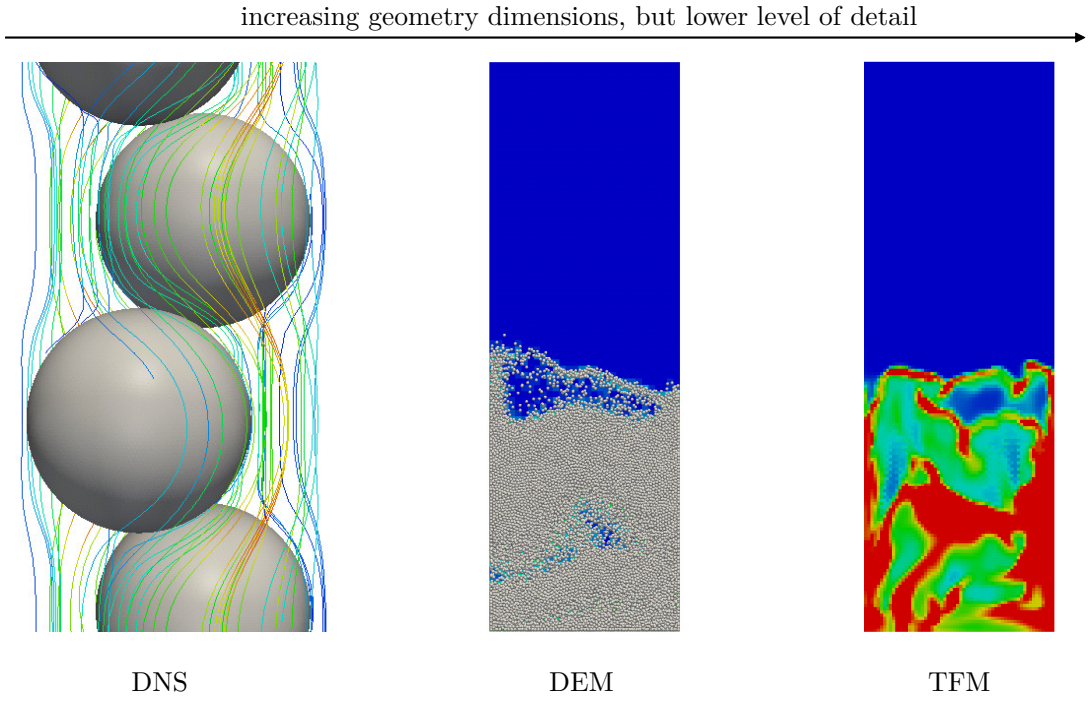

Figure 2.6: Multiscale simulation models used in engineering for fluid-solid flows: Direct Numerical Simulation (DNS), Discrete Element Model (DEM) and Two-Fluid Model (TFM).

DNS counts to the most accurate, but computational very expensive simulations. Here, the particles are fully resolved and equations for the surrounding fluid phase are calculated on a very fine numerical grid to account for a correct force coupling between the phases. The fluid flow in the vicinity of the particles is depicted accurately and the shape of each particle is fully resolved. The immersed boundary method (IBM) is a popular approach applied to model DNS in fluid-particle flows. IBM was first proposed by Peskin [63, 64] to model cardiovascular flow problems but has since been applied to arbitrary flow problems as well. The number of particles for this kind of simulation is usually limited to 1000 because of computational limitations [65]. Due to the high accuracy and high demand of computational power, this model is usually used for small-scale simulations in order to

derive models that can later be used for other less computational demanding approaches. Several drag force models have been derived using DNS [66–69], which were later applied in Eulerian-Eulerian and Eulerian-Lagrangian approaches. The Eulerian-Lagrangian model is a faster approach to simulate fluid-solid flows with the sacrifice of accuracy. As the particles are not fully resolved but rather a Lagrangian Particle Tracking (LPT) is applied, i.e., the movement of points is tracked, the numerical grid is not as fine as in DNS. Depending on the used sub-model (cf. Chapter 2.3.2), the number of particles is usually less than one million [70]. The Eulerian-Eulerian model or the Two-Fluid Model (TFM) [53, 71] uses an interpenetrating continuum approach for both the solid and the fluid phase. The solid phase is treated as a fluid. This results in a lack of tracking individual particles and has the advantage of being almost independent on the number of particles in a system. Particle-particle interaction, therefore, can not be accounted for correctly and have to be modeled by stochastic collision models. In this context it is more precise to talk about a solid phase instead of particles altogether. The TFM is especially suitable for small particles and high number of particles, in the order of up to one billion or even to one trillion particles [72]. Larger amounts of particles usually imply greater space scales, where other more abstract correlation models might be of a better use, although the speed of TFM is in theory independent of the particle number. Myöhänen and Hyppänen [73] presented a time and space scale dependent overview approach (cf. Figure 2.7) to choose between DNS, TFM and Eulerian-Lagrangian models to simulate fluid-particle flows.

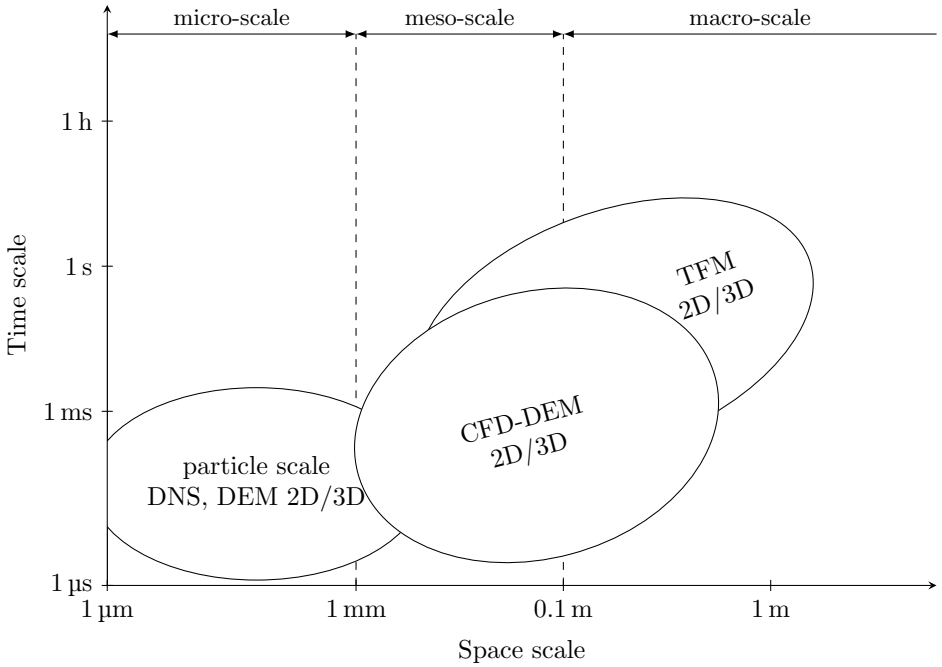

Figure 2.7: Range of application for different multiscale models (modified from [73]).

As can be seen, areas exist where multiple approaches can be applicable to simulate the multiphase-flow problem. However, the level of detail and scale of the geometry defines which approach is suitable for it [74]. Especially for industrial engineering problems the Eulerian-Lagrangian approach and TFM approaches are the most common models applied, while the Eulerian-Lagrangian model and DNS is preferred in scientific research to model fluid-solid flows in CFD [70]. A grid independency study for both the TFM and the Eulerian-Lagrangian approach is presented in Appendix A. The TFM and Eulerian-Lagrangian model will be discussed in detail in the following.

2.3.1 Two-Fluid Model

The Eulerian-Eulerian approach, also called TFM for the simulation of granular flows, is based on the work of Anderson and Jackson [72]. Both the fluid and particle phases are modeled as a continuum. Hence, the particles are not resolved and can not be individually tracked. Both phases are solved using a momentum and mass balance[5] and are coupled through a momentum exchange, mainly due to drag force. Both phases are solved using the same time-step. The mass and momentum equation follow the generic transport equation discussed in Chapter 2.2.1 with the addition of a phase fraction term ε and a term coupling the interpenetrating phases, the momentum exchange $\mathbf{M}_{\mathrm{f,s}}$. The phase fraction term ε describes the volumetric fraction of the fluid phase f. The following two equations result for the mass and momentum equation of the fluid phase:

$$\frac{\partial \varepsilon}{\partial t} + \boldsymbol{\nabla} \cdot (\varepsilon \, \mathbf{u}_{\mathrm{f}}) = 0 \tag{2.41}$$

and

$$\frac{\partial \left(\varepsilon \, \rho_{\mathrm{f}} \, \mathbf{u}_{\mathrm{f}}\right)}{\partial t} + \boldsymbol{\nabla} \cdot (\varepsilon \, \rho_{\mathrm{f}} \, \mathbf{u}_{\mathrm{f}} \, \mathbf{u}_{\mathrm{f}}) = -\varepsilon \boldsymbol{\nabla} p + \varepsilon \, \rho_{\mathrm{f}} \, \mathbf{g} + \boldsymbol{\nabla} \cdot \left(\varepsilon \, \overline{\overline{\tau}}_{\mathrm{f}}\right) + \mathbf{M}_{\mathrm{f,s}}. \tag{2.42}$$

ρ_{f}, $\mathbf{u}_{\mathrm{f}}$, p and $\mathbf{g}$ represent the density and velocity of the fluid phase, the hydrostatic pressure and the gravitational acceleration, respectively. The viscous stress tensor of the fluid phase $\overline{\overline{\tau}}_{\mathrm{f}}$ is calculated according to Equation (2.17) for a Newtonian fluid. The phase fraction of the fluid phase ε obeys a closing condition with the solid phase fraction α_{s} and therefore the solution of the mass equation for the fluid phase is sufficient and an additional differential equation for mass regarding the solid phase fraction α_{s} is redundant:

$$\alpha_{\mathrm{s}} = 1 - \varepsilon. \tag{2.43}$$

[5] The energy balance has to be included if the system is non-isothermic.

To ensure a realistic limit of particles in a cell according to the maximum close-packing of equal spheres, a maximum solid phase fraction $\alpha_{\mathrm{s,max}}$ is often introduced. It can be considered as a maximum compressibility limit for the solid phase. After the solid phase fraction reaches this value, the solid phase can not be compressed any further, as a further decrease in local spacing would be physically impossible. This value is dependent on the material properties, e.g., shape, surface energy, and is set due to empirical findings. Correlations for the maximum solid phase fraction can be found elsewhere [75]. Commonly, a maximum solid phase fraction value of $\alpha_{\mathrm{s,max}} = 0.6$ to 0.64 is assumed [76, 77].

As the solid phase is modeled with a continuum approach as well, it is treated as a fluid. Hence, the momentum equation for the solid phase is analog to the momentum equation of the fluid phase in Equation (2.42) with the addition of further closure equations for the solid phase's internal momentum transfer:

$$\frac{\partial\left(\alpha_{\mathrm{s}}\,\rho_{\mathrm{s}}\,\mathbf{u}_{\mathrm{s}}\right)}{\partial t} + \boldsymbol{\nabla}\cdot\left(\alpha \mathrm{s}\,\rho_{\mathrm{s}}\,\mathbf{u}_{\mathrm{s}}\,\mathbf{u}_{\mathrm{s}}\right) = -\alpha_{\mathrm{s}}\boldsymbol{\nabla} p + \alpha_{\mathrm{s}}\,\rho_{\mathrm{s}}\,\mathbf{g} - \boldsymbol{\nabla} p_{\mathrm{s}} + \boldsymbol{\nabla}\cdot\left(\alpha_{\mathrm{s}}\,\overline{\overline{\tau}}_{\mathrm{s}}\right) + \mathbf{M}_{\mathrm{s,f}}, \quad (2.44)$$

with the solid phase pressure p_{s}, the viscous stress tensor of the solid phase $\overline{\overline{\tau}}_{\mathrm{s}}$ and the momentum exchange $\mathbf{M}_{\mathrm{s,f}}$. In order to model the solid phase as a fluid whilst still maintaining the particulate behavior, additional closure equations are needed. Ding and Gidaspow [78] proposed the Kinetic Theory of Granular Flow (KTGF) to determine those equations. The KTGF is a modified version of the Kinetic Theory of Solids by Jenkins and Savage [79] and Lun et al. [80] and was extended to fluid-solid flows based on first problem. Formerly, the kinetic stresses, e.g., solid viscosities, had to be guessed for the simulation. In the KTGF, equations were proposed to calculate those kinetic stresses for the solid phase. However, this model is used for frictionless ideal spherical particles. Other models have since been developed to account for the roughness of particles, e.g., Zhao et al. [81] and Yang et al. [82], but the KTGF proposed by Ding and Gidaspow [78] is still the most widely applied for fluid-solid simulations [83]. Different correlations exist for each of the closure equations. Here, the most popular correlations will be presented and further methods will be mentioned.

Viscous stress tensor

For granular matter the bulk viscosity ζ_{s} can not be neglected. Hence, the equation for the viscous stress tensor of the solid phase $\overline{\overline{\tau}}_{\mathrm{s}}$ reads:

$$\overline{\overline{\tau}}_{\mathrm{s}} = \eta_{\mathrm{s}}\left[\boldsymbol{\nabla}\mathbf{u}_{\mathrm{s}} + \left(\boldsymbol{\nabla}\mathbf{u}_{\mathrm{s}}\right)^{\mathrm{T}}\right] - \left(\zeta_{\mathrm{s}} - \frac{2}{3}\eta_{\mathrm{s}}\right)\left(\boldsymbol{\nabla}\cdot\mathbf{u}_{\mathrm{s}}\right)\overline{\overline{\mathrm{I}}}. \quad (2.45)$$

Closure equations for bulk viscosity ζ_s and shear viscosity η_s are required to calculate the viscous stress tensor of the solid phase.

Solid bulk viscosity

If a packing of granular matter gets compressed or loosened, a force of resistance occurs as a result of the change in viscosity in the bulk solid phase. Lun et al. [80] presented an equation to calculate the bulk viscosity of the solid phase:

$$\zeta_\mathrm{s} = \frac{4}{3}\alpha_\mathrm{s}^2 \rho_\mathrm{s} d_\mathrm{p} g_0 \left(1+e\right) \sqrt{\frac{\theta_\mathrm{s}}{\pi}}. \tag{2.46}$$

To determine the solid bulk viscosity, the particle diameter d_p, the radial distribution function g_0, the coefficient of restitution e and the granular temperature θ_s is needed, as well as the particle concentration α_s.

Solid shear viscosity

The solid shear viscosity η_s changes due to collisions and translation of particles. Hence, the solid shear viscosity can be split up into a collisional and kinetic part, $\eta_\mathrm{s,col}$ and $\eta_\mathrm{s,kin}$, respectively:

$$\eta_\mathrm{s} = \eta_\mathrm{s,col} + \eta_\mathrm{s,kin}. \tag{2.47}$$

According to Gidaspow [15], the individual components of the solid shear viscosity, namely the collisional and kinetic part, can be calculated as:

$$\eta_\mathrm{s,col} = \frac{4}{5}\alpha_\mathrm{s} g_0 \left(1+e\right) \rho_\mathrm{s} d_\mathrm{p} \sqrt{\frac{\theta_\mathrm{s}}{\pi}} \tag{2.48}$$

and

$$\eta_\mathrm{s,kin} = \frac{10}{96}\frac{\rho_\mathrm{s} d_\mathrm{p}}{\alpha_\mathrm{s} g_0 \left(1+e\right)} \sqrt{\theta_\mathrm{s}\sqrt{\pi}} \left[1 + \frac{4}{5}\alpha_\mathrm{s} g_0 \left(1+e\right)\right]^2. \tag{2.49}$$

Nieuwland et al. [83] and Syamlal et al. [84] suggested alternative correlations to calculate the solid shear viscosity, while still maintaining the individual components of a collisional and kinetic part. Regarding highly dense granular flows, additional stress is attributed to the solid shear viscosity, as the inter-particle friction forces increase proportionally.

Therefore, a solid phase friction limit $\alpha_{\mathrm{s,fr}}$ is introduced when exceeded the additional frictional stresses are accounted for. This results to:

$$\eta_{\mathrm{s}} = \begin{cases} \eta_{\mathrm{s,col}} + \eta_{\mathrm{s,kin}}, & \text{if } \alpha_{\mathrm{s}} < \alpha_{\mathrm{s,fr}} \\ \eta_{\mathrm{s,col}} + \eta_{\mathrm{s,kin}} + \eta_{\mathrm{s,fr}}, & \text{if } \alpha_{\mathrm{s}} \geq \alpha_{\mathrm{s,fr}}. \end{cases} \tag{2.50}$$

The frictional stress solid shear viscosity $\eta_{\mathrm{s,fr}}$ can be calculated according to Johnson and Jackson [85] with:

$$\eta_{\mathrm{s,fr}} = Fr \frac{\left(\alpha_{\mathrm{s}} - \alpha_{\mathrm{s,fr}}\right)^{n}}{\left(\alpha_{\mathrm{s,max}} - \alpha_{\mathrm{s}}\right)^{P}} \sin\phi, \tag{2.51}$$

where Fr, n and P are empirical constants and ϕ presents the angle of internal friction. Ocone et al. [86] give an overview of suitable values for those variables. Other correlations for the solid shear viscosity due to friction in highly dense granular flows are found in the works of Syamlal et al. [84] and Schaeffer [87].

Solid phase pressure

The solid phase pressure p_{s} is used, to prevent unreasonable low values of local solid phase fractions. Lun et al. [80] stated a model for the solid phase pressure consisting of a kinetic part (first term) and further forces which account for inter-particle collisions (second term):

$$p_{\mathrm{s}} = \alpha_{\mathrm{s}}\rho_{\mathrm{s}}\theta_{\mathrm{s}} + 2g_0\rho_{\mathrm{s}}\alpha_{\mathrm{s}}^2\left(1 - e\right)\theta_{\mathrm{s}}. \tag{2.52}$$

The kinetic part of the solid phase pressure is proportional to the concentration of particles α_{s} and the granular temperature θ_{s}, hence due to the motion of particles. Inelastic collisions between particles account for the second part of the solid phase pressure. It consists of forces mainly due to the repulsive radial distribution function g_0 and the coefficient of restitution of the particles e. Other models were proposed by Syamlal et al. [84] and Ahmadi and Ma [88].

Analog to the additional term for friction in the solid shear viscosity $\eta_{\mathrm{s,fr}}$, the solid phase pressure exhibits an additional contribution when a highly dense granular flow is present. Johnson and Jackson [85] proposed an equation for additional solid phase pressure due to friction $p_{\mathrm{s,fr}}$:

$$p_{\mathrm{s,fr}} = Fr \frac{\left(\alpha_{\mathrm{s}} - \alpha_{\mathrm{s,fr}}\right)^{n}}{\left(\alpha_{\mathrm{s,max}} - \alpha_{\mathrm{s}}\right)^{P}}. \tag{2.53}$$

The symbols are identical to Equation (2.51).

Radial distribution function

The radial distribution function g_0 is a probability function for the collision of particles and is similar to the radial repulsive function between molecules by Chapman and Cowling [89]. It was extended to rigid spheres. Ogawa et al. [90] proposed the following equation based on the work of Alder and Wainwright [91]:

$$g_0 = \left[1 - \left(\frac{\alpha_\mathrm{s}}{\alpha_\mathrm{s,max}}\right)^{1/3}\right]^{-1}. \tag{2.54}$$

Several other often used equations for the radial distribution function can be found elsewhere [15, 92, 93]

Granular temperature

As interpenetrating continua are modeled in the TFM, particles are not simulated, but rather solid phases. The fluctuation of the individual particles can not be monitored within a continuum approach. Therefore, a transport equation for the granular temperature will be solved. The granular temperature θ_s is a measure to quantify the fluctuation of particle movement, i.e., kinetic energy of the particulate matter. The granular temperature can be calculated with:

$$\theta_\mathrm{s} = \frac{1}{3}\langle \mathbf{u}_\mathrm{s}^2 \rangle, \tag{2.55}$$

where the brackets define an averaging over velocity space. The transport equation for the granular temperature is in accordance to Ding and Gidaspow [78]:

$$\frac{3}{2}\left[\frac{\partial}{\partial t}\left(\alpha_\mathrm{s}\rho_\mathrm{s}\theta_\mathrm{s}\right) + \boldsymbol{\nabla}\cdot\left(\alpha_\mathrm{s}\rho_\mathrm{s}\mathbf{u}_\mathrm{s}\theta_\mathrm{s}\right)\right] = \left(-p_\mathrm{s}\bar{\bar{\mathrm{I}}} + \bar{\bar{\tau}}_\mathrm{s}\right) : \boldsymbol{\nabla}\mathbf{u}_\mathrm{s} + \boldsymbol{\nabla}\cdot\left(\kappa_\mathrm{s}\boldsymbol{\nabla}\theta_\mathrm{s}\right) - \gamma_\mathrm{s} - J_\mathrm{s}. \tag{2.56}$$

In this equation $\boldsymbol{\nabla}\cdot\left(\kappa_\mathrm{s}\boldsymbol{\nabla}\theta_\mathrm{s}\right)$ represents the diffusion of the fluctuating energy, κ the granular thermal conductivity, γ_s the collisional dissipation of energy and J_s the dissipation of energy due to inelastic behavior of particles.

Besides the partial differential equation for the granular temperature, an algebraic formulation can be used for the determination of θ_s. The algebraic formulation can be applied if

the dissipation of the granular energy is of a local matter and the convective and diffusive parts of Equation (2.56) can be neglected [84, 94].

Granular thermal conductivity

The conductivity of fluctuating energy is calculated by [78]:

$$\begin{aligned}\kappa_\mathrm{s} = \rho_\mathrm{s} d_\mathrm{p} \sqrt{\theta_\mathrm{s}} \cdot \Bigg(& 2\alpha_\mathrm{s}^2 g_0 \left(1+e\right) \frac{1}{\sqrt{\pi}} \\ & + \frac{9}{8}\sqrt{\pi} g_0 0.5 \left(1+e\right) \alpha_\mathrm{s}^2 \\ & + \frac{15}{16}\sqrt{\pi}\alpha_\mathrm{s} + \frac{25}{64}\sqrt{\pi}\frac{1}{\left(1+e\right) g_0}\Bigg).\end{aligned} \tag{2.57}$$

This effects only small particles, as large particle have a high granular thermal conductivity and hence, the motion in a molecular space-scale can be neglected [15]. Nieuwland et al. [83], Syamlal et al. [84], and Hrenya and Sinclair [95] proposed further models to calculate the granular thermal conductivity.

Collisional dissipation of energy

Colliding particles dissipate energy. This energy is quantified by the collisional dissipation of energy γ_s according to Lun et al. [80] and is proportional to the coefficient of restitution e, the repulsive radial distribution function g_0 and the solid phase fraction α_s:

$$\gamma_\mathrm{s} = 12\sqrt{\frac{\theta_\mathrm{s}^3}{\pi}}\left(1-e^2\right)\frac{\alpha_\mathrm{s}^2 \rho_\mathrm{s} g_0}{d_\mathrm{p}}. \tag{2.58}$$

According to this equation, highly dense granular material (g_0 and α_s high) with a high fluctuation of velocity (θ_s high) and large coefficients of restitution, results in a great energy dissipation due to particle collisions. Other equations for the calculation of the collisional dissipation of energy can be found elsewhere [84, 95].

Generation of granular energy

Due to inelastic behavior, kinetic energy of particles can either increase or decrease the granular energy. A decrease happens due to dissipation, e.g., collisions and energy loss. An increase in granular energy can occur due to the momentum exchange with the

surrounding fluid phase. This generation is quantified by J_s and can be calculated by [96]:

$$J_\mathrm{s} = 3\beta\theta_\mathrm{s} - \frac{3}{4}\frac{\beta^2 d_\mathrm{p}\left(\mathbf{u}_\mathrm{s} - \mathbf{u}_\mathrm{f}\right)^2}{\alpha_\mathrm{s}\rho_\mathrm{s}\sqrt{\pi\theta_\mathrm{s}}}. \tag{2.59}$$

The momentum exchange coefficient is defined by β. Other models can be found in the works of Lun et al. [80].

Momentum exchange coefficient

The momentum exchange $\mathbf{M}$ couples the fluid and the solid phase. Forces interacting with each other are combined to the momentum exchange either acting from the fluid to the solid phase $\mathbf{M}_\mathrm{f,s}$ or vice versa $\mathbf{M}_\mathrm{s,f}$. The momentum exchange follows Newton's third law according to:

$$\mathbf{M}_\mathrm{s,f} = -\mathbf{M}_\mathrm{f,s}. \tag{2.60}$$

A momentum exchange coefficient β is introduced to calculate the momentum exchange depending on the relative velocities of the interpenetrating phases:

$$\mathbf{M}_\mathrm{f,s} = \beta\left(\mathbf{u}_\mathrm{f} - \mathbf{u}_\mathrm{s}\right) \tag{2.61}$$

and

$$\mathbf{M}_\mathrm{s,f} = \beta\left(\mathbf{u}_\mathrm{s} - \mathbf{u}_\mathrm{f}\right). \tag{2.62}$$

The momentum exchange coefficient is composed of all the occurring coupling effects, e.g., drag, lift, virtual mass, turbulent dispersion. The contribution due to drag can be found in Chapter 2.3.3 with its derivation of a single particle to a swarm of particles including several drag models with their application. Drag results in the highest contribution to the momentum exchange [97, 98] and the virtual mass force can not be neglected for liquid-solid fluidization processes. The other contributions are of minor magnitude and can be neglected for dense granular flows [99, 100].

Virtual Mass Force

Any change of the acceleration of a particle in a surrounding fluid causes a corresponding acceleration to the fluid itself. Hence, a resisting force acts on the particle [101]. This force

is depending on the mass of the displaced fluid and the acceleration of the particle [102] and is called the virtual mass force[6] $\mathbf{F}_{\mathrm{vm}}$. Zuber [103] proposed the following equation to quantify the virtual mass force:

$$\mathbf{F}_{\mathrm{vm}} = C_{\mathrm{vm}}\, V_{\mathrm{p}}\, \rho_{\mathrm{f}} \left(\frac{\mathrm{d}\mathbf{u}_{\mathrm{f}}}{\mathrm{d}t} - \frac{\mathrm{d}\mathbf{u}_{\mathrm{s}}}{\mathrm{d}t} \right). \tag{2.63}$$

The coefficient C_{vm} can be calculated using empirical models, e.g., by Odar [104] or Schöneborn [105]. Drew et al. [106, 107] derived a value for the coefficient of $C_{\mathrm{vm}} = 0.5$ for spherical particles.

Before choosing the TFM approach for the simulation of granular flows, the limitations of this model must be considered. For example, as the TFM is a continuum approach, the particles are not resolved. Hence, particle-particle interaction can not be accounted for correctly and the simulation is heavily dependent on stochastic models [108]. Furthermore, with the presented equations only one single solid phase can be modeled. This implies, that the solid phase is consisting of monodisperse particles. In most cases, especially in industrial-scale applications, the particles are polydisperse. The TFM can be extended theoretically to infinite additional phases. Simulations for a binary particle size distribution have been successfully performed [109–111]. Additional phases for polydisperse particles result in an unreasonable high computational work as more and more equations have to be solved. A promising approach is to include a population balance model to account for polydispersity of the particles [112]. Another more practical approach is using an averaged diameter as a particle size, which is often used when simulating large-scale fluidization reactors. However, the TFM has been used for a wide range of application from FCC units, food industry to power generation [113–116].

2.3.2 Eulerian-Lagrangian Model

Using this model, a Lagrangian particle tracking (LPT) is applied to determine the pathways of the individual particles. The particles are described by points and sinks of momentum rather than resolved particles. The movement of the fluid phase is still calculated with the Navier-Stokes equations analog to the TFM (cf. Equation (2.42)) with the inclusion of the momentum exchange term between the fluid phase and the particles $\mathbf{M}_{\mathrm{f,s}}$. The void fraction ε is not based on a generic transport equation, but rather on the

[6] Sometimes also referred to as added or apparent mass force in literature.

placement of the particles in the numerical grid. The void fraction can be calculated with:

$$\varepsilon = 1 - \frac{1}{V_{\text{cell}}} \sum_{\forall \text{p} \in \text{cell}} V_{\text{p}}. \tag{2.64}$$

The volume of the individual particle is defined by V_{p} and the volume of the cell the particle is located in by V_{cell}. There are a number of different approaches on how to evaluate the void fraction for Eulerian-Lagrangian simulation, mostly on how particles overlapping to neighboring cells are treated. The simplest and most used approach is the Particle Centroid Method (PCM). Here, the whole particle volume is attributed to the cell the particle is residing at, regardless of overlapping to other cells. Other more sophisticated methods on how the determination of the void fraction and the transformation of Lagrangian to Eulerian values are handled can be found in Appendix B. As the particles are individually tracked and not comprised of a solid phase treated as a continuum according to TFM, the momentum exchange has to be based on the properties of each individual particle. A distinction has to be made between values of the individual particle and and averaged property of the solid phase based on the cell. E.g., the velocity of a particle (Lagrangian value) is represented by $\mathbf{u}_{\text{p}}$ and the velocity of the solid phase based on the cell (Eulerian value) by $\mathbf{u}_{\text{s}}$. The solid phase velocity can be calculated with the velocities of the individual particles:

$$\mathbf{u}_{\text{s}} = \frac{1}{n_{\text{p}}} \sum_{\forall \text{p} \in \text{cell}} \mathbf{u}_{\text{p}}, \tag{2.65}$$

where the number of particles located in the cell is defined by n_{p}. The momentum exchange used for the coupling between the fluid and the particles can then be expressed as:

$$\mathbf{M}_{\text{f,s}} = \frac{\sum \mathbf{F}_{\text{f,p}}}{V_{\text{cell}} \left| \mathbf{u}_{\text{f}} - \mathbf{u}_{\text{s}} \right|}. \tag{2.66}$$

$\sum \mathbf{F}_{\text{f,p}}$ represents the forces of all the particles acting on the fluid phase and vice versa. Those coupling forces can consist of forces due to drag, buoyancy, lift, pressure gradients, the Magnus effect and others. As the drag force is the major contribution to the coupling between the particles and the fluid phase (cf. Chapter 2.3.1), this force will be discussed exemplarily. Similar to the Eulerian values, the Lagrangian values for the drag force can be calculated by the momentum exchange coefficient β. Additionally, the relative velocity between the particle and the surrounding fluid phase is needed, as well as the volume of the particle:

$$\mathbf{F}_{\text{d}} = \beta \left(\mathbf{u}_{\text{f}} - \mathbf{u}_{\text{p}} \right) \frac{m_{\text{p}}}{\rho_{\text{p}}}. \tag{2.67}$$

The momentum exchange coefficient can be calculated in the same way as in the TFM with the exception of using Lagrangian values of the individual particles instead of Eulerian values of the solid phase.

The translation of the particles can be described by a force and torque balance according to Newton's second law of motion (cf. Equations (2.68) and (2.69)):

$$m_\mathrm{p} \frac{\mathrm{d}\mathbf{u}_\mathrm{p}}{\mathrm{d}t} = \sum \mathbf{F}_\mathrm{p} \tag{2.68}$$

and

$$I_\mathrm{p} \frac{\mathrm{d}\omega_\mathrm{p}}{\mathrm{d}t} = \mathbf{T}_\mathrm{p}. \tag{2.69}$$

Here, I_p is the moment of inertia, ω_p the angular velocity and $\mathbf{T}_\mathrm{p}$ the torque of the particle. $\mathbf{F}_\mathrm{p}$ stands for all the forces acting on the particles including for example gravity force. $\mathbf{F}_\mathrm{p}$ can be split up in contact and non-contact forces, $\mathbf{F}^\mathrm{c}$ and $\mathbf{F}^\mathrm{nc}$, respectively. The non-contact forces include all forces having their origin from the surrounding fluid and external factors, but also magnetic effects. The contact forces result due to collisions of particulate matter.

The Eulerian-Lagrangian model has different sub-models differing in simulation speed and accuracy. The models include the Discrete Phase Model (DPM), Discrete Element Model (DEM) and Multiphase Particle-In-Cell Model (MP-PIC). Models resulting in a high accuracy usually require the longest simulation time. Thus, it is detrimental not to know how resolved the simulation shall be. The degree of accuracy is best described by the determination of the coupling terms between the fluid phase and the particles. The following fluid-particle coupling methods can be distinguished regarding an isothermal flow:

- One-way coupling: external forces act on particles, e.g., gravity and fluid motion,
- Two-way coupling: one-way coupling & particle motion influences the fluid motion (momentum exchange),
- Four-way coupling: two-way coupling & particle-particle interactions & particle-fluid-particle interactions.

Particle-particle interaction mainly consists of particle collisions, but can also include adhesive, electrostatic and other effects. The term particle-fluid-particle interactions describes the phenomenon of a relative acceleration of fluid due to a smaller area which is occupied by particles. This effect contributes to the Navier-Stokes equation with the

introduction of the void fraction ε in Equation (2.42). Elghobashi [117] proposed a map of regimes to determine when a one-, two- or four-way coupling shall be used for fluid-particle flows including turbulences. A modified map of Elghobashi from 1994 [118] is depicted in Figure 2.8. Here, S/d_p represents the ratio between the distance between two neighboring particles and the diameter of the particles, τ_p the particle response time, τ_e the turnover time of large eddies, τ_K the Kolmogorov time scale and α_s the volume fraction of the particulate phase.

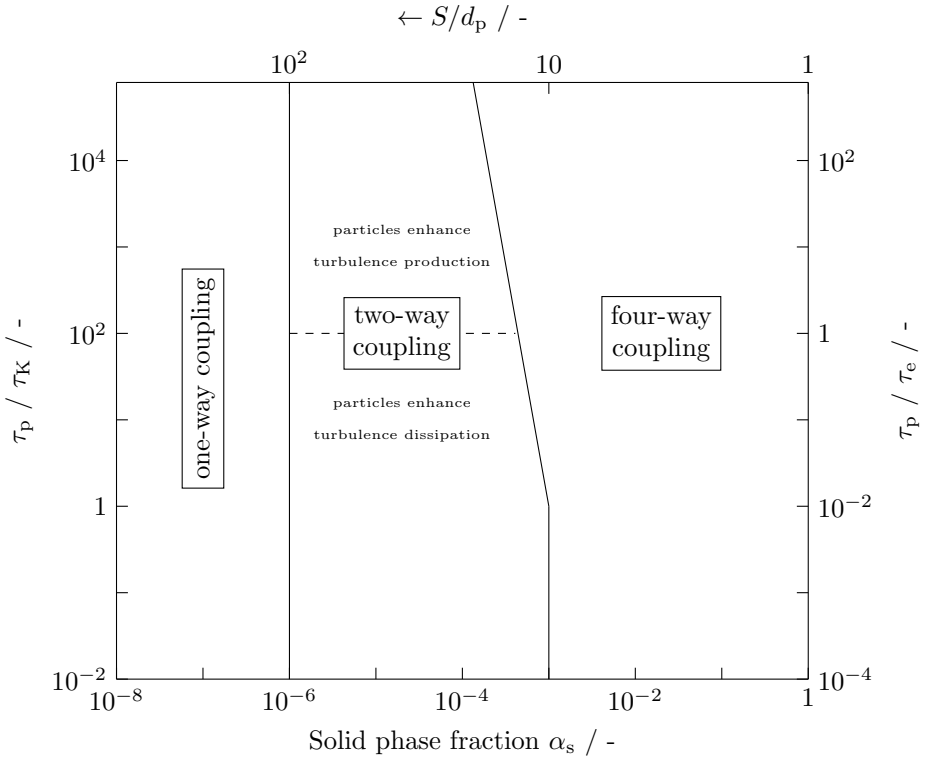

Figure 2.8: Regime map for fluid-particle coupling with particle induced turbulence production or dissipation (modified from [118]).

The map of flow regimes can be split up into a dilute and dense suspension flow at a volume fraction of the solid phase of 0.001 or an equivalent value of $S/d_\mathrm{p} = 10$. The one-way coupling approach can be applied for very dilute flows, i.e., with a solid phase volume fraction lower than $1 \cdot 10^{-6}$. The particle trajectories are only influenced by external forces, e.g., the fluid and not vice versa. Hence, the particle motions have no or a negligible effect on turbulence. Regarding dilute flows in a range of $1 \cdot 10^{-6} < \alpha_\mathrm{s} < 1 \cdot 10^{-3}$, the two-way coupling is applied and therefore the momentum exchange between the fluid and the particles must be considered. Depending on the turnover time of large eddies and the Kolmogorov time scale, τ_e and τ_K respectively, the particles can either enhance the production of eddies (favorable if τ_e and τ_K are low), or enhance the dissipation rate of turbulence energy (favorable if τ_e and τ_K are high). For fluidized bed applications a dense suspension flow is apparent and therefore a four-way coupling approach must be used. The

DPM does not include particle-particle interaction, so no four-way coupling approach is applied. This model is mainly used for highly dilute granular flows. DEM coupled with CFD (CFD-DEM) is a four-way coupled method taking particle-particle interactions into account. The MP-PIC method also includes particle-particle interactions, but does not resolve individual collisions. The last two approaches, DEM and MP-PIC will be discussed in detail in the following.

2.3.2.1 Discrete Element Model

Cundall and Strack [119] first proposed a model for particle-particle interactions based on the hard-sphere model. Using the hard-sphere model, no overlap of colliding particles is possible and the collisions are instantaneous. This is the biggest disadvantage of the hard-sphere model compared to the soft-sphere model, as only one collision can be simultaneously considered [120, 121]. Therefore, the hard-sphere model is not suitable for dense granular flows [122]. The soft-sphere model approaches collisions differently. Particles can have a minor overlap when collisions occur as the collision is simulated within a defined time-step. In order to include all acting forces correctly, the spring, slider and dashpot model was developed (cf. Figure 2.9). As can be seen, the contact forces as a result of two particles colliding $\mathbf{F}^{\mathrm{c}}$ can be further split up in a contact force in normal and tangential direction, $\mathbf{F}^{\mathrm{c}}_{\mathrm{n}}$ and $\mathbf{F}^{\mathrm{c}}_{\mathrm{t}}$, respectively. However, not only particle-particle collisions contribute to the contact forces, but also particle-wall interactions $\mathbf{F}^{\mathrm{c}}_{\mathrm{w}}$, i.e., particles hitting a stationary boundary.

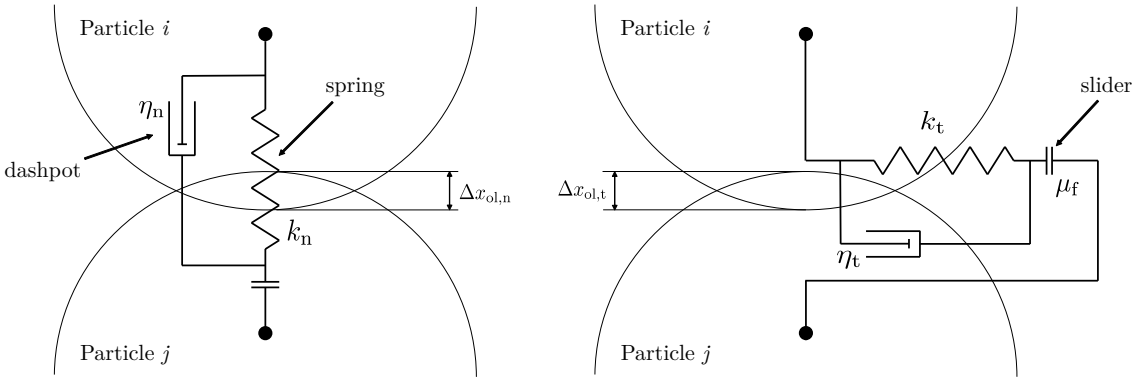

(a) Normal direction. **(b)** Tangential direction.

Figure 2.9: Spring, slider and dashpot model for particle contacts in normal (a) and tangential direction (b) (modified from [123]).

The contact force of colliding particles in normal direction $\mathbf{F}^{\mathrm{c}}_{\mathrm{n}}$ can be calculated under consideration of a spring stiffness and a damping effect according to the Hertzian spring-theory:

$$\mathbf{F}^{\mathrm{c}}_{\mathrm{n}} = -k_{\mathrm{n}} \Delta x^{b}_{\mathrm{n,ol}} \mathbf{n} - \eta_{\mathrm{n}} \mathbf{u}_{\mathrm{n,rel}}. \tag{2.70}$$

Here, the spring stiffness in normal direction is represented by k_n, the length of the overlap between two colliding particles by $\Delta x_\mathrm{n,ol}$, b has a value of 1.5 to account for the Hertzian spring theory, $\mathbf{n}$ is the unity vector in normal direction, η_n the damping coefficient for normal forces and $\mathbf{u}_\mathrm{n,rel}$ the relative velocity in normal direction between the two colliding particles. Analog to Equation (2.70) the contact force in tangential direction can be described by:

$$\mathbf{F}_\mathrm{t}^\mathrm{c} = -k_\mathrm{t}\Delta x_\mathrm{ol,t}\mathbf{t} - \eta_\mathrm{t}\mathbf{u}_\mathrm{t,slip}. \tag{2.71}$$

The parameters used here are directed in tangential direction and the slip velocity $\mathbf{u}_\mathrm{t,slip}$ is used. The normal spring stiffness is calculated with:

$$k_\mathrm{n} = \frac{4}{3}\sqrt{r_\mathrm{eff}}\frac{E}{2\left(1-\nu^2\right)}, \tag{2.72}$$

where E is Young's modulus and ν the Poisson ratio. The effective radius r_eff is calculated for two different sized particles with their respective diameter of d_1 and d_2 by:

$$r_\mathrm{eff} = 0.5\frac{d_1\,d_2}{d_1+d_2}. \tag{2.73}$$

The normal spring stiffness can be further simplified if the particles at hand are monodisperse, i.e., $d_i = \text{const}$. Using this, the effective radius reduces to $r_\mathrm{eff} = 0.25 d_\mathrm{p}$ and the normal spring stiffness to:

$$k_\mathrm{n} = \frac{1}{3}\sqrt{d_\mathrm{p}}\frac{E}{1-\nu^2}. \tag{2.74}$$

With the assumption of a constant coefficient of restitution for both a normal and tangential contact, as well as an equal time of contact for a normal and tangential collision, the spring constant in tangential direction k_t is proportional to the spring constant in normal direction k_n by [122]:

$$k_\mathrm{t} = \frac{2}{7}k_\mathrm{n}. \tag{2.75}$$

According to the Coulomb friction law, if the tangential force of the contact exceeds the Coulomb friction force $\mu_\mathrm{f}|\mathbf{F}_\mathrm{n}^\mathrm{c}|$, with μ_f being the friction coefficient, sliding occurs. The tangential component of the contact force therefore follows the equation:

$$\mathbf{F}_\mathrm{t}^\mathrm{c} = \min\left(-k_\mathrm{t}\Delta x_\mathrm{ol,t}\mathbf{t} - \eta_\mathrm{t}\mathbf{u}_\mathrm{t,slip}\ ,\ -\mu_\mathrm{f}|\mathbf{F}_\mathrm{n}^\mathrm{c}|\mathbf{t}\right). \tag{2.76}$$

The damping coefficient for contacts in normal direction η_n is defined by:

$$\eta_\mathrm{n} = \alpha_\mathrm{n}\sqrt{M_\mathrm{red}k_\mathrm{n}}\,\Delta x_\mathrm{ol,n}^{0.25}. \tag{2.77}$$

The parameter α_n is an empirical parameter depending on the coefficient of restitution in normal direction e_n and can be calculated using the following equation [120, 123]:

$$\alpha_\mathrm{n} = \begin{cases} \frac{-2\ln e_\mathrm{n}}{\sqrt{\pi^2+\ln^2 e_\mathrm{n}}} & \text{if } 0 < e_\mathrm{n} \leq 1 \\ 2 & \text{if } e_\mathrm{n} = 0. \end{cases} \tag{2.78}$$

The reduced mass for different sized particles M_red is defined with

$$M_\mathrm{red} = \frac{m_1 m_2}{m_1 + m_2} \tag{2.79}$$

and the equation can be simplified if both particles are of equal mass m_p to

$$M_\mathrm{red} = 0.5 m_\mathrm{p}. \tag{2.80}$$

With both simplifications of same-sized particles and particles with equal masses according to Equation (2.80) the damping coefficient in Equation (2.77) can be further simplified to:

$$\eta_\mathrm{n} = \alpha_\mathrm{n} \sqrt{0.5 m_\mathrm{p} k_\mathrm{n}}\, \Delta x_\mathrm{ol,n}^{0.25}. \tag{2.81}$$

The damping coefficient in tangential direction η_t is equal to the damping coefficient in normal direction η_n according to Hoef et al. [122]. The particle-wall interaction forces can be calculated accordingly with the assumption that the wall is a stationary hard surface.

With the above equations, particle movement influenced by external forces, surrounding phases and inter-particle collisions and forces can be calculated according to a soft-sphere model in DEM. Tsuji et al. [123] were the first coupling DEM with a fluid phase, called CFD-DEM. This model has since been widely applied for small-scale granular flow applications ranging from pneumatic transport to highly-packed dense beds [124–130]. Limitations for this model include the increasing computational time with the number of particles in the system [131]. As more particles are introduced, more collisions have to be accounted for. Therefore, CFD-DEM is not suitable for a high number of particles. Approaches to simulate a larger number of particles using a particle tracking method while still maintaining a reasonable computational time have been proposed and two of them will be discussed in detail in the following.

2.3.2.2 Coarse Grain Model

In order to make CFD-DEM simulations with a large number of particles more viable in terms of computational time, Sakai and Koshizuka [132] proposed the Coarse Grain (CG)

model. Using this model, a defined number of particles are lumped together to a bigger parcel. This parcel exhibits the same forces as the formerly smaller particles, important parameters are adjusted to account for the increased diameter and particle-particle collisions occur with the bigger parcels. The number of particles can be drastically reduced while still maintaining the granular flow. The CG-factor f_{CG} is introduced to quantify how many particles are merged to a parcel. The CG-factor is dependent on the particle diameters of the original smaller particles and the bigger CG-particles, $d_{\mathrm{p,orig}}$ and $d_{\mathrm{p,CG}}$, respectively. The CG-factor can then be calculated with

$$f_{\mathrm{CG}} = \frac{d_{\mathrm{p,CG}}}{d_{\mathrm{p,orig}}}. \tag{2.82}$$

Based on reduction of particle number, this means, that the particle number reduction is inversely proportional to f_{CG}^3. For example, if particles are merged together to a particle twice the diameter of the original particle, i.e., $f_{\mathrm{CG}} = 2$, eight original particles are then represented by one CG-parcel (cf. Figures2.10 and 2.11). This results in a reduction of the particle number by a factor of eight as well. Certain values have to be adjusted before and during the simulation in order to ensure a correct fluid dynamic behavior. The velocity of the CG-parcel $\mathbf{u}_{\mathrm{p,CG}}$ must be modified if the initial velocity of the original particles is not zero, $\mathbf{u}_{\mathrm{p,orig}} \neq 0$. For non-zero velocities, the initial velocity of the CG-parcel is adjusted by:

$$\mathbf{u}_{\mathrm{p,CG}} = \frac{1}{f_{\mathrm{CG}}^3} \sum_{\forall \mathrm{p} \in \mathrm{cell}} \mathbf{u}_{\mathrm{p,orig}}. \tag{2.83}$$

This means, the average velocity of the merged particles is assigned to the CG-parcel.

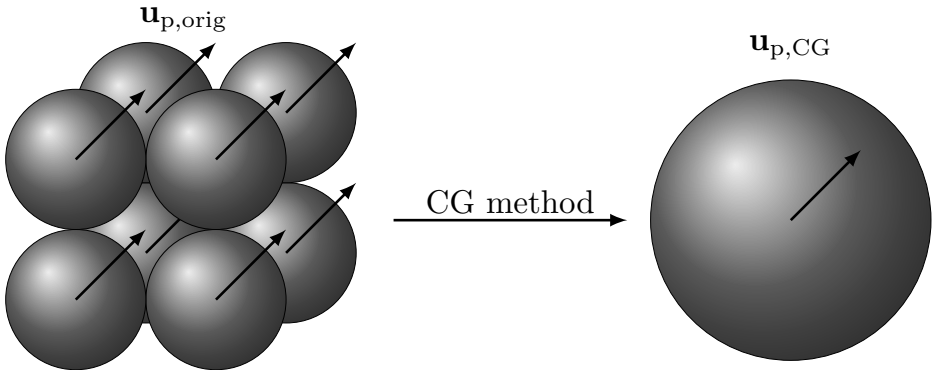

Figure 2.10: Transformation of translational motion ($\mathbf{u}_{\mathrm{p,orig}}$) of four particles to a coarse grained particle modified from [132].

The angular momentum of the CG-parcel is treated in a similar way:

$$\omega_{\mathrm{p,CG}} = \frac{1}{f_{\mathrm{CG}}^3} \sum_{\forall \mathrm{p} \in \mathrm{cell}} \omega_{\mathrm{p,orig}}. \tag{2.84}$$

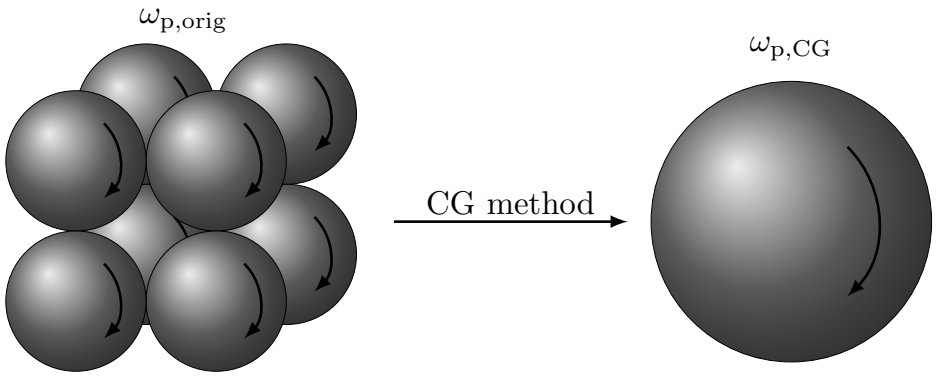

Figure 2.11: Transformation of rotational motion ($\omega_{\mathrm{p,orig}}$) of four particles to a coarse grained particle modified from [132].

All particles are assumed to have the same value and direction. The rotational movement, i.e., the angular momentum $\omega_{\mathrm{p,orig}}$, is also assumed to be equal for all merged particles.

The non contact-forces, drag, gravity and buoyancy are all dependent on the particle diameter. As the particle diameter of a CG-parcel compared to the original particles differs by a factor of f_{CG}^3, those forces have to be adjusted as well. Therefore, the drag, gravity and buoyancy force of the CG-parcel are calculated with the following equations:

$$\mathbf{F}_{\mathrm{d,CG}} = f_{\mathrm{CG}}^3 \mathbf{F}_{\mathrm{d,orig}} \tag{2.85}$$

$$\mathbf{F}_{\mathrm{g,CG}} = f_{\mathrm{CG}}^3 \mathbf{F}_{\mathrm{g,orig}} \tag{2.86}$$

$$\mathbf{F}_{\mathrm{b,CG}} = f_{\mathrm{CG}}^3 \mathbf{F}_{\mathrm{b,orig}}. \tag{2.87}$$

The calculation of the particle Reynolds number is done using the original particle diameter $d_{\mathrm{p,orig}}$ and the momentum exchange coefficient is determined accordingly. With the assumption of equal kinetic energies between the parcel and the group of particles (cf. Equation (2.88)), the contact forces of the CG-parcel in normal and tangential direction can be calculated with the use of the CG-factor f_{CG} according to Equations (2.89) and (2.90).

$$\frac{1}{2} m_{\mathrm{p,CG}} \mathbf{u}_{\mathrm{p,CG}}^2 + \frac{1}{2} I_{\mathrm{p,CG}} \omega_{\mathrm{p,CG}}^2 = f_{\mathrm{CG}}^3 \left(\frac{1}{2} m_{\mathrm{p,orig}} \mathbf{u}_{\mathrm{p,orig}}^2 + \frac{1}{2} I_{\mathrm{p,orig}} \omega_{\mathrm{p,orig}}^2 \right), \tag{2.88}$$

$$\mathbf{F}_{\mathrm{n,CG}}^{\mathrm{c}} = f_{\mathrm{CG}}^3 \mathbf{F}_{\mathrm{n,orig}}^{\mathrm{c}} \tag{2.89}$$

and

$$\mathbf{F}_{\mathrm{t,CG}}^{\mathrm{c}} = f_{\mathrm{CG}}^3 \mathbf{F}_{\mathrm{t,orig}}^{\mathrm{c}}. \tag{2.90}$$

The relationship of the small particles and the CG-parcel for the moment of inertia, $I_{\mathrm{p,orig}}$ and $I_{\mathrm{p,CG}}$, respectively, considers the transformation of the particle (and parcel) masses and diameters according to:

$$m_{\mathrm{p,CG}} = f_{\mathrm{CG}}^{3}\, m_{\mathrm{p,orig}} \tag{2.91}$$

and

$$d_{\mathrm{p,CG}} = f_{\mathrm{CG}}\, d_{\mathrm{p,orig}}. \tag{2.92}$$

Hence, the following relation for the moment of inertia is valid:

$$I_{\mathrm{p,CG}} = f_{\mathrm{CG}}^{5} I_{\mathrm{p,orig}}. \tag{2.93}$$

The torque of the coarse grained particle cluster $\mathbf{T}_{\mathrm{p,CG}}$ follows the relation of:

$$\mathbf{T}_{\mathrm{p,CG}} = f_{\mathrm{CG}}^{4} \mathbf{T}_{\mathrm{p,orig}}. \tag{2.94}$$

Other parameters, e.g., particle density, spring stiffness, Young's modulus, Poisson ratio, friction coefficients, coefficient of restitution, do not need to be modified and remain valid. The potential of faster simulation due to a particle reduction using the CG model is dependent on the CG-factor f_{CG}; a theoretical CG-factor of $f_{\mathrm{CG}} = 4$ would result in a particle number reduction of 64. The CG-factor can not be arbitrarily chosen. A couple of limits exist which must be considered for the choice of the CG-factor. Firstly, the CG-parcels must still comply with cell-to-particle size ratios. This means the parcel must not exceed the dimensions of the cells of the numerical grid, otherwise the void fraction determination as well as the calculation of solid phase properties become corrupt. Furthermore, the number of the resulting parcels must still be in an adequate high number. If two few parcels exist, then the number of collisions is drastically reduced and hence, the particle forces become erroneous. As the CG-factor f_{CG} increases, more and more particles are lumped together to a single parcel. This implies, that the individual values of the original particles, e.g., velocity or angular momentum, are now represented by a uniform value of the parcel. This means, that the individuality of particle values is reduced, which has to be considered before choosing a high CG-factor. Also the CG-factor has to be an integer number. Otherwise, a defined number of particles will be presented by a fractional number of CG-parcels.

2.3.2.3 Multiphase Particle in Cell Model

The TFM with its stochastic determination of particle collisions due to solid phase pressures and viscous stresses is applicable for monodisperse and a high number of particles. On the contrary, with CFD-DEM or the Lagrangian method in general, the individually tracked particles are implicitly coupled with the surrounding fluid phase. Different properties can be attributed to each of the particles, e.g., density, size and hardness. This method can be used for small-scale geometries and a moderate number of particles. A blend between those two models is the multiphase particle-in-cell (MP-PIC) method proposed by Andrews and O'Rourke [133]. This method is based on the particle-in-cell method for single-phase flows by Harlow [134] and was extended for multiphase flows. Here, the particles are tracked individually according to a Lagrangian treatment. Therefore, polydisperse particles, as well as particles with individual properties, can be easily simulated. Particle-particle collision are modeled according to stochastic approach and are not resolved individually. Hence, the computational expensive particle-particle collisions of DEM are not needed as they are approximated with a stochastic approach using a particle stress model.

The momentum exchange term in Equation (2.42) is substituted with the interphase momentum transfer function $\mathbf{M}_{\mathrm{f,s}}$:

$$\mathbf{M}_{\mathrm{f,s}} = \iint f\, m_{\mathrm{p}} \left[\beta \left(\mathbf{u}_{\mathrm{f}} - \mathbf{u}_{\mathrm{p}}\right) - \frac{1}{\rho_{\mathrm{p}}} \boldsymbol{\nabla} p\right]\, dm_{\mathrm{p}}\, d\mathbf{u}_{\mathrm{p}}. \tag{2.95}$$

The particle distribution function f follows the Liouville equation to solve the solid phase hydrodynamics:

$$\frac{\partial f}{\partial t} + \boldsymbol{\nabla} \cdot \left(f \mathbf{u}_{\mathrm{p}}\right) + \boldsymbol{\nabla}_{\mathbf{u}_{\mathrm{p}}} \cdot \left(f \mathbf{a}_{\mathrm{p}}\right) = 0. \tag{2.96}$$

In Equation (2.96) $\mathbf{a}_{\mathrm{p}}$ represents the acceleration of the individual particle. As particle-collisions are not resolved using a Lagrangian approach, but rather a continuum approach, the calculation of the acceleration is also dependent on a solid phase stress tensor $\overline{\overline{\tau}}_{\mathrm{s}}$ according to:

$$\mathbf{a}_{\mathrm{p}} = \beta \left(\mathbf{u}_{\mathrm{f}} - \mathbf{u}_{\mathrm{p}}\right) - \frac{1}{\rho_{\mathrm{p}}} \boldsymbol{\nabla} p + g - \frac{1}{\alpha_{\mathrm{s}} \rho_{\mathrm{s}}} \boldsymbol{\nabla} \cdot \overline{\overline{\tau}}_{\mathrm{s}} \tag{2.97}$$

Many different models were proposed to calculate the solid phase stress tensor. Often, a modified solid stress from Harris and Crighton [135] for an isotropic solid stress is used, according to:

$$\overline{\overline{\tau}}_{\mathrm{s}} = P_{\mathrm{s}} \frac{\alpha_{\mathrm{s}}^{b}}{\alpha_{\mathrm{s,max}} - \alpha_{\mathrm{s}}}. \tag{2.98}$$

P_{s} and b are modeling parameters that can be adjusted accordingly. The solid phase fraction α_{s} (Eulerian property) can be calculated by using the particle distribution function f:

$$\alpha_{\mathrm{s}} = \iint f \frac{m_{\mathrm{p}}}{\rho_{\mathrm{p}}} \, dm_{\mathrm{p}} \, d\mathbf{u}_{\mathrm{p}}. \tag{2.99}$$

The calculation of particle movements and other properties are analog to the DEM approach.

Furthermore, the MP-PIC method uses a clustering approach to further reduce the computational time. As opposed to the CG-method, where particles are lumped together to a larger parcel, in the MP-PIC method particles with identical properties, e.g., size, density, velocity and position, are treated as a parcel. For this parcel the above equations are solved in order to drastically speed-up the simulation [136].

A downside of the MP-PIC method are large numerical errors when using a high degree of particle-to-parcel ratio. Also, studies have found, that simulations using MP-PIC are not as accurate as particle-collision resolving CFD-DEM simulations, especially for the prediction of large particle clusters [137]. Furthermore, the particle stress as a continuum particle-collision property in a cell is used for all particles or parcels residing in this specific cell. Particles with different collision parameters, e.g., coefficient of restitution of friction values, may not be depicted accurately.

Using this approach industrial-scale geometries can be simulated in a reasonable amount of time [138, 139]. Lu et al. [140] simulated a hopper with a total of over 700 million particles using MP-PIC. This shows the immense potential of this simulation approach.

2.3.3 Determination of the drag coefficient

Besides the forces acting on a particle described in Chapter 2.3.2, one of the most important forces in fluid-solid flows is the drag force F_d [141, 142]. First, the drag force based on a single sphere is discussed and later the exerting drag between the fluid phase and a particulate system will be presented in detail with focus on widely applied correlations to predict the drag force.

In the simple case of a single sphere falling in a Newtonian fluid, three different forces are acting on the particle: the gravitational, buoyancy and drag force. The gravitational force is acting downwards, while the drag and buoyancy forces are acting upwards. The drag force is dependent on the cross-sectional area of the falling particle A, the dynamic pressure on the particle $\rho_\mathrm{f}\frac{u_\mathrm{f}^2}{2}$ and the drag coefficient C_d:

$$F_\mathrm{d} = A\rho_\mathrm{f}\frac{u_\mathrm{f}^2}{2}\frac{1}{C_\mathrm{d}}. \tag{2.100}$$

Rayleigh [143] performed a dimensional analysis to the flow problem and concluded that the drag coefficient is related to the Reynolds number. Lapple and Shepherd [144] collected several experimental data from different literature contributions [145–161] and averaged the findings. The resulting diagram of the drag coefficient C_d over the particle Reynolds number Re_p is often called the drag curve. This diagram is depicted in Figure 2.12[7].

The simplest way to classify the different regimes, is to determine three different areas of the curve depending on the prevailing type of flow:

- laminar region,
- intermediate region and
- turbulent region.

A more elaborate and finer distinction for the different regions can be found in the review work of Jones and Clarke [165], where the different regions are (with increasing Reynolds number):

- perfect laminar flow,

[7] The experimental data points for the drag coefficient below $Re_\mathrm{p} = 0.1$ are added from Allen [162] to extend the laminar flow region and illustrate the linear correlation of the drag coefficient according to Stokes' Law in Equation (2.101).

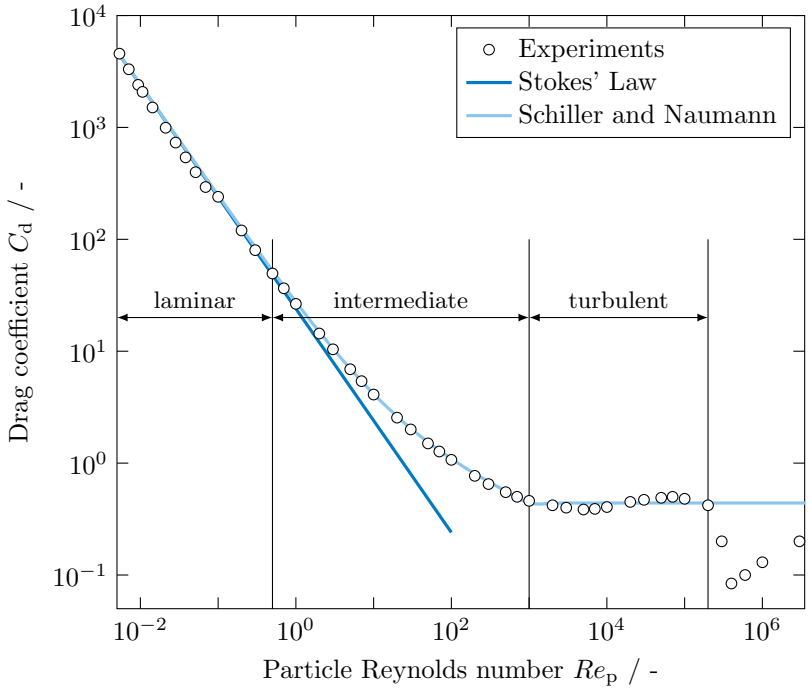

Figure 2.12: Drag curve: drag coefficient C_d depending on the particle Reynolds number Re_p based on the averaged experimental data of Lapple and Shepherd [144] for all three indicated regimes (laminar, intermediate and turbulent). Stokes' Law [163] and the correlation of Schiller and Naumann [164] complement the experimental data in their respective validated range.

- steady axisymmetric flow regime,
- steady planar-symmetric flow regime,
- unsteady planar-symmetric regime,
- unsteady asymmetric flow regime and
- turbulent wake regime.

At low Reynolds numbers the creeping flow is dominant in the laminar region. The drag coefficient in this region follows a linear correlation in the double-log diagram. Stokes [163] proposed the following equation later commonly known as the Stokes' Law for the linear correlation in the laminar region:

$$C_d = \frac{24}{Re_p}, \tag{2.101}$$

which is valid for $Re_\mathrm{p} < 0.5$. The particle Reynolds number is defined as:

$$Re_\mathrm{p} = \frac{\rho_\mathrm{f} d_\mathrm{p} \left|\mathbf{u}_\mathrm{f} - \mathbf{u}_\mathrm{p}\right|}{\eta_\mathrm{f}}. \tag{2.102}$$

In the turbulent regime Newton [166] measured a constant value for the drag coefficient independent of the Reynolds number. The later-called Newton's law for the drag coefficient in the Newton regime, i.e., the turbulent region in the range of $1000 < Re_\mathrm{p} < 200\,000$ reads as follows:

$$C_\mathrm{d} = 0.44. \tag{2.103}$$

Many different drag correlations exist for the intermediate region. One of the most widely applied and accurate drag correlations was proposed by Schiller and Naumann [164], which was later extended to be applicable for the laminar and turbulent region as well:

$$C_\mathrm{d} = \begin{cases} \frac{24}{Re_\mathrm{p}} \left(1.0 + 0.15\, Re_\mathrm{p}^{0.687}\right), & Re_\mathrm{p} \leq 1000 \\ 0.44, & Re_\mathrm{p} > 1000. \end{cases} \tag{2.104}$$

Note, that the value of the drag coefficient decreases at approximately $Re_\mathrm{p} = 200\,000$. This phenomenon is called drag-crisis. Here, the flow around the particle undergoes a critical change from laminar to turbulent in the boundary layer [167]. Hence, it is difficult to find a correlation covering the whole range of Reynolds numbers. Most of the correlations suffice with the sub-critical region below the drag crisis, i.e., $Re_\mathrm{p} < 200\,000$. The drag of a single sphere can differ quite significantly from the drag of a particulate system. More external factors, e.g., superficial velocity of the fluid due to the decreasing void fraction, have a higher influence on the drag force. In the following selected drag models for the determination of the drag coefficient for dilute and dense particle flows are presented.

Ergun drag model

Ergun [168] stated a correlation for the pressure drop of a fluid flow through granular solids. In this publication the solid phase was a packed bed and not a fluidized bed with moving particulate matter. The semi-empirical pressure drop correlation is valid in all flow regimes. A derivation from the pressure drop correlation to the momentum exchange coefficient can be seen in Equation (2.105).

$$\beta_\mathrm{Ergun} = 150 \frac{(1-\varepsilon)^2\, \eta_\mathrm{f}}{\varepsilon\, d_\mathrm{p}^2} + 1.75\,(1-\varepsilon)\, \frac{\rho_\mathrm{f}}{d_\mathrm{p}} \left|\mathbf{u}_\mathrm{f} - \mathbf{u}_\mathrm{p}\right|. \tag{2.105}$$

Here, two different terms contribute to the momentum exchange coefficient:

- a viscous part (first term) and
- a kinetic part (second term).

The viscous part is more dominant in viscous flows, i.e., laminar flows with low Reynolds numbers. At higher velocities or more specifically for turbulent flows, the kinetic part becomes more and more important. For turbulent fluidizations the viscous part can become negligible [169]. As stated above, the Ergun drag model was developed for packed beds. Hence, this model is partially suitable in regards to simulate the interphase exchange drag between the fluid and solid phase in a fluidized bed and mostly used for densely-packed granular flows. The resulting momentum exchange coefficient at different void fractions and particle Reynolds numbers is depicted in Figure 2.13a. Although the Ergun drag model is considered for densely packed solid flows, for comparison reasons the region of the void fraction was extended to $\varepsilon \to 1$.

Wen & Yu drag model

The following semi-empirical drag model proposed by Wen and Yu [170] is more accurate for dilute granular flows, $\varepsilon > 0.8$ [53, 171]. Here, they proposed a relationship between the drag coefficient of a particle in a multiparticle system and the drag coefficient of a single particle, C_d and $C_\mathrm{d,s}$, respectively:

$$\frac{C_\mathrm{d}}{C_\mathrm{d,s}} = f(\varepsilon). \tag{2.106}$$

In this equation $f(\varepsilon)$ represents a voidage function and can be expressed as $\varepsilon^{-4.65}$ according to Richardson and Zaki [172]. The drag coefficient of a single spherical particle can be calculated according to

$$C_\mathrm{d,s} = \frac{24}{Re_\mathrm{p}} \left(1 + 0.15 Re_\mathrm{p}^{0.687}\right), \tag{2.107}$$

which is valid for Reynolds numbers of up to 1000. Considering the momentum exchange coefficient β, the Wen & Yu drag correlation can be expressed as

$$\beta_\text{Wen \& Yu} = \frac{3}{4} C_\mathrm{d} \frac{\varepsilon\,(1-\varepsilon)}{d_\mathrm{p}} \rho_\mathrm{f} \left|\mathbf{u}_\mathrm{f} - \mathbf{u}_\mathrm{p}\right| \varepsilon^{-2.65} \tag{2.108}$$

and the values for the momentum exchange coefficient for varying void fractions at different particle Reynolds numbers is seen in Figure 2.13b.

Gidaspow drag model

Gidaspow [15, 78] combined the Ergun and Wen & Yu drag correlation in order to get a drag coefficient applicable for a wide range of flow regimes and granular flows, both dense and dilute. Therefore, the drag correlation of Ergun is used for dense granular flows at fluid volume fractions of $\varepsilon < 0.8$ and at increased fluid volume fractions, i.e., more dilute suspensions, the Wen & Yu correlation is used, according to:

$$\beta_{\text{Gidaspow}} = \begin{cases} 150\frac{(1-\varepsilon)^2\eta}{\varepsilon d_\text{p}^2} + 1.75\,(1-\varepsilon)\,\frac{\rho_\text{f}}{d_\text{p}}\left|\mathbf{u}_\text{f}-\mathbf{u}_\text{p}\right|, & \varepsilon < 0.8 \\ \frac{3}{4}\,C_\text{d}\frac{\varepsilon\,(1-\varepsilon)}{d_\text{p}}\,\rho_\text{f}\left|\mathbf{u}_\text{f}-\mathbf{u}_\text{p}\right|\varepsilon^{-2.65}, & \varepsilon \geq 0.8. \end{cases} \tag{2.109}$$

As the drag coefficient C_d of the Wen & Yu correlation is only suitable for Reynolds numbers of $Re < 1000$, the Schiller and Naumann [164] correlation is used (cf. Equation (2.104)).

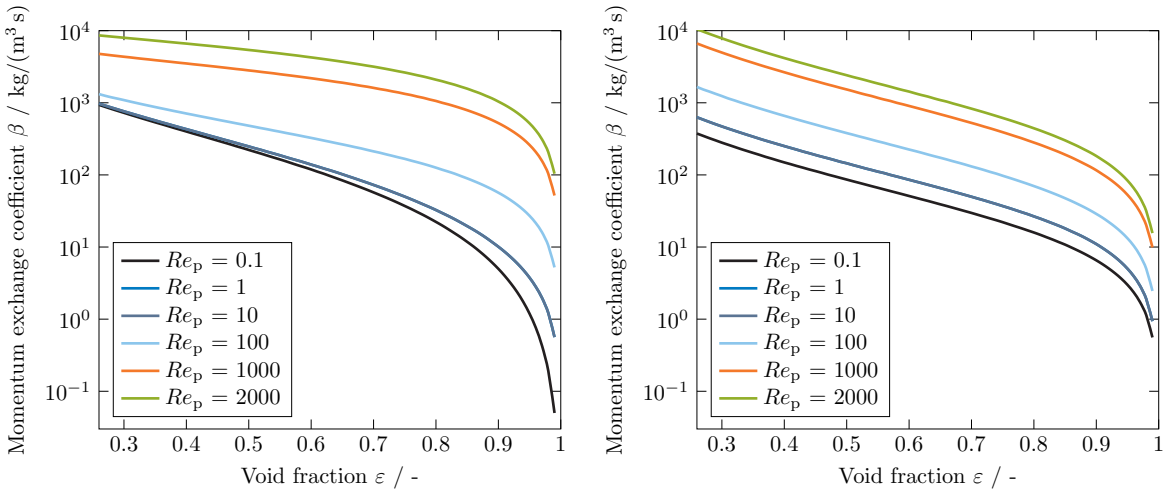

(a) Ergun drag model.

(b) Wen & Yu drag model.

Figure 2.13: Resulting momentum exchange coefficient β depending on the void fraction ε at different particle Reynolds numbers Re_p using the Ergun [168] and Wen & Yu [170] drag model.

This drag correlation is one of the widely used correlations used for dense granular flow simulations due to its simplicity and wide applicability [173]. Due to the discontinuity of the Gidaspow correlation at a fluid volume fraction of $\varepsilon = 0.8$, numerical errors and divergences can arise. The magnitude of this discontinuity increases with higher particle Reynolds number Re_p as it is depicted in Figure 2.15a. In order to prevent such divergence issues due to this discontinuity, Huilin and Gidaspow [109] introduced a weighted average of the drag correlation:

$$\beta_{\text{H\&G}} = \phi\beta_{\text{Ergun}} + (1-\phi)\,\beta_{\text{W\&Y}}, \tag{2.110}$$

with the monotonic smoothing function[8]

$$\phi = 0.5 + \frac{1}{\pi} \arctan\left[150 \cdot 1.75\,(0.8 - \varepsilon)\right]. \tag{2.111}$$

The smoothing function ϕ is depicted in Figure 2.14a for an arbitrary set-up. By means of this figure the conceptional use of the smoothing function becomes more apparent as it ensures three things in total:

- the drag correlation by Wen & Yu is applied for dilute flows ($\varepsilon > 0.8$) and
- in dense particulate regimes, i.e., $\varepsilon < 0.8$, the Ergun drag correlation is used,
- a smooth transition between the Ergun and Wen & Yu drag correlation at the step point of $\varepsilon = 0.8$ is provided.

Figure 2.14 illustrates the blended transition due to the introduction of the smoothing function ϕ of the Huilin & Gidaspow drag model. The Ergun drag model is used for densely-packed flows and for dilute flows the momentum exchange coefficient is calculated with the Wen & Yu drag model. The interface between the two drag model at a void fraction of $\varepsilon = 0.8$ shows a smooth transition between them.

In Figure 2.15 the resulting momentum exchange for both, the Gidaspow and Huilin & Gidaspow drag model, is depicted. They only differ at a void fraction of $\varepsilon = 0.8$ due to the switch between the use of the Ergun and Wen & Yu drag model. In view of the occurring discontinuity in the Gidaspow drag model, it is recommended to use the Huilin & Gidaspow drag model to avoid divergences.

[8] It must be stated, that in the original publication of Huilin and Gidaspow [109] the equation for the smoothing function ϕ is falsely displayed as it shows two errors:

1. the constant $\frac{1}{\pi}$ shall be outside of the argument of arctan instead of inside and
2. the switch term in the argument of arctan for the solid volume fraction α at a value of 0.2 should be $(\alpha - 0.2)$ instead of $(0.2 - \alpha)$.

The correct formula for the smoothing function can be found in [174, 175].

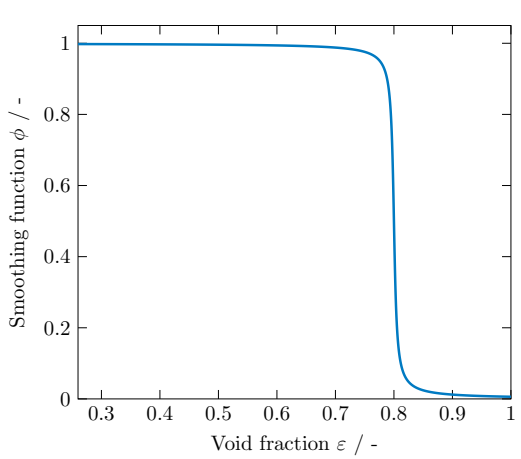

(a) Smoothing function ϕ.

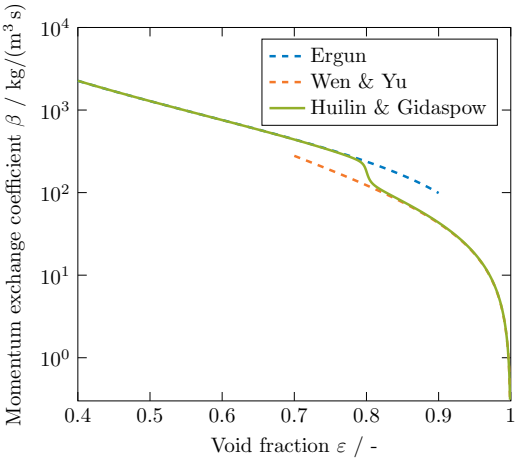

(b) Ergun, Wen & Yu and Huilin & Gidaspow drag model.

Figure 2.14: Smoothing function ϕ for different void fraction ε (a) and comparison of the resulting momentum exchange coefficient β (b) at different void fractions using the Ergun [168], Wen & Yu [170] and Huilin & Gidaspow [109] drag model.

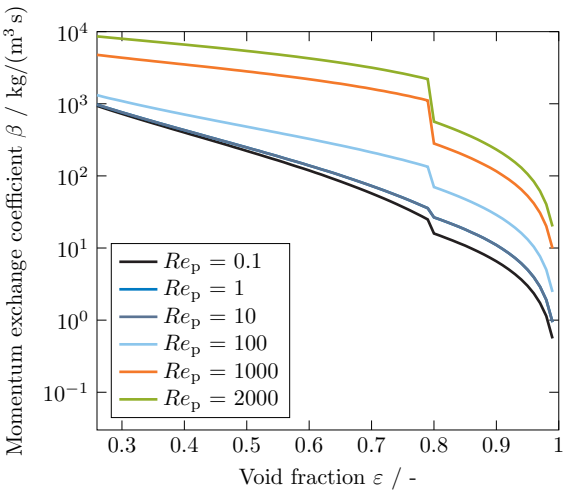

(a) Gidaspow drag model.

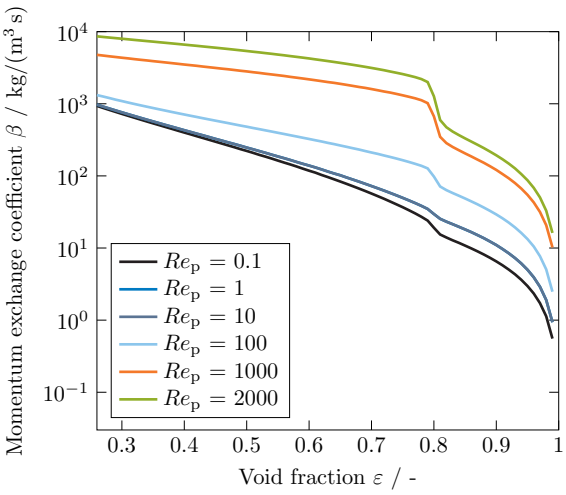

(b) Huilin & Gidaspow drag model.

Figure 2.15: Resulting momentum exchange coefficient β depending on the void fraction ε at different particle Reynolds numbers Re_p using the Gidaspow [15, 78] (a) and Huilin & Gidaspow [109] (b) drag model.

Syamlal & O'Brien drag model

A drag model depending on the terminal velocity of a group of particles used for fixed and fluidized beds was proposed by Syamlal and O'Brien [176]. The terminal velocity can

be either calculated with correlations or via experimental measurements. The proposed momentum exchange coefficient can be calculated as follows:

$$\beta_{\mathrm{S\&O}} = \frac{3}{4}\frac{\varepsilon\,(1-\varepsilon)\,\rho_{\mathrm{f}}}{d_{\mathrm{p}}}\frac{C_{\mathrm{d}}}{U_{\mathrm{r}}^2}|\mathbf{u}_{\mathrm{s}} - \mathbf{u}_{\mathrm{f}}|. \tag{2.112}$$

The function U_{r} stands for the ratio of the terminal velocity of a swarm of particles to the terminal velocity of a single particle. An explicit equation to calculate the function U_{r} can be derived from Garside and Al-Dibouni [177]:

$$U_{\mathrm{r}} = 0.5\left(a - 0.06Re_{\mathrm{p}} + \sqrt{\left(0.06Re_{\mathrm{p}}\right)^2 + 0.12Re_{\mathrm{p}}\,(2b-a) + a^2}\right). \tag{2.113}$$

Here, the function is only dependent on the Reynolds number Re_{p} and the parameters a and b. The latter parameters represent the laminar and turbulent part of the velocity ratio U_{r} and are dependent on the void fraction ε. Both of them are fitting functions and were derived with a power function similar to the approach of Richardson and Zaki [172]. The parameter a can be calculated as follows:

$$a = \varepsilon^{4.14}. \tag{2.114}$$

The accuracy of a pair equation to calculate the parameter b was greater than using a single equation:

$$b = \begin{cases} 0.8\varepsilon^{1.28} & \text{if } \varepsilon \leq 0.85 \\ \varepsilon^{2.65} & \text{if } \varepsilon > 0.85. \end{cases} \tag{2.115}$$

Although with the introduction of a two pair equation, a discontinuity is apparent, this shows almost no repercussions in terms of numerical stability, but only improvements for the accuracy. The drag coefficient C_{d} was adopted from Dalla Valle [178] and adjusted to fit the momentum exchange coefficient equation in (2.112):

$$C_{\mathrm{d}} = \left(0.63 + 4.8\sqrt{\frac{U_{\mathrm{r}}}{Re_{\mathrm{p}}}}\right)^2. \tag{2.116}$$

Figure 2.16 shows the behavior of the momentum exchange coefficient calculated with the drag model according to Syamlal & O'Brien at varying void fractions and particle Reynolds numbers.

Hill-Koch-Ladd drag model

A drag model purely based on a simulation approach was proposed by Hill, Koch and Ladd [179–181] (HKL). Using Direct Numerical Simulations they simulated gas-particle flows

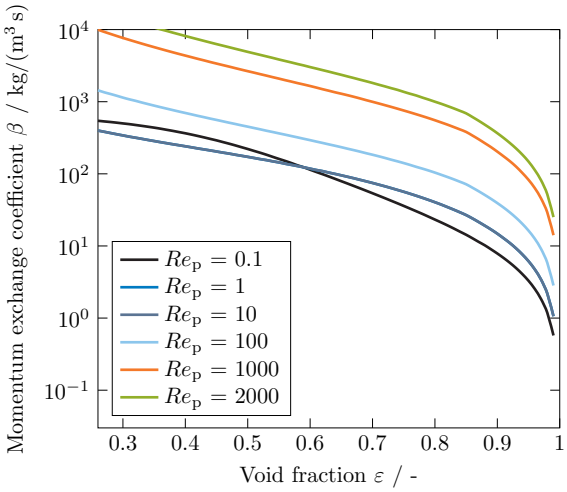

Figure 2.16: Resulting momentum exchange coefficient β depending on the void fraction ε at different particle Reynolds numbers Re_p using the Syamlal & O'Brien [176] drag model.

for both fixed beds of ordered and random spherical packings as well as fluidized beds by means of Lattice-Boltzmann methods. The simulations showed a good agreement towards experimental data and the drag model was validated covering the whole range of possible void fractions, except for very dilute flows (single sphere in a fluid), $\varepsilon_\mathrm{min} \leq \varepsilon < 1$ and for low to intermediate Reynolds numbers, $0 < Re < 120$. The momentum exchange coefficient for the HKL drag model can be expressed as [182]:

$$\beta_\mathrm{HKL} = \frac{18\eta_\mathrm{f}\alpha\,(1-\alpha)^2}{d_\mathrm{p}^2} F. \tag{2.117}$$

The dimensional drag force F is a switch function dependent on the Reynolds number[9]:

$$F = \begin{cases} F_0 + \frac{1}{4} F_1 {Re_\mathrm{p}}^2 & \text{for } Re_\mathrm{p} \leq 40 \\ F_0 + \frac{1}{2} F_3 Re_\mathrm{p} & \text{for } 40 < Re_\mathrm{p} < 120, \end{cases} \tag{2.118}$$

[9] Note, that we use here the boundaries for the switch function of $Re_\mathrm{p} = 40$, as opposed to $Re_\mathrm{p} = 20$ mentioned by Hill, Koch and Ladd [179–181]. Hill, Koch and Ladd used a modified particle Reynolds number with the particle radius instead of the particle diameter. Hence, the boundary of the Reynolds number used in this thesis (dependent on the particle diameter) is twice the Reynolds number used in the publication of Hill, Koch and Ladd. Furthermore, the prefactor in Equation (2.118) results according to this definition. For the later introduced extended HKL drag model, this applies as well.

and the needed parameters F_0, F_1 and F_3, which are all dependent on the solid volume fraction α:

$$F_0 = \begin{cases} \frac{1+3\sqrt{\frac{\alpha}{2}}+\frac{135}{64}\alpha\ln(\alpha)+17.14\alpha}{1+0.681\alpha-8.48\alpha^2+8.16\alpha^3} & \text{for } \alpha < 0.4 \\ 10\frac{\alpha}{(1-\alpha)^3} & \text{for } \alpha \geq 0.4 \end{cases} \tag{2.119}$$

$$F_1 = 0.11 + 0.00051\exp(11.6\alpha) \tag{2.120}$$

$$F_3 = 0.0673 + 0.212\alpha + 0.0232/(1-\alpha)^5 . \tag{2.121}$$

Figure 2.17 shows the resulting drag coefficient with varying Reynolds numbers and solid volume fractions, respectively. As can be seen, the HKL drag model shows two discontinuities:

- at a Reynolds number of $Re_p = 40$ (cf. Equation (2.118)) and
- at a solid volume fraction of $\alpha = 0.4$ (cf. Equation (2.119)).

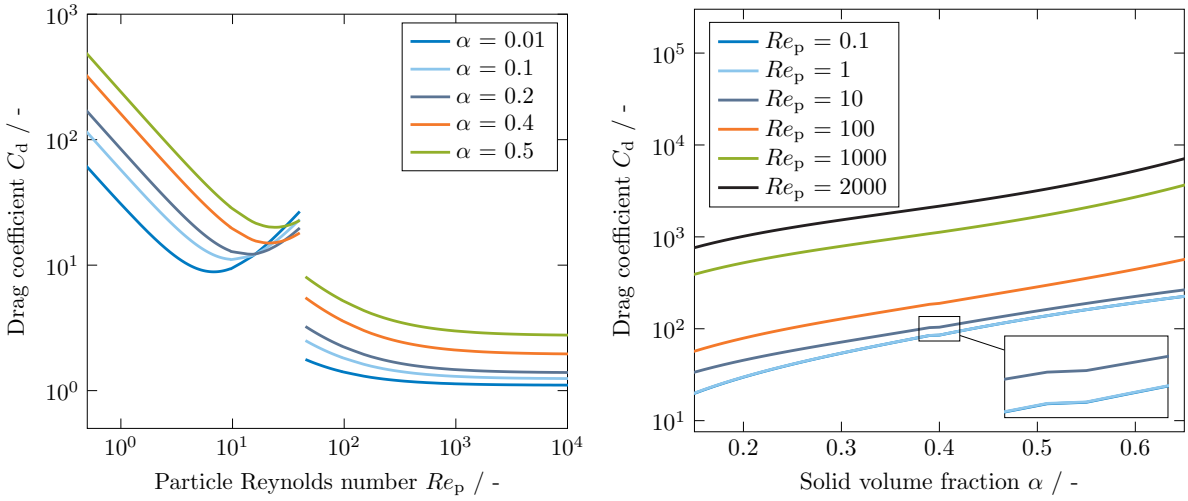

(a) C_d-dependency on Re_p **(b)** C_d-dependency on α

Figure 2.17: Resulting drag coefficient C_d depending on the particle Reynolds number Re_p (a) and solid phase volume fraction α (b).

The magnitude of both discontinuities can vary. The discontinuity for the factor F_0 based on the solid volume fraction in Equation (2.119) occurs if the fluidized bed has changing dense and dilute regions. This happens often considering for example bubbling fluidized beds. Hence, the probability for the occurrence of the discontinuity is higher for Geldart particles of type B and to some extent to type A and D as well. On the other hand, homogenous fluidizations do not show this discontinuity. The occurrence of the second discontinuity at a Reynolds number of $Re_p = 40$ due to F is dependent on the type of flow. Considering Equation (2.102) for the particle Reynolds number, fluidized bed systems with high relative velocities, e.g., spouting fluidized beds, and changing void fractions,

i.e., rapid change from dilute to dense phases and vice versa, promote the occurrence of this kind of discontinuity. Several problems arise when applying the HKL drag model. Firstly, the aforementioned discontinuities at the boundaries of $Re_\mathrm{p} = 40$ and $\alpha = 0.4$. At those regions the momentum exchange can increase or decrease in a rather significant amount, where the change at the Reynolds number boundary is of a higher impact. This phenomena can lead to numerical instabilities when applied to CFD simulations. And secondly, a problem arises for very dilute flows. The momentum exchange coefficient β in Equation (2.117) can be expressed based on the drag coefficient C_d as

$$\beta_\mathrm{HKL} = \frac{3}{4} C_\mathrm{d} \frac{\alpha\,(1-\alpha)}{d_\mathrm{p}} \rho_\mathrm{f} \left|\mathbf{u}_\mathrm{f} - \mathbf{u}_\mathrm{p}\right| \tag{2.122}$$

with

$$C_\mathrm{d} = 24 \frac{(1-\alpha)^2}{Re_\mathrm{p}} F. \tag{2.123}$$

So for very dilute flows at high Reynolds number, the following applies:

$$\lim_{\substack{\alpha\to 0 \\ Re_\mathrm{p}\to\infty}} C_\mathrm{d} \approx 1. \tag{2.124}$$

Considering a single sphere in a very dilute flow, the drag coefficient for the HKL drag model does not converge to a value of 0.44 in Newton's regime, e.g., high Reynolds numbers as opposed to Equation (2.103). Benyahia et al. [183] extended the HKL drag correlation to a wider range of void fractions with the introduction of a blending function to eliminate the occurring discontinuities and modified the equation to account for the correct drag force for very dilute flows. This drag model is often called the extended Hill-Koch-Ladd (extHKL) drag model in literature. The calculation of the momentum exchange coefficient and the drag coefficient, β and C_d, respectively, is depicted in Equations (2.122) and (2.123). The dimensionless drag force F is dependent on the degree of turbulence with the Reynolds number Re_p and the solid volume fraction α, according to

$$F = 1 + 3/16 Re_\mathrm{p} \qquad \text{for } \alpha \leq 0.01 \text{ and } Re_\mathrm{p} \leq \frac{F_2 - 1}{3/16 - \frac{1}{2}F3} \tag{2.125}$$

$$F = F_0 + \frac{1}{4} F_1 {Re_\mathrm{p}}^2 \qquad \text{for } \alpha > 0.01 \text{ and } Re_\mathrm{p} \leq \frac{F_3 + \sqrt{F_3^2 - 4F_1\,(F_0 - F_2)}}{F_1} \tag{2.126}$$

$$F = F_2 + \frac{1}{2} F_3 Re_\mathrm{p} \qquad \text{otherwise.} \tag{2.127}$$

The separate contributions for the inertial coefficients F_0, F_1, F_2 and F_3 are determined by

$$F_0 = \begin{cases} (1-w)\left[\frac{1+3\sqrt{\frac{\alpha}{2}}+\frac{135}{64}\alpha\ln(\alpha)+17.14\alpha}{1+0.681\alpha-8.48\alpha^2+8.16\alpha^3}\right] + w\left[10\frac{\alpha}{(1-\alpha)^3}\right] & \text{for } 0.01 < \alpha < 0.4 \\ 10\frac{\alpha}{(1-\alpha)^3} & \text{for } \alpha \geq 0.4 \end{cases} \tag{2.128}$$

$$F_1 = \begin{cases} \frac{\sqrt{\frac{2}{\alpha}}}{40} & \text{for } 0.01 < \alpha \leq 0.1 \\ 0.11 + 0.00051\exp(11.6\alpha) & \text{for } \alpha > 0.1 \end{cases} \tag{2.129}$$

$$F_2 = \begin{cases} (1-w)\left[\frac{1+3\sqrt{\frac{\alpha}{2}}+\frac{135}{64}\alpha\ln(\alpha)+17.89\alpha}{1+0.681\alpha-11.03\alpha_s^2+15.41\alpha_s^3}\right] + w\left[10\frac{\alpha}{(1-\alpha)^3}\right] & \text{for } 0.01 < \alpha < 0.4 \\ 10\frac{\alpha}{(1-\alpha)^3} & \text{for } \alpha \geq 0.4 \end{cases} \tag{2.130}$$

$$F_3 = \begin{cases} 0.9351\alpha + 0.03667 & \text{for } 0.01 < \alpha < 0.0953 \\ 0.0673 + 0.212\alpha + 0.0232/(1-\alpha)^5 & \text{for } \alpha \geq 0.0953 \end{cases} \tag{2.131}$$

with the blending function w

$$w = \exp\left(-10\left(0.4-\alpha\right)/\alpha\right). \tag{2.132}$$

Figure 2.18 compares the drag coefficients based on the HKL and the extHKL drag model for densely-packed, dilute and very dilute flows, $\alpha = 0.5$, 0.2 and 0.01, respectively. Three observations can be made:

1.) both, the HKL and the extHKL drag model, correctly depict the drag coefficient for a single sphere in the laminar regime ($Re_\mathrm{p} \downarrow$, $\alpha \to 0$) according to Stokes' Law in Equation (2.101),

2.) the discontinuity with the HKL drag model at a Reynolds number $Re_\mathrm{p} = 40$ vanishes for the extHKL drag model due to the introduction of the blending function w and

3.) the drag coefficient of the extHKL drag model is correctly predicted for very dilute flows at high Reynolds numbers according to the drag coefficient of a single sphere ($C_\mathrm{d} \to 0.44$) as opposed to the prediction using the HKL drag model ($C_\mathrm{d} \to 1$).

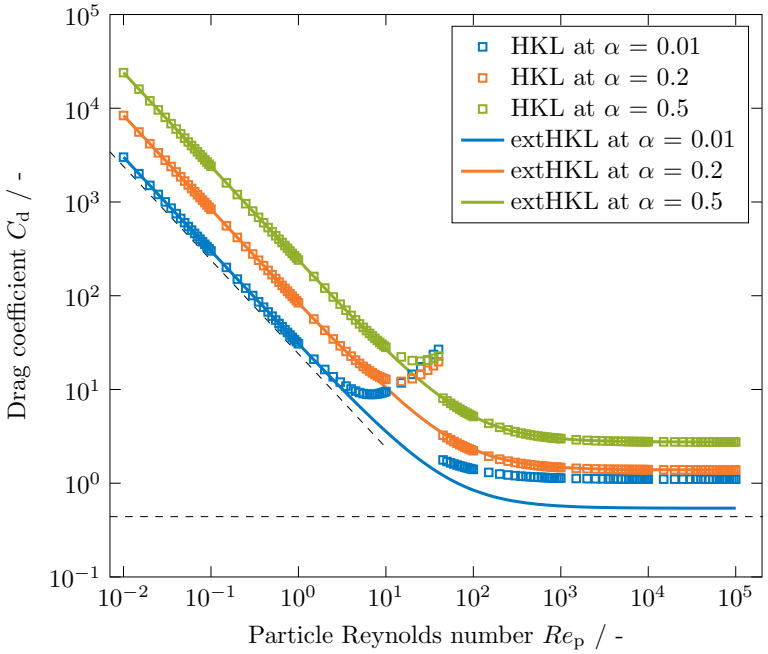

Figure 2.18: Resulting drag coefficient C_d at various particle Reynolds numbers Re_p using the HKL [179–181] and extHKL drag model [183]. Different flows are depicted: very diluted, diluted and dense gas-solid flows, $\alpha = 0.01$, 0.2 and 0.5. Stokes' Law and the drag coefficient in the turbulent regime (cf. Equations (2.101) and (2.103)) are also included.

Figure 2.19 depicts the resulting momentum exchange coefficient at different void fractions and Reynolds numbers for both the HKL and extHKL drag model. Here, only minimal distinctions are visible between both drag models. The greatest impact is due to the introduced blending function w and the adjustment to account for very dilute flows.

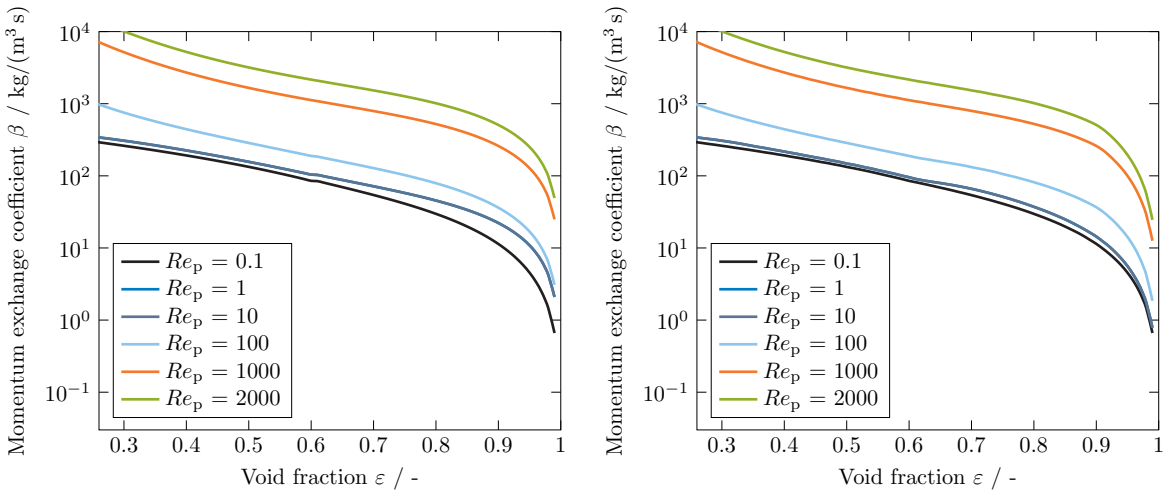

(a) HKL drag model.

(b) extHKL drag model.

Figure 2.19: Resulting momentum exchange coefficient β depending on the void fraction ε at different particle Reynolds numbers Re_p using the HKL [179–181] and extHKL [183] drag model.

Many more models to determine the drag coefficient can be found in literature. The above listed are the most common and used drag models. Other models were proposed, e.g., by Gibilaro et al. [184], Arastoopour et al. [185], Plessis [186], Felice [187], the energy-minimization multiscale (EMMS) approach [115, 188], Beetstra et al. [189], Andrews and O'Rourke [133] or Tang et al. [69, 190]. Each model has its operation range in terms of type of fluidization, Geldart classification, gas-solid or liquid-solid flow, type of reactor, e.g., spouting bed, conical reactor or fluidized bed reactor with a Wurster tube, type of flow, range of solid fraction, mono-, bi- or polydisperse systems, spherical or non-spherical particles and many more. Hence, it is important to validate the simulations with experimental findings to select an appropriate drag model, as the drag force is one of the most important forces regarding the momentum exchange between the fluid and the particles [175, 191].

3 Development of a hybrid Eulerian-Eulerian-Lagrangian model

Abstract

The simulation of gas-solid flows with CFD software is mostly performed with a Eulerian-Eulerian or a Eulerian-Lagrangian method. In this work, a solver was developed coupling the Eulerian-Eulerian and Eulerian-Lagrangian models. The gas phase was still treated in a Eulerian way as a continuum, while the particles were modeled with the Eulerian and the Lagrangian models. The number of particles treated as Lagrangian particles was defined by a modifiable parameter. The solver was validated with experimental data from the literature and compared in terms of accuracy and execution time to a pure Eulerian-Eulerian, a Eulerian-Lagrangian and an MP-PIC solver for different Lagrangian particle ratios. Accuracy and solver speed are highly dependent on the Lagrangian ratio. With this coupled Eulerian-Eulerian-Lagrangian solver, an additional degree of freedom is introduced with the Lagrangian particle ratio to modify the speed and the accuracy of the solver.

Bibliographic Information

D. Hirche, F. Birkholz, O. Hinrichsen, "A hybrid Eulerian-Eulerian-Lagrangian model for gas-solid simulations", *Chemical Engineering Journal* **2019**, *377*, 119743.

A hybrid Eulerian-Eulerian-Lagrangian model for gas-solid simulations

Author: Daniel Hirche,Fabian Birkholz,Olaf Hinrichsen

Publication: Chemical Engineering Journal

Publisher: Elsevier

Date: 1 December 2019

Journal Author Rights

3.1 Introduction

Gas-solid multiphase flows, for example in fluidized beds, have a vast field of applications. Fluidized bed reactors can be found in several industrial applications [192], e.g., in the chemical industry for fluid catalytic cracking and Fischer-Tropsch synthesis, in the metallurgical sector for the calcination of ores or in the environmental sector, for example municipal waste water treatment. It is important to understand the hydrodynamics of the gas and the particle flow when designing a reactor or optimizing the process itself. With the help of Computational Fluid Dynamics (CFD), the spatial resolution of the flows can be achieved. Due to the increasing computational power in recent years, CFD has become more popular and feasible for multiphase studies [193]. The multiphase simulation algorithms for gas-solid modeling in CFD are based on different methods and models. Figure 3.1 gives a brief overview of some gas-solid multiphase methods and the models they rely on. The Lattice Boltzmann Method (LBM) and Direct Numerical Simulations (DNS) are not of industrial interest and not considered in Figure 3.1, as the computational time is too extensive for simulating a fluidized bed. The Eulerian-Eulerian approach [53, 71, 194] defines two fluid phases, each as a continuum. In order to model a granular phase as a continuum, the Kinetic Theory of Granular Flow (KTGF) was proposed by Ding and Gidaspow [78]. They assumed ideal spherical particles and accounted for the normal impact of particle-particle and particle-wall collisions [195]. The Eulerian-Lagrangian approach models the gas-phase as a continuum according to the Eulerian theory, while the granular phase is resolved and calculated by a Lagrangian Particle Tracking (LPT). The Discrete Phase Model (DPM) tracks each particle individually according to Newton's Second Law of Motion, but does not consider particle-particle collisions. The Multiphase Particle-In-Cell (MP-PIC) [133, 196, 197] method solves the fluid phase with a continuum model (Eulerian approach) and the motion of the particles is calculated with the Lagrangian approach, while forces and stresses concerning particle interactions, e.g., drag force or interparticle stresses are calculated with the continuum approach and then mapped back to the particle's position. The most accurate and computationally demanding of the three models presented for the Lagrangian treatment of particles is the discrete element method (DEM) [119]. With this method, each particle is resolved individually and the particles undergo a 4-way coupling. The coupling between the Eulerian method and DEM was proposed by Tsuji et al. [14]. The Coarse Grained Particle Method (CGPM) [132] is a sub-model of the DEM approach, where the particles are presented as bigger clusters of particles to increase the simulation speed. In the following work, when speaking of Lagrangian models, we are referring to DEM.

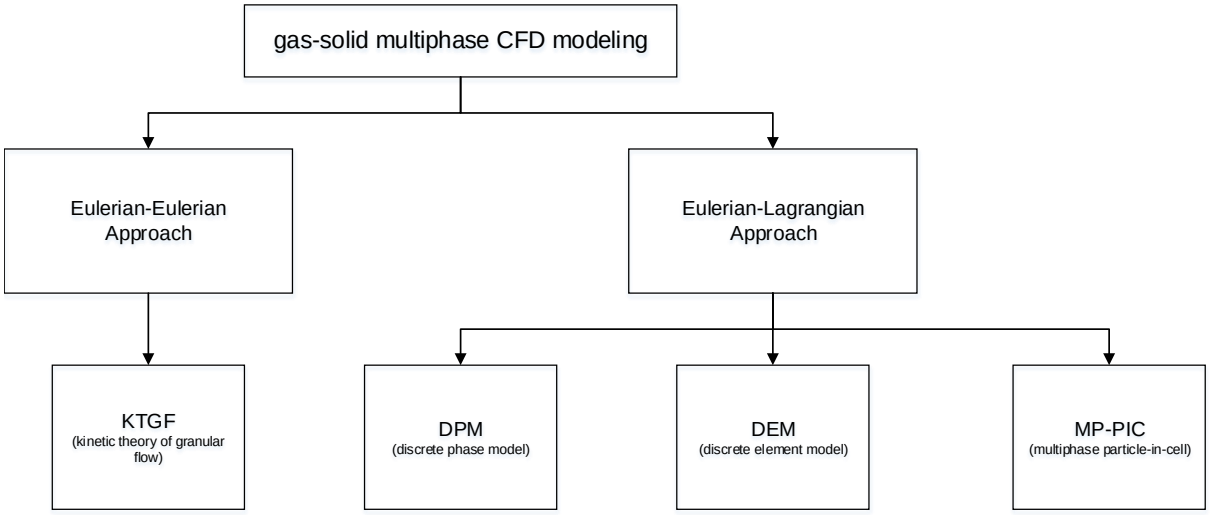

Figure 3.1: Overview of gas-solid multiphase CFD models with a Eulerian-Eulerian and a Eulerian-Lagrangian approach.

According to Tsuji et al. [14], the advantage of the Eulerian-Eulerian model is the simulation speed and the disadvantage is the lower accuracy as the modeling of the granular phase is based on several assumptions and simplifications. According to Liu et al. [198] and Loha et al. [199], the Eulerian-Eulerian model seems to be a good compromise between simulation speed and accuracy of the results. The Eulerian-Eulerian model is mostly used for pilot scale plants [61]. However, Zhao et al. [200] showed that the simulation results with the Eulerian-Eulerian model and the KTGF cannot correctly display fluidization phenomena for certain fluidized bed set-ups. The Eulerian-Lagrangian model has its advantages in a better accuracy than the Eulerian-Eulerian model due to the fact that particles are not approximated as a continuum, so the particle-particle and particle-wall collisions can be better resolved [14]. But the downside of the Lagrangian model is the relatively slow simulation speed. With an increasing number of particles, the number of equations to be solved increases proportionally. In this work, we developed a solver, coupling both the Eulerian-Eulerian and Eulerian-Lagrangian models to a Eulerian-Eulerian-Lagrangian model. The aim of this new solver was to highlight the advantages of both models: speed of the Eulerian model and accuracy of the Lagrangian model and to bridge the gap between lab scale and small pilot scale geometries. The solver was then validated with experimental data taken from Müller et al. [201, 202] and Link et al. [203]. Furthermore, the newly developed solver is compared to a Eulerian-Eulerian, a Eulerian-Lagrangian and an MP-PIC solver in terms of accuracy of the results and execution time.

3.2 Methodology

Eulerian-Eulerian and Eulerian-Lagrangian simulations differ in how the granular phase is treated. Figure 3.2 shows a schematic illustration of the treatment of the gas and solid phase for both approaches.

The geometry to be solved consists of a predefined number of three-dimensional cells according to the finite volume method (FVM). Although the mesh cells are three dimensional, the simulated flow of both gas and particle phase is of a two-dimensional nature, when a Eulerian-Eulerian approach is applied. The particle interactions for the Eulerian-Eulerian approach are calculated with statistical models, while in the Eulerian-Lagrangian approach all particle interactions are resolved and not approximated. Hence, the Eulerian-Eulerian model relies on a coarser mesh for an accurate representation of the particle interactions. The accuracy for the particle interactions for the Eulerian-Lagrangian model is not dependent on the grid size, except for the averaging of certain parameters needed for particle-fluid interaction, e.g., solid phase porosity for calculating the drag force. However, the resolution of the mesh is limited by the minimum size of a single mesh cell. In regards to a single-flow, a fluid-flow in particular, the resolution and therefore the minimum cell size are practically not limited. For simulations of multiphase-flows consisting of at least one granular phase the minimum cell volume is limited by the volume of the largest particle according to Goniva et al. [204]. It is recommended that the minimum cell size is many times larger than the volume of the biggest particle, see section 3.2.2 for further explanation. The accuracy of the Eulerian-Eulerian approach is dependent on the coarseness of the mesh due to the statistical models used. Therefore the Eulerian-Eulerian approach is usually used for medium to large scale geometries.

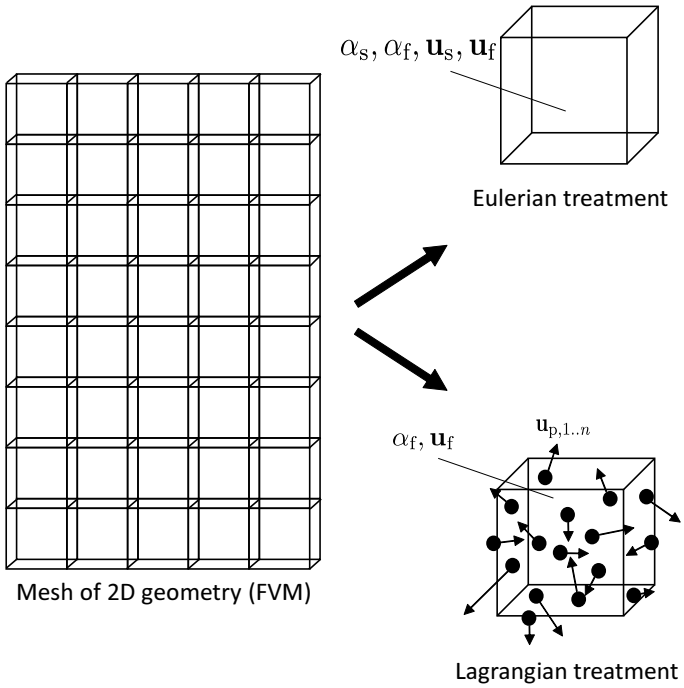

Figure 3.2: Eulerian-Eulerian and Eulerian-Lagrangian treatment for a 2D geometry with an FVM method.

Particulate flow is resolved in three dimensions, independent of the number of mesh cells, with a Lagrangian treatment of the granular phase. This condition is valid as long as the simulation is solved according to the finite volume method. The characteristic properties of the particles, e.g., particle velocity $\mathbf{u}_p$, are calculated separately according to the method of Lagrangian Particle Tracking (LPT). As opposed to the Eulerian treatment of particles, the Lagrangian treatment does not average the characteristic particle properties over the corresponding cell the particles are located in.

In regards to computational effort, the number of equations to be solved for a Eulerian-Eulerian model is smaller than for a Eulerian-Lagrangian model, with the exception of the number of mesh cells being higher than the number of total particles.

3.2.1 Eulerian-Eulerian Model

The most widely applied model for gas-solid CFD simulations is the Eulerian-Eulerian model. With this approach, both phases, gas and solid, are modeled as separate continuums which are immiscible in each other, as opposed to the Volume-of-Fluid method (VOF). In regards to the VOF method, the fluids are also immiscible, but a phase interface occurs between the two fluids, so the phase fractions are either zero or 1. But with the Eulerian-Eulerian model, there is no phase interface and, therefore, the phases

can interpenetrate each other. The governing equations for the Eulerian-Eulerian model are the continuity equation for mass conservation (cf. Equation (3.1)), and the momentum balance for a two-phase flow (cf. Equation (3.2)) for the fluid. In the following, the system is considered isothermal, hence the energy equation can be neglected and the density of the fluid phase is constant for the later simulations.

$$\frac{\partial \alpha_i}{\partial t} + \boldsymbol{\nabla} \cdot (\alpha_i \mathbf{u}_i) = 0 \tag{3.1}$$

$$\frac{\partial \left(\alpha_\mathrm{f} \rho_\mathrm{f} \mathbf{u}_\mathrm{f}\right)}{\partial t} + \boldsymbol{\nabla} \cdot (\alpha_\mathrm{f} \rho_\mathrm{f} \mathbf{u}_\mathrm{f} \mathbf{u}_\mathrm{f}) = -\alpha_\mathrm{f} \boldsymbol{\nabla} p + \alpha_\mathrm{f} \rho_\mathrm{f} \mathbf{g} + \boldsymbol{\nabla} \cdot \left(\alpha_\mathrm{f} \overline{\overline{\tau}}_\mathrm{f}\right) + \mathbf{M}_\mathrm{f,s} \tag{3.2}$$

The index i describes the two phases present for the Eulerian-Eulerian simulations. In the case of a gas-solid simulation, those phases are a continuous gas phase g and a disperse solid phase s.

The governing equations for the solid phase also include the continuity equation for mass conservation according to Equation (3.1) for the solid phase, i.e., $i = s$. The momentum equation for a solid phase, which originates from Ishii and Hibiki [194] and was reformulated by Enwald et al. [53] to apply to gas-solid flows, is

$$\frac{\partial \left(\alpha_\mathrm{s} \rho_\mathrm{s} \mathbf{u}_\mathrm{s}\right)}{\partial t} + \boldsymbol{\nabla} \cdot (\alpha_\mathrm{s} \rho_\mathrm{s} \mathbf{u}_\mathrm{s} \mathbf{u}_\mathrm{s}) = -\alpha_\mathrm{s} \boldsymbol{\nabla} p + \alpha_\mathrm{s} \rho_\mathrm{s} \mathbf{g} - \boldsymbol{\nabla} p_\mathrm{s} + \boldsymbol{\nabla} \cdot \left(\alpha_\mathrm{s} \overline{\overline{\tau}}_\mathrm{s}\right) + \mathbf{M}_\mathrm{s,f}. \tag{3.3}$$

The volume fraction α_i describes the volumetric phase fraction of each phase, while the conditions

$$0 \leq \alpha_i \leq 1 \tag{3.4}$$

and

$$\sum_i \alpha_i = 1. \tag{3.5}$$

apply to all phase fractions in each cell of the simulation.

$\mathbf{M}_{i,j}$ defines the momentum exchange term between the phases i and j. The forces that have an impact on the momentum exchange term $\mathbf{M}_{i,j}$ are, for example, drag force and resulting force due to turbulent dispersion. The drag force has in most cases the highest contribution to the momentum exchange between the fluid and particulate phases. The

momentum exchange can be calculated with the momentum exchange coefficient β for the gas-solid and solid-gas interactions, $\mathbf{M}_{\mathrm{f,s}}$ and $\mathbf{M}_{\mathrm{s,f}}$, respectively, as

$$\mathbf{M}_{\mathrm{f,s}} = \beta \left(\mathbf{u}_{\mathrm{f}} - \mathbf{u}_{\mathrm{s}} \right) \tag{3.6}$$

and

$$\mathbf{M}_{\mathrm{s,f}} = \beta \left(\mathbf{u}_{\mathrm{s}} - \mathbf{u}_{\mathrm{f}} \right). \tag{3.7}$$

Due to the definition of a closure relation, the momentum exchange terms for the gas-solid and solid-gas interactions are equal when comparing their absolute values.

Many different correlations for the calculation of the momentum exchange coefficient are proposed in the literature. This work uses the drag correlation proposed by Gidaspow [15], which is a combination of the correlations proposed by Ergun [168] and Wen and Yu [170]. The drag correlation proposed by Ergun [168] is used for gas volume fractions lower than 0.8, while the correlation from Wen and Yu [170] is used for gas volume fractions greater than 0.8. The momentum exchange coefficient β can be calculated according to the following equation:

$$\beta = \begin{cases} 150 \frac{\alpha_{\mathrm{s}}^2 \eta_{\mathrm{f}}}{\alpha_{\mathrm{f}} d_{\mathrm{p}}^2} + 1.75 \alpha_{\mathrm{s}} \frac{\rho_{\mathrm{f}}}{d_{\mathrm{p}}} |\mathbf{u}_{\mathrm{f}} - \mathbf{u}_{\mathrm{s}}|, & \alpha_{\mathrm{f}} < 0.8 \\ \frac{3}{4} C_{\mathrm{d}} \frac{\alpha_{\mathrm{f}} \alpha_{\mathrm{s}}}{d_{\mathrm{p}}} \rho_{\mathrm{f}} |\mathbf{u}_{\mathrm{f}} - \mathbf{u}_{\mathrm{s}}| \alpha_{\mathrm{f}}^{-2.65}, & \alpha_{\mathrm{f}} \geq 0.8 \end{cases} \tag{3.8}$$

The drag coefficient C_{d} is dependent on the particle Reynolds number Re_{p}

$$C_{\mathrm{d}} = \begin{cases} \frac{24}{Re_{\mathrm{p}}} \left(1.0 + 0.15 Re_{\mathrm{p}}^{0.687} \right), & Re_{\mathrm{p}} \leq 1000 \\ 0.44, & Re_{\mathrm{p}} > 1000 \end{cases} \tag{3.9}$$

with the cell-averaged particle Reynolds number for the solid phase Re_{p}, the particle phase velocity $\mathbf{u}_{\mathrm{s}}$ and the particle diameter d_{p}

$$Re_{\mathrm{p}} = \frac{\alpha_{\mathrm{f}} d_{\mathrm{p}} |\mathbf{u}_{\mathrm{f}} - \mathbf{u}_{\mathrm{s}}| \rho_{\mathrm{f}}}{\eta_{\mathrm{f}}}. \tag{3.10}$$

The viscous stress tensor is calculated as defined by Enwald et al. [53]

$$\overline{\overline{\tau}}_i = 2 \eta_i \overline{\overline{D}}_i + \left(\zeta_i - \frac{2}{3} \eta_i \right) \mathrm{Tr} \left(\overline{\overline{D}}_i \right) \overline{\overline{I}} \tag{3.11}$$

and the strain rate tensor $\overline{\overline{D}}_i$ as

$$\overline{\overline{D}}_i = \frac{1}{2} \left[\boldsymbol{\nabla} \mathbf{u}_i + \left(\boldsymbol{\nabla} \mathbf{u}_i \right)^T \right]. \tag{3.12}$$

The solid shear viscosity η_s, the solid bulk viscosity ζ_s, the solid phase pressure p_s and the solid stress tensor $\overline{\overline{\tau}}_\mathrm{s}$ are calculated according to the Kinetic Theory of Granular Flow [78]. According to this theory, the solid phase is modeled as a fluid according to the Kinetic Theory of Dense Gases by Chapman and Cowling [89], but modified to account for the particulate character of the phase.

The solid shear viscosity η_s is calculated according to Gidaspow [15]

$$\eta_\mathrm{s} = \rho_\mathrm{s} d_\mathrm{p} \sqrt{\theta_\mathrm{s}} \cdot \left(\frac{4}{5} \alpha_\mathrm{s} g_0 (1+e) \frac{1}{\sqrt{\pi}} + \frac{1}{15} \sqrt{\pi} g_0 (1+e) \alpha_\mathrm{s}^2 + \frac{1}{6} \sqrt{\pi} \alpha_\mathrm{s} + \frac{10}{96} \sqrt{\pi} \frac{1}{(1+e) g_0} \right). \tag{3.13}$$

Lun et al. [80] defines the bulk viscosity of the solid phase ζ_s as

$$\zeta_\mathrm{s} = \frac{4}{3} \alpha_\mathrm{s}^2 \rho_\mathrm{s} d_\mathrm{p} g_0 \left(1+e\right) \sqrt{\frac{\theta_\mathrm{s}}{\pi}}. \tag{3.14}$$

The solid phase pressure p_s accounts for a kinetic part and forces due to particle-particle collisions and was proposed by Lun et al. [80]:

$$p_\mathrm{s} = \alpha_\mathrm{s} \rho_\mathrm{s} \theta_\mathrm{s} + 2 g_0 \rho_\mathrm{s} \alpha_\mathrm{s}^2 \left(1-e\right) \theta_\mathrm{s} \tag{3.15}$$

with the coefficient of restitution for particle-particle collisions e, the equilibrium radial distribution function g_0 and the granular temperature θ_s. For dense granular flows frictional stress must be included for the solid shear viscosity η_s in Equation (3.13) and the solid phase pressure p_s in Equation (3.15). If the solid volume fraction α_s exceeds a predefined solid volume fraction at which frictional stress is accounted for $\alpha_\mathrm{s,fr}$, i.e., $\alpha_\mathrm{s} > \alpha_\mathrm{s,fr}$, the frictional stress part is added to both equations to get the new solid phase pressure $p_\mathrm{s,fr}$ and solid shear viscosity $\eta_\mathrm{s,fr}$:

$$p_\mathrm{s,fr} = p_\mathrm{s} + p_\mathrm{fr} \tag{3.16}$$

and

$$\eta_\mathrm{s,fr} = \eta_\mathrm{s} + \eta_\mathrm{fr}. \tag{3.17}$$

The frictional stress parts for the solid phase pressure $p_\mathrm{s,fr}$ and the solid shear viscosity $\eta_\mathrm{s,fr}$ are calculated according to following semi-empirical equations proposed by Johnson and Jackson [85]:

$$p_\mathrm{fr} = Fr \frac{\left(\alpha_\mathrm{s} - \alpha_\mathrm{s,fr}\right)^n}{\left(\alpha_\mathrm{s,max} - \alpha_\mathrm{s}\right)^P} \tag{3.18}$$

and

$$\eta_{\mathrm{fr}} = p_{\mathrm{fr}} \sin\phi. \tag{3.19}$$

The parameters Fr, n and P are empirical constants, as well as the angle of internal friction ϕ and are chosen according to Ocone et al. [86].

The radial distribution function g_0 was proposed by Ogawa et al. [90] for dense rigid spherical particles as

$$g_0 = \left[1 - \left(\frac{\alpha_{\mathrm{s}}}{\alpha_{\mathrm{s,max}}}\right)^{1/3}\right]^{-1} \tag{3.20}$$

and the granular temperature θ_{s}, which is a measure of the particle velocity fluctuation and the kinetic energy of the random motions of the particles,

$$\theta_{\mathrm{s}} = \frac{1}{3}\langle \mathbf{u}_{\mathrm{s}}^2 \rangle, \tag{3.21}$$

leading to the transport equation of the granular temperature θ_{s}

$$\frac{3}{2}\left[\frac{\partial}{\partial t}\left(\alpha_{\mathrm{s}}\rho_{\mathrm{s}}\theta_{\mathrm{s}}\right) + \boldsymbol{\nabla}\cdot\left(\alpha_{\mathrm{s}}\rho_{\mathrm{s}}\mathbf{u}_{\mathrm{s}}\theta_{\mathrm{s}}\right)\right] = \left(-p_{\mathrm{s}}\overline{\overline{I}} + \overline{\overline{\tau}}_{\mathrm{s}}\right) : \boldsymbol{\nabla}\mathbf{u}_{\mathrm{s}} + \boldsymbol{\nabla}\cdot\left(\kappa_{\mathrm{s}}\boldsymbol{\nabla}\theta_{\mathrm{s}}\right) - \gamma_{\mathrm{s}} - J_{\mathrm{s}}. \tag{3.22}$$

In the above equation, the term $\boldsymbol{\nabla}\cdot\left(\kappa_{\mathrm{s}}\boldsymbol{\nabla}\theta_{\mathrm{s}}\right)$ represents the diffusion of the fluctuating energy with κ_{s} being the granular thermal conductivity:

$$\begin{aligned}\kappa_{\mathrm{s}} = \rho_{\mathrm{s}} d_{\mathrm{p}} \sqrt{\theta_{\mathrm{s}}} \cdot \Bigg(& 2\alpha_{\mathrm{s}}^2 g_0 \left(1+e\right)\frac{1}{\sqrt{\pi}} \\ & + \frac{9}{8}\sqrt{\pi} g_0 0.5 \left(1+e\right)\alpha_{\mathrm{s}}^2 \\ & + \frac{15}{16}\sqrt{\pi}\alpha_{\mathrm{s}} + \frac{25}{64}\sqrt{\pi}\frac{1}{\left(1+e\right)g_0}\Bigg)\end{aligned} \tag{3.23}$$

γ_{s} accounts for the collisional dissipation of energy of the particles [80]

$$\gamma_{\mathrm{s}} = 12\sqrt{\frac{\theta_{\mathrm{s}}^3}{\pi}}\left(1-e^2\right)\frac{\alpha_{\mathrm{s}}^2\rho_{\mathrm{s}}g_0}{d_{\mathrm{p}}}. \tag{3.24}$$

The dissipation of energy occurring from the inelastic behavior of particle-particle collisions is accounted for with J_s [96]

$$J_{\mathrm{s}} = 3\beta\theta_{\mathrm{s}} - \frac{3}{4}\frac{\beta^2 d_{\mathrm{p}}\left(\mathbf{u}_{\mathrm{s}}-\mathbf{u}_{\mathrm{f}}\right)^2}{\alpha_{\mathrm{s}}\rho_{\mathrm{s}}\sqrt{\pi\theta_{\mathrm{s}}}}. \tag{3.25}$$

3.2.2 Eulerian-Lagrangian Model

The governing equation for a Eulerian-Lagrangian simulation differs from the equation for a Eulerian-Eulerian equation as the particles are simulated individually and not in a Eulerian approach. The equations for the fluid phase follow equation (3.2) and a single-phase flow for the fluid is assumed. The resulting solid volume fraction for Eulerian-Lagrangian simulations $\alpha_{s,L}$ due to the existence of particles is calculated with the total volume of Lagrangian particles in a specified cell $\sum_{\forall \mathrm{p} \in \mathrm{cell}} V_\mathrm{p}$ and the volume of the cell itself V_cell according to Equation (3.26).

$$\alpha_\mathrm{s,L} = \frac{1}{V_\mathrm{cell}} \sum_{\forall \mathrm{p} \in \mathrm{cell}} V_\mathrm{p} \tag{3.26}$$

The momentum exchange between the gas and particle phases $\mathbf{M}_\mathrm{f,p}$ has to be modified to account for all Lagrangian particles:

$$\mathbf{M}_\mathrm{f,p} = \beta \left(\mathbf{u}_\mathrm{f} - \overline{\mathbf{u}}_\mathrm{p} \right) \tag{3.27}$$

The momentum exchange term $\mathbf{M}_\mathrm{f,p}$ is further split up into an explicit and an implicit term due to numerical stability:

$$\mathbf{M}_\mathrm{f,p} = \frac{\sum \mathbf{F}_\mathrm{f,p}}{V_\mathrm{cell} |\mathbf{u}_\mathrm{f} - \overline{\mathbf{u}}_\mathrm{p}|} \cdot \mathbf{u}_\mathrm{f} - \frac{\sum \mathbf{F}_\mathrm{f,p}}{V_\mathrm{cell} |\mathbf{u}_\mathrm{f} - \overline{\mathbf{u}}_\mathrm{p}|} \cdot \overline{\mathbf{u}}_\mathrm{p} \tag{3.28}$$

$\overline{\mathbf{u}}_\mathrm{p}$ is the cell-averaged velocity of the particles and is calculated according to

$$\overline{\mathbf{u}}_\mathrm{p} = \frac{1}{N_\mathrm{p}} \sum_{\forall \mathrm{p} \in \mathrm{cell}} \mathbf{u}_\mathrm{p}. \tag{3.29}$$

The total number of particles in the cell is described by N_p and the velocity of the respective particle p by $\mathbf{u}_\mathrm{p}$. The calculations for the Lagrangian framework are based on Newton's Second Law of Motion, specifically the force and torque balances:

$$m_\mathrm{p} \frac{\mathrm{d}\mathbf{u}_\mathrm{p}}{\mathrm{d}t} = \sum \mathbf{F}_\mathrm{p} \tag{3.30}$$

and

$$I_\mathrm{p} \frac{\mathrm{d}\omega_\mathrm{p}}{\mathrm{d}t} = \mathbf{T}_\mathrm{p} \tag{3.31}$$

$\mathbf{F}_\mathrm{p}$ defines the forces acting on the particle. The most significant forces acting on a particle in a gas-solid fluidized bed are contact forces $\mathbf{F}_\mathrm{c}$, drag force $\mathbf{F}_\mathrm{d}$, buoyancy force $\mathbf{F}_\mathrm{b}$ and gravitational force $\mathbf{F}_\mathrm{g}$. Other particle forces, e.g., force due to virtual mass, magnetic or electrostatic forces are neglected in this work due to their low magnitude in comparison

to the other forces. The contact force $\mathbf{F}_c$ includes all forces due to particle-particle and particle-wall collisions. Those forces are calculated according to a soft-sphere model [119] with a spring-slider-dashpot model [123, 205]. A schematic overview of the acting forces modeled with the spring-slider-dashpot can be seen in Figure 3.3.

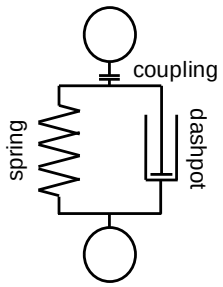

Figure 3.3: Spring-slider-dashpot for particle-particle and particle-wall interactions.

The drag force $\mathbf{F}_\mathrm{d}$ acting on a single particle in a fluidized bed can be calculated with

$$\mathbf{F}_\mathrm{d} = \frac{V_\mathrm{p}\beta}{\alpha_\mathrm{s,L}} \left(\mathbf{u}_\mathrm{f} - \mathbf{u}_\mathrm{p}\right) \tag{3.32}$$

The momentum exchange coefficient for the calculation of the drag force β is according to the Gidaspow correlation [15] (cf. Equation (3.8)). Equations (3.2), (3.8) and (3.32) for the Eulerian-Lagrangian model are dependent on the volume fractions α_i, in particular on the solid phase fraction for the Eulerian-Lagrangian simulation $\alpha_\mathrm{s,L}$. The Lagrangian solid phase fraction $\alpha_\mathrm{s,L}$ is calculated with Equation (3.26). Here, the volume of all particles in a cell is summed up and divided by the cell volume. Different methods can be used to determine which particles correspond to a specific cell, e.g., the particle center method or divided volume phase fractions. In the following simulations, the particle center method is applied. Depending on the position of the particle center, the particle is assigned to the corresponding cell. The advantage of this method lies in the relatively small computational effort, while there are two disadvantages which are illustrated in Figure 3.4.

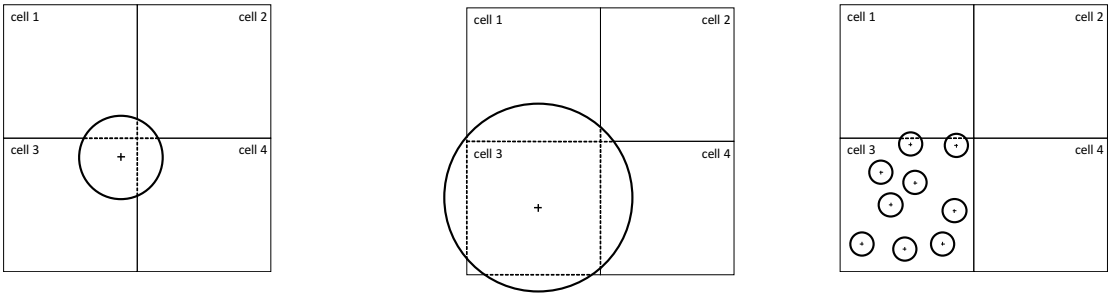

(a) **(b)** **(c)**

Figure 3.4: Determination of phase volume fractions of a Eulerian-Lagrangian simulation with the particle center method. Example with particles (●) and particle centers (+) for three different cases:
(a) Particle volume overlapping cells 1, 2, 3 and 4.
(b) Particle volume almost covering cell 3 and overlapping cells 1, 2 and 4.
(c) Cell size is many times larger than particle size.

If the center of a particle lies near a cell boundary, the volume of the particle overlaps several cells, cf. Figure 3.4a where the volume of the particle overlaps all four cells. In this case, the gas volume fraction for cells 1, 2 and 4 are zero because the particle center is located in cell 3. The calculated gas volume fraction covering cell 3 according to the particle center method is, in this case, higher than the real gas volume fraction as the whole volume of the particle is used instead of the particle volume in cell 3. The gas volume fractions in cells 1, 2 and 4 are lower than the real gas volume fractions. Another disadvantage can be seen in Figure 3.4b where a particle is larger than a cell. The volume of the particle covers almost the entire volume of cell 3. The calculated gas volume fraction is close to zero, while the other gas volume fractions are one. The simulated gas velocity in cell 3 would be very high, but the overall gas flow accuracy would decrease. This is because when the gas volume fractions of the neighboring cells are equal to zero, the gas velocity decreases again. Hence, it is important to define a minimum cell size of at least the greatest particle volume to minimize or even prevent these problems. A better case is shown in Figure 3.4c. The volume of the cells is far larger than the volume of the greatest particle. The calculation of the gas volume fraction according to the particle center method is closer to the actual gas volume fractions. The deviation stems from particles near the border with the neighboring cells. Since the particle volumes are smaller than the particle volumes of the other cases, the error of the overlapping volumes is minimized.

It can be seen that with the above equations, the computational effort rises in proportion to the number of particles in the system for a Eulerian-Lagrangian simulation if the number of mesh cells compared to the number of particles is negligible. The computational effort for a Eulerian-Eulerian simulation is proportional to the number of the mesh size and is not as demanding as for a Eulerian-Lagrangian simulation.

3.3 Coupling of Eulerian-Eulerian and Lagrangian Models

Simulating a gas-solid two-phase flow with either a Eulerian-Eulerian or a Eulerian-Lagrangian model has advantages and disadvantages in regards to simulation speed and accuracy. With the following coupling of those two models, the gas phase was still treated as a continuum and modeled according to the Eulerian approach. The granular phase, however, was modeled by the Eulerian and the Lagrangian approaches simultaneously. The open-source C++ based package OpenFOAM®[206], version 4.1, was used as software for coupling the methods and for performing the simulations.

The term $\mathbf{M}_{\mathrm{f,s}}$ in the momentum equation for the gas phase in Equation (3.2) accounts for the momentum exchange between the gas phase and the Eulerian particle phase. In order to include the additional momentum exchange between the gas phase, the Eulerian solid phase and the Lagrangian particles $\mathbf{M}_{\mathrm{f,s+L}}$, $\mathbf{M}_{\mathrm{f,s}}$ have to be modified to

$$\mathbf{M}_{\mathrm{f,s+L}} = \mathbf{M}_{\mathrm{f,s}} + \beta \left(\mathbf{u}_{\mathrm{f}} - \frac{\sum_{\forall \mathrm{p}} \mathbf{u}_{\mathrm{p}}}{N_{\mathrm{p}}} \right) \tag{3.33}$$

The momentum equation for the Eulerian solid phase and the momentum exchange term $\mathbf{M}_{\mathrm{s,f}}$ must also be modified. With the addition of the momentum due to particle-particle collisions, the new momentum exchange term for the Eulerian solid phase with the gas phase and the Lagrangian particles can be expressed with the following equation:

$$\mathbf{M}_{\mathrm{s,f+L}} = \mathbf{M}_{\mathrm{s,f}} + \frac{\sum_{\forall \mathrm{collisions}} m_{\mathrm{p}} \left(\mathbf{u}_{\mathrm{p},t+\Delta t} - \mathbf{u}_{\mathrm{p},t} \right)}{V_{\mathrm{cell}}} \tag{3.34}$$

The term $\frac{\sum_{\forall \mathrm{collisions}} m_{\mathrm{p}} \left(\mathbf{u}_{\mathrm{p},t+\Delta t} - \mathbf{u}_{\mathrm{p},t} \right)}{V_{\mathrm{cell}}}$ accounts for the volume-specific momentum of the Lagrangian particles which collide with particles of the Eulerian phase. The particles of the Eulerian solid phase are, however, not resolved in their positions. Therefore, with the combination of the Eulerian and Lagrangian treatment of the granular phase, the Eulerian solid phase will be transformed into pseudo Lagrangian particles (pseudo L-Particles). The transformed Eulerian solid phase or rather the pseudo L-particles are marked as inactive but inherit the velocities of the Eulerian solid phase (cf. Figure 3.5). The inactive nature of the pseudo L-Particles excludes those particles from the calculation in the LPT. Therefore, the collision detection mechanism by the LPT only detects collisions between Lagrangian particles and Lagrangian particles, Lagrangian particles and pseudo L-Particles, as well as Lagrangian particles and the wall. Collisions between pseudo L-particles and pseudo L-Particles, as well as pseudo L-Particles and the wall will not be considered by the collision detection mechanism.

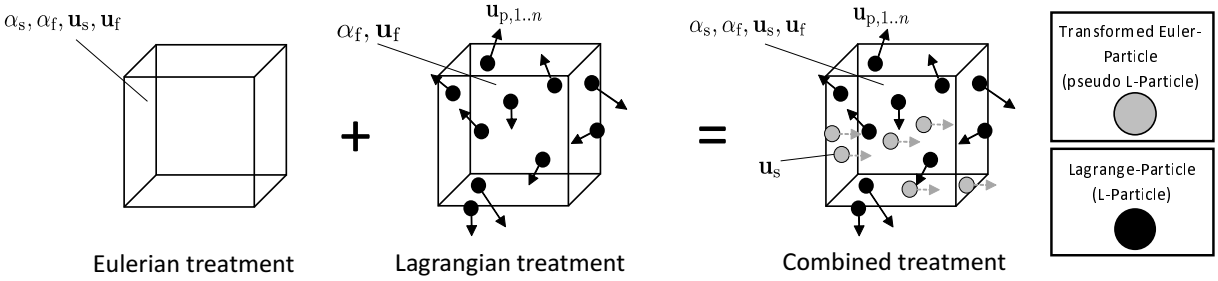

Figure 3.5: Coupling overview of Eulerian and Lagrangian treatment and introduction of transformed Eulerian particles as pseudo Lagrangian particles.

As the pseudo L-Particles are not considered by the LPT and do not change their spacial position, the position of the pseudo L-Particles has to be assigned by an algorithm. This particular algorithm is shown in Figure 3.6. In a first step, the number of cells and the spatial dimensions of each cell will be read from the simulation. This step assures the information of the whole simulation geometry and each individual cell. In the next step with the information of the geometry and cell dimensions as well as the particle diameters of the Eulerian solid phase, $d_{\mathrm{p,E}}$, all positions of possible transformed Eulerian particles (E-Particles), i.e., pseudo L-Particles in Figure 3.6, are calculated. Therefore, a hexagonal closed-packed bed of equal and ideal spheres is assumed. The solid fraction of the particle bed for this assumption is approximately 0.74 as the maximum value of the bed porosity for a hexagonal closed-packed bed $\varepsilon_{\max} \approx 0.26$. An illustration of four layers of this hexagonal closed-packed bed with the information of the geometry and cell dimensions as well as the Eulerian particle diameter can be seen in Figure 3.7. With this step, all possible positions of pseudo L-Particles will be stored in a file. This method is chosen to anticipate any problems of overlapping pseudo L-Particles if a random positioning algorithm were chosen. Those two steps are performed only once during the simulation, unless a dynamic mesh is used.

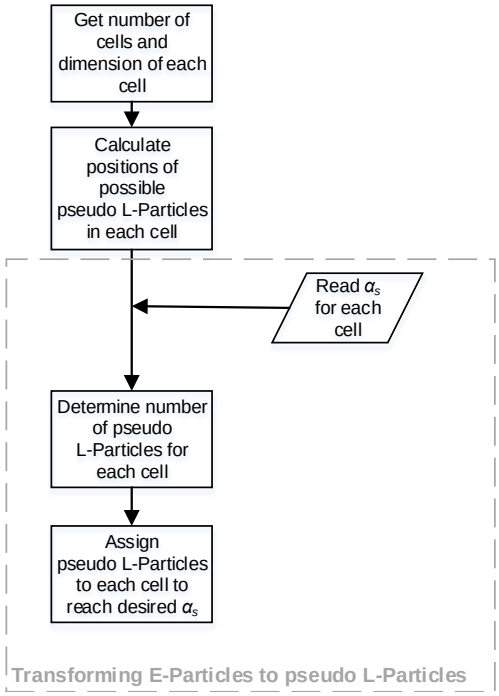

Figure 3.6: Schematic overview of algorithm for the transformation of Eulerian particles to pseudo Lagrangian particles (pseudo L-Particles).

In the third step during the simulation, the particle volume fraction of the Eulerian solid phase α_s is obtained for each cell and the number of Eulerian particles, i.e., pseudo L-particles, for each cell is calculated with

$$N_\mathrm{E} = \frac{V_\mathrm{cell}}{1/6 \pi d_\mathrm{p,E}^3} \cdot \alpha_\mathrm{s} \tag{3.35}$$

At the last step, the number of pseudo L-Particles is assigned to each cell to reach the required number of Eulerian particles N_E and, therefore, the solid phase fraction α_s.

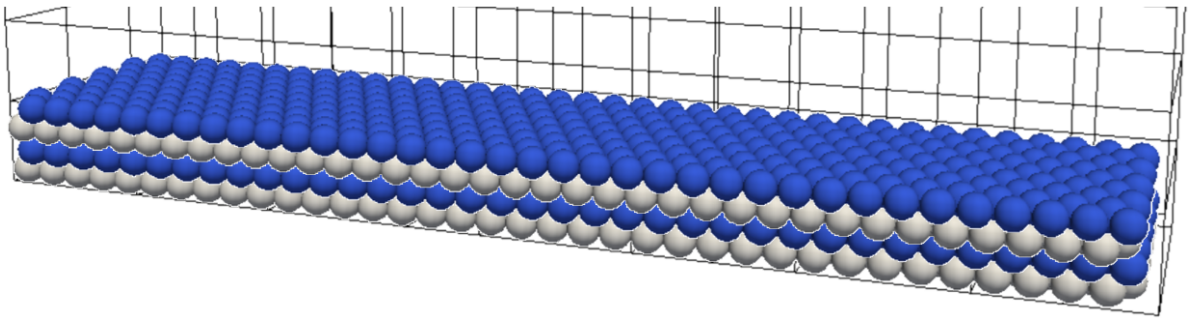

Figure 3.7: Positions of four layers for available pseudo L-Particles placed in a hexagonal closed-pack of ideal spheres.

Before the start of the simulation, the initial bed height is fixed. With the combination of the Eulerian and Lagrangian treatment of the particles, a ratio has to be defined, declaring

how many of the particles are simulated according to the Eulerian and the Lagrangian models. The following ratio R_{L} states the ratio of particles treated as Lagrangian particles, $N_{\mathrm{p,L}}$, to all particles simulated N_{p}:

$$R_{\mathrm{L}} = \frac{N_{\mathrm{p,L}}}{N_{\mathrm{p}}} \tag{3.36}$$

If this ratio is equal to 1, then the simulation consists of a pure Eulerian-Lagrangian simulation as all the granular matter is treated as Lagrangian particles. On the contrary, with a ratio of $R_{\mathrm{L}} = 0$, all simulated particles are treated as a continuum according to the Eulerian approach. A predefined ratio of $R_{\mathrm{L}} = 0.5$ equals a simulation with half of the simulated particles treated as a Eulerian continuum and the other half as Lagrangian particles. With this additional degree of freedom, the hybridity of the solver can be further adjusted to increase or decrease the number of Lagrangian particles in the simulation.

Figure 3.8 shows the complete algorithm for the coupled Eulerian-Eulerian-Lagrangian solver. Before entering the Eulerian loop, the initial parameters, e.g., particle bed height, bed porosity and Lagrangian particle ratio R_{L} are read. In the next step, the Eulerian particles (E-particles) are transformed to pseudo L-Particles according to the algorithm in Figure 3.6. With the R_{L} ratio, a defined number of Lagrangian particles (L-Particles) is introduced into each cell to reach the desired bed porosity. With the positioning of the pseudo L-Particles the simulation enters the DEM loop, i.e., the Lagrangian calculations of the particle tracking algorithm. In this loop, the fluid forces acting on the L-Particles are calculated and the Lagrangian equations for the L-Particles are solved to get the new properties, e.g., position, velocity and torque, for those particles. Furthermore, the momentum exchange between the L-Particles and pseudo L-Particles is summed up and stored for the later Eulerian loop. The pseudo L-Particles are excluded from those calculations as their positions and velocities are set by the Eulerian phase properties. If the DEM cycle time step has reached the time step of the Eulerian loop, the L-Particles are reinitialized, the DEM loop is left and the Eulerian loop is reentered. With the new positions of the L-Particles the particle volume fractions of each cell have to be recalculated. Then, the forces of the L-Particles on the E-Particles and the gas phase can be determined to solve the Eulerian equations for both the gas and solid phase in the next step. Before the next time step, the volume fractions of the E- and L-Particles as well as the velocities are combined to obtain the volume fractions and velocities of those combined phases and, therefore, the total particle phase. The velocities of the Eulerian and Lagrangian phase are weighted according to the introduced Lagrangian particle ratio R_{L}. After an increase in the time step, the E-Particles are transformed to the pseudo L-Particles again and the Eulerian- and DEM loops start all over until the end time t_{end} is reached.

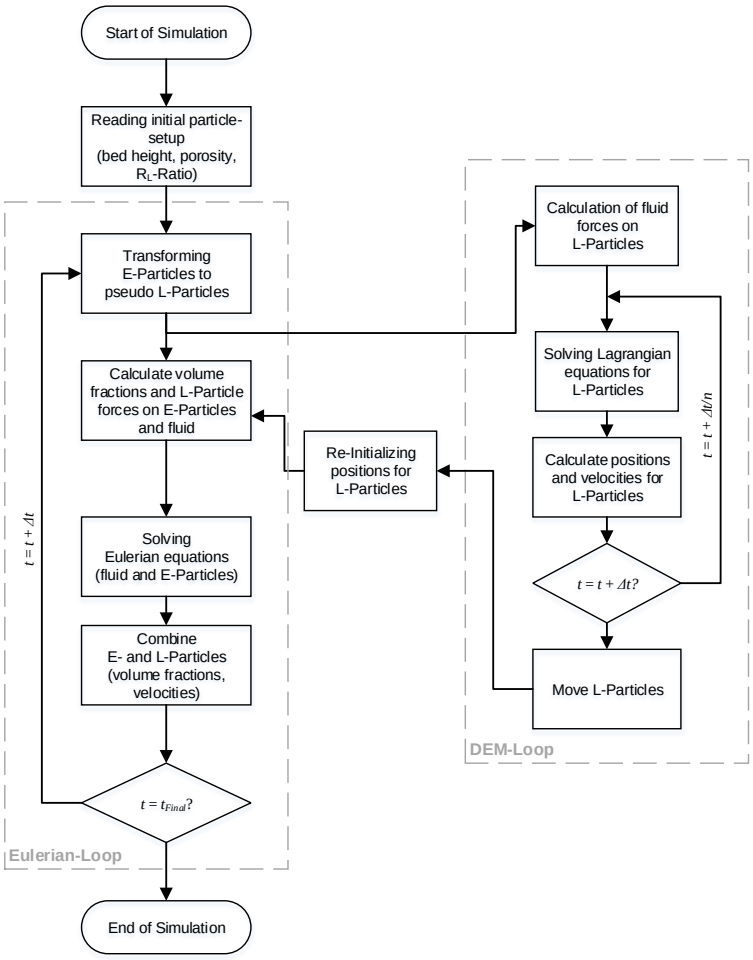

Figure 3.8: Solver algorithm for newly developed Eulerian-Eulerian-Lagrangian approach with indicated Eulerian-Eulerian and DEM loop.

3.4 Validation of proposed Eulerian-Eulerian-Lagrangian Solver

A simulation or a proposed model has to be validated with experimental data. Therefore, two benchmark cases were used to validate the proposed coupled Eulerian-Eulerian-Lagrangian solver: a 2D fluidized bed set-up by Müller et al. [201, 202] and a 3D spouted fluidized bed with aeration according to Link et al. [203].

3.4.1 2D fluidized bed

The benchmark case according to Müller et al. [201, 202] consisted of a pseudo-2D fluidized bed. Air was introduced at ambient conditions and the particles studied were poppy seeds.

The inlet velocity of the gas phase was uniform. The characteristic data for comparison, i.e., particle velocities and gas volume fractions were obtained via MR measurements by Müller et al. [201, 202]. A snapshot of the initial fluidization including the formation of a gas bubble is seen in Figure 3.9.

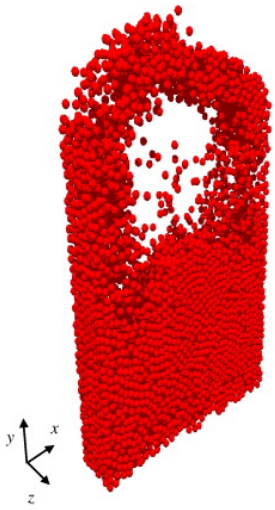

Figure 3.9: Snapshot of fluidization and bubble formation by Müller et al. [201].

3.4.1.1 Set-up

In order to validate and evaluate the newly developed Eulerian-Eulerian-Lagrangian solver in terms of accuracy and speed, the benchmark case according to Müller [201, 202] was simulated with a pure Eulerian-Eulerian, a Eulerian-Lagrangian and the proposed Eulerian-Eulerian-Lagrangian solver. The pure Eulerian-Eulerian solver was called *twoPhaseEulerFoam* and the Eulerian-Lagrangian solver *DPMFoam*. The acronym *DPM* in the *DPMFoam* solver stands for *Discrete Particle Modelling* and is in contrast to the Discrete Phase Model mentioned in Figure 3.1 a 4-way coupled CFD-DEM solver. The granular matter in the Eulerian-Eulerian solver is modeled according to KTGF, while in the Eulerian-Lagrangian solver we used a four-way coupled approach for LPT. The underlying models and parameters for the Eulerian-Eulerian, Eulerian-Lagrangian and MP-PIC solvers are listed in Table 3.1. The gas phase in all solvers was modeled in the same way and the physical properties were also equal.

Table 3.1: Overview of parameters used in the 2D fluidized bed simulation.

Geometry and Mesh	
width / mm	44
height / mm	120
depth / mm	10
cell number in x-direction / -	15
cell number in y-direction / -	37
cell number in z-direction / -	1

Physical Properties			
Gas phase		Solid phase	
		particle diameter d_p / mm	1.2
density ρ_f / kg/m^3	1.2	density $\rho_\mathrm{s,p}$ / kg/m^3	1000
kin. viscosity ν_f / m^2/s	$1.5 \cdot 10^{-5}$	sphericity ψ / -	1
inlet velocity $\mathbf{u}_\mathrm{f,in}$ / m/s	0.9	coefficient of restitution e / -	0.97
		coefficient of friction μ_fr / -	0.1
EE Simulation		EL and MP-PIC Simulation	
axial bed height h / mm	30	number of particles N_p / -	9240
initial bed porosity ε_0 / -	0.64		
drag model		Gidaspow [15]	
simulation time t_end / s		50	
time step Δt / s		$1 \cdot 10^{-4}$	

In the developed Eulerian-Eulerian-Lagrangian solver, the ratio of Lagrangian particles to all simulated particles R_L had to be defined before the simulation. For the following validation according to the benchmark fluidized bed, three different R_L-ratios were investigated, namely $R_\mathrm{L} = 20$, 50 and 80 %.

3.4.1.2 Results

The measured and time-averaged gas volume fractions $\overline{\alpha}_\mathrm{f}$ and axial velocities of the solid phase $\overline{\mathbf{u}}_\mathrm{s,y}$ were extracted from Müller et al. [201, 202] and compared to the simulation results of the Eulerian-Lagrangian, Eulerian-Eulerian, MP-PIC and Eulerian-Eulerian-Lagrangian solvers with Lagrangian particle ratios of $R_\mathrm{L} = 20$, 50 and 80 %. The time-averaging frame for the simulations was 50 s. The experimental and simulated data were obtained across the horizontal bed and at four specific axial bed heights. The comparisons of the gas volume fractions $\overline{\alpha}_\mathrm{f}$ and the axial velocity of the solid $\overline{\mathbf{u}}_\mathrm{s,y}$ are shown in Figures 3.10 and3.11.

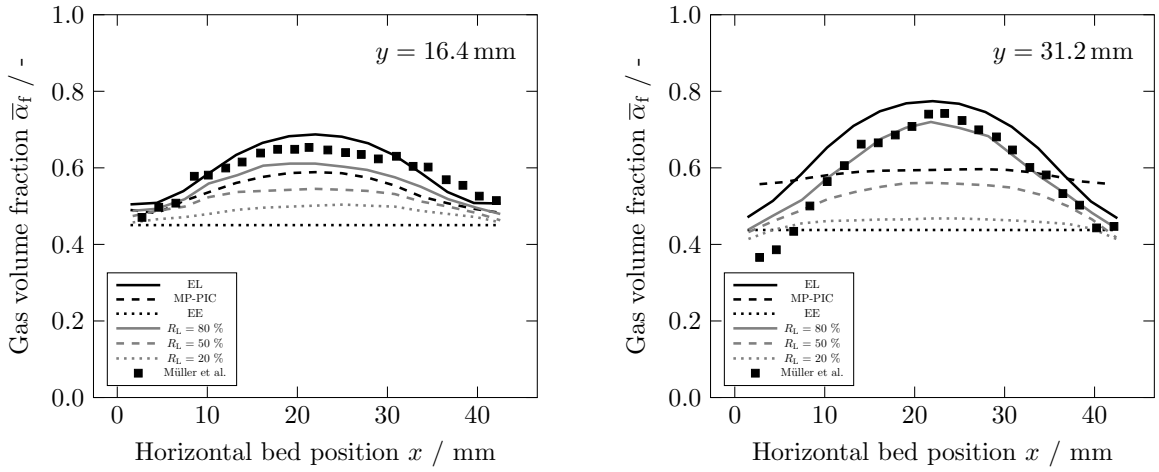

Figure 3.10: Comparison of gas volume fraction $\overline{\alpha}_f$ across horizontal bed position x at two different axial heights of $y = 16.4$ and $31.2\,\text{mm}$ with different solvers. Experimental data is taken from Müller et al. [202]. Eulerian-Lagrangian, Eulerian-Eulerian models and MP-PIC, as well as the newly developed Eulerian-Eulerian-Lagrangian model with three different Lagrangian particle ratios $R_L = 20$, 50 and 80 % are used for the solvers.

The least agreement with the experimental data was obtained with the Eulerian-Eulerian solver. Across the horizontal bed position and at two different axial heights, the gas volume fraction $\overline{\alpha}_f$ stays uniform at a value of approximately 0.44 (cf. Figure 3.10). Uniform and homogeneous fluidization with no bubble formation occurrs with this model. On the contrary, the results from Müller et al. [202] clearly show a non-uniform fluidization with a higher gas volume fraction in the mid-horizontal position compared to a lower gas fraction near the walls. Also, the snapshot from Müller et al. [202] of the initial fluidization in Figure 3.9 displays the existence and formation of gas bubbles. The formation of gas bubbles agrees with the increasing gas fraction at a larger distance from the bottom at the mid-horizontal position and the decreasing fraction near the wall, where the particles accumulate (cf. Figure 3.10b). The Eulerian-Lagrangian method shows the best agreement with the experimental data compared to the other simulation methods and slightly overpredicts the gas fraction at $y = 31.2\,\text{mm}$. The MP-PIC model underpredicts the gas fraction at a lower axial height compared to the experimental data. At a greater height, it shows a uniform gas volume fraction across the horizontal bed, like the results from the Eulerial-Eulerian solver, but at a higher gas fraction. The accuracy of the simulation results for the Eulerian-Eulerian-Lagrangian solver is highly dependent on the Lagrangian particle ratio R_L, as can be seen in Figure 3.10 for the gas fractions. The higher the R_L-ratio, the more Lagrangian particles are simulated and the more accurate the results are compared to the experimental data. It cannot be seen that the R_L-ratio is a weighting factor for the results between the Eulerian-Eulerian and Eulerian-Lagrangian simulation. An R_L-ratio of 20 % shows slightly non-uniform fluidization at the mid-horizontal position.

It is safe to conclude that the resulting accuracy of the introduced Lagrangian particles has an impact on the Eulerian particles as well due to the momentum exchange between them.

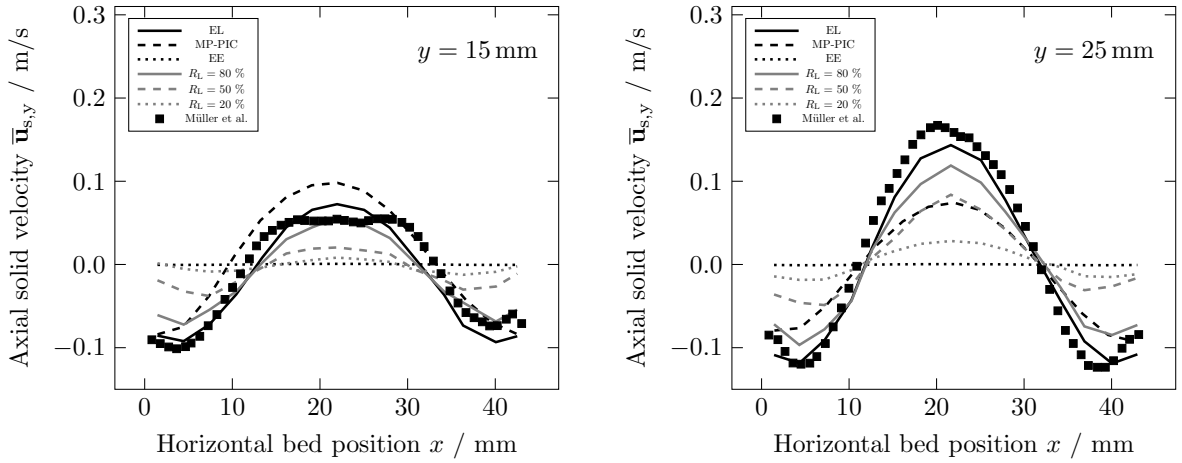

Figure 3.11: Comparison of axial solid velocity $\overline{\mathbf{u}}_{\mathrm{s,y}}$ across horizontal bed position x at two different distances from the bottom at $y = 15$ and 25 mm with different solvers. Experimental data were taken from Müller et al. [201]. Eulerian-Lagrangian, Eulerian-Eulerian and MP-PIC models, as well as the newly developed Eulerian-Eulerian-Lagrangian model with three different Lagrangian particle ratios $R_{\mathrm{L}} = 20$, 50 and 80 % are used for the solvers.

The experimental data for the time-averaged axial velocity of the solid phase $\overline{\mathbf{u}}_{\mathrm{s,y}}$ has a positive value at the middle of the horizontal bed position and the particles fall down near the walls (cf. Figure 3.11). The magnitude of the uprising velocity increases with the distance from the bottom, while the increase in magnitude of velocity near the walls is not as high as at the middle of the horizontal position. The axial velocity profile forms two local minima near the wall and one maximum at the middle of the horizontal position. At the lower axial height of $y = 15$ mm, the maximum velocity remains almost constant between the horizontal bed positions of $x = 15$ and 30 mm. As expected, the simulation results from the Eulerian-Eulerian model show no axial velocity of the solid phase over the horizontal and the two axial positions. This correlates to a homogeneous fluidized bed and to the uniform fluidization (cf. Figures 3.10a and 3.10b). These results from the Eulerian-Lagrangian simulation are in good agreement with the experimental data, while the flat plateau of the maximum velocity at an axial position of $y = 15$ mm is not well reproduced. Furthermore, the solver slightly underpredicts the axial velocity at $y = 25$ mm, but still shows the best agreement towards the experimental data compared to the other used solvers. The results obtained with the MP-PIC solver indicated that the axial particle velocity at the lower height was overpredicted. At a greater axial height the velocity was underpredicted. The accuracy of the Eulerian-Eulerian-Lagrangian solver increases with the Lagrangian particle ratio R_{L}. If more Lagrangian particles than Eulerian particles are simulated, the agreement between the simulation results and the experimental

data increases. An overall better accuracy than the MP-PIC results could be achieved with a R_{L}-ratio of 80 %.

Lastly, the newly developed Eulerian-Eulerian-Lagrangian solver was compared the other solvers in terms of its execution time for the simulations. Therefore, the execution times of all used models t_i, i.e, Eulerian-Lagrangian t_{EL}, MP-PIC $t_{\mathrm{MP\text{-}PIC}}$, Eulerian-Eulerian t_{EE} and Eulerian-Eulerian-Lagrangian with the three different R_{L} ratios of 20, 50 and 80 % $t_{\mathrm{EEL,\,0.2}}$, $t_{\mathrm{EEL,\,0.5}}$ and $t_{\mathrm{EEL,\,0.8}}$, were set in relation to the longest execution time, namely from the Eulerian-Lagrangian solver. The comparison of these execution time ratios is illustrated in Figure 3.12.

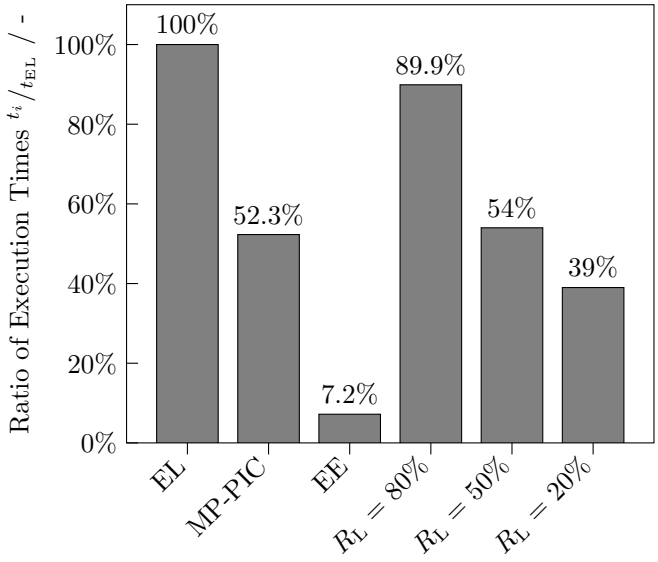

Figure 3.12: Comparison of execution times for the benchmark according to Müller et al. [201, 202] with the different solvers used. Eulerian-Lagrangian (EL), MP-PIC, Eulerian-Eulerian (EE) and the newly developed Eulerian-Eulerian-Lagrangian model with three different Lagrangian particle ratios $R_{\mathrm{L}} = 20$, 50 and 80 % are used for the solvers.

The longest execution time is obtained by the Eulerian-Lagrangian simulation, as it requires the highest computational effort due to the number of individually simulated particles. The shortest time is achieved with the Eulerian-Eulerian simulation because the particles are not resolved individually, but modeled as a continuum. The simulation speed for the MP-PIC solver is faster than the Eulerian-Lagrangian and slower than the Eulerian-Eulerian solver. The execution time for the Eulerian-Eulerian-Lagrangian solver increases with increasing Lagrangian particle ratios R_{L} and follows the equation

$$t_{\mathrm{EEL}}\left(R_{\mathrm{L}}\right) \approx R_{\mathrm{L}} \cdot t_{\mathrm{EL}} + t_{\mathrm{EE}}. \tag{3.37}$$

A short execution time for the Eulerian-Eulerian-Lagrangian solver is used for positioning and re-initializing the pseudo L-particle, i.e., transformed Eulerian particles. This overhead time can be seen at the execution times for an R_{L}-ratio of 20 and 80 %. For an R_{L}-ratio of 80 %, the overhead time makes up an accumulated amount of 2.7 % and for $R_{\mathrm{L}} = 20\,\%$ of 1.8 %. The execution time for an R_{L}-ratio of 50 % is comparable to the one of the MP-PIC solver, but smaller than the calculated execution time proposed in Equation (3.37).

3.4.2 3D spouted fluidized bed with aeration

The following fluidized bed benchmark case of Link et al. [203] represented a 3D spouted fluidized bed. Monodisperse glass beads were fluidized with air at ambient condition. The inlet velocity consisted of two different velocities: a background velocity and a spouted velocity, which has a greater magnitude than the background velocity. Link et al. [203] measured in this set-up the particle velocities with the method of position emission particle tracking. The time-averaged particle velocities at different heights are taken for the validation and comparison of our newly developed solver.

3.4.2.1 Set-up

The dimensions of the simulated geometry are shown in Figure 3.13. The number of simulated glass bead particles amounts to 44 800 for the Lagrangian simulations, i.e., Euler-Lagrange and MP-PIC. The equivalent bed height for the Eulerian solver is calculated with the assumptions of spherical particles and a maximum packing limit of $\alpha_{\mathrm{max}} = 0.64$.

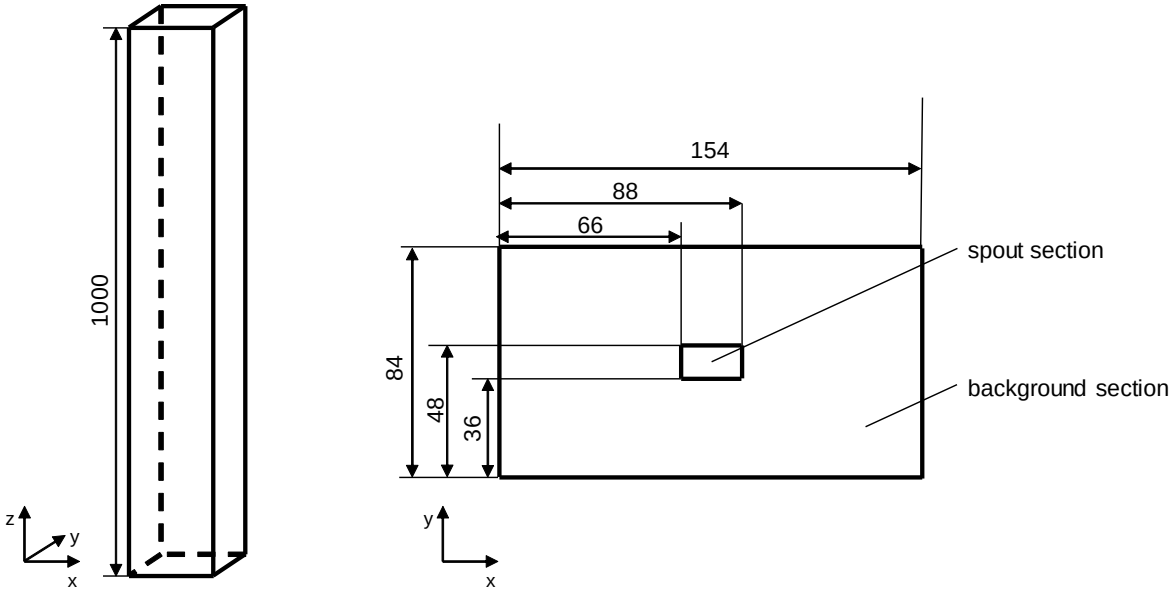

Figure 3.13: Dimensions of simulated geometry according to the experimental data for a 3D spouted fluidized bed taken from Link et al. [203].

Information about the grid size and the simulation parameters used are listed in Table 3.2. Link et al. [203] in their simulations use a grid size comparable to the *fine mesh* in Table 3.2. The accuracy of the Eulerian-Eulerian solver is dependent on statistical models to describe particle interactions. Therefore, a coarser mesh is preferable. In the following we performed the simulations with a mesh similar to Link et al. [203] and a coarser mesh, i.e., a grid size of 14 x 7 x 70 cells. The axial particle velocities $\mathbf{u}_{\mathrm{s,y}}$ are averaged for an interval of 30 s to obtain time-averaged values applying the same solvers as stated in section 3.4.1.

Table 3.2: Overview of parameters used in the 3D spouted fluidized bed with aeration simulations.

Mesh			
		coarse mesh	fine mesh
cell number in x-direction / -		14	28
cell number in y-direction / -		7	14
cell number in z-direction / -		70	100
Physical Properties			
Gas phase		Solid phase	
density ρ_f / kg/m^3	1.2	particle diameter d_p / mm	4.04
kin. viscosity ν_f / m^2/s	$1.5 \cdot 10^{-5}$	density $\rho_\mathrm{s,p}$ / kg/m^3	2526
spouted inlet velocity $\mathbf{u}_\mathrm{f,spout}$ / m/s	90	coefficient of restitution e / -	0.97
background inlet velocity $\mathbf{u}_\mathrm{f,bg}$ / m/s	2.5	coefficient of friction μ_fr / -	0.1
EE Simulation		EL and MP-PIC Simulation	
axial bed height h / m	0.33	number of particles N_p / -	44 800
initial bed porosity ε_0 / -	0.64		
	drag model	Gidaspow [15]	
	simulation time t_end / s	30	
	time step Δt / s	$5 \cdot 10^{-5}$	

3.4.2.2 Results

The time-averaged axial particle velocities $\overline{\mathbf{u}}_\mathrm{s,y}$ at axial heights of 0.15 and 0.25 m obtained with the Eulerian-Lagrangian, MP-PIC and the Eulerian-Eulerian solver using a finer and a coarser mesh are shown in Figure 3.14.

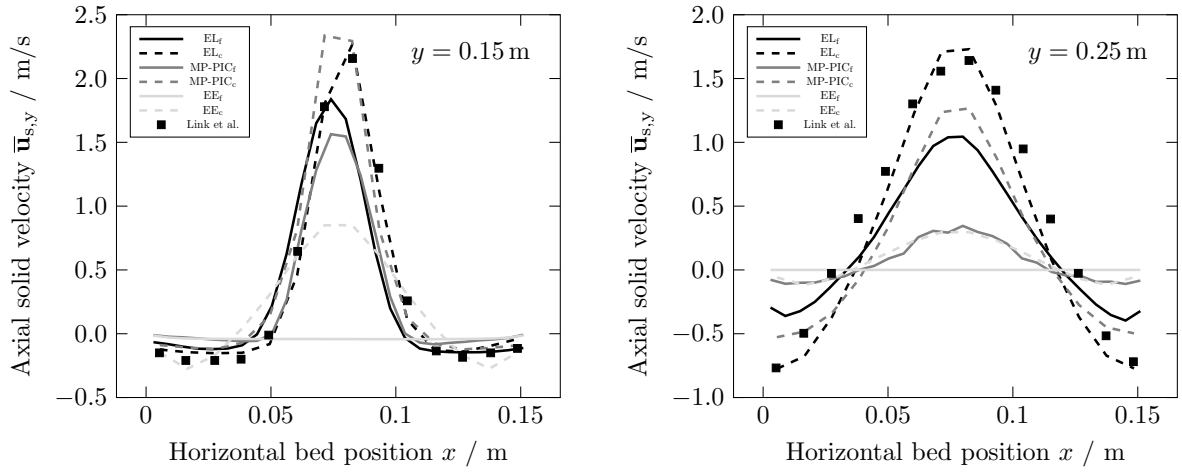

Figure 3.14: Comparison of time-averaged axial solid velocity $\overline{\mathbf{u}}_{s,y}$ across horizontal bed position x at two different distances from the bottom at $y = 0.15$ and $0.25\,\mathrm{m}$ with different solvers and a coarser (c) and a finer grid size (f). Experimental data is taken from Link et al. [203]. Eulerian-Lagrangian (EL), Eulerian-Eulerian (EE) and MP-PIC models are used for the solvers.

The grid size for this set-up was varied because a coarse mesh results in more accurate data compared to the finer mesh. The higher accuracy of the coarser mesh for the Eulerian-Lagrangian solver can be explained with the more accurate cell averaged properties, in particular for the solid phase fractions, due to the bigger cells in this simulation. The MP-PIC and the Eulerian-Eulerian solver's accuracy are dependent on statistical models. Therefore, bigger cells result in a higher accuracy. This can be seen in the comparison of the different grid sizes. The results of the finer grid sizes for all used solvers shows a lesser agreement towards the experimental data compared to the coarser grid size. For example, the particle bed for the Eulerian-Eulerian does not show a fluidization with a finer mesh, while the fluidization takes place using a coarser mesh. For both Eulerian-Lagrangian and MP-PIC solver a fluidization is observed, but the results of the coarser grid sizes agreed more to the experimental data than the results of the finer grid sizes.

Figure 3.15 shows the influence of the grid size on the execution time for the three solvers used in this simulation.

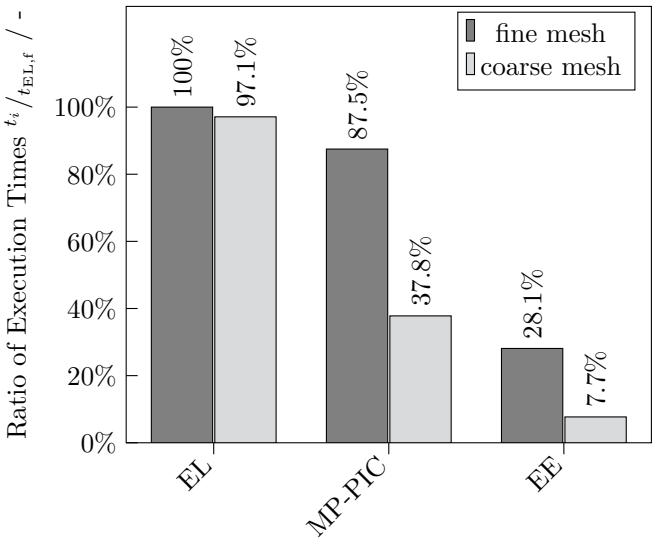

Figure 3.15: Influence of different grid sizes on the execution time for the Eulerian-Lagrangian, MP-PIC and the Eulerian-Eulerian solver. The execution times for each solver and grid size are in relation to the highest execution time, i.e., the execution time of the Eulerian-Lagrangian solver with the finer mesh $t_{\mathrm{EL,f}}$.

Although the number of cells of the finer mesh almost increases sixfold, the execution time of the coarser mesh slightly decreases for the Eulerian-Lagrangian model. The number of particles remain unchanged and the Lagrangian time-step is a fraction of the Eulerian time-step. Hence, the execution time of the Lagrangian loop accounts for the greatest amount of the total execution time. The influence of an increase in cells for the MP-PIC and the Eulerian-Eulerian solver is higher than for the Eulerian-Lagrangian solver. The simulation of the particles is not as time demanding as for the Eulerian-Lagrangian solver, therefore, the increase in execution time is due to the higher number of cells.

In the following, we performed simulations with the newly developed Eulerian-Eulerian-Lagrangian solver with the coarser mesh. The time-averaged axial particle velocities $\overline{\mathbf{u}}_{\mathrm{s,y}}$ at axial heights of 0.15 and 0.25 m for the Eulerian-Lagrangian, MP-PIC, Eulerian-Eulerian, all with the coarser mesh, and the newly developed solver with three different Lagrangian particle ratios $R_{\mathrm{L}} = 20$, 50 and 80 % are shown in Figure 3.16.

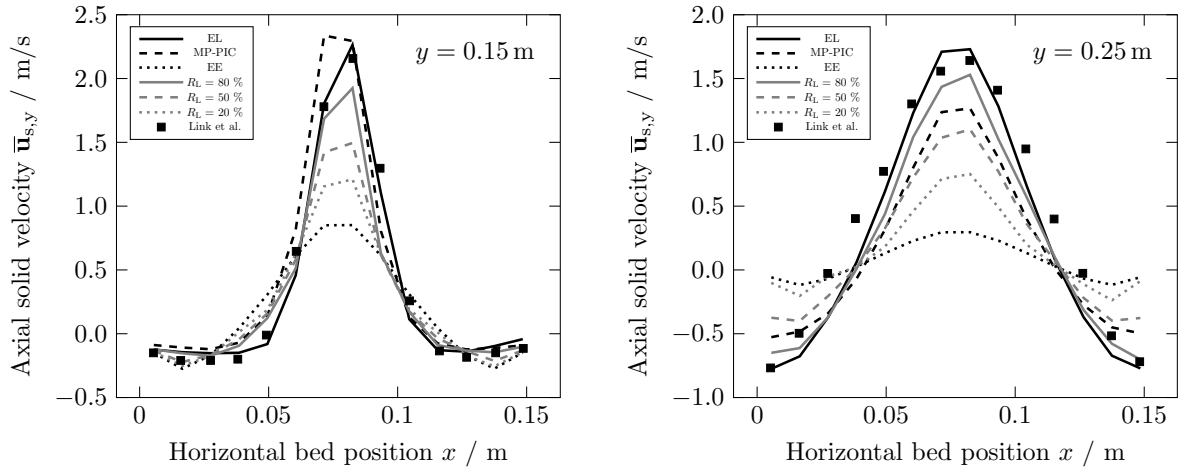

Figure 3.16: Comparison of axial solid velocity $\overline{\mathbf{u}}_{\mathrm{s,y}}$ across horizontal bed position x at two different distances from the bottom at $y = 0.15$ and $0.25\,\mathrm{m}$ with different solvers. Experimental data is taken from Link et al. [203]. Eulerian-Lagrangian, Eulerian-Eulerian and MP-PIC models, as well as the newly developed Eulerian-Eulerian-Lagrangian model with three different Lagrangian particle ratios $R_{\mathrm{L}} = 20$, 50 and 80 % are used for the solvers.

The best agreement towards the experimental data is obtained with the results of the Eulerian-Lagrangian solver for both axial heights. Regarding the results at an axial height of $y = 0.25\,\mathrm{m}$, a slight deviation between the wall and the center core of the spouting area on both sides can be observed. The results from the MP-PIC model slightly overpredict the axial velocities at the spouting area at the lower axial height, but the overall agreement towards the experimental data is still high. At a higher axial height, the MP-PIC model underpredicts the axial particle velocities. The least agreement was achieved with the Eulerian-Eulerian solver. The axial solid velocities are lower than the mreasured velocities from the experiments by Link et al. [203]. The results obtained with our newly developed Eulerian-Eulerian-Lagrangian solver showed a similar trend as in the 2D fluidized bed set-up by Müller et al. [201, 202]: with a higher Lagrangian particle ratio R_{L}, the axial velocities approximate to the results obtained with the Eulerian-Lagrangian model, as more Lagrangian particles are modeled. Therefore, the best agreement towards the experimental data was obtained with a Lagrangian particle ratio of $R_{\mathrm{L}} = 80\,\%$. At this ratio, the results are more accurate than the results obtained with the MP-PIC model. Figure 3.17 shows the execution times for simulating the 3D spouted fluidized bed with the different solvers used.

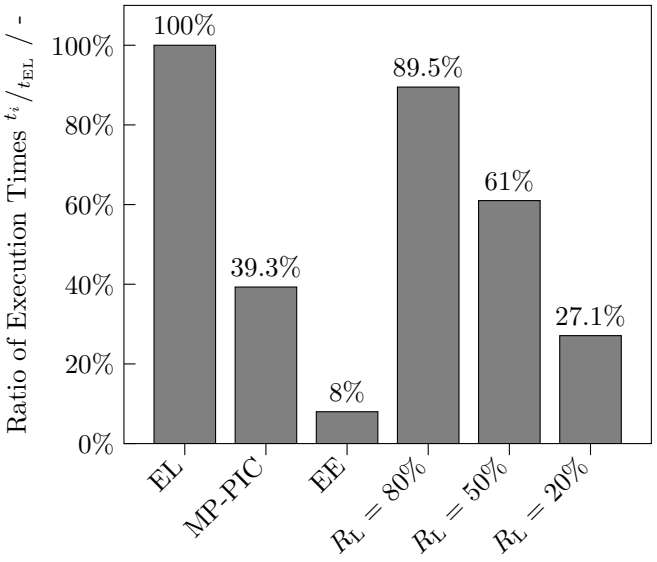

Figure 3.17: Comparison of execution times for the benchmark according to Link et al. [203] with the different solvers used. The solvers were the Eulerian-Lagrangian (EL), Eulerian-Eulerian (EE) models, MP-PIC and the newly developed Eulerian-Eulerian-Lagrangian model with three different Lagrangian particle ratios $R_{\mathrm{L}} = 20$, 50 and 80 %.

The Eulerian-Lagrangian solver had the highest execution time, as all the particles were resolved with a 4-way coupling approach, while the Eulerian-Eulerian solver had the lowest execution times of all the solvers. The execution time of the MP-PIC solver was approximately one third of the execution of the Eulerian-Lagrangian solver. The execution time of the newly developed Eulerian-Eulerian-Lagrangian solver was in accordance to the proposed equation for the the execution time in Equation (3.37).

3.5 Discussion

The simulation results from the Eulerian-Lagrangian model were the most accurate one due to the 4-way coupling of the particles. All particle interactions were resolved. The MP-PIC results showed less accurate results, but the overall accuracy was still very high. The accuracy is due to the fact of the lagrangian particle tracking and the interpolating of certain particle properties and forces. The simulation results obtained by the Eulerian-Eulerian model showed uniform fluidization with a time-averaged axial particle velocity of zero. This is due to the fact that with the KTGF, velocities in the normal direction are considered for particle-particle and particle-wall collisions, while changes for the tangential velocities are not taken into account [200]. But with changes in the tangential velocity, there are also collisions between particles, as well as particles and the wall depending on

the roughness of the particles. Zhao et al. [81] developed the Kinetic Theory of Rough Particles to account for the changes in the tangential velocity. They simulated the fluidized bed according to Müller et al. [201, 202] and obtained better results [200] than with the KTGF. In this work, we used the Eulerian method with KTGF and therefore it shows the least agreement towards the experimental data by Müller et al. [201, 202] and Link et al. [203]. Due to the statistical nature of the underlying models of the Eulerian-Eulerian approach, a coarser mesh resulted in better results for the 3D fluidized bed by Link et al. [203]. For the benchmark according to Müller et al. [201, 202] a coarsening of the mesh had no significant effect on the fluidization behavior obtained with the Eulerian-Eulerian approach. In respect to the Eulerian-Lagrangian and the MP-PIC approach, we observed a negative impact on the accuracy of the results with a coarsening of the mesh. In the simulations performed with the newly developed Eulerian-Eulerian-Lagrangian model the impact of the Lagrangian particles on the Eulerian solid phase could be seen with the adjustment of the Lagrangian particle ratio R_{L}: with an increasing ratio, the results were more accurate and approximated towards the results of the Euler-Lagrange model. The momentum exchange due to collisions between Lagrangian particles and the pseudo L-particles between the Lagrangian particles and the Eulerian solid phase has a significant impact on the accuracy, particularly the bubble formation and the axial solid velocity.

When comparing the MP-PIC model to our newly developed solver in terms of simulation results, it can be seen that the MP-PIC model overpredicts the axial particle velocities for both benchmark cases at lower axial heights and underpredicts the velocities at a larger distance from the bottom. The results for a Lagrangian particle ratio $R_{\mathrm{L}} = 80\,\%$ agreed more with the experimental data than with the results obtained with the MP-PIC model, but overall the velocities were underpredicted. The results with a ratio $R_{\mathrm{L}} = 50\,\%$ and below had a lesser agreement than the results with the MP-PIC model.

The speed of the coupled Eulerian-Eulerian-Lagrangian model clearly showed that collisions between transformed Eulerian particles, i.e., the pseudo L-Particles, were not included in the DEM loop. The simulation speed was dependent on the ratio of Lagrangian particle to all particles R_{L}. The simulation speed of the MP-PIC model is higher than for the Eulerian-Eulerian-Lagrangian solver with a R_{L}-ratio for equivalent accuracy. The Lagrangian particle ratio could be adjusted to get more accurate results with the loss at simulation speed compared to the MP-PIC model. The execution time for this R_{L}-ratio was still lower than the execution time of the Eulerian-Lagrangian solver.

3.6 Conclusion

In this study, a solver was developed coupling the Eulerian-Eulerian and Eulerian-Lagrangian models for gas-solid simulations. The treatment of the gas phase remained unchanged (Eulerian) and the granular matter was simulated with the Eulerian and the Lagrangian methods. A ratio was introduced to define the number of simulated Eulerian and Lagrangian particles that could modify the accuracy and simulation speed. To account for the momentum exchange between the Eulerian solid phase and Lagrangian particles, a transformation algorithm was introduced to transform the Eulerian particles into inactive Lagrangian particles. Those inactive Lagrangian particles inherited the properties from the Eulerian solid phase. The solver was further validated with experimental data from the literature. Depending on the ratio of introduced Lagrangian particles, the coupled Eulerian-Eulerian-Lagrangian solver showed better results than a Eulerian-Eulerian solver, while the results of a Eulerian-Lagrangian solver agreed best with experimental data from the literature. The simulation speed of the coupled solver was also dependent on the Lagrangian particle ratio and increased with this ratio. The accuracy of this newly developed solver can be higher than the results obtained with the MP-PIC model for certain R_{L}-ratios. But the simulation speed decreases accordingly.

4 Implementation of a three-level grid method for CFD-DEM simulations

Abstract

The use CFD-DEM for the simulation of dense gas-solid flows comes with limitations based on the numerical cell size depending on the diameter of the particles. With the introduction of a multi-grid approach, i.e., the calculation of the fluid phase and the solid phase are done with two separate meshes, a finer and a coarser one, this limitation can be overcome. In this work, a three-level grid approach is proposed, in which an additional numerical grid is used to transform parameters used for the solid-fluid momentum exchange from the Lagrangian to the Eulerian grid. The resolution of this newly introduced grid lies in between the resolution of the two other meshes. A conventional single- and dual-grid, as well as the newly introduced three-level grid approach were validated with experimental data in literature and afterwards compared in terms of accuracy and simulation speed. A multi-grid approach, dual- or three-level, shows a higher accuracy than the single-grid method. An additional third grid achieves in almost all cases slightly better results than the dual-grid method while the increase in simulation time is negligible. A coarsening of the solid grid has a higher effect on accuracy than the refinement of the fluid grid. Furthermore, the coarse grain method was implemented to increase simulation speed. Still, the three-level grid approach requires a deeper understanding in the resolution of the numerical grid as there are more degrees of freedom for the cell sizes, but an adequate choice of the numerical grid can drastically improve the simulation accuracy and speed in combination with a coarse grain method.

Bibliographic Information

D. Hirche, O. Hinrichsen, "Implementation and evaluation of a three-level grid method for CFD-DEM simulations of dense gas-solid flows", *Chemical Engineering Journal Advances* **2020**, *4*, 100048.

Copyright Notice

Implementation and evaluation of a three-level grid method for CFD-DEM simulations of dense gas–solid flows

Author: Daniel Hirche,Olaf Hinrichsen

Publication: Chemical Engineering Journal Advances

Publisher: Elsevier

Date: 15 December 2020

4.1 Introduction

Computational Fluid Dynamics (CFD) as a simulation approach for modeling gas-solid flows, in particular, fluidized bed [207], has been proven to be accurate in predicting the hydrodynamics, thermodynamics and chemical reactions of the system [208–213]. Several approaches exist to model gas-solid flows and the most common ones are the Lattice-Boltzmann Method (LBM), Discrete Element Method [119] coupled with CFD (CFD-DEM) [14, 123] and the Two-Fluid model (TFM) [53, 71]. While the LBM is mostly used for the investigation of small-scale systems to derive correlations used for more abstract models [214], CFD-DEM found its use in the simulation of small- to medium-scale systems with mostly larger particles [99, 215, 216], e.g., group D particles according to the Geldart classification [12]. Due to the Eulerian character in the TFM, it is used for large-scale systems [217, 218], independent of the particle size. Using CFD-DEM the particles are calculated in a Lagrangian way using DEM and the fluid flow is modeled as a continuum in a Eulerian way. In order to couple the phases, crucial parameters from both phases have to be transformed from a Lagrangian parameter to a Eulerian one and vice versa, e.g., the number of particles (Lagrangian parameter) has to be transformed to a Eulerian parameter, the void fraction. There exist certain restrictions for the applicability of CFD-DEM simulations. One of the major restrictions when using CFD-DEM is the relatively long simulation time compared to the TFM approach when simulating a high amount of particles [219]. Especially for particles with a small diameter, e.g., Geldart group B particles, the use of CFD-DEM might not be feasible in terms of simulation time. A method to increase the simulation speed for CFD-DEM simulations is the so called coarse grain (CG) method developed by Sakai and Koshizuka [132]. Here, a group of particles are lumped together to a cluster of particles forming a bigger parcel [220]. The CG method was applied for multiple geometry scales in literature, e.g., for dense medium cyclones [221]. Mass and energy conservation in this method is ensured with an introduced scaling factor. A higher scaling factor results in more particles being lumped together to a bigger parcel, hence less particles need to be simulated and the simulation speed increases. Therefore, the level of the scaling factor is limited by applicability and resulting accuracy. Takabatake et al. [222] used a scaling factor of up to three for a gas-solid spouted bed and validated their simulations with experiments. They achieved reasonable results regarding the mixing state. Even higher scaling factors were applied for the simulation of fluidized beds, e.g. a scaling factor of up to eight [223]. The CG method was also applied for the simulation of a 3 m high circulating fluidized bed reactor [224] and even larger scales with Geldart group B particles with a scaling factor of approximately 60 [225]. The higher the scaling factor, the larger the size of the particle cluster. The size of the particles can be another major problem regarding dense solid flow simulations using CFD-DEM. Peng et al. [226] proposed a cell-to-particle diameter ratio of at least 3.82 to get accurate simulation results. But bigger cells result in a worse resolution due to the coarser numerical grid size.

Hence, the choice of an adequate numerical grid size is crucial. The calculations for the Lagrangian particle tracking, i.e., the particle movement, is at first sight independent of the numerical grid. Using the finite volume method, the fluid phase is calculated on a numerical grid consisting of 3D cells. The coupling between the particles and the fluid phase is done by transforming Lagrangian to Eulerian parameters, e.g., the velocities of particles residing in a specific cell are averaged to obtain a cell-averaged value used for the fluid phase calculations. Alobaid et al. [227] proposed a dual-grid method, splitting a single numerical grid in two separate grids: a finer grid used for the calculation of the fluid phase and a coarser grid for the Lagrangian particle tracking. The implementation of a multi-grid method for CFD-DEM simulations can have multiple benefits. The major advantages are the increasing accuracy of the results, the higher resolution of the obtained data and the representation of complex or narrow geometries. With a dual-grid approach the numerical grid gets independent of the particle size, but a mapping of crucial properties between the two numerical grids becomes necessary, where a conservative interpolation method with second-order accuracy showed the best results [228]. The dual-grid approach was applied and validated in several cases, e.g., spouted fluidized beds [229] or jetting fluidized beds [230].

In the following, a three-level grid approach is proposed, extending the conventional dual-grid approach by another numerical grid for the calculation and determination of specific Eulerian parameters from Lagrangian ones. Farzaneh et al. [231] proposed a three-level grid approach, but in their work they used one grid for the fluid phase and two grids for two different sized particle phases. In our work, one grid is used for the Lagrangian particle tracking independent of the particle size. It is shown in detail how a multi-grid method consisting of two and three numerical grids can result into the aforementioned advantages. Experimental data from literature is used to validate the multi-grid method and it will be compared to a conventional CFD-DEM solver. Lastly, the additional time needed for the mapping due to the third numerical grid will be evaluated.

4.2 Methodology

First, the numerical methods for CFD-DEM are presented and in the second part the necessity and advantages of a multi-level grid method, as well as, the solving procedures will be discussed in detail.

4.2.1 Numerical Methods

The calculation of the fluid motion is based on the continuity equation (cf. Equation (4.1)) and the momentum balance based on the volume-averaged Navier-Stokes equations (cf. Equation (4.2)):

$$\frac{\partial \varepsilon}{\partial t} + \boldsymbol{\nabla} \cdot (\varepsilon \, \mathbf{u}_\mathrm{f}) = 0 \tag{4.1}$$

and

$$\frac{\partial \left(\varepsilon \, \rho_\mathrm{f} \, \mathbf{u}_\mathrm{f}\right)}{\partial t} + \boldsymbol{\nabla} \cdot \left(\varepsilon \, \rho_\mathrm{f} \, \mathbf{u}_\mathrm{f} \, \mathbf{u}_\mathrm{f}\right) = -\varepsilon \, \boldsymbol{\nabla} p + \varepsilon \, \rho_\mathrm{f} \, \mathbf{g} + \boldsymbol{\nabla} \cdot \left(\varepsilon \, \overline{\overline{\tau}}_\mathrm{f}\right) + \mathbf{M}_\mathrm{f,s}. \tag{4.2}$$

Here, $\mathbf{u}_\mathrm{f}$ represents the velocity, ρ_f the density and ε the volume fraction of the fluid phase.

The calculation of the cell-averaged volumetric fraction of the fluid phase ε in CFD-DEM simulation is dependent on the number of particles residing in the considered cell. There exist several different methods for the determination of the volumetric volume fraction, e.g., analytical, porous cube model [215] or diffusion-based models [232, 233]. In the following simulations the calculation of the volume fraction is done via the Particle Centroid Method (PCM). According to the PCM the volume of all particles residing in the considered cell $\sum_{\forall \mathrm{p} \in \mathrm{cell}} V_\mathrm{p}$ accounts for the calculation of the volume fraction of the specific phase:

$$\varepsilon = 1 - \frac{1}{V_\mathrm{cell}} \sum_{\forall \mathrm{p} \in \mathrm{cell}} V_\mathrm{p}. \tag{4.3}$$

The stress tensor of the fluid phase $\overline{\overline{\tau}}_\mathrm{f}$ is given by Enwald et al. [53]:

$$\overline{\overline{\tau}}_\mathrm{f} = \eta_\mathrm{f} \left[\boldsymbol{\nabla} \mathbf{u}_\mathrm{f} + (\boldsymbol{\nabla} \mathbf{u}_\mathrm{f})^\mathrm{T}\right] - \left(\zeta_\mathrm{f} - \frac{2}{3}\eta_\mathrm{f}\right) (\boldsymbol{\nabla} \cdot \mathbf{u}_\mathrm{f}) \, \overline{\overline{\mathrm{I}}}. \tag{4.4}$$

The momentum exchange $\mathbf{M}_\mathrm{f,s}$ accounts for the coupling forces between the fluid and the solid phase. In the later numerical implementation, $\mathbf{M}_\mathrm{f,s}$ is split up into an explicit and an implicit term due to stability reasons:

$$\mathbf{M}_\mathrm{f,s} = \frac{\sum \mathbf{F}_\mathrm{f,p}}{V_\mathrm{cell} \, |\mathbf{u}_\mathrm{f} - \mathbf{u}_\mathrm{s}|} \cdot \mathbf{u}_\mathrm{f} - \frac{\sum \mathbf{F}_\mathrm{f,p}}{V_\mathrm{cell} \, |\mathbf{u}_\mathrm{f} - \mathbf{u}_\mathrm{s}|} \cdot \mathbf{u}_\mathrm{s}, \tag{4.5}$$

with the cell-averaged velocity of the particulate phase $\mathbf{u}_\mathrm{s}$ and the coupling forces between the fluid and the particle $\mathbf{F}_\mathrm{f,p}$. The cell-averaged velocity of the solid phase $\mathbf{u}_\mathrm{s}$ is determined

in accordance to the PCM with the individual velocities of the tracked particles $\mathbf{u}_\mathrm{p}$ and the total number of particles residing in the considered cell n_p:

$$\mathbf{u}_\mathrm{s} = \frac{1}{n_\mathrm{p}} \sum_{\forall \mathrm{p} \in \mathrm{cell}} \mathbf{u}_\mathrm{p}. \tag{4.6}$$

The coupling forces between the fluid and solid phases consist of the drag, buoyancy and lift force, among others. According to Papadikis et al. [100] the drag force $\mathbf{F}_\mathrm{d}$ was determined as the major parameter for the fluid-particle force coupling. It can be calculated with the momentum exchange coefficient β, the relative velocity of the fluid phase and the individual particle $\left(\mathbf{u}_\mathrm{f} - \mathbf{u}_\mathrm{p}\right)$, the mass of the particle m_p and the corresponding density ρ_p according to

$$\mathbf{F}_\mathrm{d} = \beta \left(\mathbf{u}_\mathrm{f} - \mathbf{u}_\mathrm{p}\right) \frac{m_\mathrm{p}}{\rho_\mathrm{p}}. \tag{4.7}$$

The determination of the momentum exchange coefficient β can be done according to different models. One of the most used models is the Gidaspow model [15, 78] which is a combination of the Ergun correlation [168] for dense gas-solid flows and the correlation from Wen and Yu [170] for dilute ones:

$$\beta = \begin{cases} 150 \frac{(1-\varepsilon)^2 \eta}{\varepsilon d_\mathrm{p}^2} + 1.75 \left(1-\varepsilon\right) \frac{\rho_\mathrm{f}}{d_\mathrm{p}} \left|\mathbf{u}_\mathrm{f} - \mathbf{u}_\mathrm{p}\right|, & \varepsilon < 0.8 \\ \frac{3}{4} C_\mathrm{d} \frac{\varepsilon \left(1-\varepsilon\right)}{d_\mathrm{p}} \rho_\mathrm{f} \left|\mathbf{u}_\mathrm{f} - \mathbf{u}_\mathrm{p}\right| \varepsilon^{-2.65}, & \varepsilon \geq 0.8. \end{cases} \tag{4.8}$$

The drag coefficient C_d is dependent on the particle Reynolds number Re_p:

$$C_\mathrm{d} = \begin{cases} \frac{24}{Re_\mathrm{p}} \left(1.0 + 0.15\, Re_\mathrm{p}^{0.687}\right), & Re_\mathrm{p} \leq 1000 \\ 0.44, & Re_\mathrm{p} > 1000 \end{cases} \tag{4.9}$$

and

$$Re_\mathrm{p} = \frac{\varepsilon\, d_\mathrm{p} \left|\mathbf{u}_\mathrm{f} - \mathbf{u}_\mathrm{p}\right| \rho_\mathrm{f}}{\eta}. \tag{4.10}$$

Benyahia et al. [183] extended the Hill-Koch-Ladd (HKL) drag correlation [179, 180] from Lattice-Boltzmann simulations to a wider range of void fractions and particle Reynolds numbers, the so called extended HKL drag-model, which is another widely used equation for the calculation of the momentum exchange coefficient:

$$\beta = \frac{3}{4} \frac{C_\mathrm{d} \alpha \left(1-\alpha\right) \rho_\mathrm{f} |\mathbf{u}_\mathrm{f} - \mathbf{u}_\mathrm{p}|}{d_\mathrm{p}} \tag{4.11}$$

with the drag coefficient

$$C_\mathrm{d} = 12\frac{(1-\alpha)^2}{Re_\mathrm{p}^*}F. \tag{4.12}$$

The dimensionless drag force F is dependent on the degree of turbulence with the adjusted Reynolds number Re_p^* and the solid volume fraction α with $\alpha = 1-\varepsilon$:

$$F = 1 + 3/8Re_\mathrm{p}^* \quad \text{for } \alpha \leq 0.01 \text{ and } Re_\mathrm{p}^* \leq \frac{F_2 - 1}{3/8 - F3} \tag{4.13}$$

$$F = F_0 + F_1 Re_\mathrm{p}^{*2} \quad \text{for } \alpha > 0.01 \text{ and } Re_\mathrm{p}^* \leq \frac{F_3 + \sqrt{F_3^2 - 4F_1\left(F_0 - F_2\right)}}{2F_1} \tag{4.14}$$

$$F = F_2 + F_3 Re_\mathrm{p}^* \quad \text{otherwise,} \tag{4.15}$$

with

$$Re_\mathrm{p}^* = \frac{1}{2}Re_\mathrm{p}. \tag{4.16}$$

The separate contributions for the inertial coefficients F_0, F_1, F_2 and F_3 are determined by

$$F_0 = \begin{cases} (1-w)\left[\frac{1+3\sqrt{\frac{\alpha}{2}}+\frac{135}{64}\alpha\ln(\alpha)+17.14\alpha}{1+0.681\alpha-8.48\alpha^2+8.16\alpha^3}\right] + w\left[10\frac{\alpha}{(1-\alpha)^3}\right] & \text{for } 0.01 < \alpha < 0.4 \\ 10\frac{\alpha}{(1-\alpha)^3} & \text{for } \alpha \geq 0.4 \end{cases} \tag{4.17}$$

$$F_1 = \begin{cases} \frac{\sqrt{\frac{2}{\alpha}}}{40} & \text{for } 0.01 < \alpha \leq 0.1 \\ 0.11 + 0.00051\exp\left(11.6\alpha\right) & \text{for } \alpha > 0.1 \end{cases} \tag{4.18}$$

$$F_2 = \begin{cases} (1-w)\left[\frac{1+3\sqrt{\frac{\alpha}{2}}+\frac{135}{64}\alpha\ln(\alpha)+17.89\alpha}{1+0.681\alpha-11.03\alpha_\mathrm{s}^2+15.41\alpha_\mathrm{s}^3}\right] + w\left[10\frac{\alpha}{(1-\alpha)^3}\right] & \text{for } 0.01 < \alpha < 0.4 \\ 10\frac{\alpha}{(1-\alpha)^3} & \text{for } \alpha \geq 0.4 \end{cases} \tag{4.19}$$

$$F_3 = \begin{cases} 0.9351\alpha + 0.03667 & \text{for } 0.01 < \alpha < 0.0953 \\ 0.0673 + 0.212\alpha + 0.0232/\left(1-\alpha\right)^5 & \text{for } \alpha \geq 0.0953 \end{cases} \tag{4.20}$$

with

$$w = \exp\left(-10\left(0.4-\alpha\right)/\alpha\right). \tag{4.21}$$

The movement of the particles according to a Lagrangian way is done with the use of Newton's second law of motion with a force (cf. Equation (4.22)) and torque balance (cf. Equation (4.23)).

$$m_\mathrm{p}\frac{\mathrm{d}\mathbf{u}_\mathrm{p}}{\mathrm{d}t} = \sum \mathbf{F}_\mathrm{p}. \tag{4.22}$$

The torque of the particle $\mathbf{T}_\mathrm{p}$ is calculated with the moment of inertia I_p and the time derivative of the angular velocity ω_p:

$$I_\mathrm{p}\frac{\mathrm{d}\omega_\mathrm{p}}{\mathrm{d}t} = \mathbf{T}_\mathrm{p}. \tag{4.23}$$

The forces acting on the considered particle $\sum \mathbf{F}_\mathrm{p}$ consist of contact forces $\mathbf{F}^\mathrm{c}$ including collisions, non-contact forces $\mathbf{F}^\mathrm{nc}$ including forces due to gravity and particle-fluid interaction forces $\mathbf{F}_\mathrm{f,p}$, i.e., drag force $\mathbf{F}_\mathrm{d}$ (cf. (4.7)), pressure gradient force $\mathbf{F}_{\boldsymbol{\nabla} p}$, gravity force $\mathbf{F}_\mathrm{g}$ and buoyancy force $\mathbf{F}_\mathrm{b}$:

$$\mathbf{F}_{\boldsymbol{\nabla} p} = V_\mathrm{p}\boldsymbol{\nabla} p \tag{4.24}$$

and

$$\mathbf{F}_\mathrm{g} - \mathbf{F}_\mathrm{b} = V_\mathrm{p}\left(\rho_\mathrm{p} - \rho_\mathrm{f}\right)\mathbf{g}. \tag{4.25}$$

The contact force $\mathbf{F}^\mathrm{c}$ can result from particle-particle collisions, $\mathbf{F}^\mathrm{c}_\mathrm{p}$, or from particle-wall collisions, $\mathbf{F}^\mathrm{c}_\mathrm{w}$. Several models were proposed in literature for the force-displacement [234], most of them differentiated by linear and non-linear spring and damping models [205]. In this work, the non-linear model based on the Hertzian theory is used. Each of the above stated forces is divided according to the soft-sphere and spring, slider and dash-pot model into a normal and tangential contact force:

$$\mathbf{F}^\mathrm{c} = \mathbf{F}^\mathrm{c}_\mathrm{n} + \mathbf{F}^\mathrm{c}_\mathrm{t} \tag{4.26}$$

with the normal contact force $\mathbf{F}^\mathrm{c}_\mathrm{n}$ and and tangential contact force $\mathbf{F}^\mathrm{c}_\mathrm{t}$, respectively. According to the Hertzian spring-theory and the consideration of damping, the normal contact force can be calculated with

$$\mathbf{F}^\mathrm{c}_\mathrm{n} = -k_\mathrm{n}\Delta x^{b}_{\mathrm{n,\,ol}}\mathbf{n} - \eta_\mathrm{n}\mathbf{u}_{\mathrm{n,\,rel}}. \tag{4.27}$$

The normal spring stiffness is defined as k_n, the overlap between the two colliding particles is $\Delta x_{\mathrm{n,\,ol}}$, the exponent b for the Hertzian spring theory has a value of 1.5, $\mathbf{n}$ represents the unity vector in normal direction, the damping coefficient for the normal force is η_n and $\mathbf{u}_{\mathrm{n,\,rel}}$ defines the relative velocity of the two colliding particles in normal direction

of the collision. The normal spring stiffness k_n is dependent on the effective radius r_eff, the Young's modulus E and the Poisson ratio ν:

$$k_\mathrm{n} = \frac{4}{3}\sqrt{r_\mathrm{eff}}\frac{E}{2\left(1-\nu^2\right)}. \tag{4.28}$$

The effective radius can be calculated with the two diameters of the colliding particles d_1 and d_2:

$$r_\mathrm{eff} = 0.5\frac{d_1\,d_2}{d_1+d_2}. \tag{4.29}$$

For uniform particles of the same size, i.e., $d_1 = d_2$, the effective radius becomes $r_\mathrm{eff} = 0.25 d_\mathrm{p}$ and Equation (4.28) can be simplified to

$$k_\mathrm{n} = \frac{1}{3}\sqrt{d_\mathrm{p}}\frac{E}{1-\nu^2}. \tag{4.30}$$

The damping coefficient for the normal contact force η_n is calculated according to the heuristically equation by Tsuji et al. [123]:

$$\eta_\mathrm{n} = \alpha_\mathrm{n}\sqrt{M_\mathrm{red}k_\mathrm{n}}\,\Delta x_\mathrm{ol}^{0.25} \tag{4.31}$$

with the reduced mass of the two colliding particles M_red

$$M_\mathrm{red} = \frac{m_1\,m_2}{m_1+m_2} \tag{4.32}$$

and for uniform particles in terms of size and density

$$M_\mathrm{red} = 0.5 m_\mathrm{p}. \tag{4.33}$$

Equation (4.31) then simplifies to

$$\eta_\mathrm{n} = \alpha_\mathrm{n}\sqrt{0.5 m_\mathrm{p}k_\mathrm{n}}\,\Delta x_\mathrm{ol}^{0.25}. \tag{4.34}$$

The parameter α_n is an empirical parameter and is related to the coefficient of restitution e_n [120, 123] according to:

$$\alpha_\mathrm{n} = \begin{cases} \frac{-2\ln e_\mathrm{n}}{\sqrt{\pi^2+\ln^2 e_\mathrm{n}}} & \text{if } 0 < e_\mathrm{n} \leq 0.8 \\ 2 & \text{if } e_\mathrm{n} = 0. \end{cases} \tag{4.35}$$

The tangential component of the contact force $\mathbf{F}_\mathrm{t}^\mathrm{c}$ can be calculated with the tangential spring stiffness k_t, the tangential overlap $\Delta x_{\mathrm{ol},\,\mathrm{t}}$, the unit vector in tangential direction $\mathbf{t}$, the tangential damping coefficient η_t and the tangential slip velocity $\mathbf{u}_{\mathrm{t},\,\mathrm{slip}}$:

$$\mathbf{F}_\mathrm{t}^\mathrm{c} = -k_\mathrm{t}\Delta x_{\mathrm{ol},\,\mathrm{t}}\mathbf{t} - \eta_\mathrm{t}\mathbf{u}_{\mathrm{t},\,\mathrm{slip}}. \tag{4.36}$$

Furthermore, according to the Coulomb friction law, sliding can occur if the tangential component of the contact exceeds the Coulomb friction force $\mu_\mathrm{f}|\mathbf{F}_\mathrm{n}^\mathrm{c}|$, with μ_f being the friction coefficient. The tangential component of the contact force therefore follows the equation:

$$\mathbf{F}_\mathrm{t}^\mathrm{c} = \min\left(-k_\mathrm{t}\Delta x_{\mathrm{ol},\,\mathrm{t}}\mathbf{t} - \eta_\mathrm{t}\mathbf{u}_{\mathrm{t},\,\mathrm{slip}}\ ,\ -\mu_\mathrm{f}|\mathbf{F}_\mathrm{n}^\mathrm{c}|\mathbf{t}\right). \tag{4.37}$$

A popular method to increase the speed of CFD-DEM simulations is the coarse grain (CG) model proposed by Sakai and Koshizuka [132]. Here, several smaller particles are represented by one larger particle. A coarse grain factor f_CG is introduced describing the ratio of the diameter of the larger coarse grain particle to the original smaller particle $d_\mathrm{p,CG}/d_\mathrm{p,orig}$, therefore, the particle diameter of the larger coarse grain particle can be calculated with:

$$d_\mathrm{p,CG} = f_\mathrm{CG}\, d_\mathrm{p,orig}. \tag{4.38}$$

The total number of new coarse grain particles is decreased by a value of f_CG^3. The simulation time decreases as well, if the DEM-calculation is the speed determining step, as the number of Lagrangian equations decreases. With the assumption of the CG model that all small particles of a parcel shall resemble and evince the same physical properties and fluid dynamic behavior, several modifications for the Lagrangian equations need to be made to assure the same magnitude of forces. The forces acting on the coarse grain particle cluster, i.e., the drag force $\mathbf{F}_\mathrm{d,CG}$, gravity force $\mathbf{F}_\mathrm{g,CG}$ and buoyancy force $\mathbf{F}_\mathrm{b,CG}$ are scaled with the the coarse grain factor f_CG accordingly:

$$\mathbf{F}_\mathrm{d,CG} = f_\mathrm{CG}^3\mathbf{F}_\mathrm{d,orig} \tag{4.39}$$

$$\mathbf{F}_\mathrm{g,CG} = f_\mathrm{CG}^3\mathbf{F}_\mathrm{g,orig} \tag{4.40}$$

$$\mathbf{F}_\mathrm{b,CG} = f_\mathrm{CG}^3\mathbf{F}_\mathrm{b,orig}. \tag{4.41}$$

It is further assumed that the velocity of the coarse grained particle cluster is equal to the average velocity of the smaller particles, as well as a uniform angular velocity between the cluster and small particles, hence:

$$\mathbf{u}_\mathrm{p,CG} = \frac{1}{f_\mathrm{CG}^3}\sum_{\forall \mathrm{p}\in\mathrm{cell}}\mathbf{u}_\mathrm{p,orig} \tag{4.42}$$

and

$$\omega_{\mathrm{p,CG}} = \frac{1}{f_{\mathrm{CG}}^3} \sum_{\forall \mathrm{p} \in \mathrm{cell}} \omega_{\mathrm{p,orig}}. \tag{4.43}$$

Accordingly, regarding particle-particle collisions the cluster of small particles is considered as colliding in an identical way with the requirement of the kinetic energy of the coarse grain particle lump being equal to the sum of the individual smaller particles:

$$\frac{1}{2} m_{\mathrm{p,CG}} \mathbf{u}_{\mathrm{p,CG}}^2 + \frac{1}{2} I_{\mathrm{p,CG}} \omega_{\mathrm{p,CG}}^2 = f_{\mathrm{CG}}^3 \left(\frac{1}{2} m_{\mathrm{p,orig}} \mathbf{u}_{\mathrm{p,orig}}^2 + \frac{1}{2} I_{\mathrm{p,orig}} \omega_{\mathrm{p,orig}}^2 \right). \tag{4.44}$$

The contact forces, both in normal and tangential direction, for the cluster of coarse grained particles, $\mathbf{F}_{\mathrm{n,CG}}^{\mathrm{c}}$ and $\mathbf{F}_{\mathrm{t,CG}}^{\mathrm{c}}$, respectively, are f_{CG}^3-times the contact forces of an original particle, $\mathbf{F}_{\mathrm{n}}^{\mathrm{c}}$ and $\mathbf{F}_{\mathrm{t}}^{\mathrm{c}}$:

$$\mathbf{F}_{\mathrm{n,CG}}^{\mathrm{c}} = f_{\mathrm{CG}}^3 \mathbf{F}_{\mathrm{n}}^{\mathrm{c}} \tag{4.45}$$

and

$$\mathbf{F}_{\mathrm{t,CG}}^{\mathrm{c}} = f_{\mathrm{CG}}^3 \mathbf{F}_{\mathrm{t}}^{\mathrm{c}}. \tag{4.46}$$

The moment of inertia of the coarse grained cluster of particles $I_{\mathrm{p,CG}}$ can be calculated with the assumption of equal velocity between the coarse grained particle cluster and the individual particles (cf. Equation (4.42)), as well as the following dependencies of the particle dimensions (cf. Equation (4.38)) and masses of the coarse grained and small particles on the coarse grain factor f_{CG}:

$$m_{\mathrm{p,CG}} = f_{\mathrm{CG}}^3 m_{\mathrm{p,orig}}. \tag{4.47}$$

Hence, the following relation for the moment of inertia is valid:

$$I_{\mathrm{p,CG}} = f_{\mathrm{CG}}^5 I_{\mathrm{p,orig}}. \tag{4.48}$$

Furthermore, the torque of the coarse grained particle cluster $\mathbf{T}_{\mathrm{p,CG}}$ can be expressed with:

$$\mathbf{T}_{\mathrm{p,CG}} = f_{\mathrm{CG}}^4 \mathbf{T}_{\mathrm{p,orig}}. \tag{4.49}$$

Typically, CFD-DEM simulations are applied for lab- to small scale applications and not for industrially relevant reactor sizes due to the high amount of particles. The simulation of industrially relevant scales was formerly limited to the TFM approach, but using a Lagrangian frame provides more detailed results than the Euler-Euler method [235, 236]. The number of particles with the CG method can be lowered and therefore the simulation

time drastically reduced using CFD-DEM. Hence, the Euler-Lagrange approach with the CG method can be extended to a wider range of particle numbers, i.e., geometry scales, while still including its advantages, e.g., simulating individual particle properties and cohesion effects.A limitation for the CG method is the limited scaling of the parcels as the flow structures might not be depicted sufficiently anymore. Radl and Sundaresan [237] proposed a filtering approach to encounter this limitation. Yet another disadvantage when using the CG method is the resulting larger particle sizes, as the particle diameter limits the choice of the numerical grid size. For this special case the implementation of a multi-grid method can be useful to overcome this restriction.

4.2.2 Numerical solution

A parameter to quantify the stability of transient simulations was proposed by Courant et al. [238]:

$$Co = |\mathbf{u}_\mathrm{f}| \frac{\Delta t}{\Delta x_\mathrm{cell}}. \tag{4.50}$$

The Courant number Co describes how many cells a certain variable moves in a predefined time-step Δt. Depending on the velocity-pressure coupling algorithm the stability criterion is $Co \leq 1$ [52] for the PISO-algorithm (Pressure-Implicit with Splitting of Operators) [239]. Table 4.1 summarizes the different discretization schemes used in the following simulations.

Table 4.1: Numerical discretization employed in the simulations.

Type	Scheme
Pressure-velocity coupling	PISO [239]
Time	first-order implicit
Gradient	non-limited Gauss linear
Momentum	QUICK

4.2.3 Multi-level grid method

A dual-grid method, i.e., using two separate numerical grids for CFD-DEM simulations was first proposed by Alobaid et al. [227]. Here, the flow of the fluid phase and the particles is calculated on separate numerical grids, distinguished by their resolution. Important parameters, e.g., the void fraction ε or the momentum exchange $\mathbf{M}_\mathrm{f,s}$, are mapped between the different sized grids (cf. Figure 4.1), usually with a volume conservative mapping

method [228]. The numerical grid for the fluid phase has usually more cells than the one used for the particles and therefore the resolution is higher. The decrease in simulation

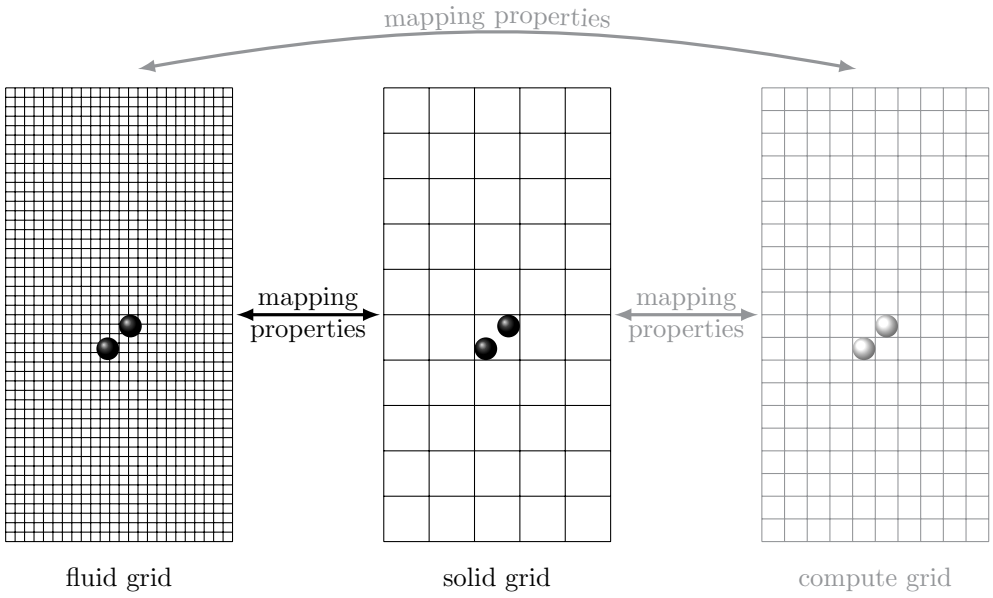

Figure 4.1: Overview of two and three (gray) different grid sizes for CFD-DEM multi-grid simulations with two exemplary particles indicated.

speed due to more cells and interpolation errors due to the mapping procedure are the biggest disadvantages of the dual-grid method. The main advantage of a dual-grid method for CFD-DEM simulations is to overcome the restriction of minimum cell size due to the requirement of the cells being larger than the particles [228]. The traditional CFD-DEM, i.e., a single-grid method, can result in difficulties regarding this requirement, as either the cells are larger than the particles which can result in a poor resolution of the fluid flow or the cell size is too small for the simulations to result in physically reasonable values or can have a negative impact on accuracy of the momentum exchange calculation between the fluid phase and particles. This issue is illustrated in Figure 4.2, as it depicts three uniform sized spherical particles in a cubic cell with a particle diameter to cell length of $\left(d_\mathrm{p}/l_\mathrm{cell} = 0.75\right)$. When using the commonly used and fast Particle Centroid Method (PCM) for void fraction determination [35, 240], a total of four different values for the void fraction ε can be obtained considering up to three particles are residing in the respected cell. In the case of particles overlapping the boundary of the cell and therefore the cell having enough void space to allocate another particle, the volume fraction of the fluid phase ε can result in a negative value and have a negative impact in numerical stability and an unphysical behavior. This is usually prevented by introducing a maximum packing limit serving as a threshold, e.g., for randomly packed spheres $\varepsilon_\mathrm{max} = 0.4$ [241]. When applying a maximum packing limit, the volume fraction of the fluid phase ε can have the following values:

- $\varepsilon = 1$ if no particles are present,
- $\varepsilon = 0.78$ if one particle is present,
- $\varepsilon = 0.56$ if two particles are present and
- $\varepsilon = \varepsilon_{\max}$ if three or more particles are present.

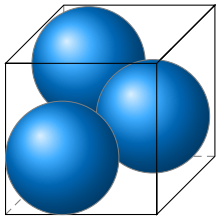

Figure 4.2: Simplified representation of a cubic cell with three uniform-sized particles $\left(d_\mathrm{p}/l_\mathrm{cell} = 0.75\right)$. The values of the fluid volume fraction ε with this $d_\mathrm{p}/l_\mathrm{cell}$-ratio are 1, 0.78, 0.56 and 0.34 for none, one, two and three particles using PCM.

The momentum exchange coefficient β in Equation (4.7) is highly dependent on the void fraction [242]. With the simplified assumption that the main contribution to the momentum exchange term is the drag force $\mathbf{F}_\mathrm{D}$, it is obvious that the resolution of the momentum exchange calculated with conventional drag correlations, e.g., Gidaspow [15, 78], Hill-Koch-Ladd (HKL) [179, 180] or the extended HKL model [183], increases if the particle diameter to cell length ratio $d_\mathrm{p}/l_\mathrm{cell}$ decreases, i.e., larger cells or smaller particles. Figure 4.3 depicts this relationship for the Gidaspow and extended HKL drag model for different particle Reynolds numbers, if four different values for the void fraction ε can be achieved due to three possible particles in a numerical cell.

As can be seen, the gradient of the momentum exchange coefficient β becomes greater with lower void fraction ε, e.g., more particles. At these regions a greater resolution of the void fraction becomes more important for a correct momentum exchange calculation between the fluid phase and the particles. Fluidized bed reactors usually operate at a range of $\varepsilon = 0.4$ to 0.8 [5, 13] and therefore this issue can be crucial for the simulation accuracy. Furthermore, the gradient of the momentum exchange coefficient increases with higher particle Reynolds numbers Re_p. High particle Reynolds numbers occur for example at high relative velocities between the fluid phase and particle $\left|\mathbf{u}_\mathrm{f} - \mathbf{u}_\mathrm{p}\right|$ (cf. Equation (4.10)). Those high relative velocities often occur in turbulent fluidized beds and in spouted fluidized beds. In conventional CFD-DEM simulations the volume fraction of the fluid phase ε is calculated on a single numerical grid and therefore the cell size is limited by the particle size. The particle size dependency can be overcome with the introduction of an additional numerical grid to decouple the fluid flow calculations and the Lagrangian particle tracking.

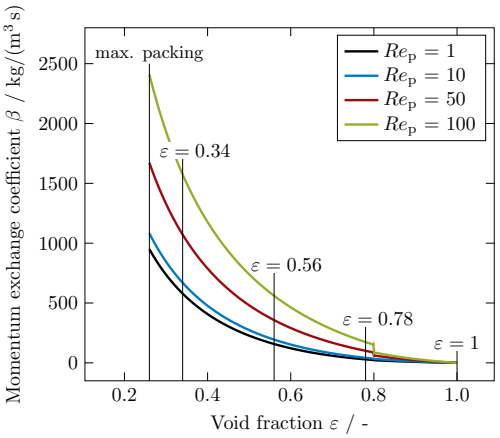

(a) Gidaspow drag model.

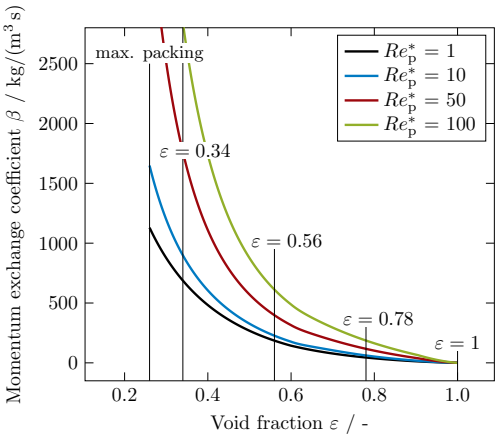

(b) Extended HKL drag model with the modified particle Reynolds number $Re_p^* = 0.5 Re_p$.

Figure 4.3: Resulting momentum exchange coefficients β depending on the void fraction ε and particle Reynolds numbers. Indicated are the maximum packing limit and the four theoretical void fraction values if $d_p/l_{cell} = 0.75$, i.e., a total of maximum three particles can reside in the cell.

In this work, three different sizes for the numerical grids are used: a fluid, a solid and a compute grid. The fluid grid has the highest resolution, where the momentum balance and the continuity equation for the fluid phase are solved. The solid grid consists of the coarsest cells. This numerical grid is used to calculate the volume fractions of the solid phase α. Important parameters to validate and evaluate the simulations are for example the volume fraction and the velocity of the solid phase, α_s and $\mathbf{u}_s$. Using a dual-grid simulation, the quality of the resolution for those parameters would be poor, as the numerical grid is coarse. Therefore, another grid, the compute grid, is introduced. The resolution of this grid is finer compared to the solid grid, but still satisfies the condition of $d_p/l_{cell} \leq 1$ to avoid unphysical values for the volume fraction.

The solving procedure for the three-level grid method is subdivided to the three different numerical grids according to Figure 4.4. The Lagrangian equations for the calculation of the particle velocities and movements are solved on the solid grid. The particles with the new positions and velocities are then mapped onto the compute grid. On this grid the Lagrangian properties are transformed to Eulerian field values. The resulting Eulerian fields, i.e., the volume fraction and the velocity of the solid phase, α and $\mathbf{u}_s$, are then mapped to the fluid grid along with the force between the fluid phase and particles from the solid grid $\mathbf{F}_{f,p}$. The momentum exchange coefficient *beta* between the fluid and solid phase used for the determination of $\mathbf{F}_{f,p}$ is not calculated with the Eulerian field values from the finer compute grid, as the resolution for the solid phase fraction from the compute grid would be too low. Therefore, with the mapped solid phase fraction α and the solid phase velocity $\mathbf{u}_s$ from the compute grid, as well as the coupling forces between the fluid

phase and particles $\mathbf{F}_{\mathrm{f,p}}$ from the solid grid, the momentum balance of the fluid phase can then be solved with those mapped parameters. The resulting new velocity and pressure field of the fluid phase is then mapped to the solid grid and the iteration loop starts again until the end time of the simulation is reached. The solving procedure for the dual-grid method is analogous, with the difference that the Eulerian field values for the solid phase fraction α and the solid phase velocity $\mathbf{u}_{\mathrm{s}}$ are calculated on the solid grid instead of the compute grid.

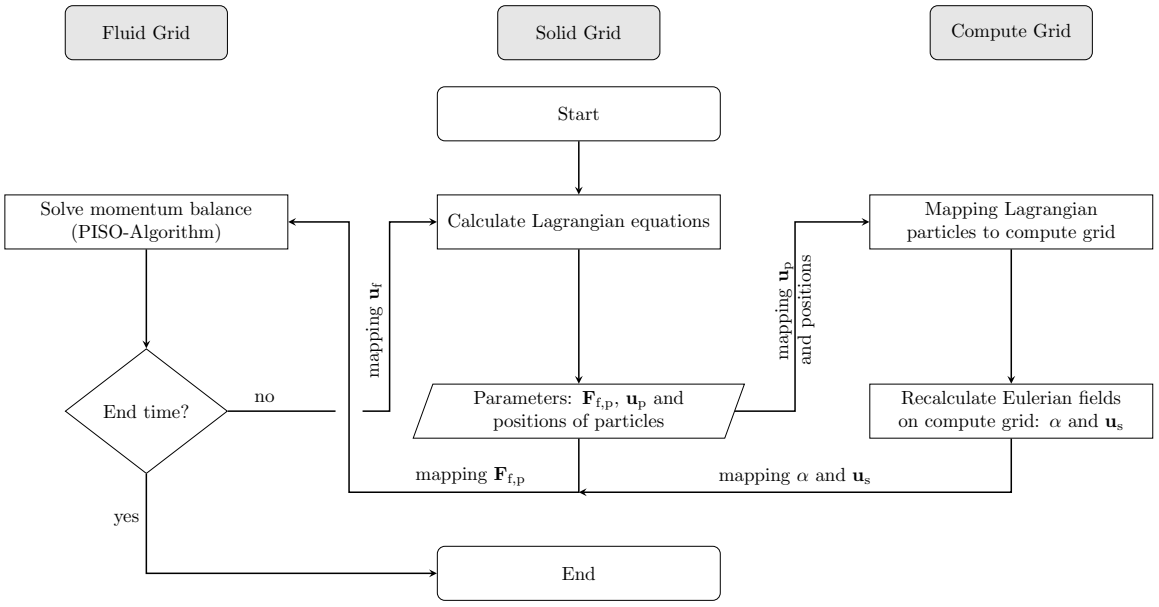

Figure 4.4: Solving procedure for the three-grid CFD-DEM simulation.

The simulations for the single-grid method were performed with the solver *DPMFoam* from the open-source package OpenFOAM® v4.x [206]. A detailed overview of the used solver *DPMFoam* can be found elsewhere [243]. The dual-grid method and the three-level grid approach were also implemented in OpenFOAM®.

4.3 Results and Discussion

The extended HKL model [183] was used in the following simulations to calculate the drag coefficient C_{d} as it was found to be most accurate in preliminary studies. In the following, the newly developed solver is validated and evaluated with three different experimental gas-solid fluidized beds:

- a jet-in fluidized bed by Buijtenen et al. [244],
- a fluidized bed by Penn et al. [245] and
- an incipient fluidized bed with a single jet by Boyce et al. [246].

At last, the simulation time for each of the different approaches, i.e., single-grid, dual-grid and three-level grid approach will be presented and discussed.

4.3.1 Single-, dual- and three-level grid approach

For each of the three different validation cases, the commonly CFD-DEM approach with a single grid, a dual-grid and the newly developed three-level grid method is used for comparison in terms of simulation accuracy and speed. The smallest cell size of the different numerical grids used for Lagrangian calculations is chosen to be 1.6-times the particle diameter [226]. Although Peng et al. [226] proposed this critical cell size ratio specifically for CFD-DEM simulations using an analytical approach for the void fraction calculation, here, this threshold is used with the PCM, as we are investigating a multi-level grid approach. Regarding the dual- and three-level grid method, the cell-to-particle diameter ratios for the fluid, solid and compute grid are varied to get an optimal ratio for each grid.

In the following, the names of the simulations based on the different grid sizes used, are abbreviated according to the ratios of the numerical grid size to the recommendation by Peng et al. [226]. This means, the name for a simulation has three values for the fluid, compute and solid grid, i.e., f_a-c_b-s_c, while f, c and s stand for fluid, compute and solid grid and a, b and c for a refinement ratio, if the value is lower than one, or for a coarsening, if the value is greater than one. For example, the single-grid approach is abbreviated with f_1-c_1-s_1 and a dual-grid approach with the coarsening of the solid grid with a factor of 1.5 to its original size is represented by f_1-c_1-$\mathrm{s}_{1.5}$. The index *1* is in accordance to the recommendations of Peng et al. [226] using CFD-DEM simulations with PCM, i.e., the cell size is 3.82 times the particle diameter. The maximum refinement of the compute grid (index *max*) stands for the lower limit of the cell size, i.e., 1.63 times the particle diameter. Although, Peng et al. [226] explicitly stated the lower limit for the cell size is only suitable when using an analytical approach for the volume fraction determination, in our simulations, it is still used as the compute grid is not used to determine the crucial fluid-particle force $\mathbf{F}_{\mathrm{f,p}}$.

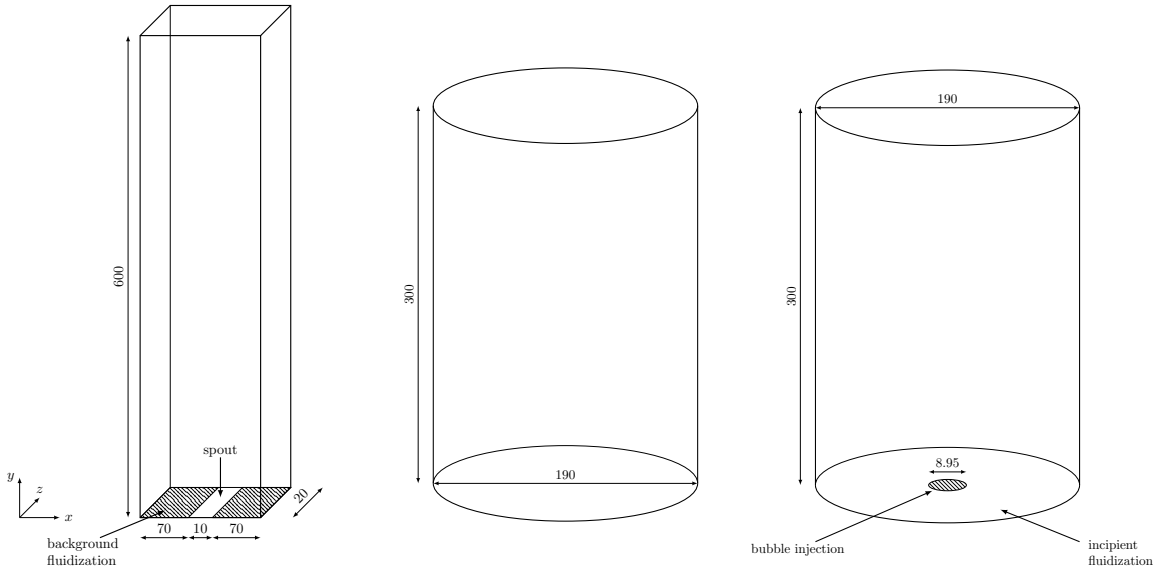

(a) Jet-in fluidized bed.

(b) Fluidized bed with CG.

(c) Single jet in an incipient fluidized bed with CG.

Figure 4.5: Simulation geometries for the pseudo 2D jet-in fluidized bed from van Buijtenen et al. [244] (a), the 3D cylindrical fluidized bed from Penn et al. [245] (b) and the 3D cylindrical incipient fluidized bed with a single jet from Boyce et al. [246] (c).

4.3.1.0.1 Jet-in fluidized bed Buijtenen et al. [244] measured the particle velocity of a pseudo 2D jet-in fluidized bed with positron emission particle tracking (PEPT) and particle image velocimetry (PIV). Figure 4.5a shows the pseudo 2D geometry used for the simulation. The height of the geometry in the simulation was reduced from 2500 mm used in the experiments to a total height of 600 mm. In preliminary studies it was found that the particle fountain never reached a height of 600 mm and therefore the total height of the geometry in the following simulations was reduced accordingly to decrease simulation time. Table 4.2 gives a brief overview of the simulation parameters used in the simulations. Further parameters and properties, e.g., normal or tangential coefficients of restitution, e_n and e_t, respectively, were chosen according to the publication of Buijtenen et al. [244]. An overview of the number of cells in each direction and total number of cells for each individual simulation case, i.e., single-grid, dual-grid and three-level grid approaches, can be found in Table S1 in the Supplementary Material.

Table 4.2: Simulation parameters and properties used for the jet-in fluidized bed by Buijtenen et al. [244].

Property	Value
Particle diameter d_p / mm	3
Number of particles n_p	12 000, 14 000 and 17 000
Particle density ρ_p / kg/m^3	2505
Fluid phase	ambient conditions
Background velocity $\mathbf{u}_\mathrm{bg}$ / m/s	4.15
Single jet velocity $\mathbf{u}_\mathrm{jet}$ / m/s	37.25
Numerical grid for single-grid approach	
Number of cells in x-direction n_x	30
Number of cells in y-direction n_y	120
Number of cells in z-direction n_z	2

The principle of ergodicity is used to obtain parameters in a dynamic system, i.e., a fluidized bed, which are comparable over time in a quasi steady-state. Therefore, the axial particle velocity of the particulate phase $\mathbf{u}_{\mathrm{s},y}$ is time-averaged over a time-frame of 20 s to obtain the time-averaged axial velocity of the particulate phase $\bar{\mathbf{u}}_{\mathrm{s},y}$.

Figure 4.6 shows the experimental obtained time-averaged axial velocity of the solid phase $\bar{\mathbf{u}}_{\mathrm{s},y}$ at an axial height of $y = 100$ mm and the corresponding simulation results from the different single-, dual-grid and three-level grid approaches for a total of 12 000 initially settled particles.

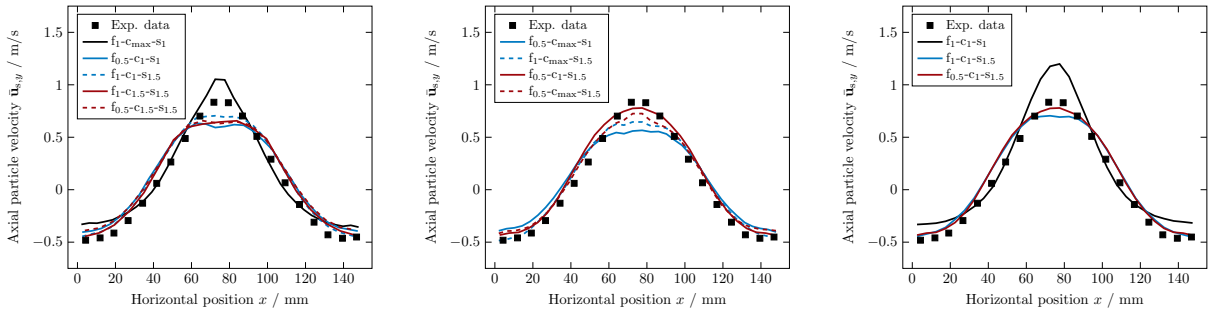

(a) Comparison of dual-grid simulations.

(b) Comparison of three-level grid simulations.

(c) Single, dual-grid (best) and three-level grid approach (best).

Figure 4.6: Comparison of the experimental axial particle velocity $\bar{\mathbf{u}}_{\mathrm{s},y}$ at a lateral height of $y = 100$ mm with simulation results of different refinements of grid sizes using a dual-grid approach (a), three-level grid approach (b) and a single-grid ($\mathrm{f_1}$-$\mathrm{c_1}$-$\mathrm{s_1}$) including the best results of the dual- and three-level grid for a total of 12 000 particles.

The resulting differences when varying the refinement and coarsening levels of the dual-grid approach are presented in Figure 4.6a. A solely refinement of the compute grid

while not modifying the fluid and compute grid (f_1-c_{max}-s_1) shows an improvement of the resulting maximum axial particle velocity compared to the single grid approach. With the refinement of the compute grid the accuracy of the volume fraction of the solid phase and the resolution of the particle velocity is increased, thus leading to a higher overall accuracy. It can be also noted, that a refinement of the fluid grid and the coarsening of the solid grid lead to an improvement of the depiction for the solid phase flow behavior in the near-wall region. However, a coarsening of the solid grid is more beneficial towards an increase in accuracy than the refinement of the fluid grid. Concluding, the simulation results with the introduction of a dual-grid approach show a better agreement than the single-grid approach.

Figure 4.6b shows the effect of modifications to the different numerical grids for the three-level grid approach. The best agreement towards the experimental data is achieved when using a refinement of the fluid grid and a coarsening of the solid grid, i.e., $f_{0.5}$-c_1-$s_{1.5}$, although all simulations with the three-level grid approach show a very good agreement in terms of accuracy.

Figure 4.6c compares the single-grid approach (f_1-c_1-s_1) and the results from the dual-grid and three-level grid approach with the best cell-size refinement and coarsening configuration, f_1-c_1-$s_{1.5}$ and $f_{0.5}$-c_1-$s_{1.5}$, respectively. In the core region of the geometry, where the jet-stream inlet is located, the highest particle velocities are observable in both experimental data and simulation results. Here, the simulation with the single-grid approach overpredicts the resulting axial particle velocity. The dual-grid and three-level approach show a better agreement for the maximum axial particle velocity than the single-grid approach in regards to the experimental data. The results from the three-level grid approach depict the experimental values best compared to the other approaches. Furthermore, in the near-wall region the results from the dual-grid and three-level grid approach are almost identical to the experimental data, while the single-grid approach has a higher agreement to the experimental values between the core area and the wall region. The overprediction of the axial velocity in the annulus region can be explained by the higher wall-effect in the pseudo 2D simulation compared to the 3D experiment. Still, the use of a multi-level grid approach shows a significant improvement in respect to the prediction of the particulate flow behavior than the simulation performed on a single grid.

The results for the various multi-grid approaches with different refinement and coarsening levels, as well as the single-grid method compared to the experimental findings from Buijtenen et al. [244] for a total of 14 000 and 17 000 initial particles are depicted in Figure 4.7 and Figure 4.8.

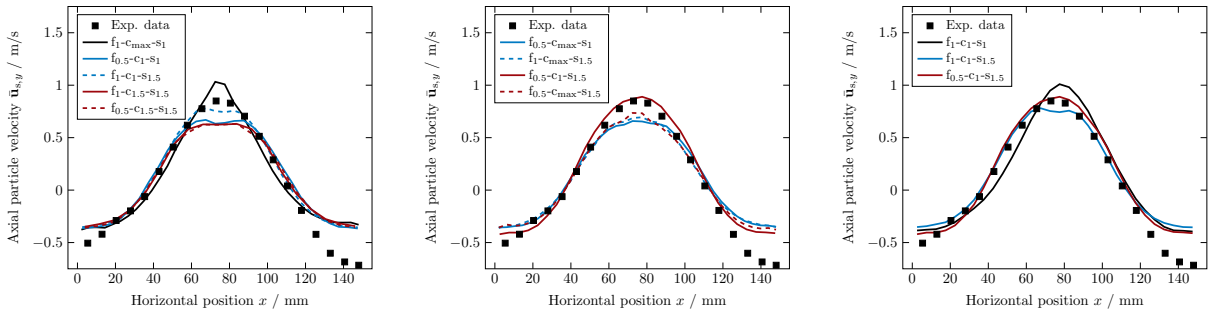

(a) Comparison of dual-grid simulations.

(b) Comparison of three-level grid simulations.

(c) Single, dual-grid (best) and three-level grid appraoch (best).

Figure 4.7: Comparison of the experimental axial particle velocity $\bar{\mathbf{u}}_{\mathrm{s},y}$ at a lateral height of $y = 100\,\mathrm{mm}$ with simulation results of different refinements of grid sizes using a dual-grid approach (a), three-level grid approach (b) and a single-grid ($\mathrm{f_1}$-$\mathrm{c_1}$-$\mathrm{s_1}$) including the best results of the dual- and three-level grid for a total of 14 000 particles.

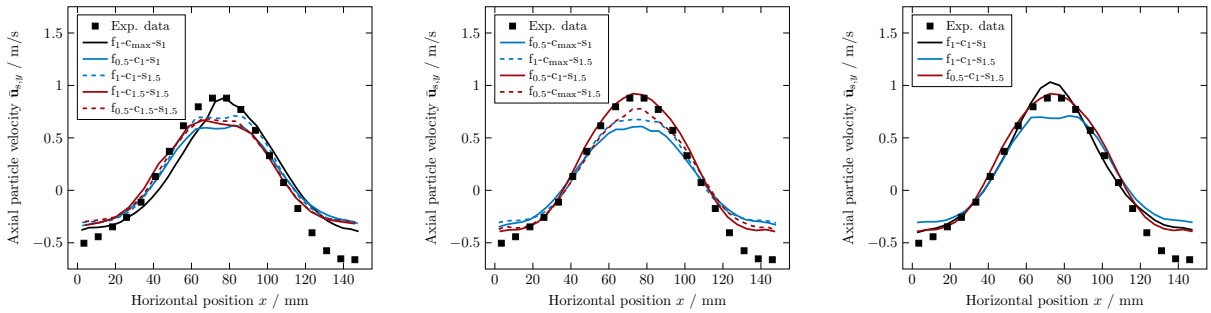

(a) Comparison of dual-grid simulations.

(b) Comparison of three-level grid simulations.

(c) Single, dual-grid (best) and three-level grid appraoch (best).

Figure 4.8: Comparison of the experimental axial particle velocity $\bar{\mathbf{u}}_{\mathrm{s},y}$ at a lateral height of $y = 100\,\mathrm{mm}$ with simulation results of different refinements of grid sizes using a dual-grid approach (a), three-level grid approach (b) and a single-grid ($\mathrm{f_1}$-$\mathrm{c_1}$-$\mathrm{s_1}$) including the best results of the dual- and three-level grid for a total of 17 000 particles.

The same observations analogies to the simulation with 12 000 particles can be made for the simulations with 14 000 and 17 000 particles:

- the single-grid approach overpredicts the axial particle velocity in the core of the fluidized bed,
- a dual-grid method can depict the experimental values better than the single-grid method and
- the best agreement between the experimental data and the simulation results is achieved with the three-level grid approach.

The influence of the different refinement levels for the compute grid, i.e., c_1 and c_{max}, where the volume fraction of the solid phase is calculated and mapped to the fluid grid and the velocity of the solid phase determined, is depicted in Figure 4.9 for a total of 12 000, 14 000 and 17 000 particles.

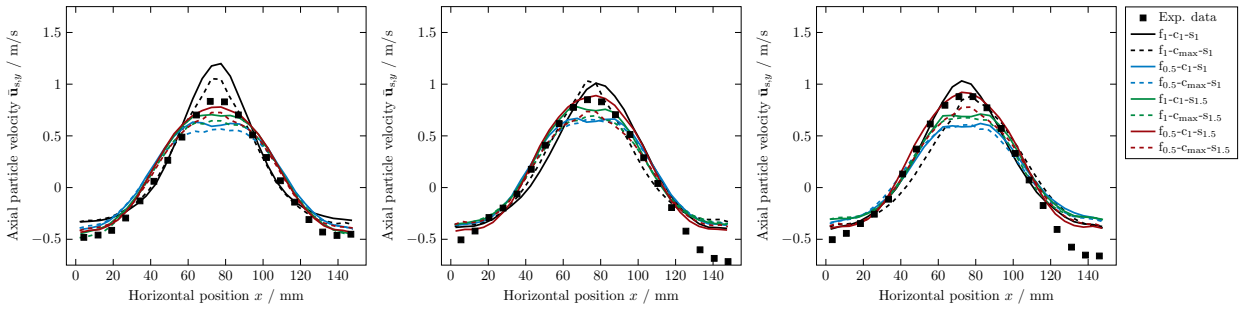

(a) 12 000 particles. **(b)** 14 000 particles. **(c)** 17 000 particles.

Figure 4.9: Comparison of the experimental axial particle velocity $\bar{\mathbf{u}}_{s,y}$ at a lateral height of $y = 100$ mm with simulation results with different compute grid sizes for a total of 12 000, 14 000 and 17 000 particles.

The best agreement between the experimental data and the simulation results can be achieved with the refinement levels of $f_{0.5}$-c_1-$s_{1.5}$. A refinement level of $f_{0.5}$-c_{max}-$s_{1.5}$, i.e., a cell to particle diameter ratio of 1.6 for the compute grid cells, show a slightly worse accuracy. For most cases the maximum refinement of the compute grid (c_{max}) results in a decrease of the maximum axial particle velocity in the core area. Comparing the single-grid (f_1-c_1-s_1) and the dual-grid approach with a maximum compute grid refinement (f_1-c_{max}-s_1), it is seen, that for all cases the refinement increases the accuracy and the experimental data is better depicted. However, an increase in cell-resolution for the compute grid does not always lead to a better accuracy in this particular case.

4.3.1.0.2 Fluidized bed with CG

The fluidization behavior and bubble dynamics in a 3D cylindrical fluidized bed was investigated by Penn et al. [245] using magnetic resonance imaging (MRI). Two different sized particles of $d_\mathrm{p} = 1$ and 3 mm with three different initial bed heights of $H_0 = 100$, 150 and 200 mm were fluidized with up to five different inlet velocities having a velocity to minimum fluidization velocity ratio of $\mathbf{u}_\mathrm{f}/\mathbf{u}_\mathrm{mf} = 1.2$, 1.5, 2, 3 and 4. The fluid used was air at ambient conditions. Here, for validation purposes, we are comparing the results of our simulations with the fluidized particles with a diameter of 1 mm. With the greatest settled bed height of 200 mm resulting in a total number of particles of close to seven million, it is obvious that a common CFD-DEM simulation would not be feasible. Therefore, the CG approach with a factor of four will be applied, i.e., 64 particles are considered as one parcel. Table 4.3 shows the simulation parameters used in the following. Due to the CG approach, the maximum number of tracked parcels can be reduced to approximately 100 000, which is in a reasonable range for a CFD-DEM simulation.

Table 4.3: Simulation parameters and properties used for the fluidized bed experiment of Penn et al. [245].

Property	Value
Particle diameter $d_\mathrm{p,CG}$ / mm	4
CG factor	4
Number of particles $n_\mathrm{p,CG}$	54 150, 81 225 and 108 300
Particle density ρ_p / kg/m^3	1040
Settled bed height H_0 / mm	100, 150 and 200
Fluid phase	ambient conditions
Inlet velocity ratios $\mathbf{u}_\mathrm{f}/\mathbf{u}_\mathrm{mf}$ / m/s	1.2, 1.5, 2, 3 and 4
Velocity at mf $\mathbf{u}_\mathrm{mf}$ / m/s	0.25

Additional parameters and properties, e.g., the coefficient of restitution e or coefficient of friction μ were adapted from Penn et al. [245]. Before presenting and discussing the simulation results of the different multi-grid approaches, it should be noted, that the overall geometry for the compute grid was slightly extended, if the compute and solid grid differed in cell size. At some refinement levels, the bounding domain of the two grids will not overlap (cf. Figure S1), resulting in a potential incorrect mapping of particles between the solid and compute grid. Further details and an analysis on the low impact towards the simulations results, when increasing the geometry of the compute grid, is given in Figure S2 in the Supplementary Material. The same geometry changes apply for the validation case based on the experiment of Boyce et al. [246] regarding the single jet injection in an incipient fluidized bed.

A comparison of the simulation results using a single-grid approach (f_1-c_1-s_1) with the experimental data for three different initial settled bed heights is depicted in Figure 4.10.

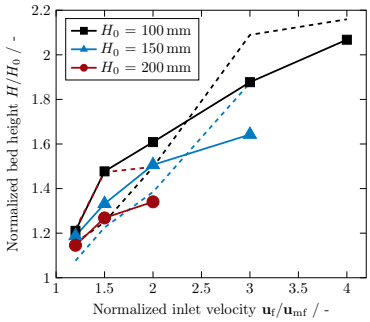

Figure 4.10: Simulation results of the normalized bed height H/H_0 with different normalized inlet velocities $\mathbf{u}_f/\mathbf{u}_{mf}$ for a single-grid approach (dashed lines) compared to the experimental data of Penn et al. [245] (marks and lines).

The simulations show an overall good agreement with the experimentally obtained normalized bed heights. The deviations between the normalized bed heights for an initial bed height of $H_0 = 150$ mm at higher inlet velocities are in comparison with the experimental data higher than with the other initial settled bed heights of $H_0 = 100$ and 200 mm. A qualitative comparison of the experimental data with the single-grid approach and various multi-grid approaches is depicted in Figure 4.11.

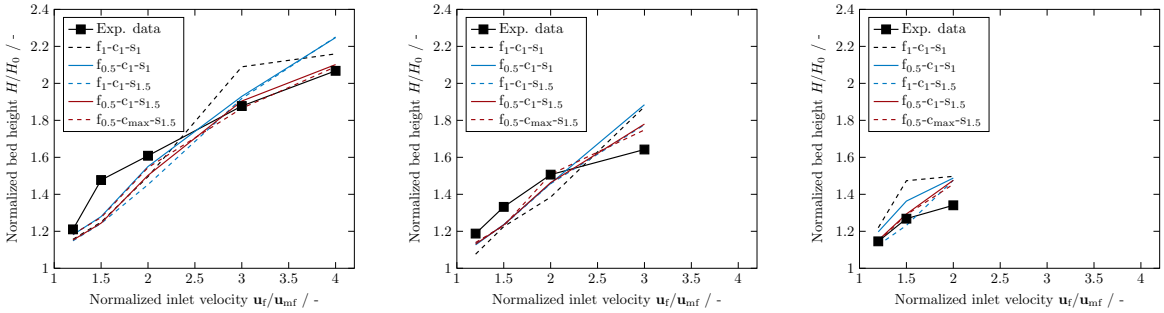

(a) $H_0 = 100$ mm. **(b)** $H_0 = 150$ mm. **(c)** $H_0 = 200$ mm.

Figure 4.11: Comparison of experimental values of Penn et al. [245] with simulation results from the single-grid (f_1-c_1-s_1), dual-grid and three-level grid approach with different refinement levels.

All single- and multi-level grid approaches slightly underpredict the resulting fluidized bed heights compared to the experimental finding obtained by Penn et al. [245] for lower inlet velocities, i.e., $\mathbf{u}_f/\mathbf{u}_{mf} \leq 2$, and initial bed heights of 100 and 150 mm. At higher inlet velocities, the single- and dual-grid approach overpredict the normalized bed height in the fluidization state, while the newly introduced three-level grid approach ($f_{0.5}$-c_1-$s_{1.5}$ and $f_{0.5}$-c_{max}-$s_{1.5}$) shows a very good agreement with the experimental data. Furthermore, for an initial settled bed height of 200 mm the best results are obtained using the three-level grid approach. The use of a dual-grid approach results in a reasonable increase in accuracy

for the fluidization behavior for all simulations, but with the introduction of a third numerical grid the best agreement towards the experimental data is achieved.

The deviations of the simulation results for various single-grid, dual-grid and three-level grid approaches from the experimental obtained normalized bed height H/H_0 at different initial settled bed heights and inlet velocities are listed in Table 4.4.

Table 4.4: Deviation of simulation from experimental data regarding the ratio of expanded bed height to initial height H/H_0 for the single-grid (S), dual-grid (D) and three-level grid approach (T).

		Type of grid		T	T	D	S	D
		H/H_0		Deviation simulation from exp. data				
			f	0.5	0.5	0.5	1	1
	$\lvert\mathbf{u}_f/\mathbf{u}_{mf}\rvert$	Exp. data	c	max	1	1	1	1
			s	1.5	1.5	1	1	1.5
$H_0 = 100\,\text{mm}$	1.2	1.21		2.1 %	2.1 %	2.4 %	4.5 %	2.3 %
	1.5	1.48		13.9 %	13.9 %	15.5 %	15.6 %	13.8 %
	2.0	1.61		4.2 %	4.0 %	3.8 %	6.8 %	4.7 %
	3.0	1.88		1.2 %	1.1 %	2.5 %	10.6 %	1.9 %
	4.0	2.07		0.7 %	2.0 %	3.1 %	4.1 %	2.6 %
$H_0 = 150\,\text{mm}$	1.2	1.19		4.1 %	4.8 %	5.1 %	9.4 %	4.4 %
	1.5	1.33		7.7 %	7.3 %	7.2 %	8.0 %	7.4 %
	2.0	1.51		0.1 %	2.9 %	3.1 %	8.1 %	3.3 %
	3.0	1.64		6.4 %	8.4 %	14.7 %	14.1 %	8.1 %
$H_0 = 200\,\text{mm}$	1.2	1.15		0.1 %	0.5 %	4.5 %	6.4 %	1.8 %
	1.5	1.27		1.7 %	2.0 %	7.5 %	16.2 %	2.9 %
	2.0	1.34		8.5 %	10.1 %	11.0 %	11.7 %	10.1 %

The use of a single-grid approach (f_1-c_1-s_1) shows the worst agreement towards the experimental data compared to a dual-grid and three-level grid method. Refining the fluid grid or coarsening the solid grid increases the accuracy of the simulation results, but in most cases the coarsening of the solid grid has a more beneficial effect than the refinement of the fluid grid. The simultaneous refinement of the fluid grid and coarsening of the fluid grid with maintaining the compute grid as is, i.e., $f_{0.5}$-c_1-$s_{1.5}$ and $f_{0.5}$-c_{max}-$s_{1.5}$, show a synergistic effect in improving further the accuracy and therefore lowering the deviation of the simulation results from the experimental data. All these observations are in accordance to the findings of the analysis of the jet-in fluidized bed benchmark case. Furthermore, the refinement of the compute grid up to the recommendations of Peng et al. [226] ($f_{0.5}$-c_{max}-$s_{1.5}$) has in almost all investigated cases a slightly better agreement in terms of accuracy towards the experimental data compared to the non refined compute

grid ($f_{0.5}$-c_1-$s_{1.5}$). However, the highest improvement of the accuracy can be contributed to the coarsening of the solid grid.

4.3.1.0.3 Single jet injection in an incipient fluidized bed with CG

The experimental set-up as used by Penn et al. [245] was used by Boyce et al. [246] and extended with a single jet injection hole. While the particles were fluidized, a single jet of air at ambient conditions was injected (cf. Figure 4.5c) and the bubble dimensions and dynamics were recorded. Table 4.5 gives an overview of the used simulation parameters. Analogous to the simulations validated with the experimental set-up by Penn et al. [245] a CG factor of $f_{\mathrm{CG}} = 4$ is used to reduce the computational costs. The number of cells for each of the following simulations is listed in Table S2.

Table 4.5: Simulation parameters and properties used for the single jet injection in an incipient fluidized bed by Boyce et al. [246].

Property	Value
Particle diameter $d_{\mathrm{p,CG}}$ / mm	4
CG factor	4
Number of particles $n_{\mathrm{p,CG}}$	108 300
Particle density ρ_{p} / kg/m^3	1040
Settled bed height H_0 / mm	200
Fluid phase	ambient conditions
Background velocity $\mathbf{u}_{\mathrm{bg}}$ / m/s	0.25
Single jet velocity $\mathbf{u}_{\mathrm{jet}}$ / m/s	52 and 85

Figures 4.12 and 4.13 show snapshots of the fountain in the fluidized of the experimental set-up and the simulations with different multi-grid approaches and refinements of each grid for jet velocities $\mathbf{u}_{\mathrm{jet}} = 52$ and $85\,\mathrm{m/s}$.

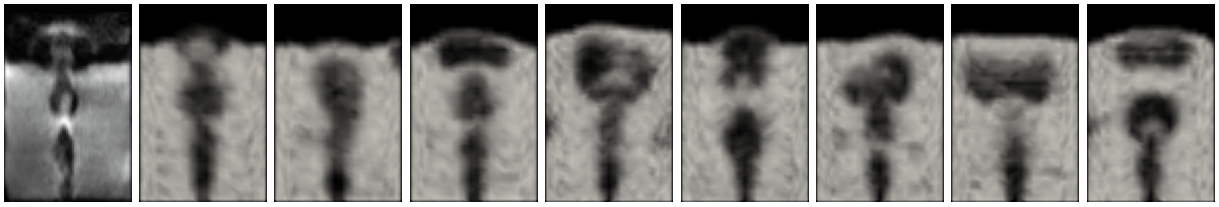

(a) Exp. (b) f_1-c_1-s_1 (c) $f_{0.5}$-c_1-s_1 (d) f_1-c_1-$s_{1.5}$ (e) $f_{0.5}$-c_1-$s_{1.5}$ (f) f_1-c_{max}-s_1 (g) $f_{0.5}$-c_{max}-s_1 (h) f_1-c_{max}-$s_{1.5}$ (i) $f_{0.5}$-c_{max}-$s_{1.5}$

Figure 4.12: Instantaneous snapshots of single jet and bubble eruption in an incipiently fluidized bed with a jet velocity of $\mathbf{u}_{\mathrm{jet}} = 52\,\mathrm{m/s}$ for the experiment by Boyce et al. [246] (a). The simulations are performed various multi-grid approaches (b) to (i).

In the experiments for both jet velocities, a narrow fountain is generated with bubbles forming and bursting when approaching the freeboard. An increase in the jet velocity

results into an increase in bubble size in the fountain area. The simulations show qualitatively similar fountain shapes in the mid region. Furthermore, bubbles are also formed and begin to burst near the freeboard in accordance to the experimental observations by Boyce et al. [246]. The experimental size of the bubble just after the breakoff from the jet and deviation from the simulation results are presented in Table 4.6.

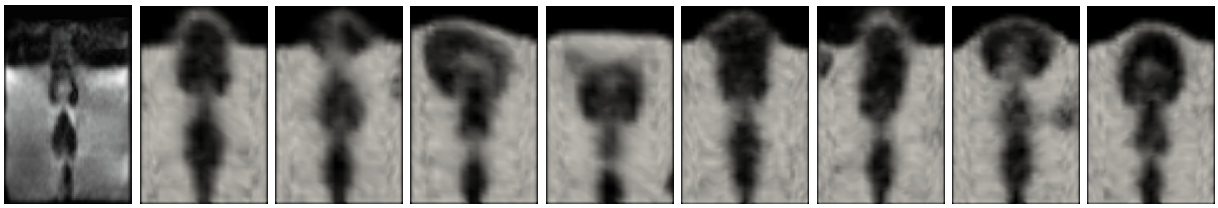

(a) Exp. (b) f_1-c_1-s_1 (c) $f_{0.5}$-c_1-s_1 (d) f_1-c_1-$s_{1.5}$ (e) $f_{0.5}$-c_1-$s_{1.5}$ (f) f_1-c_{max}-s_1 (g) $f_{0.5}$-c_{max}-s_1 (h) f_1-c_{max}-$s_{1.5}$ (i) $f_{0.5}$-c_{max}-$s_{1.5}$

Figure 4.13: Instantaneous snapshots of single jet and bubble eruption in an incipiently fluidized bed with a jet velocity of $\mathbf{u}_{\text{jet}} = 85\,\text{m/s}$ for the experiment by Boyce et al. [246] (a). The simulations are performed various multi-grid approaches (b) to (i).

At first, it is seen that the coarse grain approach shows a good agreement between the experimental and simulation results. The used CG factor of $f_{\text{CG}} = 4$ can be used for this specific setup to increase the simulation speed whilst still maintaining a reasonable accuracy. In accordance to the visual observations, the bubble size in the experiments increased with higher jet velocities $\mathbf{u}_{\text{jet}}$. The single grid approach (f_1-c_1-s_1) shows the highest deviation from the experimental results of 28.9 % and 24.3 % for jet-velocities of 52 and 85 m/s, respectively. A refinement of the compute-grid (f_1-c_{max}-s_1) results in a slight decrease in the deviation towards the experimental bubble size. Better results can be achieved with refining the fluid grid and coarsening the solid grid, i.e., $f_{0.5}$ and $s_{1.5}$. The best agreement between experiment and simulation is obtained with a simultaneously refinement and coarsening of the fluid and the solid grid, respectively, resulting in a deviation of less than 5 %. A change of the cell size of the compute grid for those particular cases has a negligible effect on the accuracy. A comparison of the deviations for the multi-grid approach while varying the grid sizes of the compute grid, i.e., f_x-c_1-s_y and f_x-c_{max}-s_y, shows an overall improvement of the simulation results when applying a finer compute grid (c_{max}) with the exception of the multi-grid approaches of $f_{0.5}$-$s_{1.5}$ and f_1-$s_{1.5}$ at a jet velocity of $\mathbf{u}_{\text{jet}} = 52\,\text{m/s}$. A comparison between the multi-grid approaches, if either the fluid grid is refined ($f_{0.5}$) or the solid grid is coarsened ($s_{1.5}$) reveals that better results are obtained when using a coarsened solid grid instead of a finer fluid grid in accordance to the findings of Alobaid et al. [227]. This effect is mostly attributed to the better accuracy in determining and calculating the momentum exchange coefficient β for the fluid-solid coupling in the momentum balance.

Table 4.6: Deviation of simulation from experimental data regarding the bubble volume V_{bub} for the single-grid (S), dual-grid (D) and three-level grid approach (T).

	Type of grid		T	T	D	T	D	T	S	D
	Exp. data		Deviation simulation from exp. data							
$\lvert\mathbf{u}_{\text{jet}}\rvert$ / m/s	V_{bub} / $10^{-5}\,\text{m}^3$	f	0.5	0.5	0.5	0.5	1	1	1	1
		c	1	max	1	max	1	max	1	max
		s	1.5	1.5	1	1	1.5	1.5	1	1
52	2.56		3.4 %	4.1 %	19.6 %	13.3 %	8.6 %	10.6 %	37.5 %	28.9 %
85	3.79		0.3 %	1.4 %	32.9 %	11.2 %	6.1 %	4.9 %	25.3 %	24.3 %

4.3.2 Simulation speed

Using an additional grid for numerical simulations always involves an increase in simulation time and resources, as important parameters must be mapped from one mesh to another. To quantify the additional simulation time needed with the implementation of a dual-grid and three-level grid method, several cases are set-up and investigated in terms of execution time used by the mapping process (compute grid), the calculation of the Lagrangian equations (solid grid) and the Eulerian equations (fluid grid). Figure 4.14 shows the simulation times needed for the jet-in fluidized bed case by Buijtenen et al. [244] using five different grid-approaches, i.e., single-, dual-grid and three-level grid approach, for a total number of 12 000 and 17 000 particles.

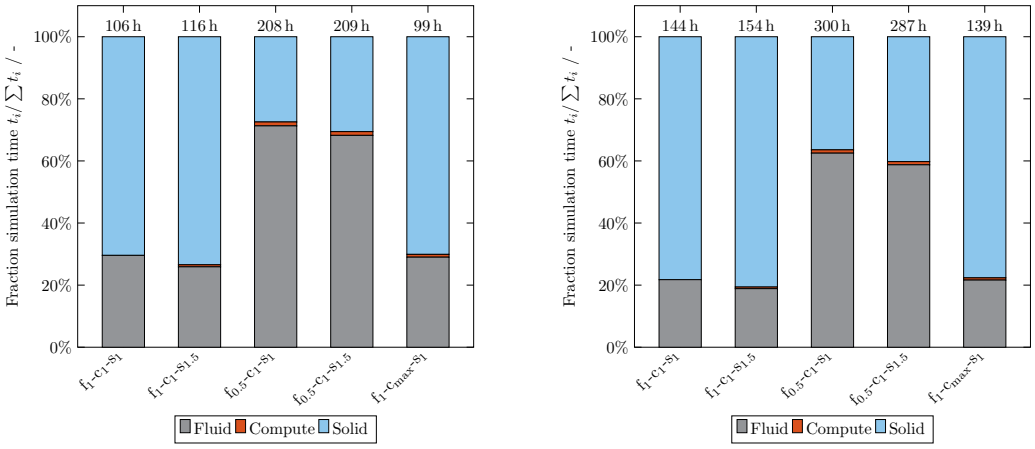

(a) 12 000 particles **(b)** 17 000 particles

Figure 4.14: Resulting fractions of simulation times for the fluid, compute and solid grid to the total simulation time $t_i/\sum t_i$ based on the jet-in fluidized bed with 12 000 and 17 000 particles with different single-, dual-grid and three-level grid approaches.

It is obvious, that the simulation time increases with a higher number of particles due to the greater workload of the Lagrangian calculations. The execution time for the mapping procedures (*compute*) is zero for the single-grid f_1-c_1-s_1 and for the dual-grid and three-level grid approaches the time needed is negligible compared to the Eulerian (*fluid*) and Lagrangian (*solid*) calculations. The amount of the mapping time depends on the number of particles in the system and the cells of the fluid grid. Therefore, with an increase in total particles and a refinement of the fluid grid (cf. $f_{0.5}$-c_1-s_1 for 17 000 particles) the time needed to transfer properties is greatest, but still marginal compared to the simulation times for the Eulerian and Lagrangian calculations. The fractions of the time needed to map all necessary properties to the total simulation time is between 0.5 and 1.7 %. The refinement of the fluid grid from 1 to 0.5 results in a massive increase of the simulation time due to the increased workload of the Eulerian calculations caused by the higher number of cells of said fluid grid. In these simulations the time-step was set

to a constant value, as in this specific cases the Co number did not exceed the numerical stability criterion being a value of one. But a greater refinement of the numerical grid for the calculation of the fluid phase can result in an additional large decrease in simulation speed due to not only the increasing number of computational cells, but a potentially needed decreased time-step. The smaller time-step originates from the dependency of the Co number from the cell size. In order to assure a constant Co number with smaller cells, the time step has to decrease as well (cf. Equation (4.50)) and the simulation speed therefore slows down. Especially for multiphase flows with high velocities the time-step needs to be adjusted to assure the numerical stability of $Co \leq 1$.

4.4 Conclusion

A conventional CFD-DEM simulation for gas-solid flow using a single-grid for the Eulerian and the Lagrangian equations was compared to a dual-grid method and a newly proposed three-level approach with the introduction of another numerical grid. Different experimental gas-solid flows, a 2D jet-in fluidized bed, a 3D cylindrical fluidized bed and a 3D cylindrical fluidized bed with a single jet, were used to validate the simulation results. Several conclusions can be made:

- the use of a multi-grid approach compared to a single-grid method results in an increase in accuracy,
- in most cases the three-level grid approach depicts the experimental data better than the dual-grid approach,
- when using a multi-grid approach, a coarsening of the Lagrangian grid results in a greater improvement in accuracy than the refinement of the Eulerian grid,
- the increase in simulation time due to the additional mapping subroutines in a multi-grid approach is negligible,
- with the use of the coarse grain method, the simulation time can be drastically reduced while still maintaining a suitable cell size for CFD-DEM simulations and
- the limiting factor of the multi-grid approach regarding simulation time is the degree of refinement of the Eulerian grid.

The set-up of a CFD-DEM simulation using a multi-grid approach requires a longer time, especially for the determination of suitable numerical grids, as two or three numerical grids have to be chosen. The necessary time needed to map the properties between the different grids is dependent on the number of particles and the number of cells of the fluid grid. An inadequate choice of the Eulerian grid can result in an enormous increase in simulation time with only a slight improvement of the accuracy. Still, the use of a multi-grid approaches is a promising tool to further increase the accuracy for dense solid flow simulations when larger particles are present. The use of more sophisticated methods for the transformation of Lagrangian values to Eulerian field values, e.g., porous cube model or diffusion-based model, with the use of the multi-level grid approach can be further investigated in terms of improvement in accuracy and change in simulation speed.

Further applications, e.g., the consideration of temperature changes or other parameters, can be made and if needed, calculated on different numerical grids. Therefore, the multi-grid approach is not limited to a two- or a three-level grid approach. The extension of this approach to polydisperse or cohesive particles is also possible. The simulation of bidisperse particles has already been done by Farzaneh et al. [231]. Hence, the polydispersity with a wide range of particle diameters shall be possible with the introduction of several grids for predefined particle diameter ranges.

Acknowledgments

D. Hirche is thankful for the support from TUM Graduate School.

Supplementary Material

Effect of geometry enlargement

The alteration of the number of numerical cells in a cylindrical geometry results for many cases in a change in local extension of the numerical cells in radial direction. Figure S1 illustrates this issue, where the *solid grid* consists of a lesser number of numerical cells, i.e., bigger cells than the *compute grid*. A magnified segment of the left side of the cylinder top view for both grids shows that the *compute grid* has a slightly higher local extension of the boundary in the numerical grid compared to the *solid grid*. When using a mapping

algorithm involving the transfer of particle properties in a Lagrangian simulation, it is possible that the position of the mapped particles of the source geometry cannot be transferred to the target geometry as the spatial boundaries do not always coincide. To overcome this issue, the geometry of the target (*compute grid*) was slightly extended. An increase of 0.2 % of the geometry in each spatial direction showed sufficient improvement to resolve this issue.

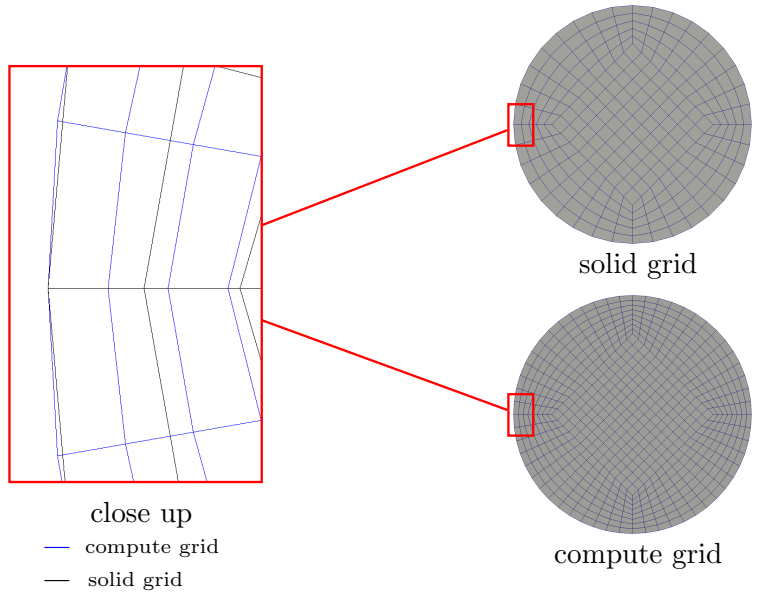

Figure S1: View on top of numerical grid for the 3D cylindrical geometry for the solid and *compute grid* (right) and close up with indicated numerical cells (left).

Possible effects of the geometry enlargement for the compute grid were further studied to quantify the error introduced by this necessary procedure. Therefore, two set-ups were used. As a base case the 3D cylindrical fluidized bed by Penn et al. [245] with a CG factor of four was taken and the numerical refinement or coarsening were specified in accordance to the case of f_1-c_1-s_1. The geometry of one grid was not enlarged (old mesh) and the other one was enlarged by a factor of 0.2 % in each spatial direction. Figure S2 depicts the resulting time-averaged volume fractions of the solid phase $\bar{\alpha}_s$ at different heights y = 50, 75 and 100 mm from the old mesh and the enlarged geometry (new mesh).

A symmetrical behavior is observable for all solid volume fractions and axial heights. Only slight deviations are obvious between the old and the new mesh. Therefore, it can be concluded that the enlargement of the compute grid by 0.2 % in the radial direction shows no significant impact on the fluid and solid phase flow. The enlargement with this factor can be used to overcome the issue of possible falsely mapped particle positions from the solid to the compute grid.

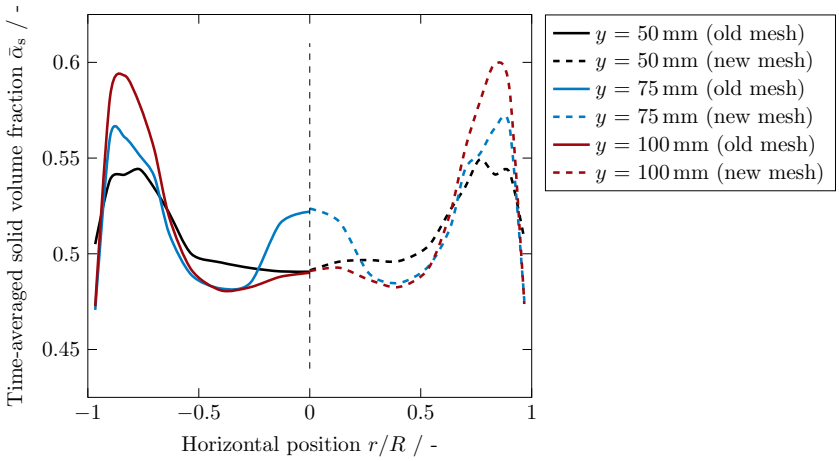

Figure S2: Resulting time-averaged volume fractions of the solid phase $\bar{\alpha}_s$ at different heights y from the old numerical grid (old mesh) and the by 0.2 % in radial direction enlarged geometry (new mesh).

Overview of numerical cells used

The number of numerical cells in each spatial direction, i.e., n_x, n_y and n_z for the number of cells in x-, y- and z-direction, used for the different numerical grids in the simulation are depicted in Table S1 for the jet-in fluidized bed by van Buijtenen et al. [244]. The *index number* represents the index of the simulation name, e.g., the number of cells in x-direction of the fluid grid in the simulation $f_{0.5}$-c_{max}-$s_{1.5}$ are 60, 36 and 20 for the fluid, compute and solid grid, respectively.

Table S1: Overview of the numerical cells for each simulation used for the jet-in fluidized bed by Buijtenen et al. [244].

Index number (mesh)	n_x	n_y	n_z	$\sum$
0.5	60	240	4	57 600
1	30	120	2	7200
1.5	20	80	1	1600
max	36	120	2	8640

Table S2 shows the number of cells used for the 3D cylindrical fluidized bed from Penn et al. [245] and the 3D cylindrical incipient fluidized bed with a single jet from Boyce et al. [246]. As opposed to Table S1, here, the spatial direction for x and y correspond to the inner cuboid according to Figure S1.

Table S2: Overview of the numerical cells for each simulation used for the 3D cylindrical fluidized bed from Penn et al. [245] and the 3D cylindrical incipient fluidized bed with a single jet from Boyce et al. [246].

Index number (mesh)	n_x [a]	n_y [a]	n_z [b]	$\sum$ [c]
0.5	18	18	67	79 596
1	9	9	33	9801
1.5	6	6	22	2904
max	14	14	54	37 800

[a] Number of cells referring to inner cuboid (cf. Figure S1).
[b] Number of cells in z-direction for whole geometry
[c] Total number of cells for whole geometry.

5 CFD-DEM study of an AnFMBR for fouling mitigation

Abstract

An anaerobic fluidized bed membrane bioreactor (AnFMBR) with granular activated carbon (GAC) particles as a scouring material was numerically investigated with the use of a CFD-DEM approach. After validation of the numerical solver, two different shapes of impediments, i.e., linear decreasing of the gap and linear de-/increasing of the gap, with variable impediment lengths were introduced to the geometry. The effects of built-in impediments, different fluid inlet velocities and particle sizes on the hydrodynamics, resulting particle momentum and required power input were evaluated and compared to the reactor geometry without an impediment. The disadvantage of reactor geometry without an impediment, i.e., the non-uniform distribution of particle momentum across the height, can be compensated with the use of built-in impediments depending on the fluid inlet velocity, particle diameter and impediment lengths. Furthermore, with the introduction of impediments the maximum achievable particle momentum can be increased or the optimum of particle momentum in regards to the power input can be shifted towards lower power inputs. The latter case is especially important for collisional- and scouring-sensitive membranes. The most promising effect towards particle momentum in terms of uniform distribution and magnitude was observed with small scouring particles (1.25 and 1.55 mm) for both impediments.

Bibliographic Information

D. Hirche, J.W. Chew, O. Hinrichsen, "CFD-DEM study of geometry changes in an AnFMBR towards particle momentum", *Chemical Engineering Journal* **2020**, *379*, 122336.

Copyright Notice

CFD-DEM study of geometry changes in an AnFMBR towards particle momentum

Author: Daniel Hirche,Jia Wei Chew,Olaf Hinrichsen

Publication: Chemical Engineering Journal

Publisher: Elsevier

Date: 1 January 2020

Journal Author Rights

5.1 Introduction

The importance of wastewater treatment has risen in the past years, especially with the use of anaerobic membrane bioreactor (MBR) technology. One of the most problematic issues in membrane bioreactors and for a continuous operation is the occurring fouling on the membrane [247] as the membrane flux decreases, i.e., lower throughput of filtrated water, or the transmembrane pressure (TMP) increases [248]. The latter results in a higher energy requirement for the filtration process. The reasons for the clogging of the membrane are mostly due to hydrodynamic forces, while the thermodynamic forces are attributed to the cause of the foulant adhesion onto the membrane [249]. Furthermore, it was shown experimentally that the chemical potential difference between the permeate molecules and the particulate layer is mainly responsible for the strength of the fouling cake resistance [250] and this was later validated by Density Functional Theory (DFT) simulations [251]. Among others, fouling control depending on the type of fouling consists of chemical cleaning of the membrane, backwashing of the permeate and scouring by gas sparging or a solid scouring material [252, 253]. The fouling mitigation through gas sparging is caused due to shear force [254] and through solid scouring materials due to mechanical force. The fouling control with the use of a scouring material is realized by increasing the feed inlet velocity and generating a fluidized bed of the solid particles, e.g., in an anaerobic fluidized bed membrane bioreactor (AnFMBR). This is a more energy efficient way than gas sparging [255]. Since smaller particles acts as foulant and contribute to pore clogging and foulant cake deposition [256], the scouring material has to be at a bigger scale. Neoh et al. [257] concluded that an AnFMBR is an efficient way for wastewater treatment with a low energy requirement. Scouring materials used in literature were zeolites [42], polyethylene terephthalate (PET), powdered activated carbon (PAC), granular activated carbon (GAC) and others [255]. Depending on the material, the scouring agents can also have an additional positive effect on fouling mitigation due to adsorption of organics, e.g., GAC. The addition of GAC particles helps reducing membrane fouling and therefore long-term operability of an AnFMBR compared to chemical cleaning [258]. Kim et al. [259] showed that with the use of fluidized GAC particles, fouling was inhibited and the power consumption in a long term operation was lowered. Wang et al. [44] presented the effect of fluidized GAC particles on fouling mitigation and the resulting power consumption with a simple reactor geometry in an AnFMBR. Cahyadi et al. [46] investigated the hydrodynamics of said AnFMBR using a Eulerian-Eulerian approach. They found a direct impact on the particle momentum towards the fouling mitigation. However, a high value of particle momentum can cause damages to sensitive membranes due to scouring and abrasion of the particles [260]. The axial distribution of the particle momentum in respect to the membrane height was not uniform according to Cahyadi et al. [46]. A uniform distribution of the particle momentum is crucial for consistent fouling mitigation by the means of mechanical scouring. Experiments for the evaluation

of fouling mitigation with different reactor geometries were conducted, e.g. cylindrical [47], rectangular shape [35] or cross-flow [261], or with various reactor set-ups, e.g., single and staged AnFMBR [262]. More complex geometries for the alteration of the fluid dynamics are not found in literature. The alteration of the fluid dynamics has a direct impact on the particle movement in an AnFMBR and therefore on the fouling mitigation. The influence of the geometry especially with built-in impediments can be significant towards an economic and feasible wastewater treatment with an AnFMBR.

In the following the effect of an alteration of the reactor geometry towards the resulting particle momentum is studied in detail. First, the numerical methods for the Eulerian-Lagrangian approach and the used closure models for the simulation of an AnFMBR are stated. Different geometries with built-in impediments are presented and four different particles sizes of GAC ranging from 1.25 to 2.05 mm with different inlet velocities for fluidization of the particle bed are investigated. The results of the simulation, i.e., resulting particle momentum and required power input are presented leading to correlations for the different geometries. The particle momentum is assessed at different heights of the membrane as well as the total particle momentum acting on the whole membrane.

5.2 Methodology

5.2.1 Numerical Methods

The governing equation for a Eulerian-Lagrangian simulation are the continuity equation and the momentum balance for the fluid phase according to a Eulerian approach (cf. Equations (5.1) and (5.2)) and the equations for the lagrangian particle tracking (LPT). This approach is often called CFD-DEM (computational fluid dynamics coupled with discrete element method).

The Eulerian approach describes cell-averaged equations for the fluid phase:

$$\frac{\partial \varepsilon}{\partial t} + \boldsymbol{\nabla} \cdot (\varepsilon \, \mathbf{u}_\mathrm{f}) = 0 \tag{5.1}$$

$$\frac{\partial \left(\varepsilon \, \rho_\mathrm{f} \, \mathbf{u}_\mathrm{f}\right)}{\partial t} + \boldsymbol{\nabla} \cdot \left(\varepsilon \, \rho_\mathrm{f} \, \mathbf{u}_\mathrm{f} \, \mathbf{u}_\mathrm{f}\right) = -\varepsilon \, \boldsymbol{\nabla} p + \varepsilon \, \rho_\mathrm{f} \, \mathbf{g} + \boldsymbol{\nabla} \cdot \left(\varepsilon \, \overline{\overline{\tau}}_\mathrm{f}\right) + \mathbf{M}_\mathrm{f,s}. \tag{5.2}$$

The volume fraction of the fluid phase for Euler-Lagrange simulations ε is calculated with the total volume of particles in a specified cell and the volume of the cell itself according to Equation (5.3):

$$\varepsilon = 1 - \frac{1}{V_{\text{cell}}} \sum_{\forall \text{p} \in \text{cell}} V_{\text{p}}. \tag{5.3}$$

The viscous stress tensor is defined by Enwald et al. [53] as

$$\overline{\overline{\tau}}_{\text{f}} = \eta_{\text{f}} \left[\boldsymbol{\nabla} \mathbf{u}_{\text{f}} + (\boldsymbol{\nabla} \mathbf{u}_{\text{f}})^{\text{T}} \right] - \left(\zeta_{\text{f}} - \frac{2}{3} \eta_{\text{f}} \right) (\boldsymbol{\nabla} \cdot \mathbf{u}_{\text{f}}) \, \overline{\overline{I}}. \tag{5.4}$$

$\mathbf{M}_{\text{f,s}}$ defines the momentum exchange term between the fluid and particulate phase and is split up into an explicit and an implicit term due to numerical stability.

$$\mathbf{M}_{\text{f,s}} = \frac{\sum \mathbf{F}_{\text{f,p}}}{V_{\text{cell}} \left| \mathbf{u}_{\text{f}} - \mathbf{u}_{\text{s}} \right|} \cdot \mathbf{u}_{\text{f}} - \frac{\sum \mathbf{F}_{\text{f,p}}}{V_{\text{cell}} \left| \mathbf{u}_{\text{f}} - \mathbf{u}_{\text{s}} \right|} \cdot \mathbf{u}_{\text{s}} \tag{5.5}$$

$\mathbf{u}_{\text{s}}$ is the cell-averaged velocity of the particles and is calculated according to

$$\mathbf{u}_{\text{s}} = \frac{1}{n_{\text{p}}} \sum_{\forall p \in cell} \mathbf{u}_{\text{p}}. \tag{5.6}$$

The total number of particles in a cell is given by n_{p} and the velocity of the respective particle by $\mathbf{u}_{\text{p}}$. The drag force $\mathbf{F}_{\text{d}}$ has the highest contribution to the exchange force between the fluid and particle $\mathbf{F}_{\text{f,p}}$ [97, 98]. The exchange force can be calculated with the momentum exchange coefficient β:

$$\mathbf{F}_{\text{f,p}} = \beta \left(\mathbf{u}_{\text{f}} - \mathbf{u}_{\text{p}} \right) \frac{m_{\text{p}}}{\rho_{\text{p}}}. \tag{5.7}$$

The density of the particulate phase is denoted with ρ_{p}. Many different correlations for the calculation of the momentum exchange coefficient are proposed in literature [84, 183, 188]. This work uses the drag correlation proposed by Gidaspow [15, 78] which is a combination of a correlation proposed by Ergun [168] and Wen and Yu [170]. The drag correlation proposed by Ergun is used for fluid volume fractions lower than 0.8, while the correlation from Wen and Yu is used for more dilute particle beds. The momentum exchange coefficient can be calculated according to the following equation:

$$\beta = \begin{cases} 150 \frac{(1-\varepsilon)^2 \eta_{\text{f}}}{\varepsilon d_{\text{p}}^2} + 1.75 \, (1-\varepsilon) \, \frac{\rho_{\text{f}}}{d_{\text{p}}} \left| \mathbf{u}_{\text{f}} - \mathbf{u}_{\text{p}} \right|, & \varepsilon < 0.8 \\ \frac{3}{4} \, C_D \frac{\varepsilon \, (1-\varepsilon)}{d_{\text{p}}} \, \rho_{\text{f}} \left| \mathbf{u}_{\text{f}} - \mathbf{u}_{\text{p}} \right| \varepsilon^{-2.65}, & \varepsilon \geq 0.8. \end{cases} \tag{5.8}$$

The drag coefficient C_D is dependent on the particle Reynolds number Re_p

$$C_\mathrm{d} = \begin{cases} \frac{24}{Re_\mathrm{p}} \left(1.0 + 0.15\, Re_\mathrm{p}^{0.687}\right), & Re_\mathrm{p} \leq 1000 \\ 0.44, & Re_\mathrm{p} > 1000 \end{cases} \tag{5.9}$$

with

$$Re_\mathrm{p} = \frac{\varepsilon\, d_\mathrm{p} \left|\mathbf{u}_\mathrm{f} - \mathbf{u}_\mathrm{p}\right| \rho_\mathrm{f}}{\eta_\mathrm{f}}. \tag{5.10}$$

The calculations for the lagrangian framework are based on Newton's second law of motion, specifically the force and torque balances. Particle-particle and particle-wall collision forces are modeled with a soft-sphere model [14, 119]. The detailed implementation of the lagrangian framework can be found in literature [243].

The virtual mass force $\mathbf{F}_\mathrm{vm}$ describes the force occurring when the added mass of the surrounding fluid phase of a particle is accelerated or decelerated [263, 264]. This force has a significant impact for liquid-solid fluidization simulations [265, 266] and can not be neglected. Zuber [103] proposed the following equation for the calculation of the virtual mass force:

$$\mathbf{F}_\mathrm{vm} = C_\mathrm{vm}\, V_\mathrm{p}\, \rho_\mathrm{f} \left(\frac{\mathrm{d}\mathbf{u}_\mathrm{f}}{\mathrm{d}t} - \frac{\mathrm{d}\mathbf{u}_\mathrm{p}}{\mathrm{d}t}\right). \tag{5.11}$$

The coefficient C_vm is commonly set to a value of 0.5 as proposed by Drew et al. [106] for non-deformable and spherical particles.

5.2.2 Geometry and Mesh

The geometry in the simulations is used according to the AnFMBR by Wang et al. [44]. For simplification purposes only the fluidized part of the AnFMBR is used as well as half of the reactor due to symmetry. Figure 5.1 illustrates the dimensions of the simulated AnFMBR-geometry with a total height of $H = 194\,\mathrm{mm}$. Figure 5.1b and c show the front and side view of the simulation geometry without a built-in impediment with the corresponding boundaries. The front and back side consists of the wall, the membrane holder and the active membrane. A symmetry of the reactor is chosen to reduce the simulation time. The sides of the AnFMBR are surrounded by walls. A uniform fluid inlet velocity is applied at the bottom, while the outlet has a fixed pressure condition at the top. The wall, membrane holder and active membrane areas have a no-slip condition for the fluid-flux and a partial slip condition for particles according to defined restitution and friction coefficients. Preliminary studies showed that the particle distribution across

the reactor height was not uniform. Thus, the geometry of the AnFMBR is modified. Impediments are introduced to alter the flow, both of the fluid and solid phase. Those impediments consist of an addition to the geometry with a uniform height of 154 mm and a variable horizontal length l_i. The horizontal lengths of the impediments are varied between 1, 3, 5 and 7 mm depending on the used GAC particle sizes, i.e., for an impediment length l_i of 7 mm the gap between the wall and membrane would be too narrow for particle sizes of 2.05 mm to pass through. Figure 5.2 shows exemplary the side views of the AnFMBR with two built-in impediments: Impediment 1 and 2. Impediment 1 consists of a linear decreasing gap to decrease the free cross-section (cf. Figure 5.2a) and therefore increases the fluid velocity. The smallest free cross-section of the geometry is reached at a height of 154 mm where the active membrane ends. The second impediment, Impediment 2, has a linear increasing narrowing up to a reactor height of 77 mm after which the narrowing decreases again with the same gradient until it reaches the reactor wall at a height of 154 mm (cf. Figure 5.2b). This set-up shall prevent a high degree of particle entrainment due to an increase in local fluid velocity. The grid size for the simulation is chosen to satisfy the condition of the volume of a single cell being greater than the particle volume [204]. Table 5.1 gives an overview of the dimensions of the geometries and the number of cells used in this study. Due to the inclined impediments the simulation of the flow has to be resolved in three dimensions, since the geometry consists of two mesh cells in the y-direction. The grid resolution can not be further refined or else the error of the calculation for the cell-averaged parameters, e.g., solid velocity or solid volume fraction, would be too high [267].

Table 5.1: Overview of geometry and mesh dimensions.

Geometry and Mesh	
height H / mm	194
width W / mm	89
depth D / mm	9
impediment height 1 h_1 / mm	154
impediment height 2 h_2 / mm	77
impediment length l_i / mm	1, 3, 5 and 7
mesh cells in x-direction	18
mesh cells in y-direction	2
mesh cells in z-direction	42

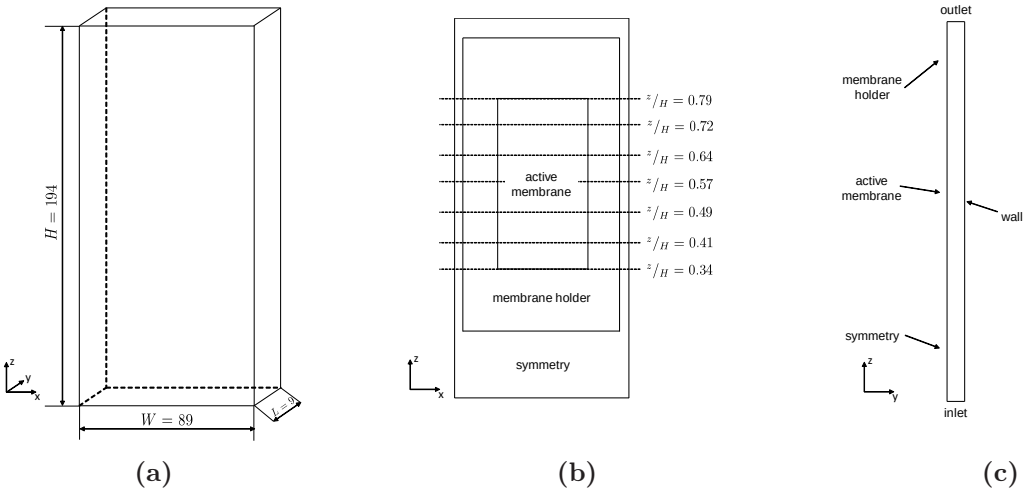

Figure 5.1: Isometric view of the geometry used in the current study (a), front view of geometry with active membrane (b) and side view of geometry with indication of boundaries (c).

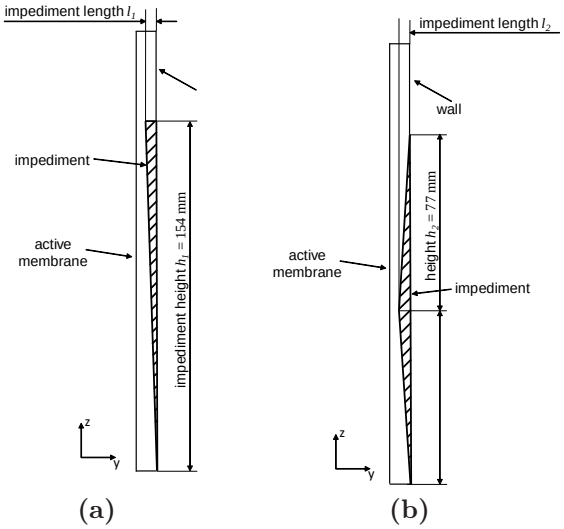

Figure 5.2: Side views of geometry with built-in impediments 1 (a) and 2 (b) with indicated impediment lengths l_i and heights h_i.

5.2.3 Simulation parameters

GAC particles are fluidized by a water feed with a uniform inlet velocity at ambient temperature and pressure. In this simulation four different diameters of GAC particles d_p, namely 1.25, 1.55, 1.85 and 2.05 mm are investigated in respect to the efficiency of membrane fouling mitigation, i.e., resulting particle momentum. Furthermore, the inlet velocity of the feed is varied to achieve particle velocities. The ratio of the actual inlet velocity and the velocity at minimum fluidization ${u_\mathrm{f}}/{u_\mathrm{mf}}$ is therefore used as an additional parameter to investigate the effect of the inlet velocities towards membrane

fouling mitigation. The velocity at minimum fluidization is dependent on the used particle diameter and is calculated according to a correlation by Wen and Yu [170] with the particle Reynolds number at minimum fluidization and Galileo number, $Re_{\mathrm{p,mf}}$ and Ga:

$$Re_{\mathrm{p,mf}} = \sqrt{33.7^2 + 0.0408\, Ga} - 33.7 \tag{5.12}$$

with the particle Reynolds number at minimum fluidization defined as

$$Re_{\mathrm{p,mf}} = \frac{\rho_{\mathrm{f}}\, d_{\mathrm{p}}\, u_{\mathrm{mf}}}{\eta_{\mathrm{f}}} \tag{5.13}$$

and the Galileo number as

$$Ga = \frac{d_{\mathrm{p}}^3\, \rho_{\mathrm{f}}\, \left(\rho_{\mathrm{p}} - \rho_{\mathrm{f}}\right) g}{\eta_{\mathrm{f}}^2}. \tag{5.14}$$

For all simulations a ${}^{u_{\mathrm{f}}}/_{u_{\mathrm{mf}}}$-ratio ranging from 3 to 11 is used. With greater impediment lengths and bigger particle sizes, i.e. $l_i \geq 5\,\mathrm{mm}$ and $d_{\mathrm{p}} \geq 1.85\,\mathrm{mm}$, only particles with a diameter of 1.25 and 1.55 mm are simulated to avoid blockage of the particles in the narrowest gap.

A modified version of the solver *DPMFoam* from the open source package OpenFOAM® [206] version 4.1 is used for the following simulations. The validity of the CFD-DEM solver and the simulation parameters are assured by comparing the simulation results with experimental data obtained by Wang et al. [44]. Therefore, the time-averaged cell based particle velocities at five different heights, namely at the height ratios at ${}^{z}/_{H} = 0.41$, 0.49, 0.57, 0.64 and 0.72 (cf. Figure 5.1b), are evaluated at different inlet feed velocities for particle sizes of 1.55 and 1.85 mm. The initial number of particles for the simulation is chosen according to the total mass of the particles in [44]. The foulant concentration in the experiments were 2 g/L Bentonite and 2 g/L Yeast in deionized water. The permeate flux was set to a value of $30\,\mathrm{L/(m^2\,h)}$ [44]. Since the permeate flux was insignificant low compared to the inlet fluidization velocity it was ignored in the following simulations. Figure 5.3 shows the comparison of the particle velocities for the simulations and the experimental data.

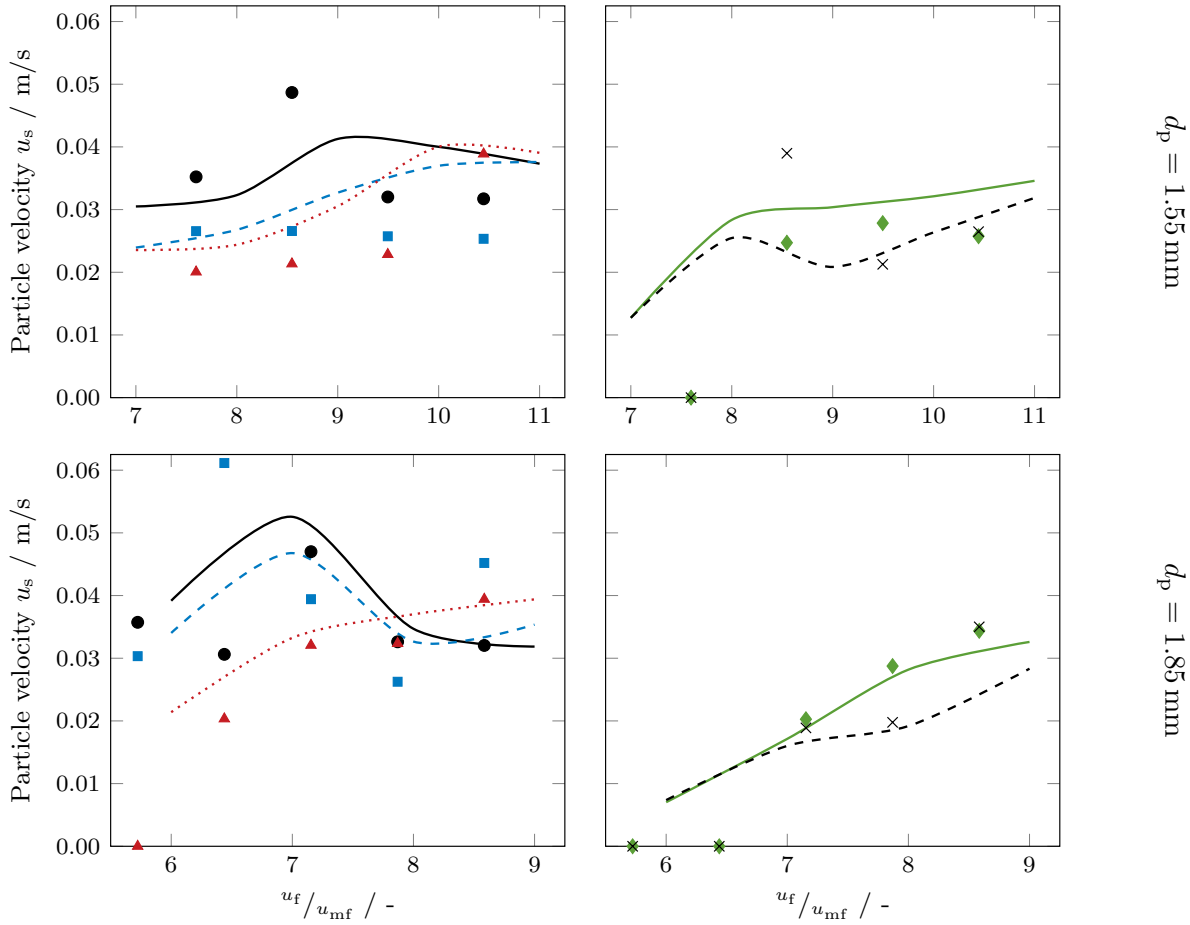

Figure 5.3: Comparison of particle velocity u_s for particle diameters of $d_p = 1.55$ and 1.85 mm. Symbols represent experimental data according to Wang et al. [44] and lines represent simulation results at the following AnFMBR height ratios z/H: 0.41 (— and ●), 0.49 (- - and ■), 0.57 (··· and ▲), 0.64 (— and ♦) and 0.72 (- - and ×).

The particle velocities differ with the particle diameter d_p and the velocity ratio u_f/u_{mf}. For a particle diameter of $d_p = 1.55$ mm the particle velocities for the simulations show an increase for increasing inlet velocities. At greater heights, $z/H \geq 0.72$, the particle velocity (experimental data) at lower feed velocities is zero, as the bed expansion has not reached the defined height. The overall trend of the particle velocities for the experimental data and the simulation results are in accordance. The same applies for a particle diameter $d_p = 1.85$ mm. At lower heights, i.e. $z/H \leq 0.49$, the particle velocities develop a maximum at a u_f/u_{mf}-ratio at approximately 7 for both experimental data and simulation results. With the comparison of the experimental data and the simulations it can be concluded that the CFD-DEM solver *DPMFoam* is validated for the here present liquid-solid fluidization.

For the following simulations the number of particles in the AnFMBR is not constant for all particle diameters considered in this work. The bed height for settled particles is assumed to be constant at a height of $h_s \approx 68$ mm with a porosity of $\varepsilon = 0.38$. The total

number of particles in the AnFMBR N_p can be calculated according to the following formula:

$$N_\mathrm{p} = \frac{V_\mathrm{s}}{V_\mathrm{p}} = \frac{(1-\varepsilon)\ h_\mathrm{s}\, L\, W}{{}^1\!/_6\, \pi\, d_\mathrm{p}^3}. \tag{5.15}$$

Table 5.2 gives an overview of the total number of particles used in the various simulations to achieve the desired settled bed height of 68 mm, as well as the simulation parameters and physical properties. Particles hitting the *outlet*-boundary will be removed from the simulation geometry and are not reintroduced. The time-steps are chosen to ensure a stable Courant-Friedrichs-Lewy criterion of $Co < 0.1$.

Table 5.2: Overview of parameters used in the simulation.

Fluid phase	
density ρ_f / kg/m^3	1000
kinematic viscosity ν_f / m^2/s	$1 \cdot 10^{-6}$
${}^{u_\mathrm{f}}\!/_{u_\mathrm{mf}}$-ratios / -	3 to 11
Particle	
density ρ_p / kg/m^3	1500
diameter d_p / mm	1.25, 1.55, 1.85 and 2.05
number of particles N_p / -	32 900, 17 250, 10 000 and 7500
particle-particle restitution coefficient e_pp / -	0.99
particle-particle friction coefficient μ_pp / -	0.3
particle-wall restitution coefficient e_pw / -	0.99
particle-wall friction coefficient μ_pw / -	0.3
turbulence model	standard k-ε [268]
time step fluid Δt_f / s	$1 \cdot 10^{-5}$
time step particle Δt_p / s	$1 \cdot 10^{-6}$

5.3 Results

To compare the data obtained from the simulations the key parameters are time-averaged in order to transfer the transient state of a fluidized bed to a quasi-stationary state. The key parameters consist of the volume fraction of the fluid phase ε, the velocity of the fluid and solid phase, $\mathbf{u}_\mathrm{f}$ and $\mathbf{u}_\mathrm{s}$, the pressure drop Δp and the magnitude of the cell-averaged particle momentum $|\mathbf{I}_\mathrm{s}|$. The cell-averaged particle momentum $\mathbf{I}_\mathrm{s}$ is calculated according to:

$$\mathbf{I}_\mathrm{s} = \sum_{\forall \mathrm{p} \in \mathrm{cell}} \mathbf{u}_\mathrm{p}\, m_\mathrm{p}. \tag{5.16}$$

The required power input is calculated with

$$P = |\mathbf{u}_\mathrm{f}|\, A\, \Delta p. \tag{5.17}$$

The key parameters are assessed at three different heights of the geometry, H_1, H_2 and H_3. They correspond to ${}^{z}/_{H}$-ratios of 0.34, 0.57 and 0.79 (cf. Figure 5.1b), i.e., the bottom, middle and top of the active membrane surface. This ensures the assessment of the particle momentum for different sections of the active membrane, especially if the active membrane surface is partially or fully covered by the fluidized bed.

The total simulated time for all studies is 150 s, while in the first five seconds the AnFMBR is filled with particles and the particles settle with no inlet velocity of the fluid. At the following 15 s the inlet velocity is set to a specific value to reach the previous defined ${}^{u_\mathrm{f}}/_{u_\mathrm{mf}}$-ratio. The remaining 130 s are used to time-average the key parameters to achieve the quasi-stationary state of the fluidized bed. Figure 5.4 compares the time-development of the area-averaged volume fraction of the fluid at a height of 50 mm for ${}^{u_\mathrm{f}}/_{u_\mathrm{mf}}$-ratios of 6 and 10. In the first five seconds the filling and settling take place and the volume fraction of the fluid decreases as the bed gets denser. Starting from the point of five seconds the fluid inlet velocity is set to the specific ${}^{u_\mathrm{f}}/_{u_\mathrm{mf}}$-ratio, the particles are fluidized and the volume fraction of the fluid increases. The gradient for the ${}^{u_\mathrm{f}}/_{u_\mathrm{mf}}$-ratio of 10 is higher compared to the ratio of 6 because the inlet velocity is higher and the bed becomes more dilute. After 20 s the volume fraction of the fluid for both values of the ${}^{u_\mathrm{f}}/_{u_\mathrm{mf}}$-ratios seem to fluctuate around a constant value. At this point the time-averaging is started. In order to obtain optimal results, the total time averaging frame for the later simulations is set to 130 s, for a total simulation time of 150 s, to obtain optimal results.

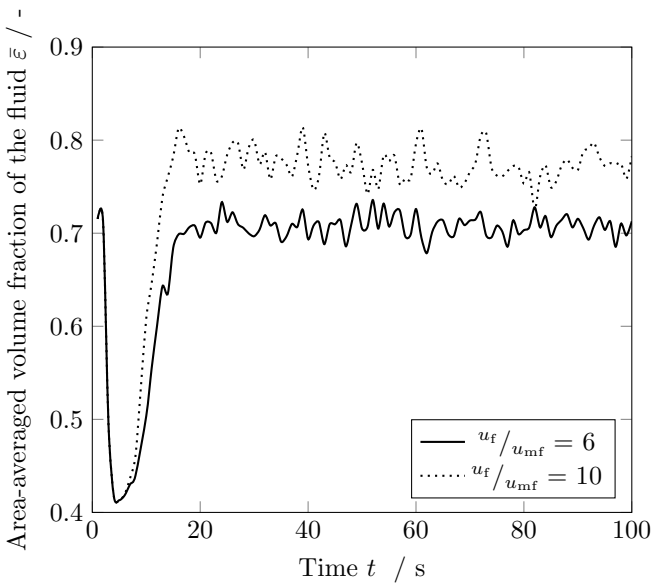

Figure 5.4: Area-averaged volume fraction of the fluid at a height of 50 mm over time for u_f/u_{mf}-ratios of 6 and 10. Time intervals between 0 - 5 s indicate the filling and settling process, 5 - 20 s the development of the fluidized state and the time-averaging frame starts at a time of 20 s.

The length of the cells in y-direction are not constant over the vertical direction as the gap between the active membrane and the wall decreases with increasing impediment lengths l_i. Therefore, the cell-averaged magnitude of the particle momentum $|\mathbf{I}_s|$ is normalized in respect to the cell volume V_{cell} to get a normalized particle momentum $|\mathbf{I}_s|_{norm}$:

$$|\mathbf{I}_s|_{norm} = \frac{|\mathbf{I}_s|}{V_{cell}}. \tag{5.18}$$

5.3.1 Resulting particle momentum at specific heights

To compare the normalized particle momentum at specific heights of the active membrane or the membrane itself, the total normalized particle momentum $\sum |\mathbf{I}_s|_{norm}$ is evaluated. Figure 5.5 shows the total normalized particle momentum at three different heights of the membrane, H_1, H_2 and H_3, for the reactor geometry with no built-in impediments and Impediment 1 with the specified impediment lengths l_1 for GAC particles with different diameters.

The following observations can be made for the resulting particle momentum at different u_f/u_{mf}-ratios for the geometry without an impediment:

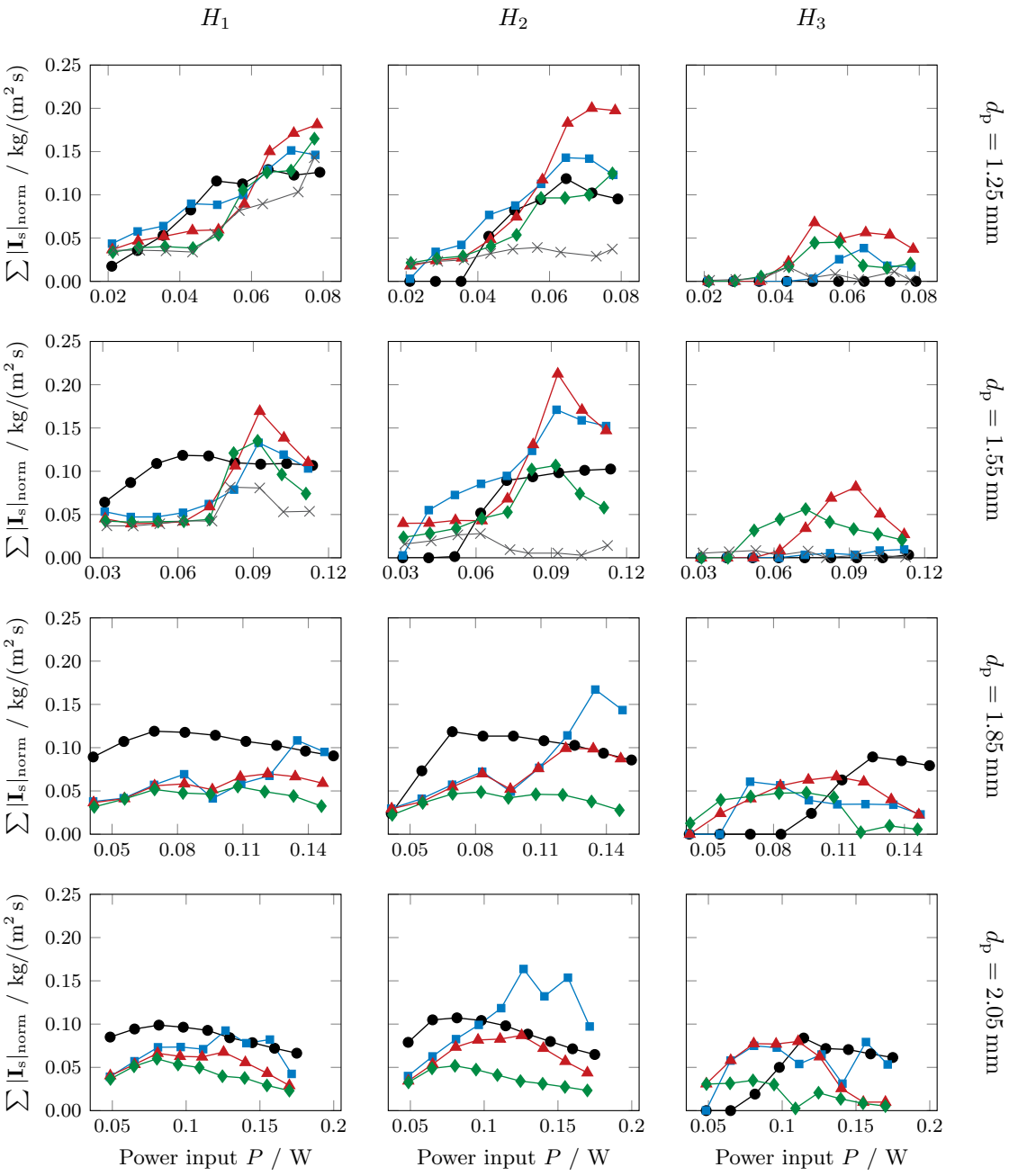

Figure 5.5: Comparison of cell-averaged normalized particle momentum (magnitude) $|\mathbf{I}_s|_{norm}$ with corresponding required power input P for particle diameters $d_p = 1.25$, 1.55, 1.85 and 2.05 mm assessed at different heights of the membrane H_1, H_2 and H_3. The different symbols correspond to the different impediment lengths of Impediment 1 (no impediment: ●, 1 mm: ■, 3 mm: ▲, 5 mm: ♦ and 7 mm: ×).

- a maximum for the particle momentum can be achieved at a specific power input with a small decline in particle momentum after the maximum is reached

- the maximum achievable particle momentum seems to be independent of the investigated height H_i

- the particle momentum is not uniformly distributed along the axial height of the membrane.

The effect of Impediment 1 on the resulting particle momentum can be summarized as followed:

- for $d_\mathrm{p} = 1.25\,\mathrm{mm}$: similar values for the particle momentum for low fluid inlet velocities compared to the geometry without an impediment and the particle momentum is still increasing at higher fluid inlet velocities

- for the other particle diameters: a maximum for the particle momentum is reached at a specific power input and is in most cases higher or almost equal to the value obtained without an impediment

- the particle momentum has a non-zero value at higher heights and at lower power inputs compared to no impediment

- an impediment length of $l_1 = 7\,\mathrm{mm}$ yields the lowest particle momentum for all heights and particle diameters.

The results for the AnFMBR with a built-in impediment according to the geometry of Impediment 2 are shown in Figure 5.6 for different power inputs, particle diameters and impediment lengths.

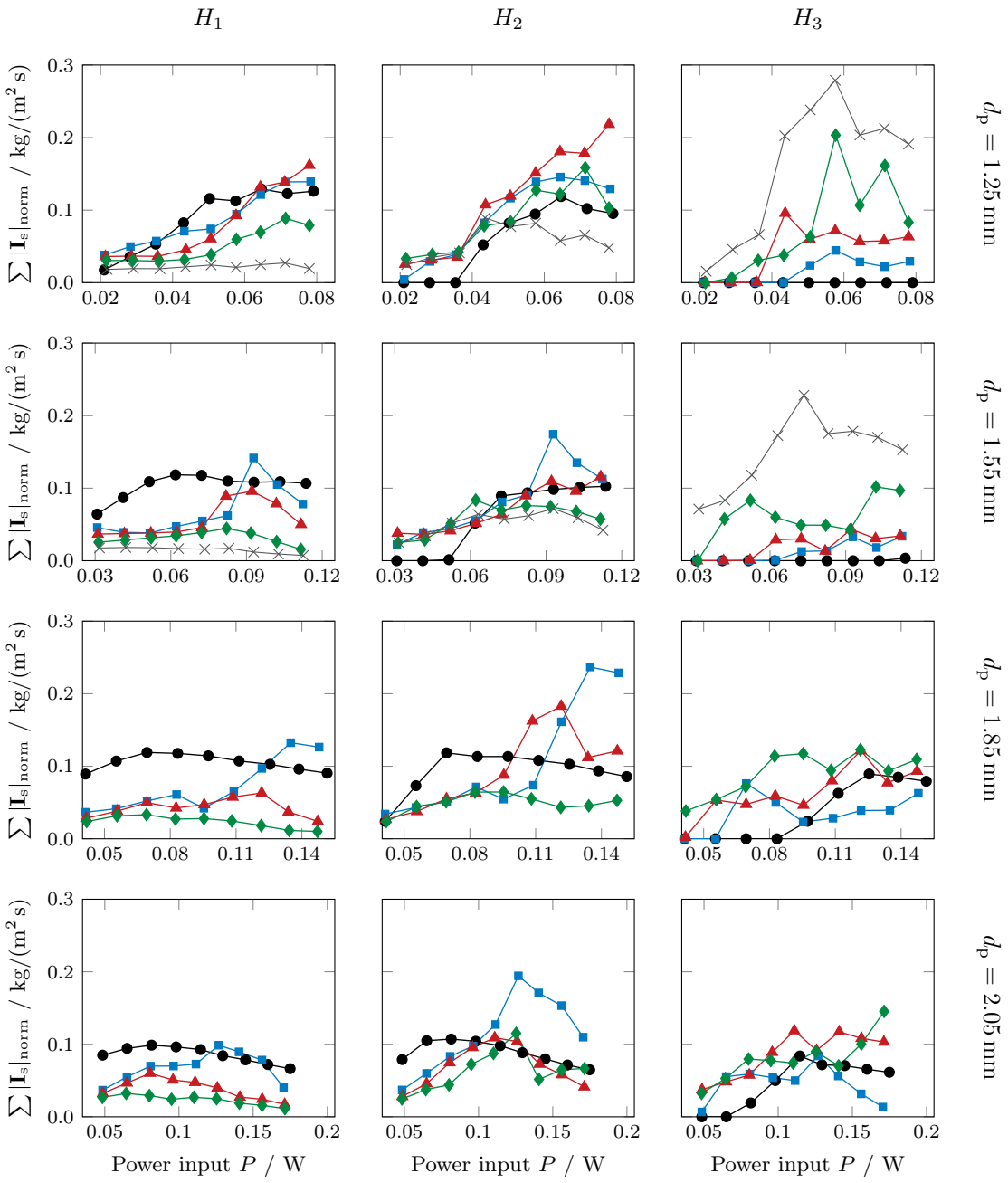

Figure 5.6: Comparison of cell-averaged normalized particle momentum (magnitude) $|\mathbf{I}_s|_{norm}$ with corresponding required power input P for particle diameters $d_p = 1.25$, 1.55, 1.85 and 2.05 mm assessed at different heights of the membrane H_1, H_2 and H_3. The different symbols correspond to the different impediment lengths of Impediment 2 (no impediment: ●, 1 mm: ■, 3 mm: ▲, 5 mm: ♦ and 7 mm: ×).

Impediment 2 shows the same effect on the particle momentum as Impediment 1 for a particle diameter of 1.25 and 1.55 mm for an impediment length of 1 and 3 mm. Furthermore the following can be observed:

- with greater impediment lengths, the particle momentum at height H_3 for higher fluid inlet velocities is higher than with Impediment 1 or without an impediment, but at lower parts of the active membrane the particle momentum tends to a value of zero

- more uniform particle momentum across the membrane heights for particle sizes of 1.85 and 2.05 mm at lower fluid inlet velocities

- highest achievable particle momentum at H_2.

An overview of the findings regarding the geometries with no built-in impediment, Impediment 1 and Impediment 2 regarding the resulting particle momentum at different heights of the membrane is summarized in Table 5.3.

Table 5.3: Summary of investigated reactor geometries with effect of particle momentum at different membrane heights.

d_p / mm	no impediment	Impediment 1	Impediment 2
1.25	no uniform distribution of $\lvert\mathbf{I}_\mathrm{s}\rvert$, at H_3 no resulting $\lvert\mathbf{I}_\mathrm{s}\rvert$	higher $\lvert\mathbf{I}_\mathrm{s}\rvert_\mathrm{max}$ for $l_1 =$ 1, 3 and 5 mm, more uniform distribution at 0.05 W for $l_1 =$ 3 and 5 mm	same as Impediment 1, better performance for $l_2 = 7$ mm
1.55	no uniform distribution of $\lvert\mathbf{I}_\mathrm{s}\rvert$, at H_3 no resulting $\lvert\mathbf{I}_\mathrm{s}\rvert$	higher $\lvert\mathbf{I}_\mathrm{s}\rvert_\mathrm{max}$ for $l_1 =$ 1 and 3 mm, more uniform distribution at 0.08 W for $l_1 =$ 3 and 5 mm	less $\lvert\mathbf{I}_\mathrm{s}\rvert$ at lower heights, highest $\lvert\mathbf{I}_\mathrm{s}\rvert_\mathrm{max}$ for $l_2 = 7$ mm at H_3
1.85	uniform distribution of $\lvert\mathbf{I}_\mathrm{s}\rvert$ for $P > 0.12$ W	lower $\lvert\mathbf{I}_\mathrm{s}\rvert$ for all l_1, except for $l_1 = 1$ mm at H_2 and low P at H_3, more uniform distribution of $\lvert\mathbf{I}_\mathrm{s}\rvert$	same as Impediment 1, but higher $\lvert\mathbf{I}_\mathrm{s}\rvert$
2.05	uniform distribution of $\lvert\mathbf{I}_\mathrm{s}\rvert$ for $P > 0.11$ W, but declining $\lvert\mathbf{I}_\mathrm{s}\rvert$ at lower heights	same as $d_\mathrm{p} = 1.85$ mm	same as Impediment 1, but higher $\lvert\mathbf{I}_\mathrm{s}\rvert$

5.3.2 Resulting particle momentum on whole membrane area

Next, the particle momentum acting on the whole active membrane area, i.e. at $y = 0$, is averaged and compared for the reactor geometry without any built-in impediments and

with Impediment 1 and Impediment 2. The particle momentum for Impediments 1 and 2 for the particle diameter of 1.25 and 1.55 mm is shown in Figure 5.7 and for the particle sizes of 1.85 and 2.05 mm in Figure 5.8.

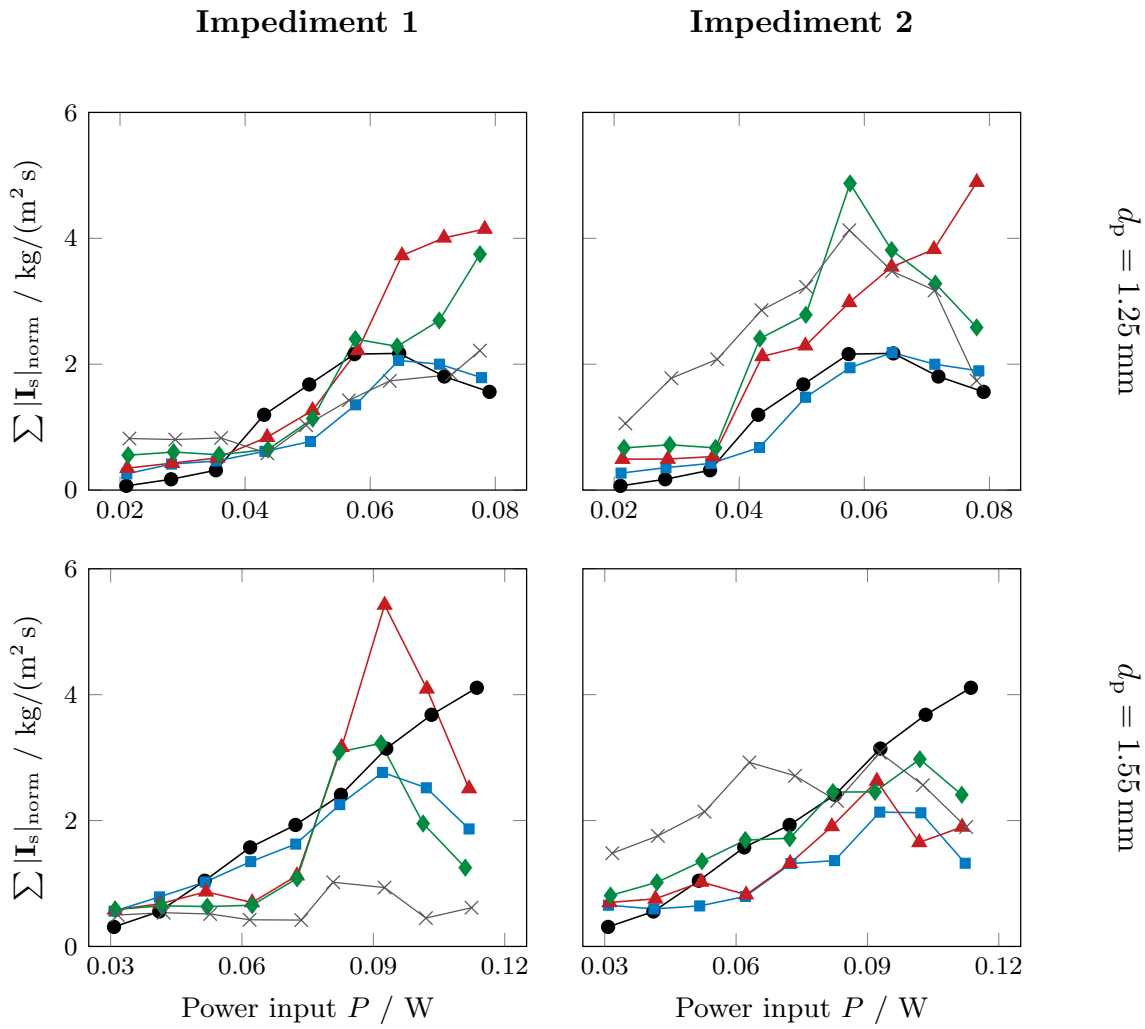

Figure 5.7: Cell-averaged normalized particle momentum (magnitude) $|\mathbf{I}_s|_{norm}$ at the active membrane with corresponding required power input P for particle diameters $d_p = 1.25$ and 1.55 mm for Impediment 1 and Impediment 2. The different symbols correspond to the different impediment lengths of Impediment 1 and Impediment 2 (no impediment: ●, 1 mm: ■, 3 mm: ▲, 5 mm: ♦ and 7 mm: ×).

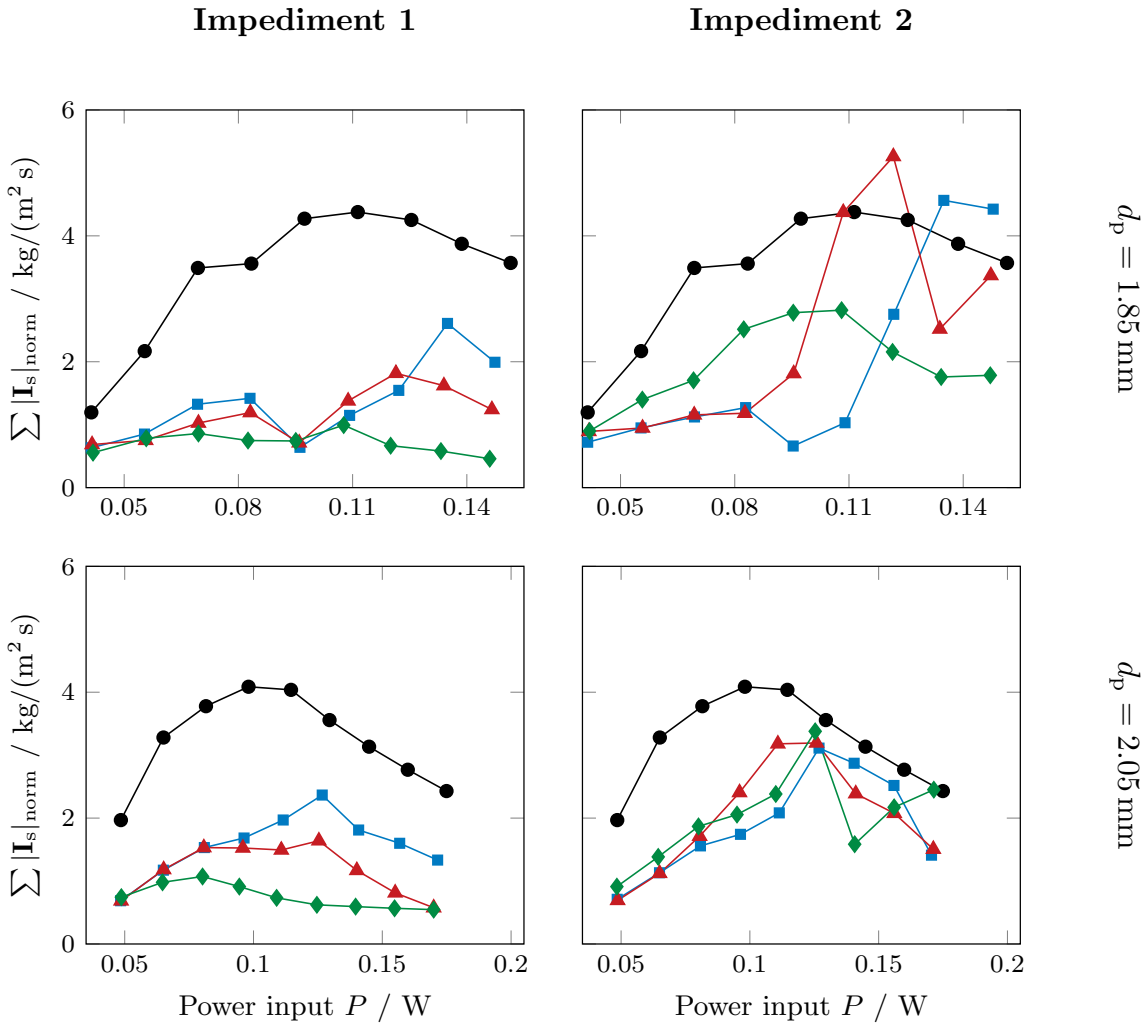

Figure 5.8: Cell-averaged normalized particle momentum (magnitude) $|\mathbf{I}_s|_{\mathrm{norm}}$ at the active membrane with corresponding required power input P for particle diameters $d_p = 1.85$ and $2.05\,\mathrm{mm}$ for Impediment 1 and Impediment 2. The different symbols correspond to the different impediment lengths of Impediment 1 and Impediment 2 (no impediment: ●, 1 mm: ■, 3 mm: ▲, 5 mm: ♦ and 7 mm: ×).

No impediments (symbols ● in Figures 5.7 and 5.8):

The particle momentum obtained from the simulations near the active membrane area without an impediment shows for all particle diameters a maximum depending on the fluid inlet velocity. The resulting momentum with a particle diameter of $d_p = 1.55\,\mathrm{mm}$ has in contrast to the other particle sizes a linear increase with the power input, a maximum of the particle momentum is not reached yet for the considered inlet fluid velocities. The maximum of the particle momentum for the greater particles is reached for a power input of $P \approx 0.11\,\mathrm{W}$, while the maximum in particle momentum for $d_p = 1.25\,\mathrm{mm}$ is achieved at $P \approx 0.065\,\mathrm{W}$. The maximum particle momentum achievable for a particle diameter

of $d_p = 1.25\,\text{mm}$ is approximately $2\,\text{kg}/(\text{m}^2\,\text{s})$ and for the particle diameters of 1.85 and 2.05 mm it is more than twice as high.

Impediment 1 (symbols ■, ▲, ♦and × for $l_1 = 1$, 3, 5 and 7 mm):

The highest particle momentum acting on the membrane for all investigated power inputs is found for the geometry with no impediment for greater particle diameters, i.e., $d_p = 1.85$ and 2.05 mm, compared to Impediment 1. The resulting particle momentum for these particle diameters also decreases with an increase of the impediment length l_1. Comparing the resulting particle momentum for a particle diameter of $d_p = 1.25\,\text{mm}$, it is obvious that at higher fluid inlet velocities the particle momentum for the impediment lengths $l_1 = 3$ and 5 mm is almost twice the value compared to the momentum obtained with no impediment. For the impediment lengths $l_1 = 1$ and 7 mm the resulting particle momentum is lower compared to no impediment. The trend of the particle momentum for the impediment lengths $l_1 = 3$ and 5 mm suggests that a maximum is not reached yet and the total value can still increase with the power input. The particle momentum for a particle diameter of 1.55 mm for the built-in impediments of Impediment 1 develops a maximum for all investigated impediment lengths l_1, while for the impediment lengths $l_1 = 3$ and 5 mm the resulting particle momentum exceeds the particle momentum of the geometry with no impediment at higher fluid inlet velocities. For the other impediment lengths, the particle momentum is lower compared to the geometry without a built-in impediment.

Impediment 2 (symbols ■, ▲, ♦and × for $l_2 = 1$, 3, 5 and 7 mm):

The resulting total particle momentum of the smallest particle size acting on the active membrane for the geometries of Impediment 2 is for all considered fluid inlet velocities higher than with no impediment, with the exception of an impediment length $l_2 = 1$ mm where the particle momentum is almost identical to the one with no impediment. A maximum of the particle momentum in regards to the power input exists for all impediment lengths l_2 at $P \approx 0.06\,\text{W}$. The particle momentum for an impediment length of $l_2 = 3$ mm, however, has not reached a maximum yet; a higher value may still be achievable for this geometry set-up. Regarding a particle size of $d_p = 1.55$ mm the resulting particle momentum with impediments is for all investigated fluid inlet velocities lower or almost at the same range as the particle momentum from no impediment. The simulation of an impediment length of $l_2 = 7$ mm shows a shifted maximum of the particle momentum towards a lower power input, resulting in a higher particle momentum at lower fluid

inlet velocities compared to the case of no built-in impediment. The particle momentum resulting from Impediment 2 with a particle diameter of $d_p = 1.85\,mm$ also shows a maximum for all investigated impediment lengths. In general, the particle momentum is lower compared to the particle momentum obtained with no built-in impediment, except with impediment lengths of $l_2 = 3$ and $5\,mm$ at higher fluid inlet velocities (cf. Figure 5.8). The results for the various impediment lengths for the greatest particle size show that the particle momentum has a defined maximum at a power input at $P \approx 0.125\,W$, but the maximum value for the particle momentum is for all impediment lengths lower than the momentum with no impediment. At higher fluid inlet velocities the achievable particle momentum with impediments is closer to the value of the particle momentum without an impediment than at lower fluid inlet velocities.

An overview of the findings regarding the geometries with no built-in impediment, Impediment 1 and Impediment 2 regarding the resulting particle momentum on the whole active membrane area is summarized in Table 5.4.

Table 5.4: Summary of investigated reactor geometries with effect of particle momentum acting on whole membrane area.

d_p / mm	no impediment	Impediment 1	Impediment 2
1.25	$\lvert\mathbf{I}_s\rvert_{max}$ at 0.06 W	higher $\lvert\mathbf{I}_s\rvert_{max}$ for $l_1 =$ 3 and 5 mm	higher $\lvert\mathbf{I}_s\rvert_{max}$ for $l_2 =$ 3, 5 and 7 mm
1.55	$\lvert\mathbf{I}_s\rvert_{max}$ not reached yet	max for all $\lvert\mathbf{I}_s\rvert$, $\lvert\mathbf{I}_s\rvert_{max}$ at 0.09 W for $l_1 = 3\,mm$	max for all $\lvert\mathbf{I}_s\rvert$, better power optimum at lower fluid velocities for $l_2 = 7\,mm$
1.85	$\lvert\mathbf{I}_s\rvert_{max}$ at 0.1 W	lower $\lvert\mathbf{I}_s\rvert$ for all l_1	higher $\lvert\mathbf{I}_s\rvert_{max}$ for $l_2 =$ 1 and 3 mm
2.05	$\lvert\mathbf{I}_s\rvert_{max}$ at 0.11 W	lower $\lvert\mathbf{I}_s\rvert$ for all l_1	lower $\lvert\mathbf{I}_s\rvert$ for all l_2, but at higher P almost equal to no impediment

5.4 Discussion

A change in geometry, in this case the addition of different shaped impediments, can alter the flow and the resulting particle momentum in an AnFMBR. The particle momentum is dependent on the number and mass of particles and their velocity. A more dense bed with a high magnitude of fluctuation in particle velocity is therefore favorable. An increase in fluid velocity leads to an increase in particle velocity, but on the downside the particle bed

gets more dilute. Thus, the particle momentum is decreasing at higher fluid inlet velocities. For these kind of applications a maximum of the particle momentum based on the fluid inlet velocity or the corresponding required power input can be found. Depending on the initial particle bed height, the fluidized bed may not cover the whole active membrane area to mitigate fouling. To increase the fluidized bed height an increase in fluid inlet velocity is needed which results in a more dilute particle bed. The main disadvantage for the reactor geometry without an impediment is the uneven lateral distribution of the particle momentum across the active membrane area: either the membrane is partially covered by the particle bed, meaning that at greater heights the particle momentum is zero, or the fluid inlet velocity is further increased to expand the particle bed to cover the whole active membrane area. The same trend of non-uniform particle distribution was observed by Wang et al. [35]. The latter case has the problem that with an increase of the fluid inlet velocity the maximum of the particle momentum has been already passed and the particle momentum is decreasing again, an optimal power input is therefore not achievable (cf. Figure 5.5). Hence, an optimal particle momentum based on the required power input across the lateral length of the membrane for all heights is not possible with the current set-up. This means, either the fluidized bed is operated at conditions to achieve a maximum particle momentum acting on the whole membrane, while the membrane is only partially covered by the particle bed (cf. Figure 5.7 for $d_\mathrm{p} = 1.25\,\mathrm{mm}$) or increasing the fluid inlet velocity to cover the whole membrane while decreasing the particle momentum and increasing the power input. With the addition of Impediment 1, linear decrease of the gap between wall and membrane, the fluid velocity increases as the gap decreases. Therefore, the particle velocity increases and the particle bed gets more diluted. This is beneficiary for low fluid velocities as the particle bed is covering the active membrane area at these low velocities while this is not the case for the particle bed of the geometry without an impediment. At higher fluid inlet velocities the particle momentum resulting from Impediment 1 surpasses the value of the benchmark for certain impediment lengths, i.e., $l_1 = 1$ and $3\,\mathrm{mm}$. Greater impediment lengths result in too high fluid velocities due to the narrow gap and the particles get entrained, the particle momentum tends to a value of zero at greater heights. Impediment 2 was investigated to minimize the entrainment at higher velocities and greater impediment lengths. Due to the increasing gap after a height of $77\,\mathrm{mm}$ of Impediment 2, the fluid velocity decreases and the particles decelerate, decreasing the probability of entrainment compared to Impediment 1. This can be best seen when comparing the particle momentum at height H_3 for $d_\mathrm{p} = 1.25\,\mathrm{mm}$ and an impediment length $l_i = 7\,\mathrm{mm}$ for Impediment 1 and 2 (cf. Figures 5.5 and 5.6). The entrainment of particles for Impediment 1 results in a value for the particle momentum close to zero. Impediment 2 mitigates the particle entrainment as the fluid velocity decreases at greater heights and therefore the particle momentum at this height has its highest values. On the downside, the particle momentum of Impediment 2 at the height H_1 tends to zero as the fluid velocity is very high at that height, resulting in a conveying

of the particles. Wang et al. [35] investigated membrane fouling effects of lab-scale and pilot-scale AnFMBRs and came to the conclusion that while the overall trend was similar, the fouling mitigation of the pilot-scale AnFMBR had a higher dependency on the spatial location than with the lab-scale geometry. Those trends were not observed in our lab-scale AnFMBR simulation. For scale-up purposes the implementation of impediments can alter the resulting particle momentum, but effects occurring at pilot-scales, e.g., channeling, should not be ignored.

5.5 Conclusion

We investigated the effect of two different shaped built-in impediments on the hydrodynamics of an AnFMBR. Before modifying the geometry of the reactor, a numerical solver based on a CFD-DEM approach was validated for the reactor geometry without an impediment based on the experimental data from Wang et al. [44]. After successful validation of the solver, the reactor geometry was modified to include two different shapes of impediments. Impediment 1 consists of a linear increasing impediment and Impediment 2 has an inclining and declining impediment. The effect of certain built-in impediments, e.g., Impediment 1 with $l_1 = 5\,\text{mm}$, $d_\text{p} = 1.55\,\text{mm}$ and ${}^{u_\text{f}}/_{u_\text{mf}} = 8$, showed a more uniform axial distribution of the particle momentum across the membrane height. The uniform particle momentum distribution along the height of the membrane was seen for Impediment 1 with impediment lengths $l_1 = 1$ and $3\,\text{mm}$ and particle sizes of 1.85 and $2.05\,\text{mm}$ for low and partially for high fluid inlet velocities. Furthermore, with the introduction of impediments the local maximum achievable particle momentum compared to the reactor geometry without impediments can be further increased, e.g., Impediment 2, $l_2 = 7\,\text{mm}$, $d_\text{p} = 1.25$ and $1.55\,\text{mm}$. However, at these conditions the distribution of the particle momentum is non-uniform as at the lowest height the particle momentum tends to a value of zero. Additionally, some specific set-ups are favored for the use of membranes sensitive to hit of irregular shaped particles as the particle momentum decreased, e.g., using the configuration of Impediment 2 with $l_2 = 5\,\text{mm}$ and $d_\text{p} = 1.55\,\text{mm}$. The problem of particle entrainment at higher velocities and greater impediment lengths for Impediment 1 was minimized with the introduction of Impediment 2. With the alteration of the geometry from a simple rectangular shape to a geometry with built-in impediments the resulting particle momentum of a AnFMBR and therefore the correlated fouling mitigation can be maximized and more evenly distributed across the whole membrane. The total run-time of the AnFMBR can be extended due to less fouling at the membrane at a longer period of time. Further design optimization of the reactor geometry can be achieved by varying the impediment height h_2 in order to get an optimal particle distribution across the membrane height whilst still maintaining a high resulting particle momentum. This can be crucial for

an industrial scale wastewater treatment with an AnFMBR to have the longest run-time for the process itself and few and short cleaning cycles of the membrane.

6 Summary

6.1 Conclusions

In this thesis, the numerical simulation of liquid-solid flows, in particular for fluidized beds, was studied by means of CFD in detail. New solvers were developed to increase the simulation speed, enhance the accuracy of the simulation results and extend the use of certain methods, e.g., the Coarse Grain (CG) method. All newly developed solvers were validated with the use of experimental data from literature and compared with conventional numerical solvers available. Also, CFD-DEM was used to model an anaerobic fluidized bed membrane reactor (AnFMBR) and improvements were proposed to maximize fouling mitigation while minimizing the required energy input.

A combination of the popular Eulerian-Eulerian and Eulerian-Lagrangian model was proposed as a hybrid Eulerian-Eulerian-Lagrangian solver. Here, a user-defined ratio can be set for the particle treatment. The particles can be simulated according to the Eulerian treatment with use of the Two-Fluid Model (TFM) or with a Lagrangian treatment by means of a four-way coupled CFD-DEM approach. If more particles are treated as a Eulerian solid phase, the simulation speed increases tremendously, but the accuracy worsens for systems where particle-particle interactions become the dominant factor. On the other side, a Lagrangian treatment of the particles can lead to higher accuracy but also longer simulation times. With the use of the hybrid Eulerian-Eulerian-Lagrangian solver another degree of freedom is introduced to speed up or increase the accuracy of fluid-solid multiphase flow simulations. The Eulerian solid phase and Lagrangian particles are coupled by means of momentum exchange. The newly developed solver was validated with a 2D fluidized bed and a 3D spouted fluidized bed taken from literature. Furthermore, the performance of the solver in terms of accuracy and simulation speed for different user-defined ratios for Eulerian or Lagrangian particle treatment (ranging from 20 % of particles treated as Lagrangian particles up to 80 %) was compared to conventional solvers using TFM, CFD-DEM and Multiphase Particle-In-Cell (MP-PIC). The accuracy of the CFD-DEM solver was highest for all investigated simulation set-ups. However, due to the individual particle tracking, the simulation speed was the lowest compared to

the other solvers. On the contrary, the solver using TFM performed very well in terms of simulation speed, but lacked a correct depiction of the experimental data, especially for larger particles. The accuracy of the results of the MP-PIC solver lies between the results obtained from the CFD-DEM and TFM solvers, as well as the simulation speed. Regarding the hybrid Eulerian-Eulerian-Lagrangian solver, the accuracy and speed are dependent on the ratio set to transform particles to either Lagrangian particles or a Eulerian phase. In the case of 80 % of particles treated in a Lagrangian way, the results for all investigated simulations were always more accurate than the results of the MP-PIC solver, but the simulation time for the hybrid solver was longer than the time used by the MP-PIC solver. A ratio of 50 % of Lagrangian particles shows almost the same accuracy and simulation time than the MP-PIC solver, depending on the number of particles. If the number of particles present is high, then the MP-PIC solver has an advantage in simulation speed. Concluding, the newly developed hybrid Eulerian-Eulerian-Lagrangian solver shows great promise for the gap between available models of the Eulerian-Eulerian and Eulerian-Lagrangian model to balance between accuracy and simulation speed. Better accuracy can be achieved with the hybrid solver compared to the MP-PIC solver if particle-collisions are the dominant factor in the system of solid-interactions.

Multi-grid approaches in CFD-DEM, where multiple numerical grids are used for simulations of multiphase flows, were investigated in Chapter 4. Besides the dual-grid approach from literature, a new method was developed to add another grid to the simulation of granular flows. Using a single-grid approach can lead to problems in the choice of cell sizes. For CFD-DEM simulations, the cell size must be larger than the particle size, preferably the cell size is a multiple of the particle diameter. This can lead to problems regarding the fluid flow resolutions, as for more accurate momentum exchange determinations a coarser numerical grid is beneficial, while a finer resolution of the cell sizes is crucial for a correct depiction of the fluid flow. Hence, a dual-grid approach can be used to decouple the fluid phase and the particles. The phases are solved on separate numerical grids: a grid with smaller cells for the fluid flow calculation and a coarser numerical grid for the Lagrangian particles. Interpolation of important parameters for the coupling between both phases, e.g., solid phase fraction, must be ensured. A very coarse cell size for the Lagrangian particles can lead to inaccurate results in regards to low resolution of solid phase properties for comparison with experimental data. Hence, an additional grid was implemented to recalculate those parameters and interpolate them to the Eulerian grid. The three-level grid approach was validated with experimental data of a 2D jet-in fluidized bed, 3D fluidized bed and a 3D fluidized bed with a single jet from literature. Furthermore, the new approach was compared to the conventional single-grid and the dual-grid approach. It was seen, that the use of the third grid results in an increase in accuracy, while the simulation speed is only slightly decreased due to interpolation calculations between the three grids. However, it must be noted, that the use of any multi-grid approach requires

careful consideration on initial cell-sizes for each grid. Still, the newly proposed multi-grid approach shows great potential for simulations where a single-grid approach cannot be applied due to cell-size to particle size issues and a dual-grid approach is too inaccurate.

In a joint German-Singaporean research project (01DP16014) an AnFMBR for wastewater treatment was modeled with a CFD-DEM solver and validated with experimental data from literature. Different particle sizes (from 1.05 to 2.05 mm) of granular activated carbon as a scouring agent were investigated to gain further insight in the fouling mitigation efficiency. It was shown, depending on the used particle size, unwanted non-uniform distributions of the resulting particle momentum on the membrane surface, i.e., fouling mitigation ability, occur. By use of geometry changes of the reactor (built-in impediments), a more uniform-distribution of resulting particle momentum was achieved while the required energy input for fluidizing the particles can be lowered. With different dimensions of the implemented impediments and fluidization velocities, the resulting particle momentum can be modified accordingly. A modification of the resulting particle momentum can be crucial for membranes sensitive for shear, hit or scrape. The most uniform particle momentum distribution at the membrane surface was obtained for particles with a size of 1.25 and 1.55 mm, which show the most promising results in terms of particle momentum, distribution and required energy.

6.2 Outlook

Regarding the newly developed hybrid Eulerian-Eulerian-Lagrangian solver (cf. Chapter 3), improvements can be made to automatically transform between Eulerian to Lagrangian particles based on a particle concentration threshold. In areas with particle clusters, i.e., high solid phase fractions, the particle phase should be treated as a continuum according to the Kinetic Theory of Granular Flow with use of the TFM. This way, the simulation speed can be drastically increased. For areas where the particle concentration is low, e.g., bubble phases, spouted areas or turbulent fluidization with a high fluid phase fraction, the particles can be tracked with a Lagrangian treatment. Furthermore, larger particles can also be treated as Lagrangian particles, so the particle-contact forces due to collision can be better depicted than with a Eulerian treatment of the collisions, i.e., a stochastic treatment.

During the joint German-Singaporean research project to increase the efficiency of wastewater treatment using an AnFMBR, more studies were made to investigate other techniques for MBRs. One other method to minimize the fouling of a membrane during the operation, is the use of a vibrating scrubber. Shear force of the induced fluid flow is used to scrub off

existing fouling particulates. For the CFD simulations a dynamic moving mesh approach was used to model the vibrating scrubber and parameter studies were made to enhance the scrubber geometry and positioning for effective fouling mitigation based on the required energy input. Further studies can be made to extend the scrubbing technique with the implementation of particles between said scrubber and the membrane. This way, not only the induced shear force of the fluid is mitigating fouling formation, but also the momentum of the particles might decrease the presence and deposition of foulant on the membrane as seen in AnFMBRs. No increase in fluid flow is needed for the fluidization of the particles, as the movement of the scrubber can induce particle movement. Due to the inertia of particles, an harmonic motion of particles will be induced to further mitigate fouling. In order to simulate such an application, a CFD-DEM solver must be coupled with a dynamic meshing approach. Such a solver already exists in OpenFOAM® version 5.x, called *DPMDyMFoam*. Problems arise, when considering the fine resolution of the numerical grid between the scrubber and the membrane where the potential particles would reside. Hence, a multi-grid approach must be applied to overcome those boundaries, when using CFD-DEM. After a successful coupling of the dynamic moving mesh CFD-DEM solver with the multi-grid approach presented in this thesis, parameter studies can be made, e.g., size, density, number of particles, to maximize fouling mitigation while minimizing the required power input, mostly used for the movement of the scrubber.

Furthermore, during this thesis a CFD-DEM solver for catalytic reactions was developed and validated for a methane reaction in a fluidized bed. This solver can be further enhanced to include more chemical reactions where the fluidized bed technology is applicable (cf. Chapter 1.1). With use of the CG method, larger reactor scales with more catalytic active particles can be simulated. The solving procedure for the kinetics of the chemical reaction are, however, the rate determining step for the simulation time. Therefore, special attention must be paid on the acceleration for solving the chemical reactions, e.g., use of GPUs instead of CPUs.

Lastly, a basic, but still robust, solver for a gas-liquid-solid flow was developed and validated with experimental data. This solver can be used to model, for example slurry-reactors. The choice of an adequate void fraction determination method is crucial (cf. Appendix B). A coupling of the gas-liquid-solid flow solver with the multi-grid approach might be beneficial for simulation speed, accuracy and further increase in robustness for the overall solver.

A Numerical Grid Independency

The results of a numerical simulation need to undergo some further investigation in order to be used for verification and validation of this data. Ideally, it is done before using the results of the simulation for further studies. First the terms verification and validation need to be defined. Generally speaking, verification answers the question "Do we solve the equations right?", while validation is implicit with the question of "Do we solve the right equations?" [269–272]. Applied to CFD, a verified simulation comprises of steps necessary that the partial differential equations are solved accurately, discretized correctly, the code of the solver is fully functional and a numerical convergence is reached. The verification process therefore does not require experimental data for comparison as it is purely of a mathematical and computational matter and hence evaluates the quality of the numerics being solved. On the other side, for the validation of a numerical simulation the comparison with experimental data is inevitable. Here, the accuracy of the prediction of the used equations, i.e., physical models, is compared with the outcomes of experiments: the numerical model is checked with results of experiments. As an adjustment to the numerics, e.g., using a different discretization scheme or a finer numerical grid, has an impact on the numerical results, it is common practice to first conduct the verification of the numerical code and afterward to verify the computational simulation with experimental data, as the verification is independent of the result of experiments. After a successful verification of the code, further changes can be made to the physical models in order to depict the "real life" physics of the experiment. The validation process is straight forward and done in several iterations, as experimental data is obtained and compared to the simulation results. Then, the physical models are adjusted and compared again. The verification process has multiple ways to get a numerical correct solution. In the following section the verification process will be limited on the numerical grid independency, as in most cases the discretization of the numerical equations using different schemes has been already intensively investigated which discretization scheme is advantageous for specific flow problems (cf. [61, 273–276]). Hence, the main focus should be on the grid independency for the verification of the simulation.

An analysis of a numerical grid is a crucial step before using the data obtained by a numerical simulation in CFD. A numerical grid independency study, also called a mesh

independency study, is a way to determine if the resolution of the used numerical grid is sufficiently fine in order to achieve a numerical independency. When a numerical independency is reached, a further refinement of the numerical grid does not result in a higher accuracy of the simulation data. Several things must be considered when a numerical grid independency study is performed. First, for the mesh independency study, several distinctly resolved meshes must be investigated, usually consisting of three meshes:

- a coarse grid,
- a medium grid and
- a fine grid.

Multiple approaches for the determination of the different sizes of each grid were proposed in literature which will be discussed in detail later. More cells in a numerical simulation set-up result in a higher resolution and in most cases in a higher accuracy. The higher accuracy in the numerical solution comes with a cost of the need to solve more equations and hence a longer simulation time. Looking back at the definition of the *Co*-number (cf. Equation (2.39)) a decrease of the cell size Δx, which is inherent performing a grid refinement, results in a decrease of the time step Δt if the flow domain does not change and a uniform Co-number is desired. Therefore, a refinement in the numerical grid shows a vast decrease in simulation speed. Once a grid independency is reached, a further refinement does not yield a higher accuracy. Therefore, the simulation results are independent of the chosen mesh size and discretization errors based on the numerical grid can be excluded.

One widely used method to quantify the discretization error and hence evaluate the grid convergence, is the Richardson extrapolation [52, 277]. Three different sized grids are needed to determine the discretization error.

With obtained arbitrary values of interest ϕ on each of the different sized numerical grids, ϕ_c, ϕ_m and ϕ_f, corresponding to the values of the coarse, medium and fine grid, the discretization error for the coarse grid $\epsilon_\mathrm{c}^\mathrm{d}$ and for the medium grid $\epsilon_\mathrm{m}^\mathrm{d}$ can be approximated with:

$$\epsilon_\mathrm{c}^\mathrm{d} \approx \frac{\phi_\mathrm{c} - \phi_\mathrm{m}}{f_\mathrm{ref}^{p_\epsilon} - 1} \tag{A.1}$$

and

$$\epsilon_\mathrm{m}^\mathrm{d} \approx \frac{\phi_\mathrm{m} - \phi_\mathrm{f}}{f_\mathrm{ref}^{p_\epsilon} - 1}. \tag{A.2}$$

The exponent p_ϵ can be calculated using the arbitrary values obtained of all three numerical grids:

$$p_\epsilon = \frac{\log \frac{\phi_\mathrm{m} - \phi_\mathrm{f}}{\phi_\mathrm{c} - \phi_\mathrm{m}}}{\log f_\mathrm{ref}}. \tag{A.3}$$

Here, f_ref represents the refinement factor of the numerical grids based on the refinement from the coarse to the medium grid [278], e.g., a refinement factor of $f_\mathrm{ref} = 2$ means, the medium level grid comprises of twice the cells as the coarse grid. Accordingly, with this method a linear scaling is implied and hence, the fine grid has twice the cells of the medium grid and four times the cells of the coarse grid. Assuming a refinement factor of $f_\mathrm{ref} = 2$, the exponent p_ϵ can be calculated according to

$$p_\epsilon = \frac{\log \frac{\phi_\mathrm{m} - \phi_\mathrm{f}}{\phi_\mathrm{c} - \phi_\mathrm{m}}}{\log 2} \tag{A.4}$$

and the discretization error of the medium sized grid as

$$\epsilon_\mathrm{m}^\mathrm{d} \approx \frac{\phi_\mathrm{m} - \phi_\mathrm{f}}{2^{p_\epsilon} - 1}. \tag{A.5}$$

The determination of the discretization error using the Richardson extrapolation is only valid if the solution converges monotonically and the numerical grid is in a uniform way.

Celik et al. [279] proposed a revised method of the Richardson extrapolation to calculate the so called Grid Convergence Index (GCI). The GCI estimates the numerical uncertainty of the numerical solution. However, it should be noted that existing model errors are not accounted for and should be excluded before performing a grid analysis. The GCI method can be conducted by the following five steps:

1. Definition of a representative grid size

A representative grid size h is defined. The determination of this grid size is dependent on the type of dimensional set-up of the geometry, i.e., if the numerical grid consists of 2D faces (areas) or 3D cells (volumes). For both cases, the representative grid size h can be calculated if the dimensions of each cell, or faces for 2D cases, are known:

$$h_\mathrm{2D} = \left(\frac{1}{N} \sum_{i=1}^{N} \Delta A_i \right)^{1/2} \tag{A.6}$$

and

$$h_{3\mathrm{D}} = \left(\frac{1}{N} \sum_{i=1}^{N} \Delta V_i \right)^{1/3} . \tag{A.7}$$

Here, the arithmetic mean value of the face areas or the cell volumes is calculated and the representative grid size h is determined by taking the second or the third root depending on the unit dimension.

2. Choosing three different sized numerical grids

The simulations are performed on three distinct numerical grids. Each of these grids varies by the number of cells, i.e., the refinement. A refinement factor r is introduced to quantify the relation of cells between the examined numerical grids:

$$r = \frac{h_{\mathrm{coarse}}}{h_{\mathrm{fine}}}. \tag{A.8}$$

According to the above equation and the definition of the representative cell size h in Equations (A.6) and (A.7), the refinement factor has to be larger than one. Empirical investigations suggest a refinement factor r of at least 1.3 [279]. Furthermore, the refinement should be performed in a systematic way, i.e., a linear increase in cells is preferred. For example, if the medium grid has twice the number of cells compared to the coarse grid, then the fine grid should have also twice the cells compared to the medium grid. This can be also applied to the resulting representative cell size instead of the number of cells in the numerical grid.

3. Calculation of the apparent order p_{GCI}

With h_{c}, h_{m} and h_{f} corresponding to the representative cell sizes for the coarse, medium and fine numerical grid, the refinement factors can be calculated as

$$r_{\mathrm{mf}} = \frac{h_{\mathrm{m}}}{h_{\mathrm{f}}} \tag{A.9}$$

and

$$r_{\mathrm{cm}} = \frac{h_{\mathrm{c}}}{h_{\mathrm{m}}}. \tag{A.10}$$

The apparent order p_{GCI} can be calculated as:

$$p_{\mathrm{GCI}} = \frac{1}{\ln\left(r_{\mathrm{mf}}\right)} \left| \ln\left(\left| \frac{\delta_{\mathrm{cm}}}{\delta_{\mathrm{mf}}} \right| \right) + q \right|. \tag{A.11}$$

δ_{cm} and δ_{mf} represent the differences between arbitrary solutions ϕ_i obtained on the specific numerical grid i, i.e., $\delta_{\mathrm{cm}} = \phi_{\mathrm{c}} - \phi_{\mathrm{m}}$ and $\delta_{\mathrm{mf}} = \phi_{\mathrm{m}} - \phi_{\mathrm{f}}$, respectively. The function of q in Equation (A.11) follows as

$$q = \ln\left(\frac{r_{\mathrm{mf}}^{p_{\mathrm{GCI}}} - s}{r_{\mathrm{cm}}^{p_{\mathrm{GCI}}} - s}\right) \tag{A.12}$$

with

$$s = \mathrm{sgn}\left(\frac{\delta_{\mathrm{cm}}}{\delta_{\mathrm{mf}}}\right). \tag{A.13}$$

In the above stated equation, sgn denotes the signum function returning the sign of its input. It is apparent, that the function q in Equation (A.12) is an implicit function corresponding to Equation (A.11). Hence, it is suggested to use an initial guess for $q = 0$ and apply a fixed-point iteration to obtain the apparent order p_{GCI} [279].

If one of the differences of the obtained solution for the different numerical grids, δ_{cm} and δ_{mf}, is close to zero, the convergence of the solution might be of an oscillatory nature and therefore, the grid convergence index approach above is not suitable. It is recommended to use further refinements of the numerical grids and repeat the calculation of the GCI.

4. Determination the extrapolated values

Now, the extrapolated values $\phi_{\mathrm{mf}}^{\mathrm{ext}}$ and $\phi_{\mathrm{cm}}^{\mathrm{ext}}$ can be calculated using the apparent order:

$$\phi_{\mathrm{mf}}^{\mathrm{ext}} = \frac{r_{\mathrm{mf}}^{p_{\mathrm{GCI}}}\phi_{\mathrm{f}} - \phi_{\mathrm{m}}}{r_{\mathrm{mf}}^{p_{\mathrm{GCI}}} - 1} \tag{A.14}$$

and for the extrapolated value using the coarse and medium resolution numerical grid

$$\phi_{\mathrm{cm}}^{\mathrm{ext}} = \frac{r_{\mathrm{cm}}^{p_{\mathrm{GCI}}}\phi_{\mathrm{m}} - \phi_{\mathrm{c}}}{r_{\mathrm{cm}}^{p_{\mathrm{GCI}}} - 1}. \tag{A.15}$$

5. Calculation of the error estimates GCI

The approximated relative and extrapolated relative errors, $\epsilon_{\mathrm{mf}}^{\mathrm{a}}$ and $\epsilon_{\mathrm{mf}}^{\mathrm{ext}}$, can be determined with the obtained solutions of the medium and fine grid, ϕ_{m} and ϕ_{f}, and the extrapolated value from step 4 $\phi_{\mathrm{mf}}^{\mathrm{ext}}$:

$$\epsilon_{\mathrm{mf}}^{\mathrm{a}} = \left|\frac{\phi_{\mathrm{f}} - \phi_{\mathrm{m}}}{\phi_{\mathrm{f}}}\right| \tag{A.16}$$

and

$$\epsilon_{\mathrm{mf}}^{\mathrm{ext}} = \left| \frac{\phi_{\mathrm{mf}}^{\mathrm{ext}} - \phi_{\mathrm{f}}}{\phi_{\mathrm{mf}}^{\mathrm{ext}}} \right|. \tag{A.17}$$

In the final step, the grid convergence index for the fine numerical grid $\mathrm{GCI}_{\mathrm{mf}}$ can be calculated as:

$$\mathrm{GCI}_{\mathrm{mf}} = 1.25 \frac{\epsilon_{\mathrm{mf}}^{\mathrm{a}}}{r_{\mathrm{mf}}^{p_{\mathrm{GCI}}} - 1}. \tag{A.18}$$

This value indicates the numerical uncertainty of the numerical grid with the fine resolution. The arbitrary solutions used for comparison of the different sized numerical grids ϕ_i should be chosen according to the underlying flow problem. Generally, it is good practice to use the pressure drop, pressure or velocities at a certain point for the evaluation of the GCI. Regarding multiphase flows, especially fluid-solid flows, the volume fraction of one phase can also be used as the arbitrary value of the solution.

The estimation of the error due to numerical discretization of the grid according to the above procedure presented by Celik et al. [279] is widely applied for CFD simulations, including single- and multiphase flow, cf. [280–289].

However, it should be pointed out, that refinement or coarsening ratios can not be varied arbitrarily for a uniform quadrilateral or hexahedral cell-based numerical grid. This is due to the fact, that for more complex geometries, e.g., several inlet streams or bends in a pipe, a fixed ratio for cell-sizes is needed. A numerical grid refinement of certain regions in the simulation geometry can falsify the value of the GCI. Therefore, this method is more applicable for simple geometries such as cylinders or cuboids. Another limitation for the refinement of the numerical cells exists for specific multiphase flow models, in particular fluid-solid flow models, such as the Two-Fluid model and the Eulerian-Lagrangian model. Problems arise if the cell size is smaller than a particle in the numerical grid.

The Two-Fluid Model is a continuum based model (cf. Chapter 2.3.1). Hence, a phase fraction is introduced to distinguish between the two phases. For the particle phase, this phase fraction represents the volume of a solid phase occupying the considered cell. As the particle phase has a defined diameter for the particles, a refinement of the numerical grid when conducting a numerical grid independency study could result in cells being smaller than the particle diameter defined for the particle phase. This can lead to problems based on which type of set-up is investigated [290]. Regarding systems where the transient process is of interest, the distribution of the particles based on the obtained phase fraction might not be useful as they are not physical. As an example, a cell comprises a solid phase fraction of 0.5 meaning that 50 % of the cell's volume is occupied by the particles. If the

dimensions of the cell are quite small compared to the particles due to the refinement of the numerical grid independency study, the solid phase looses its physical meaning and becomes a stochastic value of the dynamic system. In this specific case the principle of ergodicity[1] can be applied. The transient nature of the system is transformed to a quasi-steady state system. The solid phase fraction in such a case is then viewed as more of a stochastic probability of the particles. Therefore, a transient consideration of these particular systems, e.g., the start-up or bubble dynamics of a fluidized bed reactor, is not possible. Panday et al. [293] suggest as a rule of thumb a cell to particle size of ten, which has to be adjusted individually.

The cell-size for Eulerian-Lagrangian based models can not be arbitrary refined either. According to Chapter 2.3.2 the Eulerian-Lagrangian model treats the fluid phase as a continuum and the particles as Lagrangian trajectories. The numerical calculations of the fluid phase is done on the numerical cells, while the calculation of particle movement is almost[2] independent on the size, number and shape of the cells. As important parameters for the coupling of the fluid phase and particles including the phase fractions, as well as the velocities of the fluid phase and particles, are calculated using the geometric properties of the cell. The cell size has a defined limit for refinement size. Figure A.1 illustrates this behavior for different-sized particles located in an allocation of same-sized cells.

Three different scenarios are depicted above. Figure A.1a shows a particle smaller than the surrounding cell and the particle is fully immersed in the cell without overlapping to adjacent cells. The particle is fully embodied in the volume of the cell and the volume occupied by the particle does not approach nor exceed the cell's volume. In this specific case no issues should arise when transforming Eulerian to Lagrangian properties and vice versa, e.g., calculating the solid phase fraction. A further refinement of the cell might be possible. If this scenario is existing for the finest resolution, then the grid independency study can be performed. In the second scenario, Figure A.1b, the particle is the same size as in A.1a but the position of the particle is in a way that parts of it overlap into neighboring cells. This case can implicate issues regarding the calculation of the phase

[1] The term ergodicity stems from Ludwig Boltzmann [291] and is used in the field of statistically physics. It says that a dynamical system can be statistically averaged with a sufficient sized data set in order to represent the quasi-stationary state of the aforementioned system [292]. Regarding gas-solid flows, the principle of ergodicity and the application of it allow for a dynamic and transient system to average it and obtain a quasi-steady state system. This then can be used for comparison or further investigations.

[2] It should be noted that the term *almost* distinguishes the pure Lagrangian approach and the Eulerian-Lagrangian approach. Regarding the Lagrangian approach, only the particle movement is considered due to external forces, e.g., gravity. The Eulerian-Lagrangian approach also includes interactions between the fluid phase and the particles. In order to evaluate the coupling between the two phases correctly, it is mandatory to transform Eulerian properties to Lagrangian properties and vice versa. Hence, the term *almost* applies that the Lagrangian approach is independent on the cells of the numerical grid, but coupled with the fluid phase a coherence exists between the cells and the Lagrangian particles which must not be neglected.

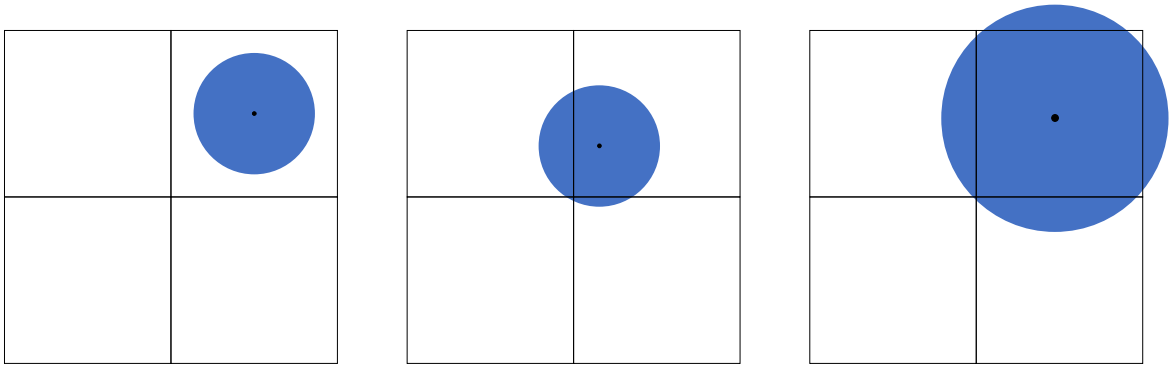

(a) Particle smaller than cell and not overlapping adjacent cells. Further refinement possible.

(b) Particle smaller than cell and overlapping. Further refinement might be possible.

(c) Particle bigger than cell. Further refinement not possible.

Figure A.1: Different scenarios for particle sizes and positions for an arbitrary cell allocation and consequences for a further grid refinement due to a grid independency study.

fraction or the solid phase velocities depending on the applied method to determine the parameters. In this case it is not recommended to use the widely applied Particle Centroid Method (PCM) but a more sophisticated one according to Appendix B. If another choice of a more sophisticated phase fraction determination like the Divided Particle Volume Model (DPVM) is not feasible due to unfavorable high calculation times, the problem at hand can be bypassed by increasing the cell-to-particle ratio. As this solution strategy can not be applied in most cases, due to loss in fluid flow resolution or incapability to model certain complex geometries, the use of another phase fraction determination approach becomes inevitable. A further refinement of the numerical grid is almost not possible. Figure A.1c shows a particle which is bigger than the underlying cell. In this case the PCM method can not be applied as the phase fraction for the solid phase would lead an unphysical value of higher than one. The use of the more precise DPVM accounts for a more accurate contribution of the particle volume to the adjacent cells, but the solid phase fraction for the underlying cell yields one. This can lead to numerical instabilities according to the momentum balance used to calculate the fluid velocity as the fluid phase fraction tends to zero, $\varepsilon \rightarrow 0$. A further refinement of the numerical grid for a grid independency study is not possible.

In conclusion, contrary to single- or multiphase flows with only fluids, the cell refinement due to grid independency studies for multiphase flows with particles modeled by TFM or CFD-DEM can not be performed arbitrarily. Careful consideration has to be paid to the resulting relation of cell to particle sizes. Overlapping particles or particles being bigger than the cell itself can lead to unphysical behavior. An upper limit for the maximum cell refinement exists for these simulation models.

B Transformation of Lagrangian to Eulerian Values

The fluid phase is discretized due to the mesh resolution, meaning the number of numerical grid cells. The Lagrangian particles are allocated as resolved points with a defined radius or shape and therefore independent of the numerical grid. Hence, the momentum exchange term between the fluid phase and the particles is approximated on a cell-level, i.e., only particles residing in a specific cell contribute to the momentum exchange to the fluid-cell and an interpolation or a transformation between Lagrangian properties and values to cell-based values is needed. The transformation of those values also involves errors in the numerical simulations depending on the cell size and the transformation procedure. The cell size can not be arbitrarily decreased for a better resolution of a two-phase flow using the Eulerian-Lagrangian model due to the hard restriction that the cell size has to be bigger than the particle size (cf. Appendix A). A method for transforming Lagrangian to Eulerian values and hence determining the void fraction[1] shall conserve the mass of all particles, can be used for a grid independency study and yields smooth transitions of the void fraction within a particle bed [294]. Several approaches exist on how the particle properties can be transformed from a Lagrangian type to a cell-based numerical grid. The most common ones include:

- the Particle Centroid Method,
- the Divided Particle Volume Method [295, 296],
- the Porous Cube Model [215],
- the Porous Sphere Model [297, 298] and

[1] The procedure for the determination of the void fraction from Lagrangian values applies in a similar way to the transformation to Eulerian solid phase velocities and momenta. Each Lagrangian particle velocity is attributed to the Eulerian grid as a fraction by using the solid phase fraction. The Eulerian momentum can be calculated with the solid phase velocity and the mass of all particles in the fluid cell. The mass of all particles in the fluid cell is again calculated with the Eulerian solid phase concentration.

- the Diffusion Based Model [232, 233].

Each of the mentioned models can be used to determine the volume fraction of particles residing in the cells of a numerical grid. Using this information, the momentum exchange term can be calculated. However, it shall be stated that this approach of using the volume fraction to determine the momentum exchange is only valid for constant density of the particles. The determination of the volume fraction is independent of the density and therefore the mass dependent momentum of each particle is falsely calculated using this method. Therefore, when simulating non-uniform dense particles the mass of each individual particle must be included to account for density differences.

B.1 Particle Centroid Method

One of the most used methods to calculate the solid phase porosity in CFD-DEM simulations is the Particle Centroid Method (PCM) [226]. The methodology of the PCM states that the solid phase volume fraction corresponding to a specific cell consists of the sum of the volumes of particles residing in said cell. The definition of the local placement of the particle and therefore the allocation to the respective cell is based on the position of the particle center. This means if the center of a particle is located in the spatial extent of a numerical cell, the volume of the regarding particle is accounted for the calculation of the solid phase fraction determination of the cell. First, this determination procedure has the advantages of being easy to implement in terms of a low complexity of code programming and hence a fast calculation for the solid phase fraction. The main disadvantage of this algorithm can be best explained with Figure B.1. Here, five (2D-)particles are allocated in a numerical grid consisting of nine computational (2D-)cells.

One of the particles is located with the total volume (or area) in one fluid cell, while the other four particles straddle neighboring cells. A higher gray gradient of the cell indicates a higher Eulerian solid phase fraction computed according to PCM. As only the particle center is defining to which cell the particle volume is attributed to, errors for the accurate void fraction determination occur. On the one hand, the four cells 2, 3, 4 and 7 are not attributed with a particle concentration as no particle center is located in each of the cells, although particle fractions are residing in those cells. On the other hand for an accurate representation cell 5 should have a higher solid phase concentration than calculated as more particle segments should be accounted to cell 5. Cells 1, 6 and 8 show a higher particle concentration than an actual representation would have suggested. The calculation of PCM is prone to an inaccurate determination of the void fraction if

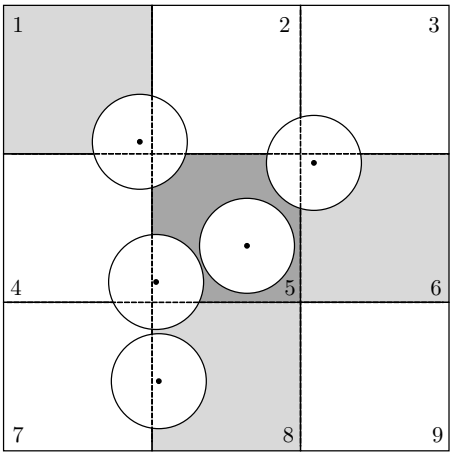

Figure B.1: Colored cells with increasing gray gradient color for increasing solid phase concentration for different positioned particles using the Particle Centroid Method (PCM).

particles straddle neighboring cells. This error becomes higher when the cell-to-particle ratio decreases, i.e., the probability for particles overlapping to other cells increases.

The advantages, however, are manifold. The PCM is a simple approach and therefore the computational implementation is of a minor effort. The computational cost for the determination of the void fraction is low as only the particle position and the corresponding cell need to be determined; no additional calculations of particle segments and algorithms to locate the neighboring cells are needed. The disadvantage of overlapping particles can be neglected for dense granular flows and if the cell-to-particle ratio is high. Then, a high number of particles resides in a cell. The fraction of the overlapping particle volume to adjacent cell is marginal compared to the total volume of particles residing in the main cell. Hence, the magnitude of erroneous contributed particle volumes is negligible.

B.2 Divided Particle Volume Method

The Divided Particle Volume Method (DPVM) is a more sophisticated method for the determination of the void fraction. An analytical approach is used to calculate the volume fraction of a particle in each corresponding cell with:

$$V_{\mathrm{p},i} = \iiint dV. \tag{B.1}$$

The distance between the particle center and the cell center is determined. Afterward, the neighboring cells in which parts of the particle volume are residing in are located. In a final step each individual volume segment is calculated according to Equation (B.1)

and attributed to the corresponding cell. A more detailed description of the mathematically equation can be found in [299]. Figure B.2 depicts an arbitrary particle and nine fluid cells. The gray gradients correspond to the calculated solid phase fractions using

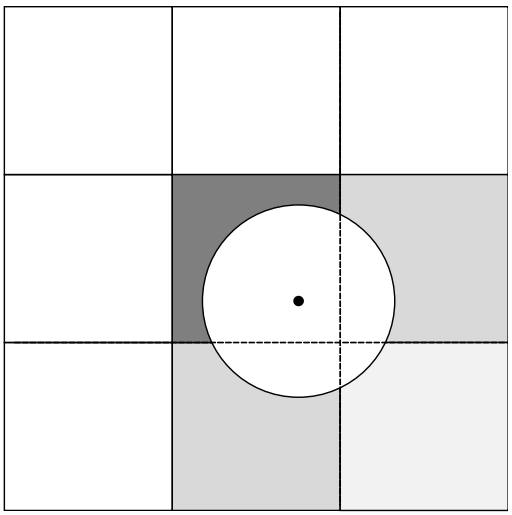

(a) Divided Particle Volume Method (DPVM).

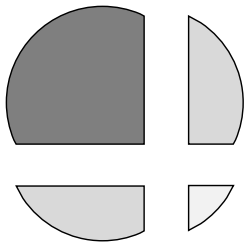

(b) Corresponding particle volume segments.

Figure B.2: Colored cells with increasing gray gradient color for increasing solid phase concentration for different positioned particles using the Divided Particle Volume Method (DPVM) (a) and corresponding particle segments divided by the corresponding cells (b).

DPVM. The different overlapping volume parts of the particle are correctly attributed to the corresponding cells. Figure B.2b shows the segmented particle. This method for the void fraction determination is the most computational demanding. The analytical Equation (B.1) must be first discretized in order to solve it numerically. The higher the discretization, the more accurate is the resulting particle volume segments, but this also brings along a higher calculation time. Furthermore, in contrary to PCM, not only one cell the particle is residing in must be located, but also the neighboring cells the particle overlaps to must be determined. A maximum of 27 cells in total have to be located in a 3D simulation using this method. For each cell the particle volume segments have to be calculated and attributed to the solid phase fraction of the cell. This implies a high amount of I/O-data and therefore a long computational time. In an arbitrary simulation with 100 000 particles this process alone could take up to 10 s per Lagrangian time-step [294]. The advantage of the DPVM is the most accurate determination of the void fraction compared to all other methods. No particle segments are falsely or incorrectly attributed to other cells. Modifications of the DPVM to enhance the calculation speed have been proposed in literature, e.g., Khawaja et al. [300] proposed a method using the DPVM but approximating the particles as cubes. Using this method, the calculation of the particle volume segments is much faster than calculating the volumes according to Equation (B.1). However, the determination of the corresponding neighboring cells remains the same. More

precise methods to determine to void fraction than the PCM but less computational expensive are discussed in the following.

B.3 Porous Cube Model

A simpler and faster model but not as accurate as DPVM is the Porous Cube Model proposed by Link et al. [215]. Here, a particle is transformed to an imaginary porous cube. The length of the cube can be set arbitrarily but is mostly set as a multiple of the particle diameter. The volume of the particle is evenly distributed to the cells which are straddled by the cube. Figure B.3 shows two different scenarios of a particle residing in a numerical grid where the Porous Cube Model is applied with different cube lengths. In the left scenario an ideal constellation between particle position, cell and cube length is depicted. Using the PCM, the volume of the particle would be assigned to any of the cells 6, 7, 10 or 11. In this case the Porous Cube Model will assign a quarter of the particle volume to each of the aforementioned cells exactly as the DPVM but with a fraction of the computational time. The second scenario on the right side of Figure B.3 shows an unfavorable constellation of particle positions, cube length and cell size. Here, the imaginary porous cube straddles twelve cells (from 1 to 12). Those cells are each assigned a twelfth of the particle volume for the void fraction determination, although the cells 1, 5 and 9 are not intersected by the particle. Only a little fraction of the cube overlaps with this cells, but the assigned particle volume is equal to the volume assigned to, for example cell 7. This cell would have been assigned the majority part of the particle volume when using DPVM.

The fast calculation and easy implementation are two big advantages of the Porous Cube Model. As the particle volumes are equally distributed to the cells straddled by the porous cube, a smoother transition of values in the void fraction fields are guaranteed as opposed to simulations using PCM or DPVM. On the other side, another tuning parameter needs to be set: the length of the porous cube. A priori parameter studies should be made to find the optimum cube length for further simulations. Furthermore, the unfavorable constellation in Figure B.3b shows that this model can yield highly inaccurate results for the void fraction in certain scenarios. This problem can be neglected if highly dense granular flows with small particles are present and moderate lengths of the porous cube are chosen. A modification of this method will be next discussed.

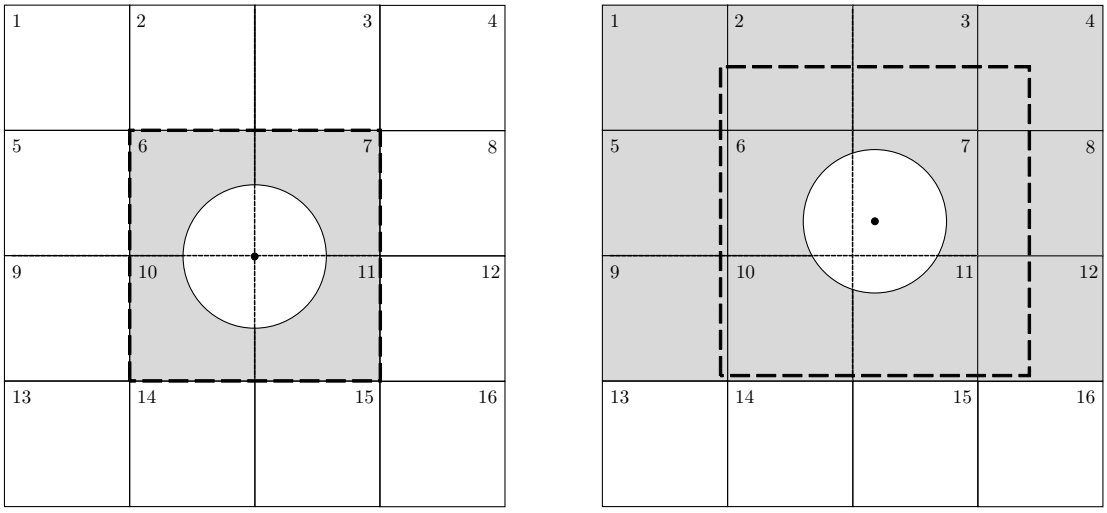

(a) Ideal constellation. **(b)** Unfavorable constellation.

Figure B.3: Colored cells with increasing gray gradient color for increasing solid phase concentration for different positioned particles using the Porous Cube Model in an ideal (a) and unfavorable constellation of particle position (b).

B.4 Porous Sphere Model

The Porous Sphere model uses an imaginary sphere as a shape [297, 298]. Figure B.4 shows an ideal and an unfavorable constellation for the void fraction determination using the Porous Sphere model.

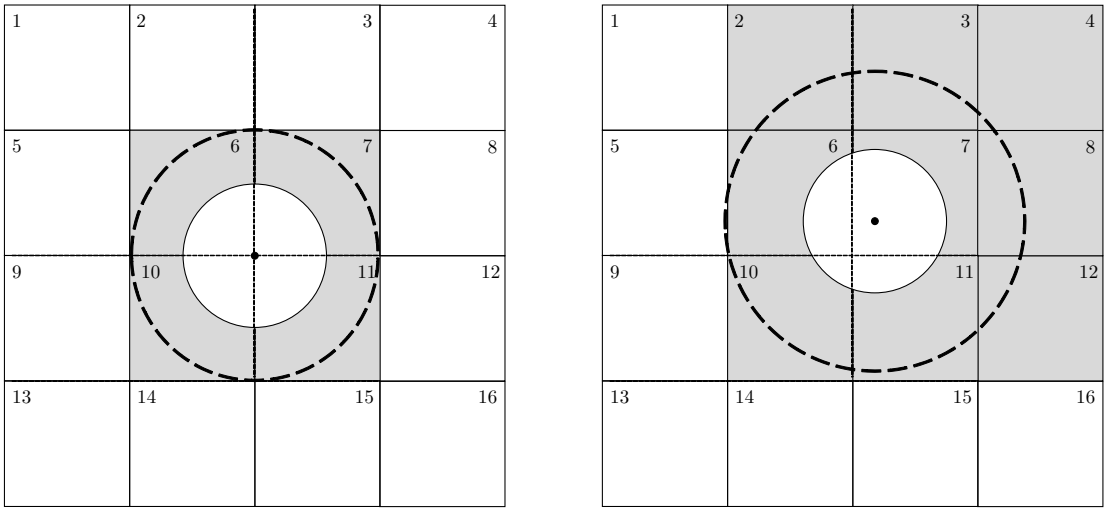

(a) Ideal constellation. **(b)** Unfavorable constellation.

Figure B.4: Colored cells with increasing gray gradient color for increasing solid phase concentration for different positioned particles using the Porous Sphere Model in an ideal (a) and unfavorable constellation of particle position (b).

Simulations and validation of this model have shown, that the use of the Porous Sphere Model results in a higher accuracy than the Porous Cube Model while maintaining an

equal fast computational time. The higher accuracy results due to the identical shape of the imaginary sphere and the particle as opposed to the particle and a cube. The other advantages and drawbacks are similar to the Porous Cube Model.

B.5 Diffusion Based Model

The Diffusion Based Model [232, 233] uses a different approach. It combines the PCM with a diffusion equation to calculate the solid phase fraction. The solid phase fraction α_s is determined by solving the following diffusion equation:

$$\frac{\partial \alpha_\mathrm{s}}{\partial \tau} = \boldsymbol{\nabla}^2 \alpha_\mathrm{s}. \tag{B.2}$$

The pseudo-time τ is calculated with the time-step of the simulation and a unit diffusion coefficient. As an initial condition for the partial differential equation, the solid phase volume fraction is initialized using the PCM:

$$\alpha_{\mathrm{s},0} = \alpha_\mathrm{s}^\mathrm{PCM}. \tag{B.3}$$

With this initial condition Equation (B.2) is solved until the pseudo-time τ reaches a predefined diffusion time T. Sun and Xiao [232] suggest a diffusion time depending on the particle diameter of $T = 9 d_\mathrm{p}^2$. The diffusion equation is discretized by pseudo-timesteps and a pseudo-timestep of $\Delta\tau = T/8$ is recommended by the authors. Figure B.5 shows an exemplary scenario of a particle with surrounding cells. The cells are colored with different gray gradients according to the calculated solid phase volume fraction using the Diffusion Based Model.

A higher diffusion coefficient or a longer pseudo-time results in a wider distribution of the solid phase concentration field. This approach is rather quick compared to DPVM and the Porous Cube or Sphere Model, as the solid phase fraction field is initialized with PCM and a diffusion equation is solved and no adjacent cells need to be located. If the numerical grid is highly resolved, i.e., a high number of cells, the Diffusion Based Model can be slower compared to the other models. The diffusion equation is solved for all cells, regardless if particles reside in the cells or not. Hence, with a higher number of particles, more diffusion equations have to be solved. The biggest advantage using this model is the smooth transition between the solid phase fraction across neighboring cells.

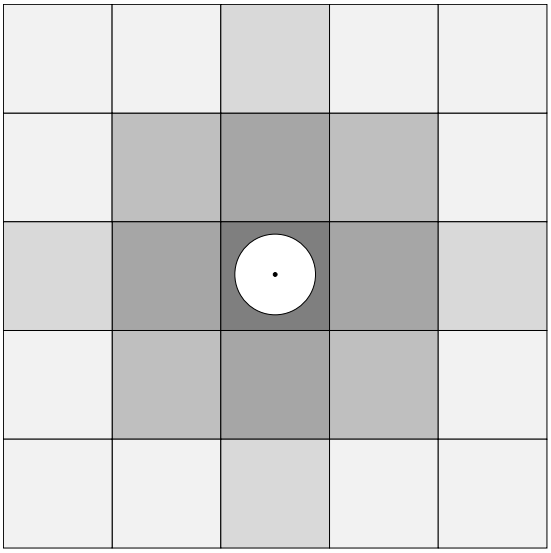

Figure B.5: Colored cells with increasing gray gradient color for increasing solid phase concentration for different positioned particles using the Diffusion Based Model.

C Bibliography

[1] R. Perry, *Perry's Chemical Engineers' Handbook*, McGraw-Hill, New York, **2008**.

[2] F. Asinger, *Methanol - Chemie- und Energierohstoff*, Springer Berlin Heidelberg, **1986**, DOI 10.1007/978-3-642-70763-6.

[3] *Fluidization*, (Eds.: J. R. Grace, J. M. Matsen), Springer US, **1980**, DOI 10.1007/978-1-4684-1045-7.

[4] J. G. Yates, P. Lettieri, *Fluidized-Bed Reactors: Processes and Operating Conditions*, Springer International Publishing, **2016**, DOI 10.1007/978-3-319-39593-7.

[5] D. Kunii, O. Levenspiel, *Fluidization Engineering*, 2nd ed., Butterworth-Heinemann, Boston, **1991**.

[6] E. W. Grohse, "Analysis of gas-fluidized solid systems by x-ray absorption", *AIChE Journal* **1955**, *1*, 358–365, DOI 10.1002/aic.690010315.

[7] G. Yasui, L. N. Johanson, "Characteristics of gas pockets in fluidized beds", *AIChE Journal* **1958**, *4*, 445–452, DOI 10.1002/aic.690040413.

[8] R. Toomey, H. Johnstone, "Gaseous fluidization of solid particles", *Chemical Engineering Progress* **1952**, *48*, 220–226.

[9] H. S. Mickley, D. F. Fairbanks, "Mechanism of heat transfer to fluidized beds", *AIChE Journal* **1955**, *1*, 374–384, DOI 10.1002/aic.690010317.

[10] D. Parker, M. Hawkesworth, C. Broadbent, P. Fowles, T. Fryer, P. McNeil, "Industrial positron-based imaging: Principles and applications", *Nuclear Instruments and Methods in Physics Research Section A: Accelerators Spectrometers Detectors and Associated Equipment* **1994**, *348*, 583–592, DOI 10.1016/0168-9002(94)90805-2.

[11] P. Foscolo, L. Gibilaro, "A fully predictive criterion for the transition between particulate and aggregate fluidization", *Chemical Engineering Science* **1984**, *39*, 1667–1675, DOI 10.1016/0009-2509(84)80100-1.

[12] D. Geldart, "Types of gas fluidization", *Powder Technology* **1973**, *7*, 285–292, DOI 10.1016/0032-5910(73)80037-3.

[13] J. R. Grace, "Contacting modes and behaviour classification of gas-solid and other two-phase suspensions", *The Canadian Journal of Chemical Engineering* **1986**, *64*, 353–363, DOI 10.1002/cjce.5450640301.

[14] Y. Tsuji, T. Kawaguchi, T. Tanaka, "Discrete particle simulation of two-dimensional fluidized bed", *Powder Technology* **1993**, *77*, 79–87, DOI 10.1016/0032-5910(93)85010-7.

[15] D. Gidaspow, *Multiphase Flow and Fluidization: Continuum and Kinetic Theory Descriptions*, Academic press, **1994**.

[16] C. Müller, D. Holland, A. Sederman, M. Mantle, L. Gladden, J. Davidson, "Magnetic Resonance Imaging of fluidized beds", *Powder Technology* **2008**, *183*, 53–62, DOI 10.1016/j.powtec.2007.11.029.

[17] H. P. Le, J.-L. Cambier, L. K. Cole, "GPU-based flow simulation with detailed chemical kinetics", *Computer Physics Communications* **2013**, *184*, 596–606, DOI 10.1016/j.cpc.2012.10.013.

[18] D. Jajcevic, E. Siegmann, C. Radeke, J. G. Khinast, "Large-scale CFD–DEM simulations of fluidized granular systems", *Chemical Engineering Science* **2013**, *98*, 298–310, DOI 10.1016/j.ces.2013.05.014.

[19] L.-S. Fan, *Gas-liquid-solid Fluidization Engineering*, Butterworths, Boston, **1989**.

[20] F. Alobaid, N. Almohammed, M. M. Farid, J. May, P. Rößger, A. Richter, B. Epple, "Progress in CFD Simulations of Fluidized Beds for Chemical and Energy Process Engineering", *Progress in Energy and Combustion Science* **2021**, 100930, DOI 10.1016/j.pecs.2021.100930.

[21] O. Molerus, "Interpretation of Geldart's type A, B, C and D powders by taking into account interparticle cohesion forces", *Powder Technology* **1982**, *33*, 81–87, DOI 10.1016/0032-5910(82)85041-9.

[22] S. Limtrakul, A. Boonsrirat, T. Vatanatham, "DEM modeling and simulation of a catalytic gas–solid fluidized bed reactor: a spouted bed as a case study", *Chemical Engineering Science* **2004**, *59*, 5225–5231, DOI 10.1016/j.ces.2004.09.020.

[23] M. S. van Buijtenen, W.-J. van Dijk, N. G. Deen, J. Kuipers, T. Leadbeater, D. Parker, "Numerical and experimental study on multiple-spout fluidized beds", *Chemical Engineering Science* **2011**, *66*, 2368–2376, DOI 10.1016/j.ces.2011.02.055.

[24] Yang, *Handbook of Fluidization and Fluid-particle Systems*, Marcel Dekker, New York, **2003**.

[25] A. Saddoud, M. Ellouze, A. Dhouib, S. Sayadi, "A Comparative Study on the Anaerobic Membrane Bioreactor Performance During the Treatment of Domestic Wastewaters of Various Origins", *Environmental Technology* **2006**, *27*, 991–999, DOI 10.1080/09593332708618712.

[26] Y. He, P. Xu, C. Li, B. Zhang, "High-concentration food wastewater treatment by an anaerobic membrane bioreactor", *Water Research* **2005**, *39*, 4110–4118, DOI 10.1016/j.watres.2005.07.030.

[27] J. Svojitka, L. Dvořák, M. Studer, J. O. Straub, H. Frömelt, T. Wintgens, "Performance of an anaerobic membrane bioreactor for pharmaceutical wastewater treatment", *Bioresource Technology* **2017**, *229*, 180–189, DOI 10.1016/j.biortech.2017.01.022.

[28] R. P. Schwarzenbach, "The Challenge of Micropollutants in Aquatic Systems", *Science* **2006**, *313*, 1072–1077, DOI 10.1126/science.1127291.

[29] B. Marrot, A. Barrios-Martinez, P. Moulin, N. Roche, "Industrial wastewater treatment in a membrane bioreactor: A review", *Environmental Progress* **2004**, *23*, 59–68, DOI 10.1002/ep.10001.

[30] A. N. Ng, A. S. Kim, "A mini-review of modeling studies on membrane bioreactor (MBR) treatment for municipal wastewaters", *Desalination* **2007**, *212*, 261–281, DOI 10.1016/j.desal.2006.10.013.

[31] G. Skouteris, D. Hermosilla, P. López, C. Negro, Á. Blanco, "Anaerobic membrane bioreactors for wastewater treatment: A review", *Chemical Engineering Journal* **2012**, *198-199*, 138–148, DOI 10.1016/j.cej.2012.05.070.

[32] P. Krzeminski, J. H. J. M. van der Graaf, J. B. van Lier, "Specific energy consumption of membrane bioreactor (MBR) for sewage treatment", *Water Science and Technology* **2012**, *65*, 380–392, DOI 10.2166/wst.2012.861.

[33] B.-Q. Liao, J. T. Kraemer, D. M. Bagley, "Anaerobic Membrane Bioreactors: Applications and Research Directions", *Critical Reviews in Environmental Science and Technology* **2006**, *36*, 489–530, DOI 10.1080/10643380600678146.

[34] P. L. McCarty, J. Bae, J. Kim, "Domestic Wastewater Treatment as a Net Energy Producer-Can This be Achieved?", *Environmental Science & Technology* **2011**, *45*, 7100–7106, DOI 10.1021/es2014264.

[35] J. Wang, B. Wu, Y. Liu, A. G. Fane, J. W. Chew, "Monitoring local membrane fouling mitigation by fluidized GAC in lab-scale and pilot-scale AnFMBRs", *Separation and Purification Technology* **2018**, *199*, 331–345, DOI 10.1016/j.seppur.2018.01.067.

[36] K. Wang, D. Cingolani, A. Eusebi, A. Soares, B. Jefferson, E. McAdam, "Identification of gas sparging regimes for granular anaerobic membrane bioreactor to enable energy neutral municipal wastewater treatment", *Journal of Membrane Science* **2018**, *555*, 125–133, DOI 10.1016/j.memsci.2018.03.032.

[37] H. Lin, W. Peng, M. Zhang, J. Chen, H. Hong, Y. Zhang, "A review on anaerobic membrane bioreactors: Applications, membrane fouling and future perspectives", *Desalination* **2013**, *314*, 169–188, DOI 10.1016/j.desal.2013.01.019.

[38] A. Ding, J. Wang, D. Lin, R. Zeng, S. Yu, Z. Gan, N. Ren, G. Li, H. Liang, "Effects of GAC layer on the performance of gravity-driven membrane filtration (GDM) system for rainwater recycling", *Chemosphere* **2018**, *191*, 253–261, DOI 10.1016/j.chemosphere.2017.10.034.

[39] C. Chen, Z. Liu, X. Huang in *Current Developments in Biotechnology and Bioengineering*, Elsevier, **2020**, pp. 335–366, DOI 10.1016/b978-0-12-819852-0.00014-2.

[40] J. Wang, B. Wu, J. W. Chew, "Membrane fouling mitigation by fluidized granular activated carbon: Effect of fiber looseness and impact on irreversible fouling", *Separation and Purification Technology* **2020**, *242*, 116764, DOI 10.1016/j.seppur.2020.116764.

[41] C. Chen, W. Guo, H. H. Ngo, S. W. Chang, D. D. Nguyen, P. D. Nguyen, X. T. Bui, Y. Wu, "Impact of reactor configurations on the performance of a granular anaerobic membrane bioreactor for municipal wastewater treatment", *International Biodeterioration & Biodegradation* **2017**, *121*, 131–138, DOI 10.1016/j.ibiod.2017.03.021.

[42] W.-H. Chen, C.-Y. Tsai, S.-Y. Chen, S. Sung, J.-G. Lin, "Treatment of campus domestic wastewater using ambient-temperature anaerobic fluidized membrane bioreactors with zeolites as carriers", *International Biodeterioration & Biodegradation* **2019**, *136*, 49–54, DOI 10.1016/j.ibiod.2018.10.010.

[43] A. Ding, H. Liang, F. Qu, L. Bai, G. Li, H. H. Ngo, W. Guo, "Effect of granular activated carbon addition on the effluent properties and fouling potentials of membrane-coupled expanded granular sludge bed process", *Bioresource Technology* **2014**, *171*, 240–246, DOI 10.1016/j.biortech.2014.08.080.

[44] J. Wang, F. Zamani, A. Cahyadi, J. Y. Toh, S. Yang, B. Wu, Y. Liu, A. G. Fane, J. W. Chew, "Correlating the hydrodynamics of fluidized granular activated carbon (GAC) with membrane-fouling mitigation", *Journal of Membrane Science* **2016**, *510*, 38–49, DOI https://doi.org/10.1016/j.memsci.2016.03.009.

[45] J. Wang, A. G. Fane, J. W. Chew, "Relationship between scouring efficiency and overall concentration of fluidized granular activated carbon (GAC) in microfiltration", *Chemical Engineering Research and Design* **2018**, *132*, 28–39, DOI https://doi.org/10.1016/j.cherd.2017.12.049.

[46] A. Cahyadi, S. Yang, J. W. Chew, "CFD study on the hydrodynamics of fluidized granular activated carbon in AnFMBR applications", *Separation and Purification Technology* **2017**, *178*, 75–89.

[47] A. Cahyadi, A. G. Fane, J. W. Chew, "Correlating the hydrodynamics of fluidized media with the extent of membrane fouling mitigation: Effect of bidisperse GAC mixtures", *Separation and Purification Technology* **2018**, *192*, 309–321, DOI 10.1016/j.seppur.2017.10.019.

[48] D. Hirche, J. W. Chew, O. Hinrichsen, "CFD-DEM study of geometry changes in an AnFMBR towards particle momentum", *Chemical Engineering Journal* **2020**, *379*, 122336, DOI 10.1016/j.cej.2019.122336.

[49] H. K. Versteeg, *An Introduction to Computational Fluid Dynamics: the Finite Volume Method*, Pearson Education Ltd, Harlow, England New York, **2007**.

[50] F. Moukalled, L. Mangani, M. Darwish, *The Finite Volume Method in Computational Fluid Dynamics*, Springer International Publishing, **2016**, DOI 10.1007/978-3-319-16874-6.

[51] T. Arens, F. Hettlich, C. Karpfinger, U. Kockelkorn, K. Lichtenegger, *Mathematik*, Springer-Verlag GmbH, **2018**.

[52] J. H. Ferziger, M. Perić, *Computational Methods for Fluid Dynamics*, Springer, **2002**.

[53] H. Enwald, E. Peirano, A.-E. Almstedt, "Eulerian two-phase flow theory applied to fluidization", *International Journal of Multiphase Flow* **1996**, *22*, 21–66, DOI 10.1016/s0301-9322(96)90004-x.

[54] R. Panton, *Incompressible Flow*, John Wiley and Sons, Inc, Hoboken, New Jersey, **2013**.

[55] H. Rusche, "Computational fluid dynamics of dispersed two-phase flows at high phase fractions", *PhD Thesis* **2002**.

[56] C. Hirt, A. Amsden, J. Cook, "An arbitrary Lagrangian-Eulerian computing method for all flow speeds", *Journal of Computational Physics* **1974**, *14*, 227–253, DOI 10.1016/0021-9991(74)90051-5.

[57] H. Jasak, "Error analysis and estimation for the finite volume method with applications to fluid flows.", *PhD Thesis* **1996**.

[58] S. V. Patankar, B. R. Baliga, "A New Finite-difference Scheme for Parabolic Differential Equations", *Numerical Heat Transfer* **1978**, *1*, 27–37, DOI 10.1080/10407787808913362.

[59] M. Peric, "A finite volume method for the prediction of three-dimensional fluid flow in complex ducts.", *PhD Thesis* **1985**.

[60] S. Muzaferija, "Adaptive finite volume method for flow prediction using unstructured meshes and multigrid approach", *PhD Thesis* **1994**.

[61] Y. Liu, O. Hinrichsen, "CFD modeling of bubbling fluidized beds using OpenFOAM®: Model validation and comparison of TVD differencing schemes", *Computers and Chemical Engineering* **2014**, *69*, 75–88, DOI 10.1016/j.compchemeng.2014.07.002.

[62] J. Crank, P. Nicolson, "A practical method for numerical evaluation of solutions of partial differential equations of the heat-conduction type", *Mathematical Proceedings of the Cambridge Philosophical Society* **1947**, *43*, 50–67, DOI 10.1017/s0305004100023197.

[63] C. S. Peskin, "Flow patterns around heart valves: A numerical method", *Journal of Computational Physics* **1972**, *10*, 252–271, DOI 10.1016/0021-9991(72)90065-4.

[64] C. S. Peskin, "The immersed boundary method", *Acta Numerica* **2002**, *11*, 479–517, DOI 10.1017/s0962492902000077.

[65] N. G. Deen, J. A. M. Kuipers, "Direct Numerical Simulation of Fluid Flow and Mass Transfer in Dense Fluid–Particle Systems", *Industrial & Engineering Chemistry Research* **2013**, *52*, 11266–11274, DOI 10.1021/ie303411k.

[66] D. Kandhai, J. J. Derksen, H. E. A. van den Akker, "Interphase drag coefficients in gas–solid flows", *AIChE Journal* **2003**, *49*, 1060–1065, DOI 10.1002/aic.690490423.

[67] M. A. van der Hoef, R. Beetstra, J. A. M. Kuipers, "Lattice-Boltzmann simulations of low-Reynolds-number flow past mono- and bidisperse arrays of spheres: results for the permeability and drag force", *Journal of Fluid Mechanics* **2005**, *528*, 233–254, DOI 10.1017/s0022112004003295.

[68] S. Tenneti, R. Garg, S. Subramaniam, "Drag law for monodisperse gas–solid systems using particle-resolved direct numerical simulation of flow past fixed assemblies of spheres", *International Journal of Multiphase Flow* **2011**, *37*, 1072–1092, DOI 10.1016/j.ijmultiphaseflow.2011.05.010.

[69] Y. Tang, E. A. J. F. Peters, J. A. M. Kuipers, S. H. L. Kriebitzsch, M. A. van der Hoef, "A new drag correlation from fully resolved simulations of flow past monodisperse static arrays of spheres", *AIChE Journal* **2014**, *61*, 688–698, DOI 10.1002/aic.14645.

[70] M. Goldschmidt, R. Beetstra, J. Kuipers, "Hydrodynamic modelling of dense gas-fluidised beds: comparison and validation of 3D discrete particle and continuum models", *Powder Technology* **2004**, *142*, 23–47, DOI 10.1016/j.powtec.2004.02.020.

[71] R. Jackson, "Locally averaged equations of motion for a mixture of identical spherical particles and a Newtonian fluid", *Chemical Engineering Science* **1997**, *52*, 2457–2469, DOI 10.1016/s0009-2509(97)00065-1.

[72] T. B. Anderson, R. Jackson, "Fluid Mechanical Description of Fluidized Beds. Equations of Motion", *Industrial & Engineering Chemistry Fundamentals* **1967**, *6*, 527–539, DOI 10.1021/i160024a007.

[73] K. Myöhänen, T. Hyppänen, "A Three-Dimensional Model Frame for Modelling Combustion and Gasification in Circulating Fluidized Bed Furnaces", *International Journal of Chemical Reactor Engineering* **2011**, *9*, DOI 10.1515/1542-6580.2571.

[74] P. Ostermeier, A. Vandersickel, S. Gleis, H. Spliethoff, "Numerical Approaches for Modeling Gas–Solid Fluidized Bed Reactors: Comparison of Models and Application to Different Technical Problems", *Journal of Energy Resources Technology* **2019**, *141*, DOI 10.1115/1.4043327.

[75] R. F. Fedors, "A relationship between maximum packing of particles and particle size", *Powder Technology* **1979**, *22*, 71–76, DOI 10.1016/0032-5910(79)85008-1.

[76] L. Oger, S. B. Savage, "Airslide flows. Part 2—Flow modeling and comparison with experiments", *Chemical Engineering Science* **2013**, *91*, 22–34, DOI 10.1016/j.ces.2012.12.042.

[77] M. W. Baltussen, K. A. Buist, E. A. Peters, J. A. Kuipers in *Bridging Scales in Modelling and Simulation of Non-Reacting and Reacting Flows. Part II*, Elsevier, **2018**, pp. 1–52, DOI 10.1016/bs.ache.2018.02.001.

[78] J. Ding, D. Gidaspow, "A bubbling fluidization model using kinetic theory of granular flow", *AIChE Journal* **1990**, *36*, 523–538, DOI 10.1002/aic.690360404.

[79] J. T. Jenkins, S. B. Savage, "A theory for the rapid flow of identical, smooth, nearly elastic, spherical particles", *Journal of Fluid Mechanics* **1983**, *130*, 187, DOI 10.1017/s0022112083001044.

[80] C. K. K. Lun, S. B. Savage, D. J. Jeffrey, N. Chepurniy, "Kinetic theories for granular flow: inelastic particles in Couette flow and slightly inelastic particles in a general flowfield", *Journal of Fluid Mechanics* **1984**, *140*, 223, DOI 10.1017/s0022112084000586.

[81] Y. Zhao, B. Lu, Y. Zhong, "Euler-Euler modeling of a gas-solid bubbling fluidized bed with kinetic theory of rough particles", *Chemical Engineering Science* **2013**, *104*, 767–779, DOI 10.1016/j.ces.2013.10.001.

[82] L. Yang, J. Padding, J. Kuipers, "Modification of kinetic theory of granular flow for frictional spheres, part II: Model validation", *Chemical Engineering Science* **2016**, *152*, 783–794, DOI 10.1016/j.ces.2016.06.015.

[83] J. J. Nieuwland, M. van Sint Annaland, J. A. M. Kuipers, W. P. M. van Swaaij, "Hydrodynamic modeling of gas/particle flows in riser reactors", *AIChE Journal* **1996**, *42*, 1569–1582, DOI 10.1002/aic.690420608.

[84] M. Syamlal, W. Rogers, T. O'Brien, "MFIX Documentation Theory Guide, US Department of Energy, Office of Fossil Energy Morgantown Energy Technology Center, Morgantown", *West Virginia. USA* **1993**.

[85] P. C. Johnson, R. Jackson, "Frictional-collisional constitutive relations for granular materials, with application to plane shearing", *Journal of Fluid Mechanics* **1987**, *176*, 67, DOI 10.1017/s0022112087000570.

[86] R. Ocone, S. Sundaresan, R. Jackson, "Gas-Particle flow in a duct of arbitrary inclination with particle-particle interactions", *AIChE Journal* **1993**, *39*, 1261–1271, DOI 10.1002/aic.690390802.

[87] D. G. Schaeffer, "Instability in the evolution equations describing incompressible granular flow", *Journal of Differential Equations* **1987**, *66*, 19–50, DOI 10.1016/0022-0396(87)90038-6.

[88] G. Ahmadi, D. Ma, "A thermodynamical formulation for dispersed multiphase turbulent flows", *International Journal of Multiphase Flow* **1990**, *16*, 323–340, DOI 10.1016/0301-9322(90)90062-n.

[89] S. Chapman, T. Cowling, "The Mathematical Theory of Non-Uniform Gases", *Cambridge Mathematical Library* **1970**.

[90] S. Ogawa, A. Umemura, N. Oshima, "On the equations of fully fluidized granular materials", *Zeitschrift für angewandte Mathematik und Physik* **1980**, *31*, 483–493, DOI 10.1007/bf01590859.

[91] B. J. Alder, T. E. Wainwright, "Studies in Molecular Dynamics. II. Behavior of a Small Number of Elastic Spheres", *The Journal of Chemical Physics* **1960**, *33*, 1439–1451, DOI 10.1063/1.1731425.

[92] D. Ma, G. Ahmadi, "An equation of state for dense rigid sphere gases", *The Journal of Chemical Physics* **1986**, *84*, 3449–3450, DOI 10.1063/1.450229.

[93] S. Torquato, "Nearest-neighbor statistics for packings of hard spheres and disks", *Physical Review E* **1995**, *51*, 3170–3182, DOI 10.1103/physreve.51.3170.

[94] P. Ostermeier, S. DeYoung, A. Vandersickel, S. Gleis, H. Spliethoff, "Comprehensive investigation and comparison of TFM, DenseDPM and CFD-DEM for dense fluidized beds", *Chemical Engineering Science* **2019**, *196*, 291–309, DOI 10.1016/j.ces.2018.11.007.

[95] C. M. Hrenya, J. L. Sinclair, "Effects of particle-phase turbulence in gas-solid flows", *AIChE Journal* **1997**, *43*, 853–869, DOI 10.1002/aic.690430402.

[96] M. Y. Louge, E. Mastorakos, J. T. Jenkins, "The role of particle collisions in pneumatic transport", *Journal of Fluid Mechanics* **1991**, *231*, 345, DOI 10.1017/s0022112091003427.

[97] N. Yang, W. Wang, W. Ge, J. Li, "CFD simulation of concurrent-up gas-solid flow in circulating fluidized beds with structure-dependent drag coefficient", *Chemical Engineering Journal and the Biochemical Engineering Journal* **2003**, *96*, 71–80, DOI 10.1016/j.cej.2003.08.006.

[98] O. Ayeni, C. Wu, K. Nandakumar, J. Joshi, "Development and validation of a new drag law using mechanical energy balance approach for DEM-CFD simulation of gas-solid fluidized bed", *Chemical Engineering Journal and the Biochemical Engineering Journal* **2016**, *302*, 395–405, DOI 10.1016/j.cej.2016.05.056.

[99] A. D. Renzo, F. P. D. Maio, "Homogeneous and bubbling fluidization regimes in DEM-CFD simulations: Hydrodynamic stability of gas and liquid fluidized beds", *Chemical Engineering Science* **2007**, *62*, 116–130, DOI 10.1016/j.ces.2006.08.009.

[100] K. Papadikis, A. Bridgwater, S. Gu, "CFD modelling of the fast pyrolysis of biomass in fluidised bed reactors, Part A: Eulerian computation of momentum transport in bubbling fluidised beds", *Chemical Engineering Science* **2008**, *63*, 4218–4227, DOI 10.1016/j.ces.2008.05.045.

[101] C. T. Crowe, J. D. Schwarzkopf, M. Sommerfeld, Y. Tsuji, *Multiphase Flows with Droplets and Particles*, Taylor & Francis Ltd., **2011**.

[102] L. M. Milne-Thomson, *Theoretical Hydrodynamics*, Dover Publications, **2013**.

[103] N. Zuber, "On the dispersed two-phase flow in the laminar flow regime", *Chemical Engineering Science* **1964**, *19*, 897–917, DOI 10.1016/0009-2509(64)85067-3.

[104] F. Odar, "Verification of the proposed equation for calculation of the forces on a sphere accelerating in a viscous fluid", *Journal of Fluid Mechanics* **1966**, *25*, 591–592, DOI 10.1017/s0022112066000272.

[105] P.-R. Schöneborn, "The interaction between a single particle and an oscillating fluid", *International Journal of Multiphase Flow* **1975**, *2*, 307–317, DOI 10.1016/0301-9322(75)90016-6.

[106] D. Drew, L. Cheng, R. Lahey, "The analysis of virtual mass effects in two-phase flow", *International Journal of Multiphase Flow* **1979**, *5*, 233–242, DOI 10.1016/0301-9322(79)90023-5.

[107] D. Drew, R. Lahey, "The virtual mass and lift force on a sphere in rotating and straining inviscid flow", *International Journal of Multiphase Flow* **1987**, *13*, 113–121, DOI 10.1016/0301-9322(87)90011-5.

[108] A. Bakshi, C. Altantzis, A. Bershanska, A. Stark, A. Ghoniem, "On the limitations of 2D CFD for thin-rectangular fluidized bed simulations", *Powder Technology* **2018**, *332*, 114–119, DOI 10.1016/j.powtec.2018.03.048.

[109] L. Huilin, D. Gidaspow, "Hydrodynamics of binary fluidization in a riser: CFD simulation using two granular temperatures", *Chemical Engineering Science* **2003**, *85*, 22–31.

[110] P. Ostermeier, A. Vandersickel, S. Gleis, H. Spliethoff, "Three dimensional multi fluid modeling of Geldart B bubbling fluidized bed with complex inlet geometries", *Powder Technology* **2017**, *312*, 89–102, DOI 10.1016/j.powtec.2017.02.015.

[111] P. Ostermeier, A. Vandersickel, M. Becker, S. Gleis, H. Spliethoff, "Hydrodynamics and heat transfer around a horizontal tube immersed in a Geldart b bubbling fluidized bed", *International Journal of Computational Methods and Experimental Measurements* **2017**, *6*, 71–85, DOI 10.2495/cmem-v6-n1-71-85.

[112] A. Passalacqua, F. Laurent, E. Madadi-Kandjani, J. Heylmun, R. Fox, "An open-source quadrature-based population balance solver for OpenFOAM", *Chemical Engineering Science* **2018**, *176*, 306–318, DOI 10.1016/j.ces.2017.10.043.

[113] P. J. Stopford, "Recent applications of CFD modelling in the power generation and combustion industries", *Applied Mathematical Modelling* **2002**, *26*, 351–374, DOI 10.1016/s0307-904x(01)00066-x.

[114] B. Xia, D.-W. Sun, "Applications of computational fluid dynamics (cfd) in the food industry: a review", *Computers and Electronics in Agriculture* **2002**, *34*, 5–24, DOI 10.1016/s0168-1699(01)00177-6.

[115] N. Yang, W. Wang, W. Ge, L. Wang, J. Li, "Simulation of heterogeneous structure in a circulating fluidized-bed riser by combining the two-fluid model with the EMMS approach", *Industrial & Engineering Chemistry Research* **2004**, *43*, 5548–5561.

[116] J. Wang, W. Ge, J. Li, "Eulerian simulation of heterogeneous gas–solid flows in CFB risers: EMMS-based sub-grid scale model with a revised cluster description", *Chemical Engineering Science* **2008**, *63*, 1553–1571, DOI 10.1016/j.ces.2007.11.023.

[117] S. Elghobashi, "Particle-laden turbulent flows: direct simulation and closure models", *Applied Scientific Research* **1991**, *48*, 301–314, DOI 10.1007/bf02008202.

[118] S. Elghobashi, "On predicting particle-laden turbulent flows", *Applied Scientific Research* **1994**, *52*, 309–329, DOI 10.1007/bf00936835.

[119] P. A. Cundall, O. D. L. Strack, "A discrete numerical model for granular assemblies", *Géotechnique* **1979**, *29*, 47–65, DOI 10.1680/geot.1979.29.1.47.

[120] N. Deen, M. van Sint Annaland, M. van der Hoef, J. Kuipers, "Review of discrete particle modeling of fluidized beds", *Chemical Engineering Science* **2007**, *62*, 28–44, DOI 10.1016/j.ces.2006.08.014.

[121] H. Zhu, Z. Zhou, R. Yang, A. Yu, "Discrete particle simulation of particulate systems: Theoretical developments", *Chemical Engineering Science* **2007**, *62*, 3378–3396, DOI 10.1016/j.ces.2006.12.089.

[122] M. van der Hoef, M. Ye, M. van Sint Annaland, A. Andrews, S. Sundaresan, J. Kuipers in *Computational Fluid Dynamics*, Elsevier, **2006**, pp. 65–149, DOI 10.1016/s0065-2377(06)31002-2.

[123] Y. Tsuji, T. Tanaka, T. Ishida, "Lagrangian numerical simulation of plug flow of cohesionless particles in a horizontal pipe", *Powder Technology* **1992**, *71*, 239–250, DOI 10.1016/0032-5910(92)88030-l.

[124] C. Yang, Y. Duan, H. Hu, "Application of CFD-DEM to the study of solid exchange in a dual-leg fluidized bed", *Particuology* **2013**, *11*, 636–646, DOI 10.1016/j.partic.2013.01.008.

[125] F. Alobaid, B. Epple, "Improvement, validation and application of CFD/DEM model to dense gas–solid flow in a fluidized bed", *Particuology* **2013**, *11*, 514–526, DOI 10.1016/j.partic.2012.05.008.

[126] A. C. Varas, E. Peters, J. Kuipers, "CFD-DEM simulations and experimental validation of clustering phenomena and riser hydrodynamics", *Chemical Engineering Science* **2017**, *169*, 246–258, DOI 10.1016/j.ces.2016.08.030.

[127] Z.-M. Shi, H.-C. Zheng, S.-B. Yu, M. Peng, T. Jiang, "Application of CFD-DEM to investigate seepage characteristics of landslide dam materials", *Computers and Geotechnics* **2018**, *101*, 23–33, DOI 10.1016/j.compgeo.2018.04.020.

[128] S. Wang, K. Luo, C. Hu, J. Lin, J. Fan, "CFD-DEM simulation of heat transfer in fluidized beds: Model verification, validation, and application", *Chemical Engineering Science* **2019**, *197*, 280–295, DOI 10.1016/j.ces.2018.12.031.

[129] E. R. Santana, G. Pozzetti, B. Peters, "Application of a dual-grid multiscale CFD-DEM coupling method to model the raceway dynamics in packed bed reactors", *Chemical Engineering Science* **2019**, *205*, 46–57, DOI 10.1016/j.ces.2019.04.025.

[130] S. Kuang, M. Zhou, A. Yu, "CFD-DEM modelling and simulation of pneumatic conveying: A review", *Powder Technology* **2020**, *365*, 186–207, DOI 10.1016/j.powtec.2019.02.011.

[131] M. V. Tabib, S. T. Johansen, S. Amini, "A 3D CFD-DEM Methodology for Simulating Industrial Scale Packed Bed Chemical Looping Combustion Reactors", *Industrial & Engineering Chemistry Research* **2013**, *52*, 12041–12058, DOI 10.1021/ie302028s.

[132] M. Sakai, S. Koshizuka, "Large-scale discrete element modeling in pneumatic conveying", *Chemical Engineering Science* **2009**, *64*, 533–539, DOI 10.1016/j.ces.2008.10.003.

[133] M. Andrews, P. O'Rourke, "The multiphase particle-in-cell (MP-PIC) method for dense particulate flows", *International Journal of Multiphase Flow* **1996**, *22*, 379–402, DOI 10.1016/0301-9322(95)00072-0.

[134] F. H. Harlow, "The particle-in-cell method for numerical solution of problems in fluid dynamics", **1962**, DOI 10.2172/4769185.

[135] S. E. Harris, D. G. Crighton, "Solitons, solitary waves, and voidage disturbances in gas-fluidized beds", *Journal of Fluid Mechanics* **1994**, *266*, 243–276, DOI 10.1017/s0022112094000996.

[136] X. Chen, J. Wang, "A comparison of two-fluid model, dense discrete particle model and CFD-DEM method for modeling impinging gas–solid flows", *Powder Technology* **2014**, *254*, 94–102, DOI 10.1016/j.powtec.2013.12.056.

[137] S. Benyahia, J. E. Galvin, "Estimation of Numerical Errors Related to Some Basic Assumptions in Discrete Particle Methods", *Industrial & Engineering Chemistry Research* **2010**, *49*, 10588–10605, DOI 10.1021/ie100662z.

[138] S. Kraft, F. Kirnbauer, H. Hofbauer, "CPFD simulations of an industrial-sized dual fluidized bed steam gasification system of biomass with 8 MW fuel input", *Applied Energy* **2017**, *190*, 408–420, DOI 10.1016/j.apenergy.2016.12.113.

[139] T. Dymala, T. Wytrwat, S. Heinrich, "MP-PIC simulation of circulating fluidized beds using an EMMS based drag model for Geldart B particles", *Particuology* **2021**, *59*, 76–90, DOI 10.1016/j.partic.2021.07.002.

[140] H. Lu, X. Guo, W. Zhao, X. Gong, J. Lu, "Experimental and CPFD Numerical Study on Hopper Discharge", *Industrial & Engineering Chemistry Research* **2014**, *53*, 12160–12169, DOI 10.1021/ie403862f.

[141] J. Li, J. Kuipers, "Gas-particle interactions in dense gas-fluidized beds", *Chemical Engineering Science* **2003**, *58*, 711–718, DOI 10.1016/s0009-2509(02)00599-7.

[142] D. Patil, M. van Sint Annaland, J. Kuipers, "Critical comparison of hydrodynamic models for gas–solid fluidized beds - Part I: bubbling gas–solid fluidized beds operated with a jet", *Chemical Engineering Science* **2005**, *60*, 57–72, DOI 10.1016/j.ces.2004.07.059.

[143] L. Rayleigh, "XIX. On the instability of cylindrical fluid surfaces", *The London Edinburgh and Dublin Philosophical Magazine and Journal of Science* **1892**, *34*, 177–180, DOI 10.1080/14786449208620304.

[144] C. E. Lapple, C. B. Shepherd, "Calculation of Particle Trajectories", *Industrial & Engineering Chemistry* **1940**, *32*, 605–617, DOI 10.1021/ie50365a007.

[145] H. Allen, "The motion of a sphere in a viscous fluid", *The London Edinburgh and Dublin Philosophical Magazine and Journal of Science* **1900**, *50*, 323–338.

[146] J. Zeleny, L. McKeehan, "The terminal velocity of fall of small spheres in air", *Physical Review* **1910**, *30*, 535.

[147] H. D. Arnold, "Limitations imposed by slip and inertia terms upon Stoke's law for the motion of spheres through liquids", *The London Edinburgh and Dublin Philosophical Magazine and Journal of Science* **1911**, *22*, 755–775.

[148] C. Wieselsberger, "Der Luftwiderstand von Kugeln", *Zeitschrift für Flugtechnik und Motorluftschiffahrt* **1914**, *5*, 140–145.

[149] G. Shakespear, "Experiments on the resistance of the air to falling spheres", *The London Edinburgh and Dublin Philosophical Magazine and Journal of Science* **1914**, *28*, 728–734.

[150] O. Silvey, "The fall of mercury droplets in a viscous medium", *Physical Review* **1916**, *7*, 106.

[151] F. S. Schmidt, *Zur beschleunigten Bewegung kugelförmiger Körper in widerstehenden Mitteln*, E. Glausch, **1919**.

[152] H. Krey, *Widerstand von Sandkörnern und Kugeln bei der Bewegung im Wasser als Grundlage der Schwemmstoffbewegung in unseren Flüssen*, Mittler, **1921**.

[153] L. Prandtl, C. Wieselsberger, A. Betz, *Ergebnisse der Aerodynamischen Versuchsanstalt zu Göttingen - I. Lieferung*, Göttingen University Press, **2009**, DOI 10.17875/gup2009-100.

[154] D. L. Bacon, E. G. Reid, "The resistance of spheres in wind tunnels and in air", *NACA Report No. 185* **1924**.

[155] A. Knodel, "Über die Gasströmung in Röhren und den Luftwiderstand von Kugeln", *Annalen der Physik* **1926**, *385*, 533–587.

[156] H. Liebster, "Über den Widerstand von Kugeln", *Annalen der Physik* **1927**, *387*, 541–562.

[157] O. Flachsbart, "Recent researches on the air resistance of spheres", *Physikalische Zeitschrift* **1927**, *28*.

[158] R. Lunnon, "Fluid resistance to moving spheres", *Proceedings of the Royal Society of London. Series A Containing Papers of a Mathematical and Physical Character* **1928**, *118*, 680–694.

[159] J. Schmiedel, "Experimentelle Untersuchungen über die Fallbewegung von Kugeln and Scheiben in reibenden Flüssigkeiten", *Physikalische Zeitschrift* **1928**, *29*, 593–609.

[160] E. N. Jacobs, "Sphere Drag-Tests II: The Variable Density Wind Tunnel", *NACA Report No. 312* **1929**.

[161] C. B. Millikan, "The boundary layer and skin friction for a figure of revolution", *Trans. ASME* **1932**, *3*, 29–43.

[162] T. Allen, *Particle Size Measurement*, Springer Netherlands, **1990**, DOI 10.1007/978-94-009-0417-0.

[163] G. Stokes, "On the effect of internal friction of fluids on the motion of pendulums", *Transactions of the Cambridge Philosophical Society* **1850**, *9*, 106.

[164] L. Schiller, A. Naumann, "Über die grundlegenden Berechnungen bei der Schwerkraftaufbereitung", *Zeitschrift des Vereines Deutscher Ingenieure* **1933**, *77*, 318–320.

[165] D. Jones, D. Clarke, "Simulation of Flow Past a Sphere using the FluentCode", *Department of Defence (Defence Science and Technology Organization)* **2008**.

[166] I. Newton, *Mathematical Principles of Natural Philosophy*, A. Strahan, **1802**.

[167] W. R. Goossens, "Review of the empirical correlations for the drag coefficient of rigid spheres", *Powder Technology* **2019**, *352*, 350–359, DOI 10.1016/j.powtec.2019.04.075.

[168] S. Ergun, "Fluid flow through packed columns", *Chemical Engineering Progress* **1952**, *48*, 89–94.

[169] S. Ahmadi, F. Sefidvash, "Study of Pressure Drop in Fixed Bed Reactor Using a Computational Fluid Dynamics (CFD) Code", *ChemEngineering* **2018**, *2*, 14, DOI 10.3390/chemengineering2020014.

[170] C. Y. Wen, Y. H. Yu in Chemical Engineering Progress Symposium Series, *Vol. 62*, **1966**, pp. 100–111.

[171] J. Kuipers, K. V. Duin, F. V. Beckum, W. V. Swaaij, "A numerical model of gas-fluidized beds", *Chemical Engineering Science* **1992**, *47*, 1913–1924, DOI 10.1016/0009-2509(92)80309-z.

[172] J. Richardson, W. Zaki, "Sedimentation and fluidisation: Part I", *Transactions of the Institution of Chemical Engineers* **1954**, *32*, 35–53, DOI 10.1016/s0263-8762(97)80006-8.

[173] C. Loha, H. Chattopadhyay, P. K. Chatterjee, "Assessment of drag models in simulating bubbling fluidized bed hydrodynamics", *Chemical Engineering Science* **2012**, *75*, 400–407, DOI 10.1016/j.ces.2012.03.044.

[174] A. Fluent in *Release 2021 R1, Theory Guide*, ANSYS, Inc, **2021**.

[175] M. A. El-Emam, L. Zhou, W. Shi, C. Han, L. Bai, R. Agarwal, "Theories and Applications of CFD–DEM Coupling Approach for Granular Flow: A Review", *Archives of Computational Methods in Engineering* **2021**, DOI 10.1007/s11831-021-09568-9.

[176] M. Syamlal, T. O'Brien, "Computer Simulation of Bubbles in Fluidized Beds", *AIChE Symposium* **1989**, *85*, 22–31.

[177] J. Garside, M. R. Al-Dibouni, "Velocity-Voidage Relationships for Fluidization and Sedimentation in Solid-Liquid Systems", *Industrial & Engineering Chemistry Process Design and Development* **1977**, *16*, 206–214, DOI 10.1021/i260062a008.

[178] J. Dalla Valle, *Micromeritics: The Technology of Fine Particles*, Pitman, **1948**.

[179] R. J. Hill, D. Koch, A. J. C. Ladd, "The first effects of fluid inertia on flows in ordered and random arrays of spheres", *Journal of Fluid Mechanics* **2001**, *448*, 213–241, DOI 10.1017/s0022112001005948.

[180] R. J. Hill, D. Koch, A. J. C. Ladd, "Moderate-Reynolds-number flows in ordered and random arrays of spheres", *Journal of Fluid Mechanics* **2001**, *448*, 243–278, DOI 10.1017/S0022112001005936.

[181] D. L. Koch, R. J. Hill, "Inertial Effects in Suspension and Porous-Media Flows", *Annual Review of Fluid Mechanics* **2001**, *33*, 619–647, DOI 10.1146/annurev.fluid.33.1.619.

[182] G. Bokkers, M. van Sint Annaland, J. Kuipers, "Mixing and segregation in a bidisperse gas–solid fluidised bed: a numerical and experimental study", *Powder Technology* **2004**, *140*, 176–186, DOI 10.1016/j.powtec.2004.01.018.

[183] S. Benyahia, M. Syamlal, T. J. O'Brien, "Extension of Hill–Koch–Ladd drag correlation over all ranges of Reynolds number and solids volume fraction", *Powder Technology* **2006**, *162*, 166–174, DOI 10.1016/j.powtec.2005.12.014.

[184] L. Gibilaro, R. D. Felice, S. Waldram, P. Foscolo, "Generalized friction factor and drag coefficient correlations for fluid-particle interactions", *Chemical Engineering Science* **1985**, *40*, 1817–1823, DOI 10.1016/0009-2509(85)80116-0.

[185] H. Arastoopour, P. Pakdel, M. Adewumi, "Hydrodynamic analysis of dilute gas—solids flow in a vertical pipe", *Powder Technology* **1990**, *62*, 163–170, DOI 10.1016/0032-5910(90)80080-i.

[186] J. P. D. Plessis, "Analytical quantification of coefficients in the Ergun equation for fluid friction in a packed bed", *Transport in Porous Media* **1994**, *16*, 189–207, DOI 10.1007/bf00617551.

[187] R. D. Felice, "The voidage function for fluid-particle interaction systems", *International Journal of Multiphase Flow* **1994**, *20*, 153–159, DOI 10.1016/0301-9322(94)90011-6.

[188] J. Li, *Particle-Fluid Two-Phase Flow: The Energy-Minimization Multi-Scale Method*, Metallurgical Industry Press, **1994**.

[189] R. Beetstra, M. A. van der Hoef, J. A. M. Kuipers, "Drag force of intermediate Reynolds number flow past mono- and bidisperse arrays of spheres", *AIChE Journal* **2007**, *53*, 489–501, DOI 10.1002/aic.11065.

[190] Y. Tang, E. A. J. F. Peters, J. A. M. Kuipers, "Direct numerical simulations of dynamic gas-solid suspensions", *AIChE Journal* **2016**, *62*, 1958–1969, DOI 10.1002/aic.15197.

[191] Y. Zhang, J. M. Reese, "The drag force in two-fluid models of gas–solid flows", *Chemical Engineering Science* **2003**, *58*, 1641–1644, DOI 10.1016/s0009-2509(02)00659-0.

[192] M. Rüdisüli, T. J. Schildhauer, S. M. Biollaz, J. R. van Ommen, "Scale-up of bubbling fluidized bed reactors - A review", *Powder Technology* **2012**, *217*, 21–38, DOI 10.1016/j.powtec.2011.10.004.

[193] Y. Tsuji, "Multi-scale modeling of dense phase gas-particle flow", *Chemical Engineering Science* **2007**, *62*, 3410–3418, DOI 10.1016/j.ces.2006.12.090.

[194] M. Ishii, T. Hibiki, *Thermo-Fluid Dynamics of Two-Phase Flow*, Springer, **2010**.

[195] B. G. M. van Wachem, PhD thesis, TU Delft, **2000**.

[196] D. Snider, "An Incompressible Three-Dimensional Multiphase Particle-in-Cell Model for Dense Particle Flows", *Journal of Computational Physics* **2001**, *170*, 523–549, DOI 10.1006/jcph.2001.6747.

[197] P. J. O'Rourke, P. (Zhao, D. Snider, "A model for collisional exchange in gas/liquid/solid fluidized beds", *Chemical Engineering Science* **2009**, *64*, 1784–1797, DOI 10.1016/j.ces.2008.12.014.

[198] Y. Liu, G. Li, S. Kallio, "Hydrodynamic Modeling of Dense Gas-Particle Turbulence Flows Under Microgravity Space Environments", *Microgravity Science and Technology* **2010**, *23*, 1–11, DOI 10.1007/s12217-010-9199-4.

[199] C. Loha, H. Chattopadhyay, P. K. Chatterjee, "Euler-Euler CFD modeling of fluidized bed: Influence of specularity coefficient on hydrodynamic behavior", *Particuology* **2013**, *11*, 673–680, DOI 10.1016/j.partic.2012.08.007.

[200] Y. Zhao, B. Lu, Y. Zhong, "Influence of collisional parameters for rough particles on simulation of a gas-fluidized bed using a two-fluid model", *International Journal of Multiphase Flow* **2015**, *71*, 1–13, DOI 10.1016/j.ijmultiphaseflow.2014.12.002.

[201] C. R. Müller, D. J. Holland, A. J. Sederman, S. A. Scott, J. S. Dennis, L. F. Gladden, "Granular temperature: Comparison of Magnetic Resonance measurements with Discrete Element Model simulations", *Powder Technology* **2008**, *184*, 241–253, DOI 10.1016/j.powtec.2007.11.046.

[202] C. R. Müller, S. A. Scott, D. J. Holland, B. C. Clarke, A. J. Sederman, J. S. Dennis, L. F. Gladden, "Validation of a discrete element model using magnetic resonance measurements", *Particuology* **2009**, *7*, 297–306, DOI 10.1016/j.partic.2009.04.002.

[203] J. M. Link, N. G. Deen, J. A. M. Kuipers, X. Fan, A. Ingram, D. J. Parker, J. Wood, J. P. K. Seville, "PEPT and discrete particle simulation study of spout-fluid bed regimes", *AIChE Journal* **2008**, *54*, 1189–1202, DOI 10.1002/aic.11456.

[204] C. Goniva, C. Kloss, N. G. Deen, J. A. Kuipers, S. Pirker, "Influence of rolling friction on single spout fluidized bed simulation", *Particuology* **2012**, *10*, 582–591, DOI 10.1016/j.partic.2012.05.002.

[205] D. Zhang, W. Whiten, "The calculation of contact forces between particles using spring and damping models", *Powder Technology* **1996**, *88*, 59–64, DOI 10.1016/0032-5910(96)03104-x.

[206] H. G. Weller, G. Tabor, H. Jasak, C. Fureby, "A tensorial approach to computational continuum mechanics using object-oriented techniques", *Computational Physics* **1998**, *12*, 620, DOI 10.1063/1.168744.

[207] W. Zhong, A. Yu, G. Zhou, J. Xie, H. Zhang, "CFD simulation of dense particulate reaction system: Approaches, recent advances and applications", *Chemical Engineering Science* **2016**, *140*, 16–43, DOI 10.1016/j.ces.2015.09.035.

[208] J. Li, D. J. Mason, A. S. Mujumdar, "A Numerical Study of Heat Transfer Mechanisms in Gas-Solids Flows Through Pipes Using a Coupled CFD and DEM Model", *Drying Technology* **2003**, *21*, 1839–1866, DOI 10.1081/drt-120025511.

[209] F. P. D. Maio, A. D. Renzo, D. Trevisan, "Comparison of heat transfer models in DEM-CFD simulations of fluidized beds with an immersed probe", *Powder Technology* **2009**, *193*, 257–265, DOI 10.1016/j.powtec.2009.03.002.

[210] Y.-Q. Zhuang, X.-M. Chen, Z.-H. Luo, J. Xiao, "CFD-DEM modeling of gas-solid flow and catalytic MTO reaction in a fluidized bed reactor", *Computers & Chemical Engineering* **2014**, *60*, 1–16, DOI 10.1016/j.compchemeng.2013.08.007.

[211] X. Ku, T. Li, T. Løvås, "CFD-DEM simulation of biomass gasification with steam in a fluidized bed reactor", *Chemical Engineering Science* **2015**, *122*, 270–283, DOI 10.1016/j.ces.2014.08.045.

[212] P. Ostermeier, F. Fischer, S. Fendt, S. DeYoung, H. Spliethoff, "Coarse-grained CFD-DEM simulation of biomass gasification in a fluidized bed reactor", *Fuel* **2019**, *255*, 115790, DOI 10.1016/j.fuel.2019.115790.

[213] S. Golshan, R. Sotudeh-Gharebagh, R. Zarghami, N. Mostoufi, B. Blais, J. Kuipers, "Review and implementation of CFD-DEM applied to chemical process systems", *Chemical Engineering Science* **2020**, *221*, 115646, DOI 10.1016/j.ces.2020.115646.

[214] N. G. Deen, E. Peters, J. T. Padding, J. Kuipers, "Review of direct numerical simulation of fluid-particle mass, momentum and heat transfer in dense gas-solid flows", *Chemical Engineering Science* **2014**, *116*, 710–724, DOI 10.1016/j.ces.2014.05.039.

[215] J. Link, L. Cuypers, N. Deen, J. Kuipers, "Flow regimes in a spout-fluid bed: A combined experimental and simulation study", *Chemical Engineering Science* **2005**, *60*, 3425–3442, DOI 10.1016/j.ces.2005.01.027.

[216] S. Yang, Y. Sun, L. Zhang, Y. Zhao, J. W. Chew, "Numerical investigation on the effect of draft plates on spouting stability and gas-solid characteristics in a spout-fluid bed", *Chemical Engineering Science* **2016**, *148*, 108–125, DOI 10.1016/j.ces.2016.03.010.

[217] M. Detamore, M. Swanson, K. Frender, C. Hrenya, "A kinetic-theory analysis of the scale-up of circulating fluidized beds", *Powder Technology* **2001**, *116*, 190–203, DOI 10.1016/s0032-5910(00)00397-1.

[218] V. Verma, N. G. Deen, J. T. Padding, J. Kuipers, "Two-fluid modeling of three-dimensional cylindrical gas-solid fluidized beds using the kinetic theory of granular flow", *Chemical Engineering Science* **2013**, *102*, 227–245, DOI 10.1016/j.ces.2013.08.002.

[219] C. Moliner, F. Marchelli, N. Spanachi, A. Martinez-Felipe, B. Bosio, E. Arato, "CFD simulation of a spouted bed: Comparison between the Discrete Element Method (DEM) and the Two Fluid Model (TFM)", *Chemical Engineering Journal* **2019**, *377*, 120466, DOI 10.1016/j.cej.2018.11.164.

[220] M. Sakai, M. Abe, Y. Shigeto, S. Mizutani, H. Takahashi, A. Viré, J. R. Percival, J. Xiang, C. C. Pain, "Verification and validation of a coarse grain model of the DEM in a bubbling fluidized bed", *Chemical Engineering Journal* **2014**, *244*, 33–43, DOI 10.1016/j.cej.2014.01.029.

[221] K. Chu, J. Chen, A. Yu, "Applicability of a coarse-grained CFD-DEM model on dense medium cyclone", *Minerals Engineering* **2016**, *90*, 43–54, DOI 10.1016/j.mineng.2016.01.020.

[222] K. Takabatake, Y. Mori, J. G. Khinast, M. Sakai, "Numerical investigation of a coarse-grain discrete element method in solid mixing in a spouted bed", *Chemical Engineering Journal* **2018**, *346*, 416–426, DOI 10.1016/j.cej.2018.04.015.

[223] J. E. Hilton, P. W. Cleary, "Comparison of non-cohesive resolved and coarse grain DEM models for gas flow through particle beds", *Applied Mathematical Modelling* **2014**, *38*, 4197–4214, DOI 10.1016/j.apm.2014.02.013.

[224] A. Stroh, F. Alobaid, M. von Bohnstein, J. Ströhle, B. Epple, "Numerical CFD simulation of 1 MWth circulating fluidized bed using the coarse grain discrete element method with homogenous drag models and particle size distribution", *Fuel Processing Technology* **2018**, *169*, 84–93, DOI 10.1016/j.fuproc.2017.09.014.

[225] A. Stroh, A. Daikeler, M. Nikku, J. May, F. Alobaid, M. von Bohnstein, J. Ströhle, B. Epple, "Coarse grain 3D CFD-DEM simulation and validation with capacitance probe measurements in a circulating fluidized bed", *Chemical Engineering Science* **2019**, *196*, 37–53, DOI 10.1016/j.ces.2018.11.052.

[226] Z. Peng, E. Doroodchi, C. Luo, B. Moghtaderi, "Influence of void fraction calculation on fidelity of CFD-DEM simulation of gas-solid bubbling fluidized beds", *AIChE Journal* **2014**, *60*, 2000–2018, DOI 10.1002/aic.14421.

[227] F. Alobaid, J. Ströhle, B. Epple, "Extended CFD/DEM model for the simulation of circulating fluidized bed", *Advanced Powder Technology* **2013**, *24*, 403–415, DOI 10.1016/j.apt.2012.09.003.

[228] J. Su, Z. Gu, C. Chen, X. Y. Xu, "A two-layer mesh method for discrete element simulation of gas-particle systems with arbitrarily polyhedral mesh", *International Journal for Numerical Methods in Engineering* **2015**, *103*, 759–780, DOI 10.1002/nme.4911.

[229] F. Alobaid, "A particle-grid method for Euler-Lagrange approach", *Powder Technology* **2015**, *286*, 342–360, DOI 10.1016/j.powtec.2015.08.019.

[230] S. Deb, D. K. Tafti, "A novel two-grid formulation for fluid-particle systems using the discrete element method", *Powder Technology* **2013**, *246*, 601–616, DOI 10.1016/j.powtec.2013.06.014.

[231] M. Farzaneh, S. Sasic, A.-E. Almstedt, F. Johnsson, D. Pallarès, "A novel multigrid technique for Lagrangian modeling of fuel mixing in fluidized beds", *Chemical Engineering Science* **2011**, *66*, 5628–5637, DOI 10.1016/j.ces.2011.07.060.

[232] R. Sun, H. Xiao, "Diffusion-based coarse graining in hybrid continuum-discrete solvers: Applications in CFD-DEM", *International Journal of Multiphase Flow* **2015**, *72*, 233–247, DOI 10.1016/j.ijmultiphaseflow.2015.02.014.

[233] R. Sun, H. Xiao, "Diffusion-based coarse graining in hybrid continuum-discrete solvers: Theoretical formulation and a priori tests", *International Journal of Multiphase Flow* **2015**, *77*, 142–157, DOI 10.1016/j.ijmultiphaseflow.2015.08.014.

[234] A. D. Renzo, F. P. D. Maio, "Comparison of contact-force models for the simulation of collisions in DEM-based granular flow codes", *Chemical Engineering Science* **2004**, *59*, 525–541, DOI 10.1016/j.ces.2003.09.037.

[235] B. van Wachem, S. Sasic, "Derivation, simulation and validation of a cohesive particle flow CFD model", *AIChE Journal* **2007**, *54*, 9–19, DOI 10.1002/aic.11335.

[236] V. Salikov, S. Antonyuk, S. Heinrich, V. S. Sutkar, N. G. Deen, J. Kuipers, "Characterization and CFD-DEM modelling of a prismatic spouted bed", *Powder Technology* **2015**, *270*, 622–636, DOI 10.1016/j.powtec.2014.05.026.

[237] S. Radl, S. Sundaresan, "A drag model for filtered Euler-Lagrange simulations of clustered gas-particle suspensions", *Chemical Engineering Science* **2014**, *117*, 416–425, DOI 10.1016/j.ces.2014.07.011.

[238] R. Courant, K. Friedrichs, H. Lewy, "Über die partiellen Differenzengleichungen der mathematischen Physik", *Mathematische annalen* **1928**, *100*, 32–74.

[239] R. Issa, "Solution of the implicitly discretised fluid flow equations by operator-splitting", *Journal of Computational Physics* **1986**, *62*, 40–65, DOI 10.1016/0021-9991(86)90099-9.

[240] Z. Peng, B. Moghtaderi, E. Doroodchi, "A modified direct method for void fraction calculation in CFD-DEM simulations", *Advanced Powder Technology* **2016**, *27*, 19–32, DOI 10.1016/j.apt.2015.10.021.

[241] F. Marchelli, C. Moliner, B. Bosio, E. Arato, "A CFD-DEM sensitivity analysis: The case of a pseudo-2D spouted bed", *Powder Technology* **2019**, *353*, 409–425, DOI 10.1016/j.powtec.2019.05.035.

[242] R. Stanly, G. Shoev, "Detailed analysis of recent drag models using multiple cases of mono-disperse fluidized beds with Geldart-B and Geldart-D particles", *Chemical Engineering Science* **2018**, *188*, 132–149, DOI 10.1016/j.ces.2018.05.030.

[243] C. Fernandes, D. Semyonov, L. L. Ferrás, J. M. Nóbrega, "Validation of the CFD-DPM solver DPMFoam in OpenFOAM® through analytical, numerical and experimental comparisons", *Granular Matter* **2018**, *20*, 1–18, DOI 10.1007/s10035-018-0834-x.

[244] M. van Buijtenen, K. Buist, N. Deen, J. Kuipers, T. Leadbeater, D. Parker, "Numerical and experimental study on spout elevation in spout-fluidized beds", *AIChE Journal* **2011**, *58*, 2524–2535, DOI 10.1002/aic.12765.

[245] A. Penn, C. M. Boyce, T. Kovar, T. Tsuji, K. P. Pruessmann, C. R. Müller, "Real-Time Magnetic Resonance Imaging of Bubble Behavior and Particle Velocity in Fluidized Beds", *Industrial & Engineering Chemistry Research* **2018**, *57*, 9674–9682, DOI 10.1021/acs.iecr.8b00932.

[246] C. Boyce, A. Penn, M. Lehnert, K. Pruessmann, C. Müller, "Effect of liquid bridging on bubbles injected into a fluidized bed: A magnetic resonance imaging study", *Powder Technology* **2019**, *343*, 813–820, DOI 10.1016/j.powtec.2018.11.091.

[247] Z. Trad, C. Vial, J.-P. Fontaine, C. Larroche, "Modeling of hydrodynamics and mixing in a submerged membrane bioreactor", *Chemical Engineering Journal and the Biochemical Engineering Journal* **2015**, *282*, 77–90, DOI 10.1016/j.cej.2015.04.119.

[248] J. R. Banu, D. K. Uan, S. Kaliappan, I. T. Yeom, "Effect of sludge pretreatment on the performance of anaerobic/ anoxic/ oxic membrane bioreactor treating domestic wastewater", *International Journal of Environmental Science & Technology* **2011**, *8*, 281–290, DOI 10.1007/bf03326216.

[249] L.-G. Shen, Q. Lei, J.-R. Chen, H.-C. Hong, Y.-M. He, H.-J. Lin, "Membrane fouling in a submerged membrane bioreactor: Impacts of floc size", *Chemical Engineering Journal* **2015**, *269*, 328–334, DOI 10.1016/j.cej.2015.02.002.

[250] J. Chen, M. Zhang, F. Li, L. Qian, H. Lin, L. Yang, X. Wu, X. Zhou, Y. He, B.-Q. Liao, "Membrane fouling in a membrane bioreactor: High filtration resistance of gel layer and its underlying mechanism", *Water Research* **2016**, *102*, 82–89, DOI 10.1016/j.watres.2016.06.028.

[251] M. Zhang, H. Hong, H. Lin, L. Shen, H. Yu, G. Ma, J. Chen, B.-Q. Liao, "Mechanistic insights into alginate fouling caused by calcium ions based on terahertz time-domain spectra analyses and DFT calculations", *Water Research* **2018**, *129*, 337–346, DOI 10.1016/j.watres.2017.11.034.

[252] F. Meng, S.-R. Chae, A. Drews, M. Kraume, H.-S. Shin, F. Yang, "Recent advances in membrane bioreactors (MBRs): Membrane fouling and membrane material", *Water Research* **2009**, *43*, 1489–1512, DOI 10.1016/j.watres.2008.12.044.

[253] L. Liu, J. Tian, C. Luo, C. Chen, J. Liu, Z. Ma, X. Lu, "Research on in situ continuous off-line chemical cleaning in full-scale membrane bioreactors", *Bioresource Technology Report* **2018**, *4*, 186–192, DOI 10.1016/j.biteb.2018.10.005.

[254] P. R. Bérubé, E. R. Hall, P. M. Sutton, "Parameters Governing Permeate Flux in an Anaerobic Membrane Bioreactor Treating Low-Strength Municipal Wastewaters: A Literature Review", *Water Environment Research* **2006**, *78*, 887–896, DOI 10.2175/106143005x72858.

[255] M. Aslam, A. Charfi, G. Lesage, M. Heran, J. Kim, "Membrane bioreactors for wastewater treatment: A review of mechanical cleaning by scouring agents to control membrane fouling", *Chemical Engineering Journal and the Biochemical Engineering Journal* **2017**, *307*, 897–913, DOI 10.1016/j.cej.2016.08.144.

[256] K.-U. Do, R. J. Banu, D.-H. Son, I.-T. Yeom, "Influence of ferrous sulfate on thermochemical sludge disintegration and on performances of wastewater treatment in a new process: Anoxic-oxic membrane bioreactor coupled with sludge disintegration step", *Biochemical Engineering Journal* **2012**, *66*, 20–26, DOI 10.1016/j.bej.2012.04.013.

[257] C. H. Neoh, Z. Z. Noor, N. S. A. Mutamim, C. K. Lim, "Green technology in wastewater treatment technologies: Integration of membrane bioreactor with various wastewater treatment systems", *Chemical Engineering Journal and the Biochemical Engineering Journal* **2016**, *283*, 582–594, DOI 10.1016/j.cej.2015.07.060.

[258] D.-W. Gao, Q. Hu, C. Yao, N.-Q. Ren, W.-M. Wu, "Integrated anaerobic fluidized-bed membrane bioreactor for domestic wastewater treatment", *Chemical Engineering Journal and the Biochemical Engineering Journal* **2014**, *240*, 362–368, DOI 10.1016/j.cej.2013.12.012.

[259] J. Kim, K. Kim, H. Ye, E. Lee, C. Shin, P. L. McCarty, J. Bae, "Anaerobic Fluidized Bed Membrane Bioreactor for Wastewater Treatment", *Environmental Science and Technology* **2011**, *45*, 576–581, DOI 10.1021/es1027103.

[260] J. Li, Z. Ge, Z. He, "A fluidized bed membrane bioelectrochemical reactor for energy-efficient wastewater treatment", *Bioresource Technology* **2014**, *167*, 310–315, DOI 10.1016/j.biortech.2014.06.034.

[261] H. J. Tanudjaja, V. V. Tarabara, A. G. Fane, J. W. Chew, "Effect of cross-flow velocity, oil concentration and salinity on the critical flux of an oil-in-water emulsion in microfiltration", *Journal of Membrane Science* **2017**, *530*, 11–19, DOI 10.1016/j.memsci.2017.02.011.

[262] J. Bae, C. Shin, E. Lee, J. Kim, P. L. McCarty, "Anaerobic treatment of low-strength wastewater: A comparison between single and staged anaerobic fluidized bed membrane bioreactors", *Bioresource Technology* **2014**, *165*, 75–80, DOI 10.1016/j.biortech.2014.02.065.

[263] M. Ishii, K. Mishima, "Two-fluid model and hydrodynamic constitutive relations", *Nuclear Engineering and Design* **1984**, *82*, 107–126, DOI 10.1016/0029-5493(84)90207-3.

[264] H. Marschall, R. Mornhinweg, A. Kossmann, S. Oberhauser, K. Langbein, O. Hinrichsen, "Numerical Simulation of Dispersed Gas/Liquid Flows in Bubble Columns at High Phase Fractions using OpenFOAM®. Part I - Modeling Basics", *Chemical Engineering and Technology* **2011**, *34*, 1311–1320, DOI 10.1002/ceat.201100161.

[265] X. Huang, "CFD modeling of liquid-solid fluidization: Effect of drag correlation and added mass force", *Particuology* **2011**, *9*, 441–445, DOI 10.1016/j.partic.2011.03.005.

[266] G. Liu in *Granularity in Materials Science*, InTech, **2018**, DOI 10.5772/intechopen.79696.

[267] D. Hirche, F. Birkholz, O. Hinrichsen, "A hybrid Eulerian-Eulerian-Lagrangian model for gas-solid simulations", *Chemical Engineering Journal* **2019**, *377*, 119743, DOI 10.1016/j.cej.2018.08.129.

[268] F.-S. Lien, M. A. Leschziner, "A Pressure-Velocity Solution Strategy for Compressible Flow and Its Application to Shock/Boundary-Layer Interaction Using Second-Moment Turbulence Closure", *Journal of Fluids Engineering* **1993**, *115*, 717, DOI 10.1115/1.2910204.

[269] P. Roache, *Verification and Validation in Computational Science and Engineering*, Hermosa Publishers, Albuquerque, N.M, **1998**.

[270] I. Babuska, J. Oden, "Verification and validation in computational engineering and science: basic concepts", *Computer Methods in Applied Mechanics and Engineering* **2004**, *193*, 4057–4066, DOI 10.1016/j.cma.2004.03.002.

[271] W. L. Oberkampf, T. G. Trucano, C. Hirsch, "Verification, validation, and predictive capability in computational engineering and physics", *Applied Mechanics Reviews* **2004**, *57*, 345–384, DOI 10.1115/1.1767847.

[272] P. J. Roache, "Perspective: Validation—What Does It Mean?", *Journal of Fluids Engineering* **2009**, *131*, DOI 10.1115/1.3077134.

[273] M. A. Alves, P. J. Oliveira, F. T. Pinho, "A convergent and universally bounded interpolation scheme for the treatment of advection", *International Journal for Numerical Methods in Fluids* **2002**, *41*, 47–75, DOI 10.1002/fld.428.

[274] C.-W. Shu, "High-order Finite Difference and Finite Volume WENO Schemes and Discontinuous Galerkin Methods for CFD", *International Journal of Computational Fluid Dynamics* **2003**, *17*, 107–118, DOI 10.1080/1061856031000104851.

[275] J. Aubin, D. Fletcher, C. Xuereb, "Modeling turbulent flow in stirred tanks with CFD: the influence of the modeling approach, turbulence model and numerical scheme", *Experimental Thermal and Fluid Science* **2004**, *28*, 431–445, DOI 10.1016/j.expthermflusci.2003.04.001.

[276] D. Deglon, C. Meyer, "CFD modelling of stirred tanks: Numerical considerations", *Minerals Engineering* **2006**, *19*, 1059–1068, DOI 10.1016/j.mineng.2006.04.001.

[277] L. F. Richardson, "The approximate arithmetical solution by finite differences of physical problems involving differential equations, with an application to the stresses in a masonry dam", *Philosophical Transactions of the Royal Society of London. Series A Containing Papers of a Mathematical or Physical Character* **1911**, *210*, 307–357, DOI 10.1098/rsta.1911.0009.

[278] P. J. Roache, "Need for control of numerical accuracy", *Journal of Spacecraft and Rockets* **1990**, *27*, 98–102, DOI 10.2514/3.26113.

[279] I. B. Celik, U. Ghia, P. J. Roache, C. J. Freitas, H. Coleman, P. E. Raad, "Procedure for Estimation and Reporting of Uncertainty Due to Discretization in CFD Applications", *Journal of Fluids Engineering* **2008**, *130*, 078001, DOI 10.1115/1.2960953.

[280] A. Gandhir, Y. Hassan, "Computational Analysis of Fluid Flow in Pebble Bed Modular Reactor Using Different Turbulence Models", **2010**, DOI 10.1115/fedsm-icnmm2010-30974.

[281] B. Estejab, PhD thesis, Virginia Polytechnic Institute and State University, Blacksburg, Virginia.

[282] A. Volk, U. Ghia, C. Stoltz, J. Hecht, J. Stamper, "Quantification of Numerical and Modeling Errors in Simulation of Fluid Flow Through a Fixed Particle Bed", **2016**, DOI 10.1115/fedsm2016-7561.

[283] A. K. Sahu, V. Raghavan, B. Prasad, "Temperature effects on hydrodynamics of dense gas-solid flows: Application to bubbling fluidized bed reactors", *International Journal of Thermal Sciences* **2018**, *124*, 387–398, DOI 10.1016/j.ijthermalsci.2017.10.028.

[284] P. J. Donaubauer, L. Schmalhorst, O. Hinrichsen, "2D flow fields in fixed-bed reactor design: a robust methodology for continuum models", *Chemical Engineering Science* **2019**, *208*, 115137, DOI 10.1016/j.ces.2019.07.055.

[285] C. Jäkel, S. Kelm, K. Verfondern, H.-J. Allelein, "Validation of a 3D multiphase-multicomponent CFD model for accidental liquid and gaseous hydrogen releases", *International Journal of Hydrogen Energy* **2019**, *44*, 8807–8818, DOI 10.1016/j.ijhydene.2018.10.024.

[286] M. Moein-Jahromi, M. Kermani, "Three-dimensional multiphase simulation and multi-objective optimization of PEM fuel cells degradation under automotive cyclic loads", *Energy Conversion and Management* **2021**, *231*, 113837, DOI 10.1016/j.enconman.2021.113837.

[287] S. K. Senapati, S. K. Dash, "Gas–solid flow in a diffuser: Effect of inter-particle and particle–wall collisions", *Particuology* **2021**, *57*, 187–200, DOI 10.1016/j.partic.2021.01.006.

[288] H. Islam, C. G. Soares, "Assessment of uncertainty in the CFD simulation of the wave-induced loads on a vertical cylinder", *Marine Structures* **2021**, *80*, 103088, DOI 10.1016/j.marstruc.2021.103088.

[289] S. Dabiri, A. Noorpoor, M. Arfaee, P. Kumar, W. Rauch, "CFD Modeling of a Stirred Anaerobic Digestion Tank for Evaluating Energy Consumption through Mixing", *Water* **2021**, *13*, 1629, DOI 10.3390/w13121629.

[290] P. Ostermeier, F. Dawo, A. Vandersickel, S. Gleis, H. Spliethoff, "Numerical calculation of wall-to-bed heat transfer coefficients in Geldart B bubbling fluidized beds with immersed horizontal tubes", *Powder Technology* **2018**, *333*, 193–208, DOI 10.1016/j.powtec.2018.04.028.

[291] L. Boltzmann, "Über die Eigenschaften monozyklischer und anderer damit verwandter Systeme", *Crelles Journal* **1884**, *98*, 86–94.

[292] G. Gallavotti, "Ergodicity, ensembles, irreversibility in Boltzmann and beyond", *Journal of Statistical Physics* **1995**, *78*, 1571–1589.

[293] R. Panday, L. J. Shadle, M. Shahnam, R. Cocco, A. Issangya, J. S. Spenik, J. C. Ludlow, B. Gopalan, F. Shaffer, M. Syamlal, C. Guenther, S. R. Karri, T. Knowlton, "Challenge problem: 1. Model validation of circulating fluidized beds", *Powder Technology* **2014**, *258*, 370–391, DOI 10.1016/j.powtec.2014.02.010.

[294] D. A. Clarke, A. J. Sederman, L. F. Gladden, D. J. Holland, "Investigation of Void Fraction Schemes for Use with CFD-DEM Simulations of Fluidized Beds", *Industrial & Engineering Chemistry Research* **2018**, *57*, 3002–3013, DOI 10.1021/acs.iecr.7b04638.

[295] C. Wu, A. Berrouk, K. Nandakumar, "Three-dimensional discrete particle model for gas–solid fluidized beds on unstructured mesh", *Chemical Engineering Journal* **2009**, *152*, 514–529, DOI 10.1016/j.cej.2009.05.024.

[296] C. Wu, J. Zhan, Y. Li, K. Lam, A. Berrouk, "Accurate void fraction calculation for three-dimensional discrete particle model on unstructured mesh", *Chemical Engineering Science* **2009**, *64*, 1260–1266, DOI 10.1016/j.ces.2008.11.014.

[297] L. Jing, C. Y. Kwok, Y. F. Leung, Y. D. Sobral, "Extended CFD-DEM for free-surface flow with multi-size granules", *International Journal for Numerical and Analytical Methods in Geomechanics* **2015**, *40*, 62–79, DOI 10.1002/nag.2387.

[298] Q. Kang, D. He, N. Zhao, X. Feng, J. Wang, "Hydrodynamics in unbaffled liquid-solid stirred tanks with free surface studied by DEM-VOF method", *Chemical Engineering Journal* **2020**, *386*, 122846, DOI 10.1016/j.cej.2019.122846.

[299] L. Wang, J. Ouyang, C. Jiang, "Direct calculation of voidage in the fine-grid CFD-DEM simulation of fluidized beds with large particles", *Particuology* **2018**, *40*, 23–33, DOI 10.1016/j.partic.2017.11.010.

[300] H. A. Khawaja, S. A. Scott, M. S. Virk, M. Moatamedi, "Quantitative Analysis of Accuracy of Voidage Computations in CFD-DEM Simulations", *The Journal of Computational Multiphase Flows* **2012**, *4*, 183–192, DOI 10.1260/1757-482x.4.2.183.

List of Figures

List of Tables

List of Publications

Journal Publications

- D. Hirche, F. Birkholz, O. Hinrichsen, "A hybrid Eulerian-Eulerian-Lagrangian model for gas-solid simulations", *Chemical Engineering Journal* **2019**, *377*, 119743, DOI 10.1016/j.cej.2018.08.129.

- D. Hirche, J.W. Chew, O. Hinrichsen, "CFD-DEM study of geometry changes in an AnFMBR towards particle momentum", *Chemical Engineering Journal* **2020**, *379*, 122336, DOI 10.1016/j.cej.2019.122336.

- D. Hirche, O. Hinrichsen, "Implementation and evaluation of a three-level grid method for CFD-DEM simulations of dense gas-solid flows", *Chemical Engineering Journal Advances* **2020**, *4*, 100048, DOI 10.1016/j.ceja.2020.100048.

Oral Presentations

- D. Hirche, F. Birkholz, O. Hinrichsen, "Approach to a hybrid Eulerian-Eulerian-Lagrangian Model for Gas-Solid Simulations", 25th International Symposium on Chemical Reaction Engineering, Florence, Italy, **2018**.

- D. Hirche, O. Hinrichsen, "Evaluation of a Dual-Grid Method for Multiscale TFM and CFD-DEM Simulations of Dense Gas-Solid Flows", FLUIDIZATION XVI, Guilin, China, **2019**.

- D. Hirche, D.-I. Mehelean, O. Hinrichsen, "Assessing different volume fraction determinations in three-phase flow simulations using CFD-VoF-DEM", 4th Indo-German Workshop, Berlin, Germany, **2020**.

- O. Hinrichsen, D. Hirche, "Evaluation of a three-level grid approach for the simulation of granular flows", 26th International Symposium on Chemical Reaction Engineering & 9th Asia-Pacific Chemical Reaction Engineering Symposium, Delhi, India, **2021**.

Poster Presentations

- Hirche D., Birkholz, F., Hinrichsen, O., "Approach to a hybrid Eulerian-Eulerian-Lagrangian Model for Gas-Solid Simulations", Jahrestreffen Reaktionstechnik, Würzburg, Germany, **2018**.

- Hirche D., Hinrichsen, O., "Numerical Study in Effect of built-in Impediment in an Anaerobic Fluidized Bed Membrane Reactor for Fouling Mitigation", XXIII International Conference on Chemical Reactors, Ghent, Belgium, **2018**.

- Hirche D., Hinrichsen, O., "A dual-grid method for dense gas-solid flow using CFD-DEM", Jahrestreffen Reaktionstechnik, Würzburg, Germany, **2019**.

- Hirche D., Hinrichsen, O., "Improvement of CFD-DEM simulations using a three--level grid method", Jahrestreffen Reaktionstechnik, Würzburg, Germany, **2021**.

- Bauer C., Fernengel J., Hirche, D., Hinrichsen, O., "Influence of material properties on porosity of numerically generated random packed beds of spheres", 26th International Symposium on Chemical Reaction Engineering & 9th Asia-Pacific Chemical Reaction Engineering Symposium, Delhi, India, **2021**.